

**STRUCTURE-PROPERTY RELATIONSHIPS IN LEAD HALIDE
PEROVSKITES FOR SOLAR CELLS**

A Dissertation
Presented to
The Academic Faculty

by

Juanita Hidalgo

In Partial Fulfillment
of the Requirements for the Degree
Doctor of Philosophy in the
School of Materials Science and Engineering

Georgia Institute of Technology
August 2023

COPYRIGHT © 2023 BY JUANITA HIDALGO

STRUCTURE-PROPERTY RELATIONSHIPS IN LEAD HALIDE PEROVSKITES FOR SOLAR CELLS

Approved by:

Dr. Juan-Pablo Correa-Baena, Advisor
School of Materials Science and Engineering
Georgia Institute of Technology

Dr. Faisal Alamgir
School of Materials Science and Engineering
Georgia Institute of Technology

Dr. Hamid Garmestani
School of Materials Science and Engineering
Georgia Institute of Technology

Dr. Angus Wilkinson
School of Chemistry and Biochemistry
Georgia Institute of Technology

Dr. Nazanin Bassiri-Gharb
School of Materials Science and Engineering
Woodruff School of Mechanical Engineering
Georgia Institute of Technology

Date Approved: June 26, 2023

Para Baba y Yita,

ACKNOWLEDGEMENTS

This work has been possible with the significant and valuable contributions of a great number of people. I would like to express my gratitude to my advisor, Professor Juan-Pablo Correa-Baena, for his unwavering trust in me right from the beginning when I presented my research work at the conference in Cali, Colombia. I am truly grateful for Juan-Pablo's guidance and immense support throughout my entire PhD. Thanks to Juan-Pablo for cultivating and improving my scientific communication skills, which I appreciate, and think are the key to development. I would also like to extend a special appreciation to my friend and colleague, Dr. Carlo Perini, for his support, scientific discussions, and hours spent brainstorming new hypotheses and ideas, and piecing together the scientific puzzle. I sincerely thank to all the other *Energy Materials Lab* members who have contributed to my PhD experience, namely Yu An, Diana LaFollette, Sanggyun Kim, and Mac Jones.

Further, I would like to express my gratitude to Professor Susan Schorr for trusting, supporting my research, and welcoming me into her department at the Helmholtz Zentrum Berlin for one year. I am also thankful to Dr. Joachim Breternitz for his scientific guidance, invaluable feedback, and advice. I am truly grateful to Susan and Joachim for their major guidance in the field of crystallography, which has been fundamental to this dissertation. I would like to extend my thanks to all the other members of the Helmholtz Zentrum Berlin who have supported, taught, and guided me since the beginning of my PhD, including Professor Antonio Abate, Dr. Nga Phung, Dr. Silver-Hamill Turren-Cruz, and Ana Palacios-Saura. Your presence made my time in Berlin more fulfilling, and you have played an integral role in my PhD journey.

I would like to thank Dr. Ruipeng Li, for his invaluable assistance with the GIWAXS measurements and analysis, core of this dissertation. I would also like to acknowledge the contributions of all the theoretical collaborators who have had a significant impact on the outcomes of this dissertation. Our countless hours of calls and months of discussions have been instrumental in shaping

the research in this dissertation. I extend my acknowledgment to Dr. Waldemar Kaiser and Professor Joshua S. Kretchmer. In addition, I thank the members of my PhD committee, namely Professor Nazanin Bassiri-Gharb, Professor Angus Wilkinson, Professor Hamid Garmestani, and Professor Faisal Alamgir, for asking about the big “why” of my research, thus guiding this dissertation. I also want to thank Professor Pablo Ortiz from Universidad de los Andes, who first introduced me to the world of perovskite research in 2016.

I am grateful for the financial support I have received throughout my PhD from various fellowships. Firstly, I want to thank the Georgia Tech Fellowship Graduate Assistance in Areas of National Need (GAANN). Secondly, I extend my acknowledgment to the Graduate Education for Minorities (GEM) fellowship. Thirdly, I am thankful for the German Academic Exchange Service (DAAD) scholarship, which allowed me to conduct one year of research at the Helmholtz Zentrum Berlin, Germany.

Finally, I would like to express my heartfelt gratitude to my grandfather, *Baba*, who inspired me to pursue a PhD with his own PhD achievement. I extend this gratitude to my whole Familia Manzano Díaz, and to my Familia Hidalgo. I am extremely thankful to my parents, César and Patricia, and sister, María, for their unwavering support, engaging conversations, and constant company throughout this PhD adventure, *gracias!* I have special and immense gratitude for Giulio, who has supported me and lived with me on this PhD journey, long and short distance, guiding me toward the overarching purpose of science.

TABLE OF CONTENTS

ACKNOWLEDGEMENTS	iv
LIST OF TABLES	ix
LIST OF FIGURES	x
LIST OF SYMBOLS AND ABBREVIATIONS	xvii
SUMMARY	xx
CHAPTER 1. Introduction	1
1.1 Energy Background	1
1.2 Solar Energy and Photovoltaics	3
1.3 Perovskite Solar Cells: Opportunities and Challenges	5
1.4 Aim of this Dissertation	7
CHAPTER 2. Background	10
2.1 Lead Halide Perovskites	11
2.1.1 Crystal Structure	11
2.1.2 Low-dimensional Ruddlesden-Popper Structures	18
2.1.3 Electronic and Optical Properties	20
2.2 Perovskite Solar Cells	25
2.3 Polycrystalline Perovskite Films from Solution	27
2.3.1 Colloids and Intermediate Phases	29
CHAPTER 3. Experimental Methods	32
3.1 Lead Halide Perovskite Fabrication	33
3.1.1 Precursor Solution	33
3.1.2 Thin Film Deposition	36
3.1.3 Post-deposition Treatments	36
3.2 Solar Cell Fabrication	39
3.3 Characterization of the Structure by X-ray Scattering	40
3.3.1 Grazing Incidence Wide-Angle X-ray Scattering	40
3.3.2 X-ray Diffraction	46
3.3.3 Small Angle X-ray Scattering	48
3.4 Elemental Chemistry Characterization	49
3.4.1 Surface Chemistry by X-ray Photoelectron Spectroscopy	49
3.4.2 Bulk Chemistry by X-ray Fluorescence and Operando X-ray Beam Induced Current	50
3.5 Morphology and Optical Properties Characterization	51
3.5.1 Scanning Electron Microscopy	51
3.5.2 UV-VIS Spectroscopy	52
3.6 Solar Cell Characterization	53
3.6.1 Photovoltaic Performance	53
3.6.2 Impedance Spectroscopy	55

CHAPTER 4. Crystallographic Orientation in Halide Perovskites	56
4.1 The Role of the Solvent and A-site Cation	58
4.1.1 Early Stages of Crystallization	61
4.1.2 Preferred Crystallographic Orientation	63
4.1.3 Mechanisms for Preferred Orientation	67
4.1.4 Solar Cell Performance and Ionic Movement	70
4.1.5 Conclusions	74
4.2 Humidity-Induced Crystallographic Reorientations and Effects on Charge Carrier Extraction in Perovskite Solar Cells	75
4.2.1 Morphology of the LHP Thin Films	76
4.2.2 Elemental Chemistry by XPS	78
4.2.3 Structural Analysis of the LHP Thin Films	79
4.2.4 Optical Properties	83
4.2.5 Perovskite Solar Cell Performance	85
4.2.6 Chemical Composition and Induced Current Mapping	87
4.2.7 Reorientation Mechanism	89
4.2.8 Conclusions	91
4.3 Chapter Conclusions	92
CHAPTER 5. Undesired Phase Transformations in Halide Perovskites	93
5.1 Structural Phase Transformations	95
5.2 Surface Chemistry	98
5.3 Chemical Reaction Mechanism	100
5.4 Conclusions	105
CHAPTER 6. Preventing Phase Transformations in Halide Perovskites	106
6.1 The Role of PEA I	107
6.1.1 PEA I on Pure FAPI	109
6.1.2 PEA I on CsFA Improves H ₂ O Stability	120
6.1.3 The Role of PEA I Conclusions	123
6.2 The Role of Br at Low Temperatures	123
6.2.1 Properties and Structure at Room Temperature and 300 K	125
6.2.2 (Cs,FA)Pb(I,Br) ₃ Temperature Phase Diagram	130
6.2.3 Br addition Improves Stability at Low Temperatures	133
6.2.4 Conclusions	135
CHAPTER 7. Conclusions and Outlook	137
7.1 Insights and Opportunities: Crystallization and Facet Properties	137
7.2 Insights and Opportunities: Perovskites and Non-Perovskites	139
7.3 Insights and Opportunities: Strategies to Stabilize the Perovskite	141
7.4 Insights and Opportunities in Advanced Characterization	142
APPENDIX A. Supporting information: Crystallographic Orientation	144
A.1 Solvent and A-site Cation Role	144
A.1.1 Theoretical Calculations Methods	144
A.1.2 Early Stages of Crystallization	146
A.1.3 Structural Analysis	146
A.1.4 Perovskite Solar Cells	150

A.1.5	Impedance Spectroscopy	152
A.2	Crystallographic Reorientation	153
A.2.1	Surface Chemistry by XPS	153
A.2.2	Structure Analysis by XRD	155
A.2.3	Structure Analysis by GIWAXS	162
A.2.4	Optical Properties	165
A.2.5	Perovskite Solar Cells	165
APPENDIX B. Supporting Information: Undesired Phase Transformations In Halide Perovskites		167
B.1	Experimental Details	167
B.2	GIWAXS Characterization Setup	168
B.3	Structural Phase Transformations	169
B.4	Surface Chemistry	178
B.5	Bulk Chemistry	185
B.6	DFT Calculations	189
B.6.1	Surface Models and Computational Details	189
B.6.2	Modeling of Reactions	190
B.6.3	DFT Model of Hydration	190
B.6.4	DFT Supporting Information	191
B.6.5	DFT Superoxide Formation	194
APPENDIX C. Supporting Information: Preventing PHase Transformations in Halide Perovskites		199
C.1	PEAI in FAPI	199
C.1.1	Structural Analysis	199
C.1.2	Surface Morphology and XPS	202
C.1.3	Photoluminescence and THz	204
C.1.4	FAPI Perovskite Solar Cells	207
C.2	PEAI on CsFA: Humidity Exposure	208
C.2.1	DFT Calculations	208
C.2.2	In-situ humidity by GIWAXS	209
C.2.3	CsFA Perovskite Solar Cells	211
C.3	The Role of Br at Low Temperatures	215
C.3.1	UV-VIS	215
C.3.2	Le Bail Refinements	216
C.3.3	In-situ Low-Temperature Powder XRD	220
APPENDIX D. Peer-Reviewed Publications		227
REFERENCES		230

LIST OF TABLES

Table 2.1	Crystal structure of lead halide perovskites studied in this dissertation.	14
Table 2.2	Crystal structure of non-perovskite phases studied in this dissertation.	16
Table 2.3	Bandgaps of different single-cation single-halide LHP compositions.	22
Table 2.4	Bandgaps of Non-Perovskite Phases from DFT.	23
Table 3.1	Atomic scattering factors.	43

LIST OF FIGURES

Figure 1.1	World Final Energy Consumption in Mtoe (mega tonnes of oil equivalent, 1 toe equals to 41.868 GJ), taken from the International Energy Agency (IEA) Sankey open website.	1
Figure 1.2	Pie charts of the percentage in total net production of energy for all the OECD countries taken from the Monthly Electricity Statistics from the IEA (International Energy Agency).	2
Figure 1.3	Best Cell-Efficiency chart for the 1st, 2nd, and 3rd generations of single junction PVs. Data taken from NREL chart. ¹² Dashed-line indicates the SQ limit of single-junction maximum efficiency.	4
Figure 1.4	Polymorphism in APbX ₃ includes a (left) perovskite phase and (center, right) non-perovskite phases.	6
Figure 1.5	Graphical representation of the aim of this	8
Figure 1.6	Schematic summarizing the parts, chapters, and topics of this dissertation. Part one (blue), part two (green), and part three (orange).	9
Figure 2.1	Lead halide perovskite structure ABX ₃ (A) A, B and X site in the perovskite structure (B) Calculated tolerance factor in ascendent order for selected perovskite compositions.	12
Figure 2.2	Structure-field maps for tolerance factor t versus the octahedral factor for halide perovskites. ²⁹	13
Figure 2.3	Perovskite crystal systems for FA-rich LHPs.	15
Figure 2.4	Non-perovskite crystal structure adapted by APbX ₃ compositions.	17
Figure 2.5	Schematic of the Cs _x FA _{1-x} PbI ₃ phase diagram with estimated phase-transition positions. Reprinted with permission from <i>Chem. Mater.</i> 2020, 32, 2282-2291. Copyright 2020 American Chemical Society	18
Figure 2.6	Electronic structure of defect intolerant semiconductors versus defect tolerant LHPs versus. Reproduced with permission from <i>Chem. Mater.</i> 2017, 29, 4667-4674. Copyright 2017 American Chemical Society.	20
Figure 2.7	Bandgap of perovskites depending on dimensionality and number of n layers of the low-dimensional structures.	25
Figure 2.8	Maximum power conversion efficiency as a function of bandgap and experimental values achieved.	26
Figure 2.9	Perovskite solar cell architecture n-i-p.	27

Figure 2.10	Crystallization from solution, adapted LaMer diagram to perovskites. This dissertation will focus on the I stage, the precursor solution.	28
Figure 2.11	Schematic of the precursor salts in solution and perovskite colloids formation. (A) Mixture of AX and PbX ₂ , followed by (B) particle interaction and formation of Pb-X octahedra with differences in bonds, forming edge-, face- and or corner-sharing octahedra. (C) Overall schematic of colloids formation in solution.	30
Figure 2.12	Generalized schematic of the crystallization products of LHP in different solvents (A) DMF, and (B) DMSO.	31
Figure 3.1	Schematic of the fabrication steps of lead halide perovskites. (left) Preparation of the precursor solution by mixing the halide salts in a polar solvent DMF, DMF:DMSO or DMSO, (center) Thin film deposition by spin coating using the antisolvent method, (right) post-deposition annealing at high temperature.	33
Figure 3.2	Humidity exposure of LHP films for <i>ex-situ</i> measurements. (left) First, the LHP is deposited, as described in Figure 3.1, inside a nitrogen glovebox. Subsequently, (center) the film is exposed to air and humidity, outside the glovebox, with a controlled humidity of around 75%. Humidity exposure is for 24 hours, and after (right), the LHP is characterized or returned to the nitrogen glovebox for storage.	38
Figure 3.3	Schematic of the setup for humidity exposure for <i>in-situ</i> GIWAXS measurements. The relative humidity is controlled by the flow of a dry gas, either air or nitrogen, passing through a water bubbler and then into the measurement chamber. The setup is shown in Appendix B, Figure BS1.	39
Figure 3.4	Schematic of the grazing incidence wide angle X-ray scattering (GIWAXS) setup by irradiating a synchrotron X-ray with an incident angle (α_i) relative to the thin film sample, scattering in the xy and z directions resulting in a 2D GIWAXS scattering pattern q_z versus q_r .	42
Figure 3.5	Calculated X-ray (13.5 keV) penetration depth as a function of the incident angle (α_i) in FAPbI ₃ thin films.	44
Figure 3.6	Qualitative information on crystallographic orientation from GIWAXS patterns. (left) A complete scattering ring indicative of random orientation. (center) Arc indicative of preferred orientation, and (right) sharp Bragg spot indicative of a high degree of preferred orientation. Figure modified and reproduced with permission from <i>Chem. Rev.</i> 2012, 112, 5488-5519. Copyright 2012 American Chemical Society.	45
Figure 4.1	Particle interactions in the precursor solution. (A) SAXS data for the four studied systems MAPbBr ₃ in DMF or DMSO, and FAPbBr ₃ in DMF or DMSO. (B) Schematic of the particle interaction in DMF and DMSO interpreted from SAXS data, A is MA or FA, and d is the interparticle distance.	62

- Figure 4.2 Figure Interplay of solvent and A-site cation in the crystallographic orientation of lead bromide films studied by GIWAXS. (A,B) 2D GIWAXS patterns in DMF, DMF:DMSO (4:1 volume), and DMSO for (A) MAPbBr₃ and (B) FAPbBr₃. (C,D) Azimuthal integration profiles of the main Debye-Scherrer rings (100 and 110) as a function of the χ angle from GIWAXS for three solvent systems for (C) MAPbBr₃ and (D) FAPbBr₃. (E) FWHM and error bar of the azimuthal peak for MAPbBr₃ and FAPbBr₃ as a function of the solvent. 67
- Figure 4.3 Results of the DFT calculation for the representative (100) and (110) surfaces of MAPbBr₃ and FAPbBr₃. (A) Surface energy of the analyzed structures computed for surfaces with PbBr₂ or FABr/MABr termination. (B) Energy difference between the corresponding (110) and (100) surfaces. (C) Representative final structures of the FABr/MABr terminated calculation for MAPbBr₃ and FAPbBr₃. The inorganic lattice of the bottom surface that demonstrates the PbBr₂ phase was frozen throughout the calculation. (D) Pictorial representation of the increased surface disorder due to the presence of two competing surfaces in FAPbBr₃. 69
- Figure 4.4 Electrical properties of solar cell. (A) Perovskite solar cell architecture where A in APbBr₃ is MA or FA in DMSO, (B) Box plots of the solar cell characterization from J-V curve open circuit voltage, and absolute hysteresis index of the power conversion efficiency (PCE). (C,D) Impedance spectroscopy measurements for MAPbBr₃ and FAPbBr₃ solar cells. (C) Equivalent circuit used for the analysis of the impedance spectra, (D) Recombination and transport resistance for different applied biases (R_{rec+tr}), low-frequency capacitance for different applied biases (C_{dr}), and low-frequency resistor (R_{dr}). 72
- Figure 4.5 SEM images for each studied condition of LHP on top of ITO substrates and the grain size histogram (fitted by a log-normal distribution) from 5 analyzed images per condition. Without humidity exposure (w/o H₂O) and exposed to humidity (H₂O) for 24 hours RH ~70%. Stoichiometry Pb:A ratio is 1.09: 1 for EL, and 0.95: 1 for EO. Scale bar is 1 μ m. 77
- Figure 4.6 Elemental chemistry by XPS surface composition: element (Z) to Pb atomic percentage ratio (Z:Pb) calculated from XPS for Pb 4f, Br 3d (square), C 1s (circle), N 1s (triangle), and O 1s (star) for each of the studied conditions. Without humidity exposure (w/o H₂O) and exposed to humidity (H₂O) for 24 hours RH ~70%. Stoichiometry Pb:A ratio is 1.09: 1 for EL, and 0.95: 1 for EO. 78
- Figure 4.7 Structure of CsMAFA films by XRD. (A) XRD pattern with characteristic simple cubic LHP peaks labeled and (B) micro strain calculated from the Williamson-Hall plot method. The results were calculated from 4 different series of XRD patterns, and the average and standard deviation are shown. Without humidity exposure (w/o H₂O) and exposed to humidity (H₂O) for 24 hours RH ~70%. Stoichiometry Pb:A ratio is 1.09: 1 for EL, and 0.95: 1 for EO. 80
- Figure 4.8 GIWAXS with different stoichiometric content without (w/o) exposure to humidity (H₂O) for (A) EL and (B) EO. Integrated intensity plots in the 82

azimuth angle (χ) along the ring at q_r (1.012) corresponding to the plane (001) for a cubic structure at different incident angles α , 0.1° (surface) and 0.5° (bulk) for (C) EL and (D) EO. Schematic of the hypothesized rearrangement of the crystal orientations at the surface and bulk in the (001) plane for (E) EL and (F) EO.

- Figure 4.9 Optical measurements: (A) steady state normalized PL spectra for EL and EO LHP deposited over FTO, (B) band gap from the PL emission peak and (C) UV-VIS absorption spectra. Without humidity exposure (w/o H₂O) and exposed to humidity (H₂O) for 24 hours RH ~70%. Stoichiometry Pb:A ratio is 1.09: 1 for EL, and 0.95: 1 for EO. 84
- Figure 4.10 Solar cell characterization. (A) Boxplots of J_{sc}, and PCE showing the distribution of all measured devices in a reverse bias for different stoichiometries with or without exposure to humidity *J-V* curves of the best pixel for (B) EL and (C) EO devices without (w/o) and with exposure to humidity (H₂O). Inset graphs show the maximum power point tracking (MPPT) for 170 s for a random pixel studied (not corresponding to same pixel from *J-V* curve). (D,E) Average PCE_{MPPT} from the stability aging test by maximum power point tracking (MPPT) for 170 hours from a total of 10 pixels for (D)EL (D) and (E) EO. 87
- Figure 4.11 XRF for the elemental ratio between Br:Pb and XBIC for the different set of solar cells (A) EL and (B) EO, with and without humidity treatment. Scale bar is 5 mm (C) Boxplot and normal distribution of the integrated XBIC data for EL and EO solar cells. 88
- Figure 4.12 Reorientation mechanism in excess organics CsMAFA LHP thin films. 90
- Figure 5.1 Humidity-induced structural phase transformations by *in-situ* GIWAXS. The structural phases analyzed are (A) tetragonal b-perovskite of space group *P4/mbm* (left), 2H FAPbI₃ hexagonal non-perovskite phase of space group *P6₃/mmc* (center), and orthorhombic d-CsPbI₃ non-perovskite phase of space group *Pnma* (right). By *in-situ* GIWAXS we studied the phase transformations of CsFA b-perovskite in (B) H₂O/Air, (D) H₂O/N₂, (F) dry air, and where (C, E, G) are the corresponding integrated areas of the main scattering peak of each phase. 97
- Figure 5.2 Surface chemistry by XPS. XPS spectrum of the peaks: (A) N 1s, (B) I 3d, (C) O 1s of CsFA perovskite, FAI, and PbI₂ films w/o and after H₂O/Air exposure. For the CsFA perovskite films, panel (D) Atomic ratio of Iodine (I), Cesium (Cs), Nitrogen (N, FA), or Oxygen (O) normalized to lead (Pb), w/o and after H₂O/Air exposure. CsFA perovskite films without (w/o) H₂O exposure (green) were fabricated in a nitrogen glovebox and exposed to room atmosphere while mounting the XPS measurement. CsFA films after H₂O/Air exposure (blue) were fabricated in a nitrogen glovebox, exposed to humidity, and then measured. 100
- Figure 5.3 DFT calculation of iodide oxidation and superoxide formation on the perovskite surface. Panel (A) visualizes the formation of IO_n⁻ species upon oxidation of surface iodide ions [Rx. 1]; from left to right: hypoiodite, IO⁻; iodite, IO₂⁻; iodate, IO₃⁻; and periodate, IO₄⁻. All oxidized species are 103

explicitly highlighted, and reaction energies are given (see computational methods for details). (B) Reaction mechanism [Rx. 2 and 3] of (left) lead (II) iodate, $\text{Pb}(\text{IO}_3)_2$, formation by consumption of oxygen molecules, and (right) removal of $\text{Pb}(\text{IO}_3)_2$ resulting in a surface vacancy VPbI_2 . The following color code is used for the atomic representations: purple, I; cyan, Pb; blue, N; green, Cs; gray, C; white, H; red, O.

- Figure 5.4 Surface and bulk mechanism when CsFA is exposed to $\text{H}_2\text{O}/\text{Air}$. (I) H_2O is adsorbed on the CsFA surface, promoting the loss of FAI (g). Surface vacancies are created leading to preferential oxygen binding sites, favoring the oxidation of iodide and energetically favorable (II) formation of $\text{Pb}(\text{IO}_3)_2$, which will (III) create a PbI_2 vacancy. Surface vacancies and the loss of FAI will lead to faster phase segregation and (IV) phase transformations from mixed-cation perovskite into single-cation non-perovskite phases. 104
- Figure 6.1 FAPI-PEAI experimental design. (A) Schematic representation of the preparation of PEAI-treated FAPI films by spin coating PEAI as a post-deposition process after FAPI annealing. (B) Schematic showing the suggested structure at the surface and bulk after PEAI deposition into the 3D FAPI perovskite. (C) The solar cell device architecture adopted in this study. 110
- Figure 6.2 GIWAXS analysis of the untreated FAPI films. (A) 2D pattern at two different incident angles 0.05° for the surface, 0.5° for the bulk. (B) circular average showing the ranges where LD PEAI-based, hexagonal polytypes, and perovskite peaks are expected. (C) Schematic of crystallographic phases observed at the surface and bulk of FAPI. The legend of the non-perovskite phases is shown in the schematics. 112
- Figure 6.3 GIWAXS analysis of the 1 mg/mL PEAI-treated FAPI. (A) 2D GIWAXS pattern at two different incident angles 0.05° for the surface, 0.5° for the bulk. (B) Circular average showing the ranges where LD PEAI-based, hexagonal polytypes, and perovskite peaks are present. (C) Schematic of crystallographic phases in the FAPbI_3 surface and bulk. The legend of the non-perovskite phases is shown in the schematics. 113
- Figure 6.4 GIWAXS analysis of the 5 mg/mL PEAI-treated FAPI. (A) 2D GIWAXS pattern at two different incident angles 0.05° for the surface, 0.5° for the bulk. (B) circular average showing the ranges where LD PEAI-based, hexagonal polytypes, and perovskite peaks are present. (C) schematic of crystallographic phases in the FAPbI_3 surface and bulk. The legend of the non-perovskite phases is shown in the schematics. 114
- Figure 6.5 Surface chemistry by XPS on FAPI films treated with PEAI. (A) C 1s, (B) N 1s, and (C) Pb 4f spectra. 116
- Figure 6.6 The effect of PEAI concentrations on (A) PL emission and (B) trPL carrier lifetime. (C) Charge carrier mobilities from THz. 1 mg/mL PEAI is labeled “1 PEAI” and 5 mg/mL PEAI is labeled “5 PEAI”. 117

Figure 6.7	FAPI Solar Cells. (A) Open circuit voltage (V_{OC}) and (B) PCE for solar cells with FAPI untreated and treated with PEAI. The data points are plotted in boxplots which show the median (central line) and the lower and upper quartiles (25% and 75%) (bottom and top lines of the box, respectively). (C) J-V curves of a high-performing device of the FAPI untreated and treated with 5 mg/mL of PEAI.	119
Figure 6.8	PEAI layer to stabilize the CsFA perovskite in H_2O /Air. Panel (A) shows H_2O adsorption energy on a CsFA surface and CsFA-PEAI surface calculated by DFT. From GIWAXS measurements in Figure CS14, (B) is the integrated area of the main scattering peak of each phase in H_2O /Air, and (C) the 2D GIWAXS patterns from the surface and bulk measurements after 600 min exposed to H_2O /Air for the (left) PEAI-treated CsFA films, and (right) untreated-CsFA.	121
Figure 6.9	The effect of PEAI layer on perovskite solar cells with (A) n-i-p architecture. We evaluated the solar cell performance. Panel (B) shows the current density-voltage curve and stabilized PCE of a high-efficiency device, and (C) shows the statistics of the PCE in box plots for the CsFA-untreated and PEAI-treated, w/o and with H_2O exposure. The inset pictures show the device after H_2O /Air exposure before depositing the Spiro-OMeTAD and Au layers. We evaluated the long-term stability by tracking the maximum power point of 16 devices under the stress of one sun and constant electrical measurement. We plot (D) the average and normalized power, equivalent to PCE, of the measurements done at 25 °C, dry air, and one sun illumination.	122
Figure 6.10	Mixed-cation and mixed-halide perovskite compositions of study. (A) Selected compositions to study the <i>in-situ</i> phase transitions from 300 K to 23 K, (B) Bandgap from UV-VIS at room temperature.	127
Figure 6.11	Structure from powder XRD at 300 K. (A) XRD patterns for different Cs-Br concentrations for the $(Cs,FA)Pb(I,Br)_3$ compositions at 300 K and vacuum, (B) Structural phases from Le Bail refinements, (C) Calculated unit cell volume for the $(Cs,FA)Pb(I,Br)_3$ compositions at 300 K.	130
Figure 6.12	Composition – Temperature phase diagram. Mixed-halide Mixed-cation lead halide perovskites in the $(Cs,FA)Pb(I,Br)_3$ compositional space. (A) without Cs (Cs_0Br_x) as a function of Br, (B) Cs 5% (Cs_5Br_x) as a function of Br, (C) Cs 17% ($Cs_{17}Br_x$) as a function of Br.	132
Figure 6.13	The effect of adding Br into the $(Cs,FA)PbI_3$ lead halide perovskites by <i>in-situ</i> X-ray diffraction in a Cs 5 % composition. (left) Temperature versus diffraction plot from 21.5-27 °, and (right) one-dimensional diffraction patterns in two ranges of 2θ , from 11-15 ° and 21.5-32 °. (A) Cs 5 %, and no Br (0 %), (B) Cs 5 % adding Br 17 %.	135
Figure 7.1	Future work for in-depth and further understanding of: (I) The early stages of crystallization to control the structure and properties of polycrystalline films, nanocrystals, and or quantum dots of LHPs, and (II) the LHP facet properties and synthesis optimization for optimal design.	139

Figure 7.2	The non-perovskite hexagonal FAPbI ₃ structure and opportunity to investigate its structural, optical, and electronic properties further, into a new application space.	140
Figure 7.3	Adding Br to the CsFA perovskite has shown to stabilize the perovskite phase when exposed to H ₂ O/Air. Future work should focus in understanding the role of Br in stabilizing the perovskite phase.	142
Figure 7.4	Summary schematic of the experimental methods used in this dissertation to understand the chemistry–structure–property–performance relationships in LHPs for solar cells.	143

LIST OF SYMBOLS AND ABBREVIATIONS

LHP	Lead halide perovskite
FA	Formamidinium
MA	Methylammonium
PEA	Phenethylammonium
CsFA	(Cs,FA)PbI ₃ perovskite
CsMAFA	(Cs,MA,FA)Pb(I,Br) ₃ perovskite
EO	Excess organics, A-site, in the stoichiometry of A:Pb
EL	Excess Pb in the stoichiometry of A:Pb
FAPbI ₃	FAPbI ₃
A	A-site halide in the APbX ₃ structure
X	X-site halide in the APbX ₃ structure
t	Goldschmidt tolerance factor
H	Hexagonal structural phases
2H	Fully hexagonal structure face-sharing octahedra
4H	Hexagonal structure face-sharing and some corner-sharing octahedra
6H	Hexagonal structure face-sharing and some corner-sharing octahedra
α	Cubic APbX ₃ perovskite space group <i>Pm$\bar{3}$m</i>
β	Tetragonal APbX ₃ perovskite space group <i>P4/m\bar{b}m</i>
γ	Orthorhombic APbX ₃ perovskite space group <i>P4/m\bar{b}m</i> or <i>Pbma</i>
δ Cs	Orthorhombic CsPbI ₃ space group <i>Pnma</i>
DMF	4,4-Dimethyl formamide
DMSO	Dimethyl sulfoxide
CB	Chlorobenzene

RP	Ruddlesden-Popper structure
3D	Three-dimensional perovskite
2D	Two-dimensional
LD	Low-dimensional
H ₂ O	Water vapor, humidity
w/o	without
RH	Relative humidity
GIWAXS	Grazing-incidence wide-angle X-ray scattering
q	X-ray scattering vector
α_i	X-ray incident angle
χ	Angle of azimuthal profile from GIWAXS patterns
XRD	X-ray diffraction
θ	Diffraction angle
FWHM	Full width at half maximum
SAXS	Small-angle X-ray scattering
XRF	X-ray fluorescence
XBIC	X-ray beam induced current
XPS	X-ray photoelectron spectroscopy
SEM	Scanning electron microscopy
UV-VIS	Ultraviolet-visible
E_g	Bandgap
PL	Photoluminescence
trPL	Time resolved photoluminescence
DFT	Density Functional Theory
SOC	Spin-orbit coupling

PV	Photovoltaic
SJ	Single junction
SQ	Shockley-Queisser
PSC	Perovskite solar cell
PCE	Power conversion efficiency
J-V	Current density – voltage curve
J _{sc}	Short circuit current density
V _{oc}	Open circuit voltage
FF	Fill factor
MPP	Maximum power point
FS	Forward scan
RS	Reverse scan
HI	Hysteresis index
HTL	Hole transport layer
ETL	Electron transport layer
TCO	Transparent conductive oxide
FTO	Fluorine-doped tin oxide
ITO	Indium-doped tin oxide
Spiro-OMeTAD	2,2',7,7'-Tetrakis[N,N-di(4-methoxyphenyl)amin]-9,9'-spirobifluorene
mp-	mesoporous
c-	compact
OECD	Organization for Economic Co-operation and Development
LCOE	Levelized Cost of Electricity

SUMMARY

Lead halide perovskites (LHPs) solar cells, particularly FA-based, have made impressive advancements in solar energy conversion, achieving high power conversion efficiencies exceeding 26% for a single junction device. However, the limited long-term stability of these devices has hindered their commercialization. The instability issues are influenced by both internal and external factors, leading to rapid degradation of the perovskite phase and overall device performance. Various strategies have been used to stabilize the perovskite phase, but it is crucial to investigate the underlying mechanisms that govern the structural characteristics of the polycrystalline thin films. This dissertation tackles the challenges associated with the instability of LHPs by investigating the complex relationship between structure, properties, and performance in perovskite solar cells. Advanced X-ray characterization techniques are employed to examine the structural properties of FA-based compositions. Understanding the mechanisms and establishing correlations between structure and properties is possible to lay the foundation of a more robust, stable, and efficient material. This dissertation presents a first step toward the design and optimization of LHPs.

The first part of this dissertation explores the crystallographic orientation in lead bromide perovskites, demonstrating that the solvent and organic cation used in the precursor solution significantly affect the preferred orientation of the deposited perovskite thin films. The solvent affects the early stages of crystallization and induces preferred orientation by preventing colloidal particle interactions. The choice of organic cation influences the degree of crystallographic orientation, with methylammonium-based perovskites showing a higher degree of orientation than formamidinium-based ones due to a lower surface energy of a specific perovskite facet. These findings identify the importance of understanding (1) the

precursor solution chemistry, (2) the facet properties and their correlation with the structural properties of the polycrystalline LHP film, and (3) the effect of crystallographic orientation on charge carrier transport in perovskite solar cells.

The second part of this dissertation studies the mechanisms causing FA-based lead iodide perovskites to degrade under water and oxygen exposure. Contrary to common knowledge on humidity-induced degradation, this dissertation reveals the synergistic role of water and oxygen in accelerating phase instability of LHPs. The study uncovers a surface reaction pathway involving the dissolution of formamidinium iodide (FAI) by water followed by the oxidation of iodide, playing a crucial role in causing the subsequent and irreversible undesired phase transformations from perovskite into non-perovskite phases. The interplay of *in-situ* experimental techniques with theoretical calculations provides a detailed understanding of the degradation mechanisms, establishing a foundation to design more durable and efficient materials. Finally, this dissertation delves into strategies for stabilizing the perovskite phase. A hydrophobic molecule, phenethylammonium iodide (PEAI), stabilizes FA-based perovskites. Adding PEAi hinders undesired phase transformations and leads to a more stable material with improved solar cell power conversion efficiency and enhanced charge carrier mobilities and lifetimes. Further, adding Br to mixed cation lead iodide perovskites improves their phase stability at low temperatures.

Overall, understanding structure-property-performance relationships in lead halide perovskites is key for resolving the main challenge of instability in perovskite solar cells. This dissertation lays the groundwork for future research efforts to investigate the fundamentals of LHPs, improve their stability, and broaden their applications in solar cells and beyond.

CHAPTER 1. INTRODUCTION

1.1 Energy Background

The urgent need for a clean and sustainable energy production system has been emphasized by the growing energy demand, existing energy infrastructure, and the impact of climate change. Developing new energy conversion technologies is one of the most significant scientific challenges of this century.^{1,2} Energy plays a crucial role in sustaining our living standards, education, and overall development.¹ Over the past 20 years, global energy consumption has increased by 37 % ³ (**Figure 1.1**). However, the majority of energy production still heavily relies on fossil fuels, resulting in the release of greenhouse gases such as CO₂.¹ This has contributed to the rising concentrations of greenhouse gas in the atmosphere, thus expediting climate change.^{1,4}

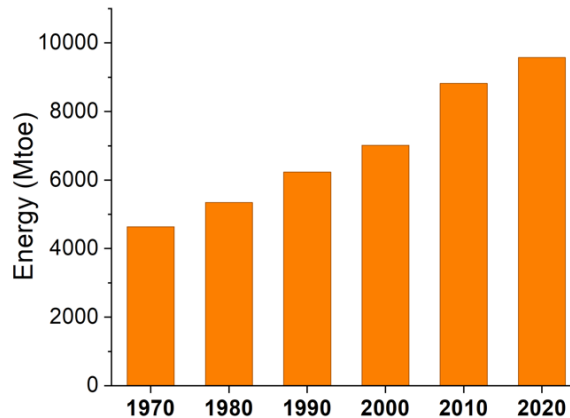


Figure 1.1 World Final Energy Consumption in Mtoe (mega tonnes of oil equivalent, 1 toe equals to 41.868 GJ), taken from the International Energy Agency (IEA) Sankey open website.³

Renewable energies, on the other hand, derive from clean natural resources that are not depleted over time.⁵ In order to address climate change and reduce greenhouse gas emissions, there has been a gradual increase in the production and utilization of renewable energy sources.

The share of renewable energy in the total energy mix has risen from 13.7 % in 2012 to 20.9 % in 2022 in the United States.⁶ As a result, the cost of renewable energy has been decreasing, making it a more competitive alternative to fossil fuels and facilitating the transition to a renewable energy system.

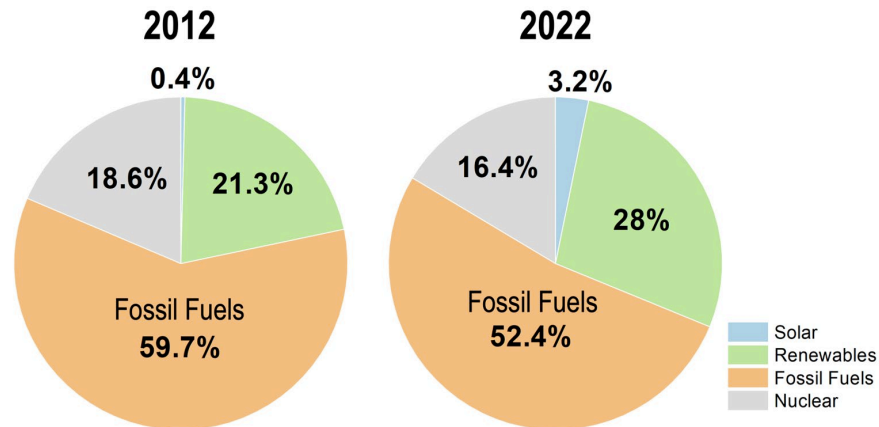


Figure 1.2 Pie charts of the percentage in total net production of energy for all the OECD countries taken from the Monthly Electricity Statistics from the IEA (International Energy Agency).⁶

Policies and incentives have been put in place to support the adoption of renewable energy sources and further drive down costs.⁷ Consequently, renewable energy production has increased from 21.7 % in 2012 to 31.2 % in 2022 for all the countries part of the Organization for Economic Co-operation and Development (OECD) (**Figure 1.2**).⁶ However, despite this growth and improvement of renewable energy technologies, fossil fuels still account for 53 % of global energy production (**Figure 1.2**).⁶ Moreover, first-world countries continue to heavily rely on fossil fuels,⁸ presenting a significant barrier to a complete transition to renewable energy. The challenge lies not only in developing renewable energy technologies but also in phasing out fossil fuels and ensuring a complete energy transition. While renewable energy prices are becoming competitive, there remains a major challenge in developing cost-effective technologies that are equally efficient.

1.2 Solar Energy and Photovoltaics

Solar energy, produced by converting sunlight into electricity, is a significant player among renewable energy alternatives. Currently, it accounts for 10 % of the total renewables and 3.2 % of global energy production (**Figure 1.2**). There is vast potential in utilizing more solar energy to meet our world's energy consumption needs. In the past decade, global solar energy production has increased by a staggering 700 % (**Figure 1.2**). The attractiveness of solar energy has been on the rise due to declining costs and advancements in solar technology, such as the decreased in the levelized cost of electricity (LCOE).^{9,10} To further reduce the LCOE, it is necessary to improve solar cell efficiency and develop low-cost technologies.^{9,10} Therefore, growing solar energy technologies play a pivotal role in transitioning from fossil fuels to renewables, offering low-carbon emission options to meet energy demands and sustain the energy market.

One prominent solar energy technology is photovoltaics (PVs), which employ semiconductor materials to convert solar energy into electricity.¹ Since the discovery of the PV effect in 1839 by Edmond Becquerel and the fabrication of the first silicon solar cell by Bell Labs in 1954,¹ silicon PV systems have gained significant traction in the energy market.^{1,9} Currently, China leads the world's solar energy production, accounting for 31 % of the global solar energy generation and 36 % of the world's solar plant capacity. The United States also ranks among the top producers, contributing 15 % to worldwide solar energy production.⁵ Despite solar energy being a major source of power on our planet, the efficiencies of single junction (SJ) PV devices are theoretically limited to 33 %, the Shockley-Queisser (SQ) limit.¹¹ This limit considers losses from solar spectra mismatch and radiative recombination.¹

Therefore, there is ample opportunity to optimize materials and interfaces to enhance efficiency and reduce further the LCOE associated with these energy conversion systems.

PV technologies are categorized into generations based on materials and development over time. The first PV generation consists of silicon-based technologies, which were the pioneering solar cell technologies starting in 1954. The second PV generation encompasses thin-film solar cells that employ alternative semiconductor materials like cadmium telluride (CdTe), cadmium sulfide (CdS), or copper indium gallium selenide (CIGS). The third PV generation, also known as “next-generation” solar cells, are the emerging and under-development technologies. Examples include dye-sensitized solar cells (DSSC), organic solar cells (OSC), and perovskite solar cells (PSC), along with other novel materials for PV applications.¹¹ Perovskite materials have been used as promising complements to existing silicon and other semiconducting materials, serving as absorber layers in solar cells. The main goal of PV research remains in improving efficiencies and lowering the costs to facilitate a complete transition to renewable energy sources.

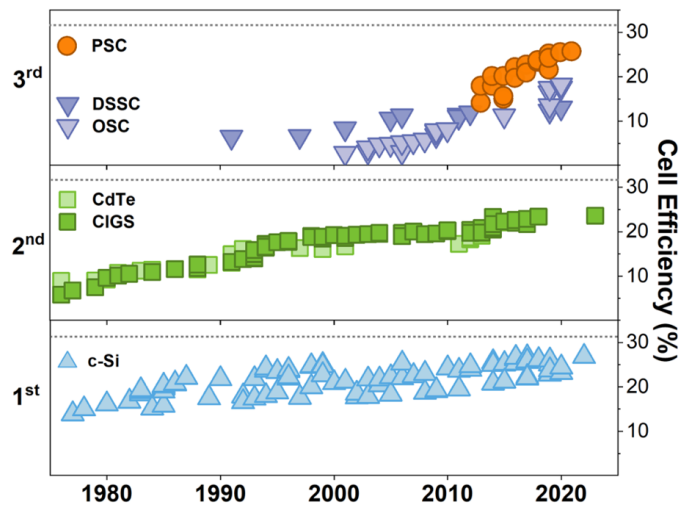


Figure 1.3 Best Cell-Efficiency chart for the 1st, 2nd, and 3rd generations of single junction PVs. Data taken from NREL chart.¹² Dashed-line indicates the SQ limit of single-junction maximum efficiency.

The progress of solar cells is often measured by comparing the highest research-cell efficiencies achieved. **Figure 1.3** shows the efficiency growth over time and across different PV generations.¹² PSCs (represented by orange dots) have exhibited remarkable advancement in just 12 years of development, highlighting their potential for solar energy conversion. The maximum efficiency of PSCs reported to date is 26.1 %, ¹³ matching the efficiency of silicon-based SJ cells.

1.3 Perovskite Solar Cells: Opportunities and Challenges

Lead halide perovskites (LHPs) are the most used semiconductors in PSCs mainly because of their advantages, including excellent optoelectronic properties and low-cost processing.^{9,14} One of their main advantages is their compositional tunability, allowing for the incorporation of multiple ions within the same structure and enabling control over their optical and electrical properties. This versatility has led to the inclusion of various organic and inorganic cations, expanding the range of properties within the LHP family. Notably, their bandgap, which determines the energy levels of the semiconductor, can be adjusted, making it paramount to optimize the alignment with other layers in PSCs.

Among the LHP compositions, formamidinium (FA, $\text{CH}(\text{NH}_2)_2$) lead iodide (FAPbI_3) has gained significant attention due to its ideal bandgap of 1.48 eV for PV applications, allowing greater spectral absorption.¹⁵ In fact, FA-based LHP compositions have achieved some of the highest reported efficiencies in solar cells, reaching up to 26.1 %.¹³ However, despite their impressive performance, LHPs suffer from long-term instability, jeopardizing their commercial deployment.^{16–18} Especially, LHPs based on FA, present structural instability and different polymorphs.^{19,20}

The perovskite structure is characterized by corner-sharing octahedra, as depicted in **Figure 1.4** (left). However, at room temperature, the thermodynamically stable phase of FAPbI₃ adapts a hexagonal non-perovskite structure with face-sharing octahedra, as shown in **Figure 1.4** (center).¹⁹ Other polymorphs of LHP compositions exhibit edge-sharing octahedra forming an orthorhombic structure, also shown in **Figure 1.4** (right).^{16,21} It is important to note that non-perovskite phases can negatively impact the performance of PSCs.¹⁶

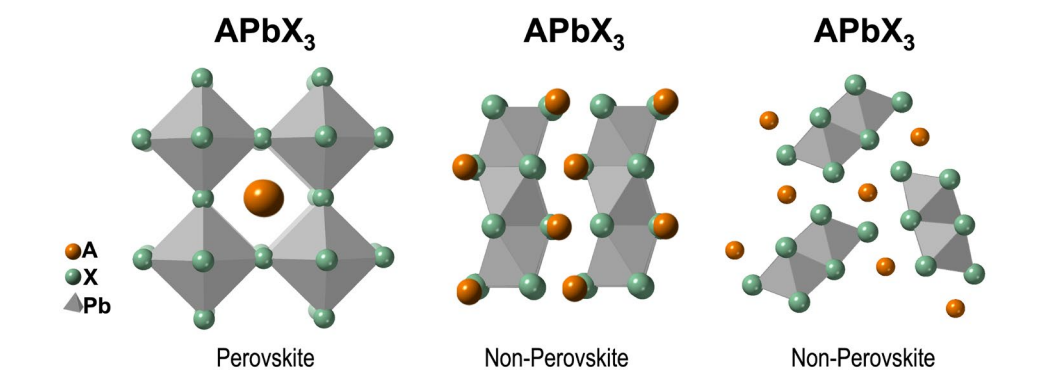


Figure 1.4 Polymorphism in $APbX_3$ includes a (left) perovskite phase and (center, right) non-perovskite phases.

Despite their unique optoelectronic properties, LHPs are highly unstable when exposed to external factors such as humidity, oxygen, UV light, applied voltage bias, and temperature.^{16,22–24} A deeper understanding of the degradation mechanisms is still required to make PSCs suitable for outdoor applications and commercialization. To enhance phase stability and solar cell efficiency, researchers have undertaken compositional engineering of LHPs, incorporating multiple A-site cations (e.g., methylammonium (MA), cesium (Cs), and FA) and multiple X-site halides (e.g., iodine (I) and bromine (Br)).²⁵ In the case of complex mixed-ion compositions and FA-based LHPs, it is essential to identify the factors influencing their structural properties. However, there is a lack of comprehensive understanding regarding

the dominant factors governing the structure and behavior of FA-based LHPs, as well as the underlying reasons for their transformation under external factors.

To address these knowledge gaps, advanced characterization techniques, such as synchrotron-based X-ray methods, provide valuable insights into the atomic, nano, and microscale properties related to the structural and chemical characteristics of LHPs. Such information is critical for understanding the limitations on PSC performance and long-term stability. Only a limited number of studies have investigated the *in-situ* effects of external factors on the material's transformation and the *operando* behavior of devices. Establishing structure-property relationships and comprehending the *in-situ* transformation of materials are crucial steps toward designing more stable perovskite materials with desired optical and electric properties for enhanced solar cell performance.

1.4 Aim of this Dissertation

The main aim of this dissertation is to address the instability challenges that have hindered the development and commercialization of LHP-based solar cell technologies. This dissertation focuses on studying structure-property relationships in LHPs using X-ray scattering techniques. Additionally, X-ray absorption techniques are employed to gain insights into the chemistry of LHPs, thereby merging structural and chemical information. The ultimate objective is to understand how internal and external factors affect the chemistry, structure, and properties (mainly optical and electronic) of FA-based LHPs and how these impact the performance and stability of PSCs. This fundamental understanding will contribute to designing robust and stable materials for solar cell applications, supporting the global energy transition. **Figure 1.5** illustrates the principal aim of this dissertation, which is to identify

structure-property relationships in LHPs for optimizing their stability and performance in solar cells via chemical design.

This dissertation is divided into three main parts and seven chapters, as summarized in **Figure 1.6**. The first part introduces the theoretical fundamentals and experimental methods employed in this research. **Chapter 2** provides a theoretical and state-of-the-art background relevant to the dissertation, and **Chapter 3** describes the main experimental methods used for the material fabrication and characterization, including an explanation of the X-ray scattering and absorption techniques employed.

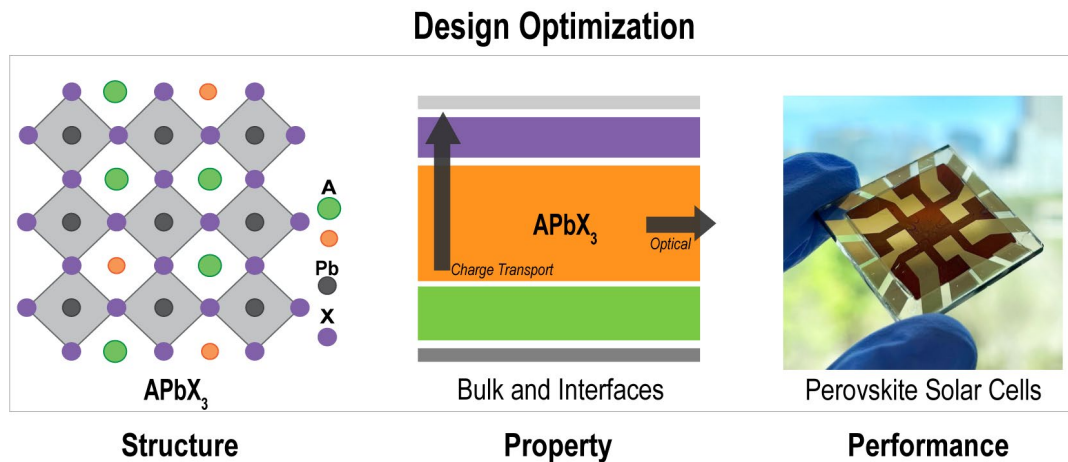


Figure 1.5 Graphical representation of the aim of this dissertation.

The second and third parts delve into the main results and discussion of this dissertation. The second part, **Chapter 4**, presents the factors that dominate crystallographic orientation in polycrystalline LHPs thin films and how this orientation affects the electrical properties of the PSCs. It is shown that the choice of solvent and A-site cation influences the preferred crystallographic orientation in lead bromide perovskites, leading to enhanced charge carrier extraction in PSCs.

The third part explores the effect of external factors on the structural phase transformations of LHPs. **Chapter 5** investigates the mechanisms underlying phase instability in FA-based LHPs when exposed to water and oxygen. The interplay between bulk phase transformations and surface chemical reactions is elucidated, providing a detailed understanding of the degradation mechanism and the synergistic role of water and oxygen in accelerating undesired phase transformations. Building upon the insights from **Chapter 5**, **Chapter 6** proposes strategies to prevent phase transformations in halide perovskites. First, using phenethylammonium iodide as a top layer on FA-based LHP films impedes undesired phase transformations, resulting in improved phase stability and better performance of solar cells when exposed to humidity. Second, adding Br to the mixed-cation FA-based LHP compositions demonstrates improved phase stability at low temperatures.

Lastly, **Chapter 7** concludes this dissertation. This chapter proposes additional opportunities to advance LHP design based on the gained understanding of structure-property relationships. This knowledge is highly valuable for advancing PSCs and will aid the global energy transition into renewable technologies.

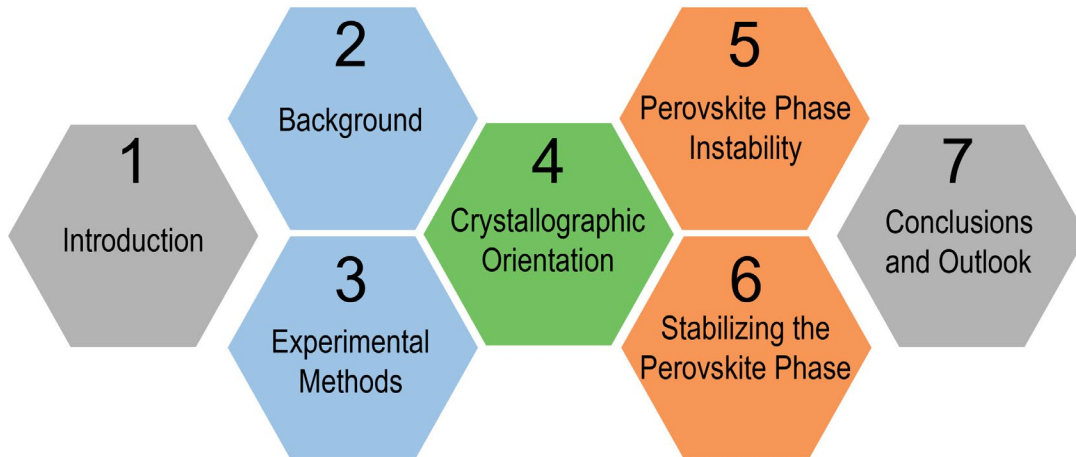


Figure 1.6 Schematic summarizing the parts, chapters, and topics of this dissertation. Part one (blue), part two (green), and part three (orange).

CHAPTER 2. BACKGROUND

This chapter has parts from the following review article:

“The Role of Dimensionality on the Optoelectronic Properties of Oxide and Halide Perovskites, and their Halide Derivatives”, *Advanced Energy Materials*, 2022, 12, 2100499, by Robert L. Z. Hoyer, **Juanita Hidalgo**, Robert A. Jagt, Juan-Pablo Correa-Baena, Thomas Fix, and Judith L. MacManus-Driscoll.

My contribution: I wrote section 3 completely, “From 3D to 0D: Effect of Dimensionality on Recombination and Charge-Carrier Transport in Lead Halide Perovskites”. In addition, I discussed and wrote part of the conclusions.

2.1 Lead Halide Perovskites

This dissertation addresses the energy challenges by studying energy materials such as perovskites. Perovskites, with the chemical formula ABX_3 , have shown impressive potential in energy-related applications, such as photovoltaics.²⁶ The major advantage of perovskites is their compositional tunability of the A and B sites, resulting in various compositions with different electronic, optical, and structural properties that can be adjusted to design a specific property.²⁷ In this dissertation, I will discuss about lead halide perovskites (LHPs), $APbX_3$, a low-cost technology for solar cells with superb power conversion efficiency.¹⁴

2.1.1 *Crystal Structure*

The term ‘perovskite’ refers to the mineral with the chemical composition $CaTiO_3$, named after the mineralogist Count Lev. A von Perovski.^{28,29} For this reason, the term perovskite determines the materials with similar crystal structure to $CaTiO_3$. The general composition for LHPs is of the chemical formula ABX_3 , where A is an organic and or inorganic cation, B is Pb, and X is a halide. In LHPs, Pb cations are octahedrally coordinated with the X-site halides (I, Br, or Cl). The lead-halide octahedra form a corner-sharing array, giving rise to a cubic, tetragonal, or orthorhombic three-dimensional (3D) structure. The cuboctahedra cavities (voids between octahedra) are occupied by the A-site cation, which needs to fall within a narrow range of ionic radii for the perovskite phase to be achieved.³⁰ In general, single-ion LHPs compositions have in the A-site: methylammonium CH_3NH_3 (MA), formamidinium $(CH)_2NH_2$ (FA), or Cs, and in the X-site: I, or Br as shown in **Figure 2.1A**.

The Goldschmidt tolerance factor can quantitatively describe the perovskite structure,³¹ which is defined in Equation 1, where r_A , r_B and r_X are the ionic radii of the A, B, and X-site as shown in **Figure 2.1**.¹⁴

$$t = \frac{r_A + r_B}{\sqrt{2}(r_B + r_X)} \quad (1)$$

Goldschmidt proposed that a perovskite structure phase would form if the value of the tolerance factor was close to 1.0, forming an ideal cube.²⁹ It has also been found that a cubic perovskite structure is possible if t lies in the approximate range of 0.9 to 1.0.^{29,32} Thus, for LHPs, the A-site cation size will determine the perovskite's phase and stability. A tolerance factor greater than 1, a large A, and a small B will lead to a hexagonal packing of the AX_3 layers resulting in a non-perovskite hexagonal phase.²⁹ A tolerance factor between 0.71 and 0.9 will distort the cuboctahedra coordination, resulting in a crystal structure of lower symmetry than cubic, such as tetragonal or orthorhombic.²⁹

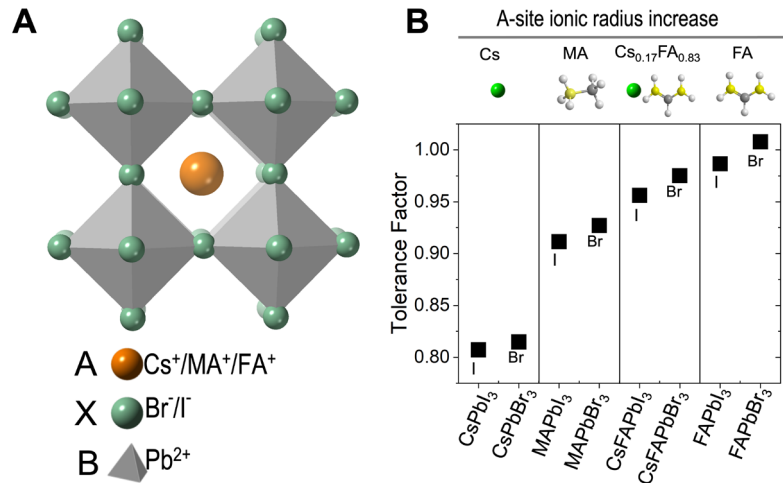


Figure 2.1 Lead halide perovskite structure ABX_3 (A) A, B, and X site in the perovskite structure (B) Calculated tolerance factor in ascending order for selected perovskite compositions.

In the case of LHPs, the tolerance factor was calculated for different compositions assuming $r_{Cs^+} = 1.67 \text{ \AA}$, $r_{MA^+} = 2.17 \text{ \AA}$, $r_{FA^+} = 2.53 \text{ \AA}$, $r_{Pb^{2+}} = 1.19 \text{ \AA}$, $r_{Br^-} = 1.96 \text{ \AA}$, $r_{I^-} = 2.20 \text{ \AA}$.¹⁶ Here, the weighted average at the A-site of the two different ions (i.e., Cs and FA) is applied to define an effective ionic radius³² to compute the tolerance factor for compositions $Cs_{0.17}FA_{0.83}PbBr_3$ ($CsFAPbBr_3$) and $Cs_{0.17}FA_{0.83}PbI_3$ ($CsFAPbI_3$). A smaller A-site cation, such as Cs and MA, leads to a smaller tolerance factor, while Br, with a smaller radius, accounts for a slightly larger tolerance factor (**Figure 2.1B**). Therefore, the ion size of A-site cations and the halide have opposite effects on tolerance factor and the degree of size mismatch between A-site cations and PbX_6 octahedra in structure. Given that the tolerance factor alone does not precisely predict the perovskite phase limits, the tolerance factor has been plotted against the ratio of the radii of the B-site cation to the X-site cation to define an octahedral factor r_B/r_X . The structure-field diagram was plotted for halide perovskites as shown in **Figure 2.2**, showing combinations between AB and X that lead to perovskite structure phase formation and those that do not.²⁹

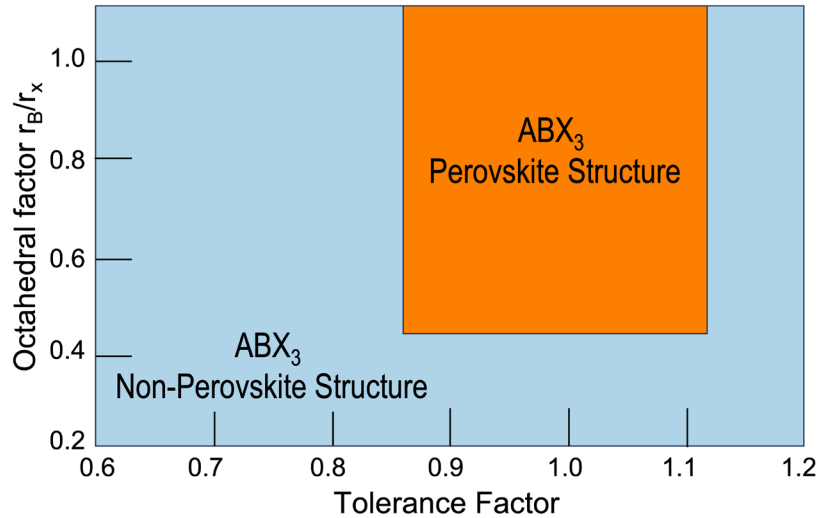


Figure 2.2 Structure-field maps for tolerance factor t versus the octahedral factor for halide perovskites.²⁹

Table 2.1 Crystal structure of lead halide perovskites studied in this dissertation.

Perovskite	Temperature	Crystal Structure	Space Group	Ref.
MAPbI ₃	> 327 K	Cubic	$Pm\bar{3}m$	33
	165 - 327 K	Tetragonal	$I4/mcm$	33,34
	< 165 K	Orthorhombic	$Pnma$	33
MAPbBr ₃	>255K	Cubic	$Pm\bar{3}m$	35
	155-255	Tetragonal	$I4/mcm$	35
	<150	Orthorhombic	$Pnma$	35
FAPbI ₃	300	Cubic	$Pm\bar{3}m$	19
	200	Tetragonal	$P4/mbm$	19
	<140			
FAPbBr ₃	>262	Cubic	$Pm\bar{3}m$	36
	160-262	Tetragonal	$P4/mbm$	36
	<160	Orthorhombic	$Pnma$	36
CsPbI ₃	>550K	Cubic	$Pm\bar{3}m$	37
	450-550K	Tetragonal		
	< 450 K	Orthorhombic	$Pbnm$	37,38
CsPbBr ₃	>403 K	Cubic	$Pm\bar{3}m$	39
	361-403 K	Tetragonal	$P4/mbm$	39
		Orthorhombic	$Pnma$	39
(Cs,FA)PbI ₃		Tetragonal	$P4/mbm$	40
(Cs,MA,FA)Pb(I,Br) ₃		Cubic	$Pm\bar{3}m$	41

Depending on the perovskite composition and temperature, the crystal structure is classified into different crystal systems such as cubic, tetragonal, or orthorhombic, as shown in **Figure 2.3**. Among the crystal systems, depending on the composition, the perovskite will be classified into different space groups. **Table 2.1** summarizes the main LHPs investigated in this dissertation, showing the differences in their crystallographic properties.

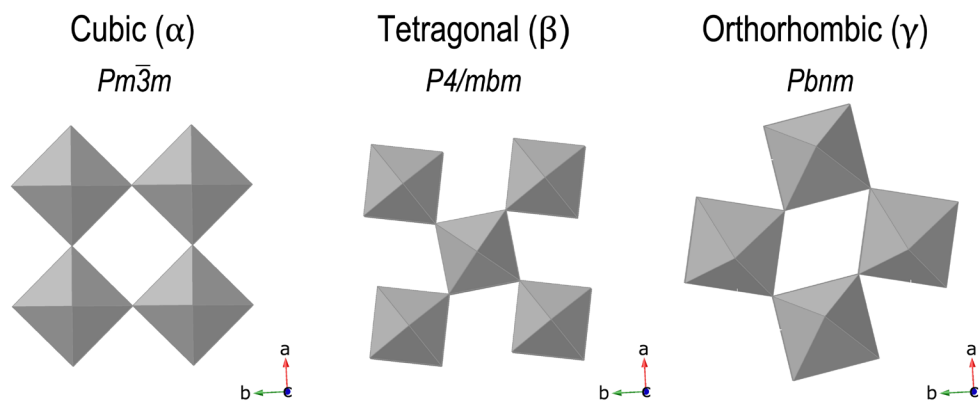


Figure 2.3 Perovskite crystal systems for FA-rich LHPs.

2.1.1.1 Polymorphism

FAPbI₃ has shown to be the most promising LHP to achieve high efficiencies in single-junction solar cells.¹⁵ The FAPbI₃ perovskite phase is known as the “black” phase, or α phase when forming a cubic crystal structure with the space group $Pm\bar{3}m$ (**Table 2.1**). Further, it has been shown that FAPbI₃ adopts a tetragonal structure at 285 K of the space group $P4/mbm$, which differs from its MA counterpart, MAPbI₃ (**Table 2.1**). However, the tolerance factor of FAPbI₃ close to one is on the limit of creating a corner-sharing perovskite structure, given that it can transform easily into the hexagonal phase. Therefore, FAPbI₃ has been shown to have different polymorphs.¹⁹ Different studies have investigated the structure of FAPbI₃, showing its polymorphism and strategies to obtain the perovskite phase structure.¹⁶ Even if different strategies in the synthesis have allowed obtaining a FAPbI₃ perovskite phase at room temperature, Weber et al. showed that the stable phase at room temperature of FAPbI₃ is the face-sharing hexagonal phase, also known as the “yellow” phase, delta phase, or 2H phase corresponding to the crystal space group $P6_3/mmc$ ¹⁹ (**Table 2.2, Figure 2.4**). In addition,

Gratia et al. identified other hexagonal polytypes of FA-rich perovskites when mixed with MA and Br.²⁰

Hexagonal polytypes are intermediate crystal structures between the fully corner-sharing perovskite and the fully face-sharing hexagonal phase 2H (space group and lattice parameters in **Table 2.2**). Hexagonal polytypes such as 4H and 6H (**Figure 2.4**) have both corner-sharing and face-sharing octahedra. After identifying these hexagonal polytypes, more works have identified other polytypes up to 11H, highlighting the importance of studying and understanding their properties.⁴²

Table 2.2 Crystal structure of non-perovskite phases studied in this dissertation.

Non-perovskites	polytype	Crystal Structure	Space Group	Lattice Parameters	Ref.
	2H	Hexagonal	$P6_3/mmc$	a: 8.67, c: 7.90	20
FAPbI ₃	4H	Hexagonal	$P6_3/mmc$	a: 8.81, c: 15.2	20
	6H	Hexagonal	$P6_3/mmc$	a: 8.84, c: 22.45	20
CsPbI ₃		Orthorhombic	$Pnma$	a: 10.45, b: 4.80 c: 17.77	43

CsPbI₃ is also polymorph by adapting a perovskite phase only above 450 K.³⁸ The tolerance factor of CsPbI₃ is on the lower limit to form a perovskite (**Figure 2.1**). Therefore, below 450 K, CsPbI₃ forms an edge-sharing orthorhombic structure known as δ Cs, shown in **Figure 2.4**. Further, CsPbI₃ has been mixed with FAPbI₃ to form a mixed-cation Cs_xFA_{1-x}PbI₃ (CsFAPbI₃) stabilized perovskite structure.^{32,40,44} Mixed-cation CsFAPbI₃ has shown improved stability of the perovskite phase and has allowed more accessible synthesis routes at room temperature to obtain the desired crystal structure.³² Theoretical calculations have shown that adding the smaller A-site cation Cs into the FAPbI₃ structure results in the contraction of the cuboctahedra voids from the corner-sharing octahedra structure, resulting in the strain of the

PbI₆ octahedra, leading to stronger hydrogen bonding between the amine groups of the FA and the iodide.⁴⁵ The decreased size of the voids leads to less FA motion and less octahedral tilting at low temperatures.^{45,46} The Cs-substitution limit has been determined to be around 15% to obtain the perovskite phase. Beyond 15% of Cs in the compositional matrix, the CsFAPbI₃ phase segregates into perovskite and non-perovskite structures, such as the thermodynamically stable 2H and δ Cs.⁴⁰ **Figure 2.5** shows the reported phase diagram of CsFAPbI₃ perovskites, showing the changes in crystallographic properties and mixed phases as a function of temperature and Cs content in the FAPbI₃ perovskites.

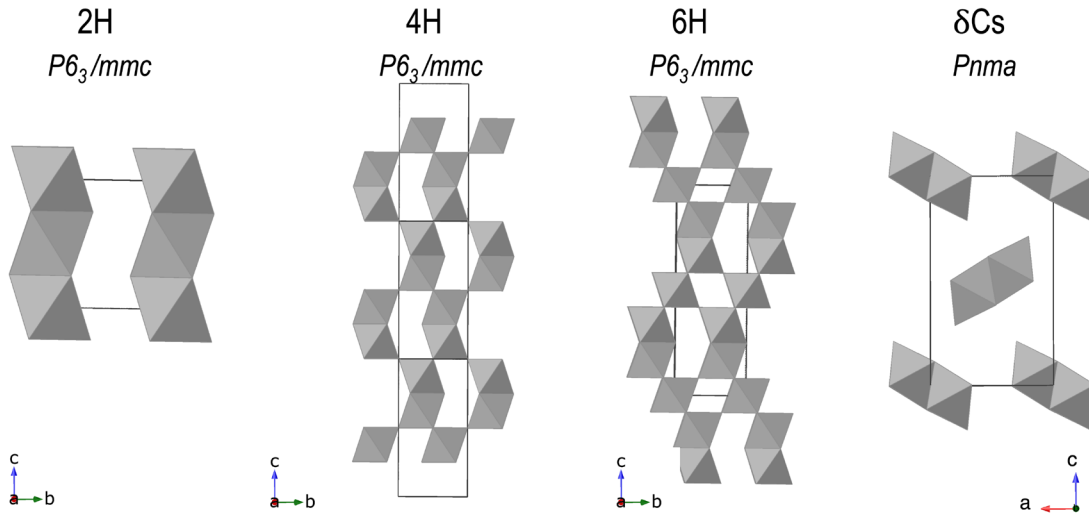


Figure 2.4 Non-perovskite crystal structure adopted by APbX₃ compositions.

Other strategies have been used to stabilize the FAPbI₃ perovskite phase, for example, incorporating smaller cations such as MA. Adding a short alkylammonium cation such as MAcl to the precursor solution has been used to obtain the highest PCE reported in PSCs.¹³ Hui et al. stabilized the black phase FAPbI₃ perovskite by varying the solvent of the precursor solution and using the ionic liquid, methylamine formate, instead of commonly used solvents such as dimethylformamide (DMF) and dimethyl sulfoxide (DMSO).⁴⁷ Park et al. added

isopropylammonium chloride to the FAPbI₃ perovskite precursor solution to achieve stable and long-term operational PSCs with one of the highest certified PCEs of 23.9%.⁴⁸

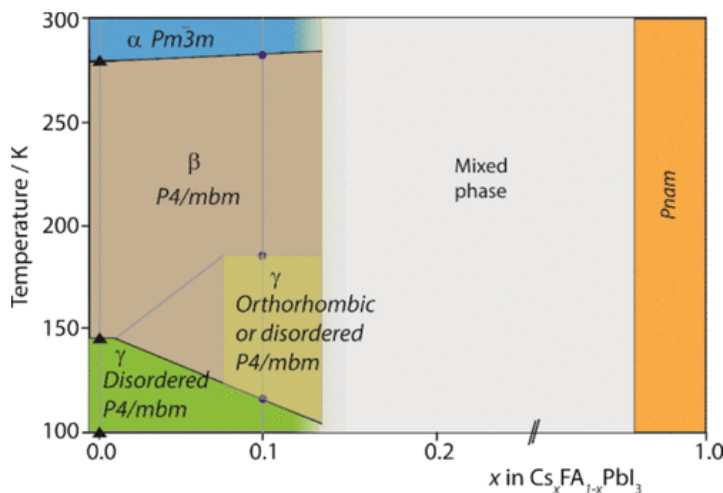


Figure 2.5 Schematic of the Cs_xFA_{1-x}PbI₃ phase diagram with estimated phase-transition positions. Reprinted with permission from *Chem. Mater.* 2020, 32, 2282-2291. Copyright 2020 American Chemical Society.

2.1.2 Low-dimensional Ruddlesden-Popper Structures

Lead halide Ruddlesden-Popper (RP) structures have also been named 2D perovskite structures as they are a layered derivative of the perovskite ABX₃. The general formula is R₂A_{n-1}Pb_nX_{3n+1} where R is the bulky monovalent organic cation that sandwiches the inorganic layer, *n* is the number of PbX₆ layers between the R organic ligands, and A is the small A-site cation that can fit within the cuboctahedra voids of the inorganic layers, and X is the halide. The 2D perovskites comprise a monolayer of inorganic corner-sharing lead-halide octahedra sandwiched between organic ligands above and below the monolayer. By contrast, quasi-2D structures have *n* number of inorganic monolayers between the organic ligands. Increasing the value of *n* from 1 to infinite tunes the structural dimensionality from 2D to 3D (the complete network of corner-sharing octahedra). The organic ligands, or bulky cations used to form the

RP phase in LHPs are typically alkyl chains or phenyl groups. Two of the most common bulky cations are phenethylammonium (PEA) and butylammonium (BA).

The 2D structures can offer several advantages over the 3D counterparts in terms of improved environmental stability. The replacement of 3D perovskites with RP phases has enhanced humidity stability due to the hydrophobic side chains of the long-chained organic cations.⁴⁹ For example, Smith et al. used PEA as a moisture barrier for 2D-RP LHP layers, obtaining films that did not decompose over the entire 46-day stability test in ambient air with 52% relative humidity. In that study, MAPbI₃ started degrading to PbI₂ within 4 days under the same conditions.⁵⁰ Liao et al. also improved stability over MAPbI₃ by using a low-dimensional BA-Cs-based RP LHP.⁵¹ In general, perovskites with PEA or BA, apart from acting as moisture barriers, lack of specific functionality and do not directly contribute to the optoelectronic properties other than indirectly through modifying the crystal structure or sometimes by modifying the exciton binding energy.⁵²

Mixed 3D and 2D structures are known as multi-dimensional perovskites. This can be achieved by mixing all the phases together into the bulk, or by having different structural phases at the surfaces and interfaces. For example, 2D LHPs have been used as surface treatments to create a top layer of the 3D bulk perovskite, forming a “capping layer”, that can act as an interfacial passivation layer.⁵³ The environmental stability can be improved by forming a “capping layer” of 2D LHP on a 3D LHP bulk.⁵³ The surface of LHPs is where defects are easily formed. Therefore, passivating these defects is essential to achieve the highest efficiencies in solar cells. In 2017, Grancini et al. fabricated 3D MAPbI₃ films where the surface was capped by a 2D perovskite using amino valeric acid iodide.⁵⁴ To analyze the effect of the 3D/2D interface on the electronic properties, they used first-principles calculations to

determine the local density of states. From the calculations, they observed that the formation of a mixed 3D-2D perovskite widened the bandgap of the 3D material in the interface, which could form a barrier to reduce electron recombination. Ma et al. also improved device stability by capping the 3D MAPbI_{3-x}Cl_x with an organic layer of cyclopropyl ammonium iodide. The hybrid composition was stable for 40 days compared to 8 days of the pristine 3D material.⁵⁵

2.1.3 Electronic and Optical Properties

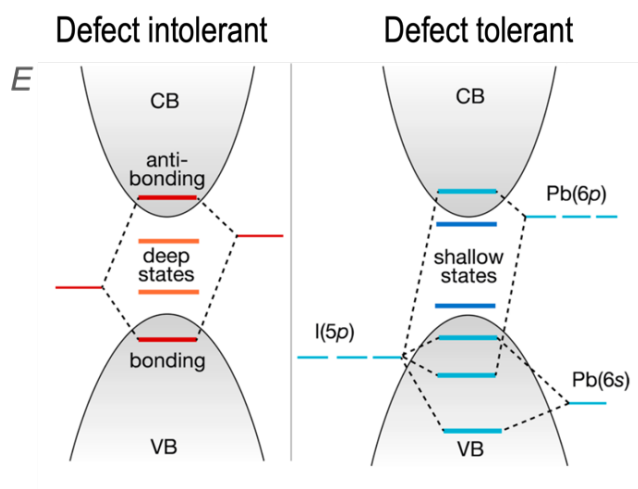


Figure 2.6 Electronic structure of defect intolerant semiconductors versus defect tolerant LHPs versus. Reproduced with permission from *Chem. Mater.* 2017, 29, 4667-4674. Copyright 2017 American Chemical Society.

LHPs have outstanding optoelectronic properties, namely high charge-carrier mobilities, long diffusion lengths, tunable bandgaps, long charge carrier lifetimes, and high absorption coefficients.⁵⁶ In addition, LHPs are defect-tolerant (**Figure 2.6**).⁵⁷ To a large extent, the beneficial properties of the LHPs can be attributed to the presence of Pb. The *s* and *p* orbitals of the Pb²⁺ cations hybridize with the *p* orbitals of the I⁻ anions to form an electronic structure that is conducive to traps being shallow rather than deep, as seen in **Figure 2.6**.⁵⁷⁻⁵⁹ Defect tolerance has been key in enabling LHP thin films to be grown by simple solution-based

methods (previous section) at low temperatures while achieving and surpassing those of other thin film and polycrystalline silicon solar cells.⁶⁰

2.1.3.1 Bandgap

LHPs are semiconductors, acting as the photo absorber layer in PSCs. Semiconductors are characterized by having a bandgap E_g , which makes their optical properties important for solar cell applications. In an ideal semiconductor, the photons with energy higher than the E_g are absorbed by promoting an electron from the valence band to the conduction band.¹¹ Therefore, the onset of the absorption spectrum occurs at the energy of the bandgap. The bandgap is the primary quantity defining how many charge carriers are generated from solar photons with an energy greater than or equal to the E_g . Maximizing the number of photons that contribute to charge carriers in solar cells would require optimizing the E_g .⁶¹ When tuning the bandgap to reach high-efficiency solar cells, there is a tradeoff between harvesting as many photons as possible and maximizing the energy of the extracted charges.¹¹

LHPs exhibit a direct bandgap, where the conduction band minimum is aligned with the valence band maximum. In LHPs, the valence band is dominated by the Pb-*s* and I-*p* orbitals, whereas the conduction band is contributed to the empty Pb-*p* orbital, as shown in **Figure 2.6** for the defect-tolerant material.⁶² In addition, owing to Pb²⁺ being a heavy metal cation, there is strong spin-orbit coupling, leading to smaller bandgaps, which also favors shallow trap formation.⁵⁸ The A-site cation does not contribute to the density of states. However, its size and rotation can affect the Pb-halide bond by changing the volume of the structure and distortion. These changes in composition and structure can modify the bandgap of the material.⁶³

In view of the compositional and structural versatility of LHPs, the bandgap can vary and be tuned. Low-bandgap LHPs are generally used for SJ solar cells, while high-bandgap materials can be used for multi-junction solar cells. Multi-junction solar cells are several solar cells stacked on top of each other with different bandgaps to overcome the SQ limit and reduce thermalization losses.¹¹ **Table 2.3** shows the bandgap of some single-cation and single-halide LHPs. Further, different studies have established relationships on the bandgap as the X-site halide or A-site cation is replaced.⁶²⁻⁶⁴

Table 2.3 Bandgaps of different single-cation single-halide LHP compositions.

Perovskite	Bandgap E(eV) ⁶³
FAPbI ₃	1.51
MAPbI ₃	1.59
CsPbI ₃	1.72
FAPbBr ₃	2.25
MAPbBr ₃	2.30
CsPbBr ₃	2.31

2.1.3.2 Bandgap of Non-Perovskites

The optical properties and bandgap of FA and Cs non-perovskite phases have not been widely investigated. There is a consensus that they are detrimental to solar cell performance,¹⁶ but little information is available regarding their electronic and optical properties. Density functional theory (DFT) calculations with and without spin-orbit coupling (SOC) have shown the bandgaps of these materials, reported only in the last years.^{21,65,66} **Table 2.4** shows the

calculated bandgaps corresponding to the non-perovskite phases studied in this dissertation, the hexagonal FAPbI₃ (2H), and the orthorhombic CsPbI₃ (δ Cs).

From **Table 2.4**, we see that the bandgap increases for the non-perovskite phases, with edge- or face-sharing octahedra, compared to the perovskites that are corner-sharing (**Table 2.3**). Kamminga et al. studied the effect that the connectivity of the metal-halide octahedra has on the bandgap in lead iodide systems by DFT.⁶⁷ The bandgap size strongly depends on the dimensionality of the inorganic network and on the number of iodides shared between two adjacent Pb ions. This number of shared iodides varies from the corner-, edge-, or face-sharing octahedra. From theoretical and experimental data, the bandgap increases with the number of shared iodides. Increasing the connectivity from corner-, *via* edge-, to face-sharing causes a significant increase in the bandgap.⁶⁷

Table 2.4 Bandgaps of Non-Perovskite Phases from DFT.

Non-perovskites	Polytype	Space Group	Bandgap		
			Method	E (eV)	Ref.
FAPbI ₃	2H	$P6_3/m$	GGA-PBE	2.7	⁶⁵
			G0WO + SOC	3.54	⁶⁵
CsPbI ₃		$Pnma$	GGA-PBE	2.17	⁶⁶
			PBE-SOC	2.64	²¹

Specifically, from the structural analysis of the hexagonal face-sharing 2H phase, the rearrangement in the Pb-I-Pb angles increases the average Pb-I bond lengths from the perovskite phase (α,β) to the hexagonal phase. The increase in the Pb-I bond reduces the orbital interactions between Pb and I atoms. This increases the bandgap from 1.47 eV (α -FAPbI₃) to 3.54 eV (2H-FAPbI₃).⁶⁵ Additionally, the band structures for the 2H hexagonal

phase show an indirect bandgap (phonon-assisted) for this structural phase.⁶⁵ Despite the theoretical differences in bandgap between the hexagonal FAPbI₃ and the perovskite structures, no experimental work has studied the optical properties of the hexagonal structure in depth.

In the case of δ Cs, the edge-sharing orthorhombic structure of CsPbI₃, the six iodides connected to the Pb atom do not form equal-length Pb-I bonds, creating irregular octahedrons.⁶⁶ Therefore, this non-perovskite CsPbI₃ has a larger bandgap than its perovskite counterpart and remains a direct bandgap semiconductor. Experimentally, Dastidar et al. showed that the perovskite phase of CsPbI₃, with a bandgap of ~ 1.73 eV, transformed into a wide bandgap material with a “yellow” phase after being exposed to a relative humidity of 33% for 75 min.⁶⁸ In summary, little is known about the electronic and optical properties of the non-perovskite phases. However, given their large bandgap, it is known they are poor absorbers for solar cells hence unwanted phases for this application.

2.1.3.3 Low-dimensional Structures Bandgap

Changing the dimensionality of the perovskite also influences the bandgap (**Figure 2.7**), which affects the performance of these materials in devices. By engineering the composition and dimensionality of these materials, it is possible to tune their structure and optoelectronic properties to the optimal values for the desired application. For example, 2D RP structures have the advantage of bandgap tunability through the composition and structural dimensionality.⁶⁹ Due to quantum confinement effects, 2D RP structures exhibit larger optical bandgaps compared to the 3D LHPs (**Figure 2.7**).

Further, the bandgap of a single-layered perovskite ($n=1$) can be tuned by controlling the interlayer spacing and the structural distortion in the perovskite layer.^{49,70} The interlayer spacing can be modified by increasing or decreasing the length of the organic molecular cation R. The bandgap can be modulated from 1.59 to 2.36 eV in iodide-based RP structures by controlling the number of inorganic layers between the organic ligands. Despite the increase in stability of low-dimensional perovskites, their charge carrier transport properties are not ideal for solar cells as they have large exciton binding energies.⁵²

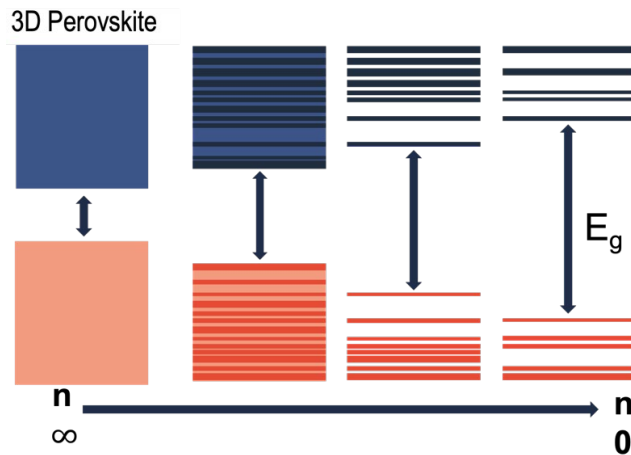


Figure 2.7 Bandgap of perovskites depending on dimensionality and number of n layers of the low-dimensional structures.²¹⁰

2.2 Perovskite Solar Cells

LHPs possess exceptional optical and electronic properties, along with their tunability, which has made them ideal candidates for use as photo absorbers in PSCs, achieving impressive solar-to-electric power conversion efficiencies of over 26% (**Figure 1.3, Chapter 1**). As briefly mentioned in **Chapter 1**, the SJ solar cell efficiency has been theoretically limited by the SQ limit. Photons with energy above the bandgap will be lost *via* thermalization, and below the bandgap will not be absorbed. Therefore, the SQ was calculated for a step function dependent

on the semiconductor's bandgap, as shown in **Figure 2.8**.¹¹ The optimal bandgap between 1.1 and 1.4 eV allows maximum theoretical efficiency of $\sim 33\%$. The plot shows the efficiency of LHPs (“perovskite”) by 2016, which was from MAPbI₃ perovskite. However, 26% was reported for a FAPbI₃-based perovskite this year.

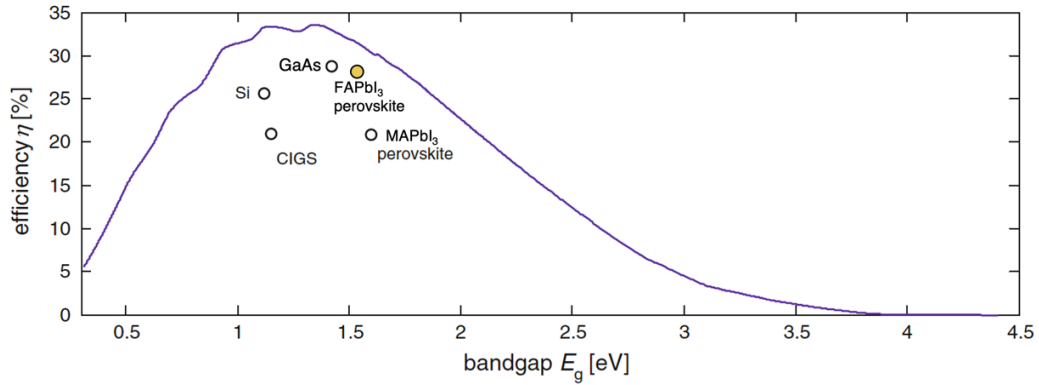


Figure 2.8 Theoretical maximum power conversion efficiency as a function of bandgap and experimental values achieved. Reproduced and modified with permission from Springer Nature 2016 (License number 554960481789)¹¹

The solar cell is based on the photovoltaic effect, creating a voltage across a material when illuminated. The first step of the solar cell is for the LHP to absorb photons, thus generating electron-hole pairs.²⁹ These electrons and holes are separated by the device, allowing the electrons to move through an external circuit. For PSCs, the LHP is the absorber layer in the center of the device, sandwiched between selective transport layers for holes and electrons. Two electrodes are on each side of the selective contacts to close the electric circuit. PSCs can adopt several architectures depending on the selected hole and electron transport layers (HTL and ETL, respectively). Further, numerous studies have focused on optimizing and selecting these transport layers, as they are equally important to the absorber layer to assure and optimize the charge carrier transport through the device.^{71–73} In this dissertation, the solar

cells fabricated and evaluated have an n-i-p architecture, with the ETL on the bottom, side of illumination (**Figure 2.9**).

In **Figure 2.9**, the bottom electrode is a transparent conductive oxide (TCO), fluorine-doped tin oxide (FTO). As an ETL, a thin, compact titanium dioxide layer (c-TiO₂) is used with a top mesoporous anatase (mp-TiO₂) polymorph. The absorber layer is the LHP. The HTL is the molecule 2,2',7,7'-Tetrakis[N,N-di(4-methoxyphenyl)amin]-9,9'-spirobifluorene (Spiro-OMeTAD). The counter electrode, the top electrode, in this case, is gold (Au). As observed, PSCs are a stack of layers, therefore, studying the interfaces and selective contacts in these devices are necessary to understand and optimize this technology. The study of interfaces, structure, and properties between surfaces and the bulk of the materials is paramount.

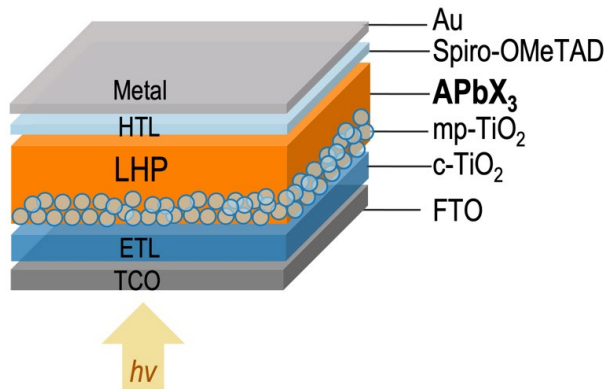


Figure 2.9 Perovskite solar cell architecture n-i-p

2.3 Polycrystalline Perovskite Films from Solution

One main advantage of LHPs is their solution and low-temperature processability, leading to low-cost processes to achieve high-efficiency materials.⁷⁴ LHPs are crystallized from solution, forming a polycrystalline film that is then used as the absorber layer in PSCs. For this reason,

it is important to understand the processes involved in the crystallization of films from solution. According to Ke et al., the fabrication of perovskite films experience three stages, including (1) the precursor solution, (2) wet thin film, and (3) solid-state film, all of which have unique physical, chemical, and structural conditions.⁷⁴ From the classical nucleation theory, the crystallization is divided into nucleation and growth.⁷⁴⁻⁷⁷ In LHPs, nucleation and growth occur in the liquid and solid-liquid phases (i.e., solvated or colloidal nanoparticles). Therefore, nucleation and growth are sensitive to the fabrication procedures and variables that will influence the morphology and crystallinity of the obtained films.⁷⁴

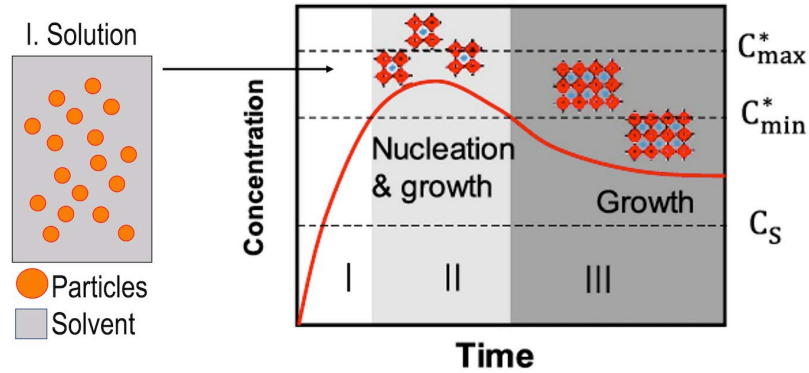


Figure 2.10 Crystallization from solution, adapted LaMer diagram to perovskites. This dissertation will focus on the I stage, the precursor solution. This figure is modified and reproduced with permission. © IOP Publishing 2019. All rights reserved.⁷⁴

Basic nucleation theory and the LaMer process^{74,78} have been used to explain the nucleation and growth process from solution in LHPs (**Figure 2.10**). This process is divided into three stages (1) the solution, pre-nucleation, (2) “Burst” nucleation, and (3) growth by diffusion. Pre-nucleation occurs in the evaporation of the solvent, where the concentration of the solution increases up to the solubility limit C_s . Further solvent loss makes the solution supersaturated, without nucleation processes taking place, until it reaches the minimum supersaturation limit C_{min}^* . The “Burst” nucleation refers to the stage of nucleation and

growth from solution, where particles start to precipitate and grow from solution. After, the growth will continue by diffusion, but no further nucleation will occur. This growth can occur, for example, due to Ostwald ripening or coalescence processes.^{77,78} The state-of-the-art methods used to understand, vary, and control the nucleation and growth of LHPs are reviewed elsewhere.^{74,75}

The colloidal nature of the perovskite precursor solution plays a crucial role in the nucleation and growth of perovskites.⁷⁹ It is important to understand in-depth what happens at the initial precursor solution stage and the relationship with the crystallographic properties of the polycrystalline film. In this dissertation, **Chapter 4** focuses on the first stage of the crystallization process to understand how variations in the precursor solution influence the crystallographic properties of LHP films.

2.3.1 *Colloids and Intermediate Phases*

The formation of LHPs from solution starts by mixing the precursor chemicals that constitute APbX_3 in a non-polar solvent. The precursor chemicals are the lead halide salt PbX_2 and the A-site cation salt AX that will later form the APbX_3 perovskite (**Figure 2.11A**). This process is driven by forming ionic bonds and hydrogen bonds between the precursors at low temperatures.⁷⁴ It has been suggested that these interactions form colloids, made of a soft coordination complex as a lead poly-halide framework between the organic and inorganic components, and can be structurally tuned by the coordination degree.⁸⁰ **Figure 2.11B** shows a schematic of possible interactions between ions and solvent in the precursor solution, forming different nanostructures. For example, iodide plumbate complexes of PbI_3^- and PbI_4^{2-} in solution have been seen by the UV-VIS absorption peaks at 370 nm and 425 nm. This occurs given that the Lewis acid Pb^{2+} center can be coordinated by a Lewis base from six

directions. Therefore, there is competition between the I⁻ ions and the organic solvent over the coordination between Pb²⁺ depending on their binding strength. For this reason, solvated phases between the PbI₂ – solvent or AX-PbI₂-solvent form create fibrous structures in solution.⁷⁴

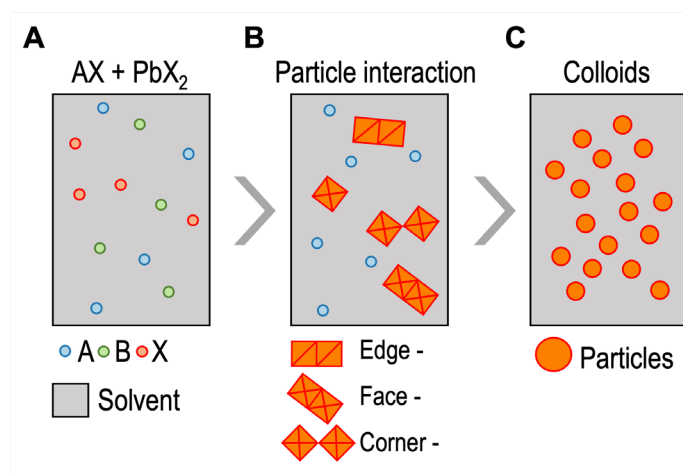


Figure 2.11 Schematic of the precursor salts in solution and perovskite colloids formation. (A) Mixture of AX and PbX₂, followed by (B) particle interaction and formation of Pb-X octahedra with differences in bonds, forming edge-, face- and or corner-sharing octahedra. (C) Overall schematic of colloids formation in solution.

Petrov et al. showed that the solvated phases are dependent on the LHP composition. In particular, the A-site cation and the X-site halide. They showed how different crystal phases formed depending on the composition and solvent, explained by forming different intermediate adducts and solvate phases. **Figure 2.12** shows the crystallization products from FA, MA, I, and Br LHPs in two of the two most widely used solvents, DMF and DMSO. Therefore, even if there is knowledge of the formation of colloids in solution, there is no clarity on the nature, structure, and composition. Due to the diversity in solvate phases, the schematic in **Figure 2.11B** shows the possibility of different colloids in the solution. In **Figure 2.11C**, the schematic is generalized to show that overall, there are particles in the solution that will then influence the nucleation and growth of the LHPs. There is little information about

the nature of these colloids.^{81–83} However, it has been suggested that the DMSO-solvated phases slow the crystallization, allowing the formation of larger grains.⁸⁴ Understanding the colloidal nature and the presence of a solvated phase is important to further understand how it impacts the formation and crystallization of the perovskite.

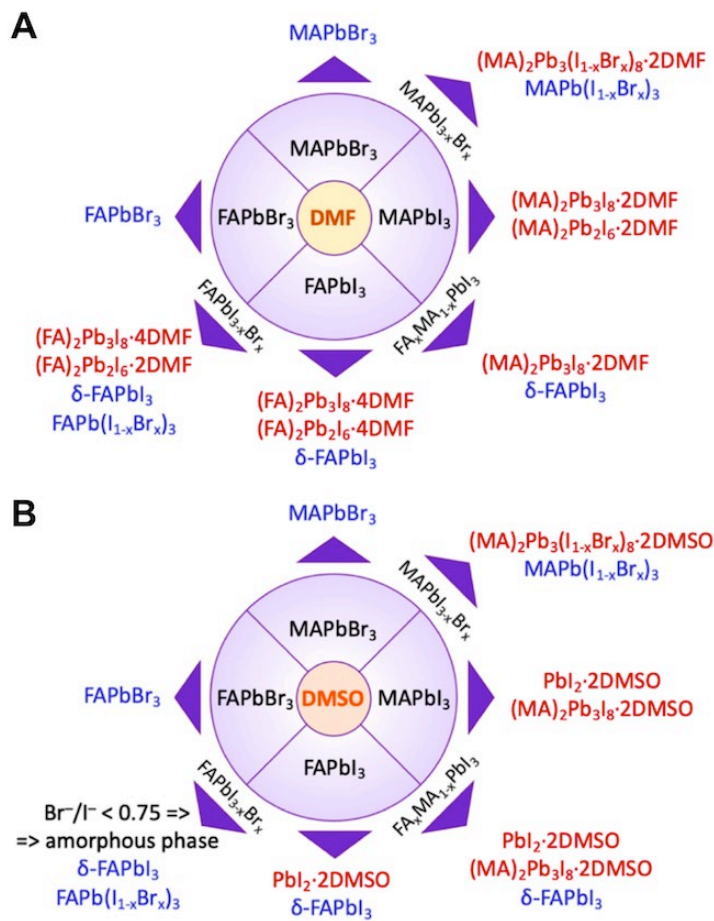


Figure 2.12 Generalized schematic of the crystallization products of LHP in different solvents (A) DMF, and (B) DMSO. Reproduced with permission from *Chem. Mater.* 2020, 32, 7739-7745. Copyright 2020 American Chemical Society.

CHAPTER 3. EXPERIMENTAL METHODS

This chapter has parts from the following published review article:

“Imaging and Mapping Characterization Tools for Perovskite Solar Cells”, *Advanced Energy Materials*, 2019, 9, 1900444, by **Juanita Hidalgo**, Andrés-Felipe Castro-Méndez, and Juan-Pablo Correa-Baena. (License Number 5554970960690)

My contribution: I wrote sections 4 and 5 completely on “Synchrotron-based Mapping Techniques” and “Spectroscopy and Mapping Techniques”. In addition, I discussed and wrote a large part of the introduction and conclusions.

This chapter describes the general experimental procedures, main characterization techniques, and other secondary characterization tools used in this dissertation.

3.1 Lead Halide Perovskite Fabrication

Lead halide perovskite thin films were fabricated from solution-based methods by (1) preparing a precursor solution and (2) depositing the solution by spin coating into a glass, glass/indium tin oxide (ITO), or glass/fluorine-doped tin oxide (FTO) substrate. After deposition, (3) the samples were annealed at high temperatures for 20 to 30 min (**Figure 3.1**). Other additional post-deposition treatments were done and described in this section. All the fabrication process took place in a nitrogen glove box with controlled oxygen and relative humidity close to 0 ppm.

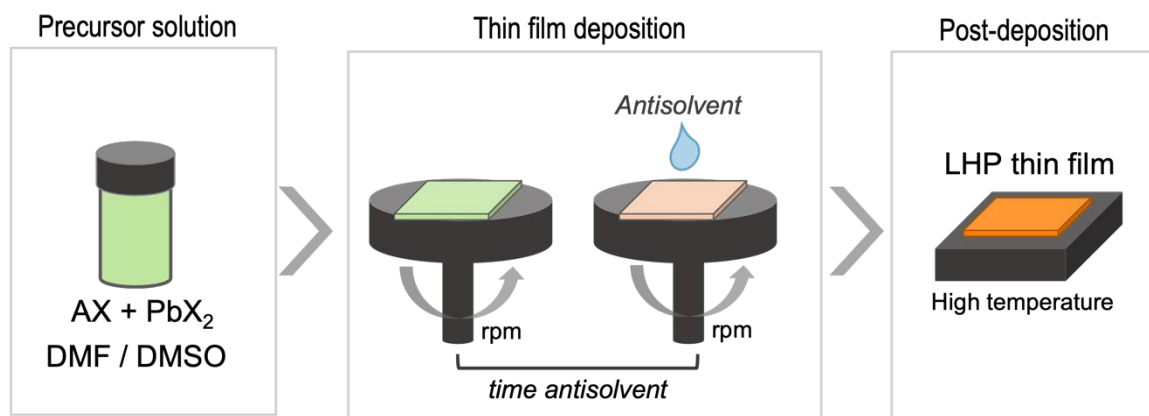


Figure 3.1 Schematic of the fabrication steps of lead halide perovskites. (left) Preparation of the precursor solution by mixing the halide salts in a polar solvent DMF, DMF:DMSO or DMSO, (center) Thin film deposition by spin coating using the antisolvent method, (right) post-deposition annealing at high temperature.

3.1.1 Precursor Solution

The LHP precursor solutions were prepared by mixing the precursor salts, AX with PbX₂, in a solvent. A refers to the different A-site cations (i.e., MA, FA, Cs), and X to the different

halides (i.e., Br, I). The solvents used were pure dimethylformamide (DMF, Sigma Aldrich 99 %), pure dimethylsulfoxide (DMSO, Sigma Aldrich 99 %), or a volume mix of DMF : DMSO in a ratio of 2:1 or 4:1. The powders were weighted in a vial, and then, the solvent was added. The solution was mixed for one hour at 600 revolutions per minute (rpm) in a vortex inside the sealed vial. The solutions were kept in nitrogen before any characterization measurement at room temperature. The following paragraphs specify the concentration and amounts for the different LHP compositions (A-site, X-site).

Lead Bromide APbBr₃: APbBr₃ perovskite precursor solution was prepared for A: MA or FA by mixing MABr (Dyename, 99.99%) or FABr (Dyename, 99.99%) with PbBr₂ (Tokyo Chemical Industry TCI, 99.99% purity) to form a 1.24 M solution. The solvents used were pure DMF, pure DMSO, or a volume ratio of 4:1 DMF : DMSO. The solution stoichiometry had a 5% molar excess of the organic cation.

Formamidinium Lead Iodide FAPbI₃: FAPbI₃ was synthesized using PbI₂ (TCI, 99% purity) dissolved in a mixture of DMF: DMSO in a 4:1 volume ratio. First, we weighted the PbI₂ and added the solvents to form a 1.50 M solution of PbI₂. The PbI₂ solution was heated for 20 min at 80° C. Second, we weighted FAI powder (Sigma Aldrich, 99% purity) in another vial. After, the PbI₂ solution was added to the FAI vial and mixed for 20 min to obtain FAPbI₃ with a final concentration of 1.24 M. The solution stoichiometry had a 5% molar excess of Pb.

Mixed Cation Lead Iodide (Cs,FA)PbI₃: Cs_{0.17}FA_{0.83}PbI₃ (CsFA) was prepared from the following precursor powders: PbI₂ (TCI, 99.99 % purity), FAI (Great Solar), and CsI (Sigma-Aldrich) in a mixture of DMF : DMSO with a volume ratio of 2:1 to form a 1.2 M solution. The molar ratio between Cs and FA was 0.17 to 0.83. The solution stoichiometry had a 5%

molar excess of PbI_2 .

Mixed Cation Mixed Halide $(\text{Cs,FA})\text{Pb}(\text{I,Br})_3$. Mixed cation and mixed halide $\text{Cs}_y\text{FA}_{1-y}\text{Pb}(\text{I}_x\text{Br}_{1-x})_3$ perovskites were prepared with different molar ratios of Cs:FA (y) and Br:I (x). The precursor powders used were CsI (Sigma), FAI (TCI), PbI_2 (TCI), and PbBr_2 (TCI). The precursor powders were weighted on the same vial to form a 0.5 M solution in a mixed solvent of gamma-Butyrolactone (GBL) and DMF with a volume ratio 2:1. The precursor solution was mixed at 600 rpm and 60° C for one hour. The solutions were stoichiometric.

Triple Cation Mixed Halide $(\text{Cs,MA,FA})\text{Pb}(\text{I,Br})_3$ LHP $\text{Cs}_{0.05}(\text{MA}_{0.17}\text{FA}_{0.83})_{0.95}\text{Pb}(\text{I}_{0.83}\text{Br}_{0.17})_3$ (CsMAFA) was synthesized using PbBr_2 (TCI), PbI_2 (TCI), MABr (Dynamo), FAI (Dynamo), and CsI (Sigma). First, we weighted the PbI_2 and PbBr_2 separately and added the solvent (DMF : DMSO, 4:1 volume) to form a 1.50 M solution of PbI_2 and PbBr_2 , respectively. This stock solution was mixed overnight at 60° C. Second, we weighted FAI and MABr powders separately in two vials. The PbI_2 stock solution was added to the FAI vial to form a FAPbI_3 solution with a final concentration of 1.24 M. The PbBr_2 stock solution was added to the MABr vial to form a MAPbBr_3 solution with a final concentration of 1.24 M. Then, MAPbBr_3 and FAPbI_3 were mixed in a 17:83 volume ratio (MAFA solution). Finally, a solution of 1.5 M of CsI in DMSO was added to the MAFA solution in a volume ratio of 5:95 Cs : MAFA, to form the triple cation CsMAFA perovskite. Additionally, the changes in stoichiometry of these precursor solutions were evaluated. The A : Pb ratios are 9% excess Pb (EL) and 5% excess organics (EO), with no changes in the CsI addition for all stoichiometries.

Bulky Cation PEAI: A solution of PEAI powder (Sigma Aldrich) with a concentration 1 mg/mL or 5 mg/mL was prepared in 2-propanol (Anhydrous, Sigma Aldrich). The solution was mixed for one hour before deposition.

3.1.2 Thin Film Deposition

The LHP precursor solution was spin-coated on a glass substrate covered with a TCO (ITO or FTO). The substrates were cleaned by sonication for 15 min in (1) a 2% solution of a neutral soap, (2) acetone, and (3) isopropanol and then dried with a nitrogen gun. After, the substrates went under a UV-Ozone light for 15 min and were taken inside the glovebox. In the glove box, the precursor solution was deposited on top of the substrates to form the LHP thin films via spin coating. Specifically, 80 μ L of precursor solution was added to the substrate in a spin coater. Subsequently, the spin coating process consisted of a two-step program: first at 1000 rpm for 10 s (acceleration of 1000 rpm/s) and then at 6000 rpm for 20 s (acceleration of 2000 rpm/s). During the spin coating process, 250 μ L of chlorobenzene (CB, Sigma 99.50%) was added dynamically. For the perovskites in pure DMF, the CB was added 15 s after the start of the spinning process, whereas for perovskites in DMSO or DMF : DMSO, the CB was added at 25 s.

PEAI Deposition

The solution of PEAI was deposited by spin coating dynamically, on top of the LHP film, at 5000 rpm with an acceleration of 5000 rpm/s for 20 s.

3.1.3 Post-deposition Treatments

After the perovskite deposition by spin coating, immediately after, the substrates were annealed inside the nitrogen glovebox. The annealing conditions were as follows, depending on the composition. These conditions were previously optimized in our laboratory to obtain a pure and high symmetry perovskite phase.

Lead Bromide APbBr₃: 100 °C for 30 min.

Formamidinium Lead Iodide FAPbI₃: 150 °C for 15 min.

Mixed Cation Lead Iodide (Cs,FA)PbI₃: 150 °C for 15 min.

Mixed Cation Mixed Halide (Cs,FA)Pb(I,Br)₃: 100 °C for 15 min.

Triple Cation Mixed Halide (Cs,MA,FA)Pb(I,Br)₃: 100 °C for 1 hour.

Bulky Cation Phenethyl Ammonium Iodide (PEAI): No annealing.

3.1.3.1 Exposure to Humidity

After LHP thin film deposition and annealing, some of the studies in this dissertation involved studying the effect of humidity on LHPs. To evaluate the changes in LHPs due to humidity exposure, two types of treatments were done depending on whether the characterization measurement was *ex-situ* or *in-situ*.

Ex-situ Characterization

After LHP deposition and annealing, the LHP films are exposed to humidity. As illustrated in **Figure 3.2**, LHP films were exposed to humid air with high relative humidity (RH) of 80% in ambient air and dark for 24 hours. The samples were returned to the nitrogen glove box before the subsequent *ex-situ* characterization measurements or before other layer's deposition. Films

exposed to humid air are labeled “H₂O/Air”, and those not exposed are labeled without humidity “w/o H₂O”, with the latter being the control samples. This humidity treatment was done in the *Energy Materials Lab* at Georgia Tech.

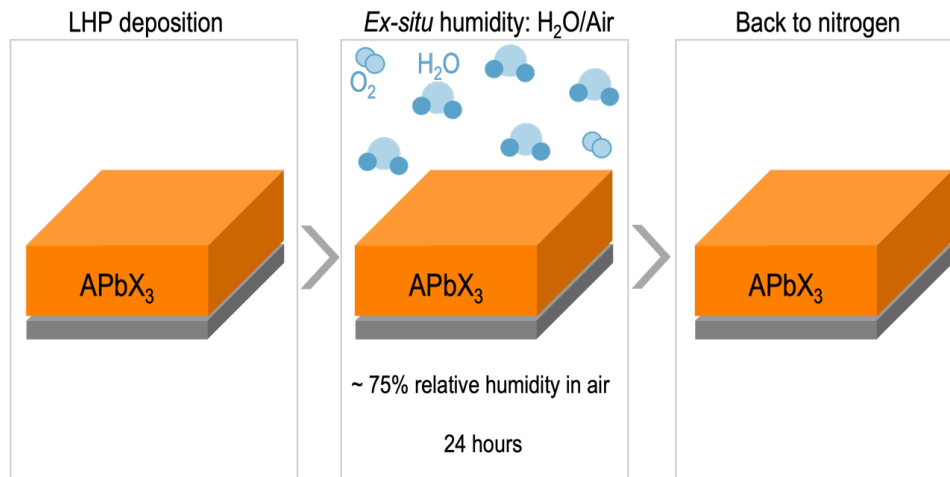


Figure 3.2 Humidity exposure of LHP films for *ex-situ* measurements. (left) First, the LHP is deposited, as described in Figure 3.1, inside a nitrogen glovebox. Subsequently, (center) the film is exposed to air and humidity, outside the glovebox, with a controlled humidity of around 75%. Humidity exposure is for 24 hours, and after (right), the LHP is characterized or returned to the nitrogen glovebox for storage.

In-situ Characterization

The LHP films for *in-situ* characterization techniques were deposited on glass/ITO or glass/FTO/TiO₂. For the *in-situ* measurements, a controlled relative humidity chamber with an experimental setup was used, as shown in the schematic in **Figure 3.3**. This setup was used to measure *in-situ* X-ray scattering (explanation of the GIWAXS in the following section). For an RH of 100 %, all the gas in the chamber came from a water bubbler. The humidity carrier gas into the water bubbler was either dry air or nitrogen (N₂). A controller was used to monitor the RH inside the chamber as the experiments took place. For the “Dry Air” experiments,

the same line of dry air was sent directly to the measurement chamber. This humidity treatment was done at the National Synchrotron Light Source II at Brookhaven National Lab.

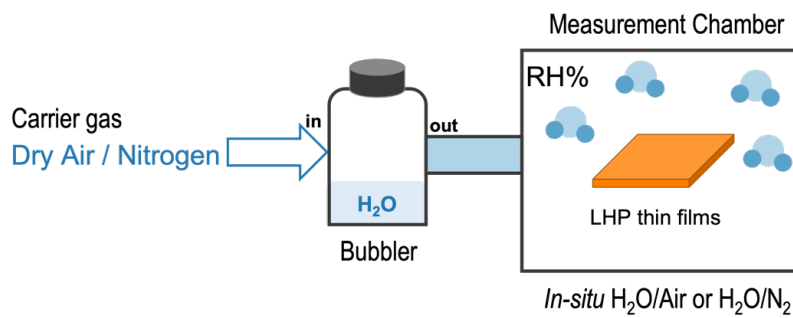


Figure 3.3 Schematic of the setup for humidity exposure for *in-situ* GIWAXS measurements. The relative humidity is controlled by the flow of a dry gas, either air or nitrogen, passing through a water bubbler and then into the measurement chamber. The setup is shown in Appendix B, Figure BS1.

Solar Cell Fabrication

The LHP solar cells fabricated had an n-i-p architecture as described and shown in **Chapter 2, Figure 2.9**. As an electron transport layer, a compact layer of TiO₂ (c-TiO₂) was deposited by spray pyrolysis at 450 °C from a solution containing 480 μL acetylacetonate (Sigma-Aldrich, ≥ 99%), 720 μL titanium diisopropoxide bis(acetylacetonate) 75 wt. % in isopropanol (Sigma-Aldrich) and 10.8 mL of ethanol (Sigma-Aldrich, ≥ 99.5%). The solution was sprayed using O₂ as carrier gas in cycles with 30 s intervals until finishing the solution. The c-TiO₂ was annealed at 450 °C for 30 min. Subsequently, a mesoporous TiO₂ layer (mp-TiO₂) was deposited by spin coating a TiO₂ paste (Sigma Aldrich) in ethanol (150 mg/mL) for 10 s at 4000 rpm and annealed for 10 min at 100 °C. The mp-TiO₂ layer follows a sintering process found in other articles⁸⁵ reaching 450 °C for 30 min. After, the LHP solution was deposited by spin coating, as explained previously. Later, as the hole transport layer, Spiro-OMeTAD

28.4 mM solution was prepared (36.15 mg prepared in 1 mL chlorobenzene), adding 14.5 uL of Co (II) salt (FK209 Sigma-Aldrich, 300 mg per 1mL of acetonitrile), 8.8 uL of LiTFSI (Sigma-Aldrich, 520 mg per 1 mL of acetonitrile) and 14.4 uL of tert-butylpyridine (Sigma-Aldrich). The hole transport layer solution was spin coated dynamically at 3000 rpm for 30 s. Finally, a layer of 50 nm of Au (Alfa Aesar or Kurt Lesker) was thermally evaporated on top to finish the device.

3.2 Characterization of the Structure by X-ray Scattering

To unravel the structure of LHP polycrystalline thin films, synchrotron-based X-ray scattering techniques were used. Synchrotron-based X-ray techniques allow to probe the structure from a micro to a molecular level with improved energy and spatial resolution, higher throughput, reduced sample damage and varied *in-situ* and *operando* setups. Synchrotron X-rays have a high flux, brilliance, and collimation, which are important for weakly scattering samples, such as the LHP, that have organic components.⁸⁶ X-ray scattering is widely used to study the structure of a solid on an atomic and molecular level.^{86,87} The X-rays are irradiated on the LHP, the scattering object, and then scattered.⁸⁸ These scattered patterns reveal information about the arrangement of atoms in the sample and are used to determine the crystal structure and orientation of these structures.⁸⁷ The positions and intensities of the scattering profiles are a Fourier transform of the electron density in the sample.⁸⁶

3.2.1 *Grazing Incidence Wide-Angle X-ray Scattering*

To study the structure of polycrystalline LHP thin films, grazing incidence wide-angle X-ray scattering (GIWAXS) was used. Wide angle X-ray scattering allows probing the small order of magnitude at the atomic scale to acquire of information about the crystallographic structure

and nanostructure.⁸⁸ Synchrotron X-ray radiation is useful for investigating the small volume of the studied sample.⁸⁸ In addition, the incident X-ray is fixed at a grazing incident angle α_i , allowing to minimize the unwanted background scattering from the bulk and obtaining scattering from the surface of the film.⁸⁷ The general sample setup for GIWAXS is shown in the schematic of **Figure 3.4**.

Penetration depth control is one of the main advantages of GIWAXS. By varying α_i , the X-ray will penetrate and scatter from different depths in the sample.⁸⁶⁻⁸⁸ The incident angle α_i is compared to a critical angle α_c , dependent on the sample and refractive index, to determine the penetration depth. The critical angle considers the refraction phenomena of X-rays at the interfaces between different media.⁸⁷ Below α_c , the X-rays undergo total external reflection; there is only an evanescent wave within the refracting medium, penetrating typically only a few nanometers.⁸⁷ In contrast, above α_c , the reflected wave propagates into the bulk.⁸⁸ It is important to consider that the penetration depth will also depend on α_f , the exit angle of the scattered vector.⁸⁹ Overall, the scattering depth is strongly dominated by the selection of α_i below or above α_c .

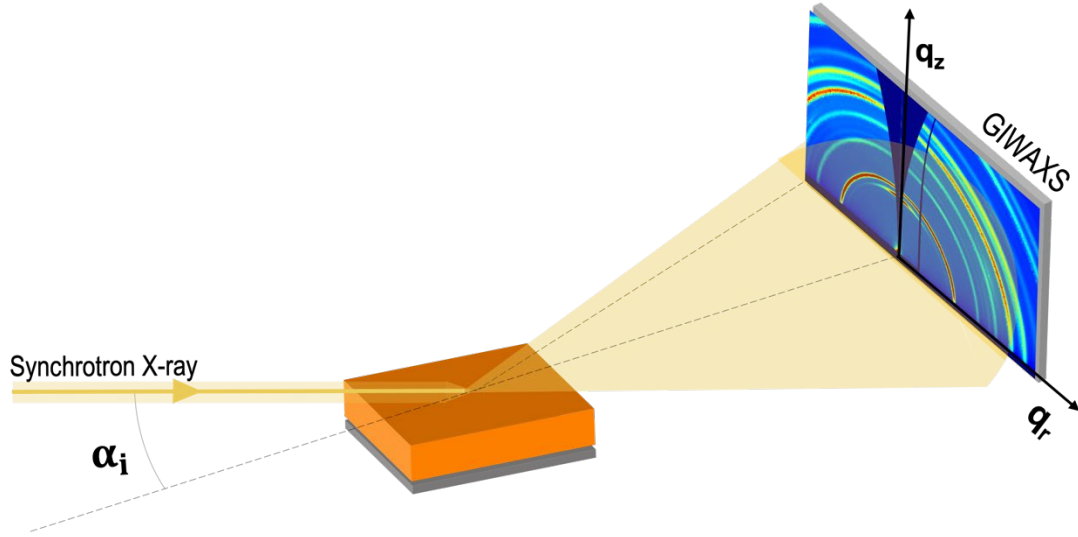


Figure 3.4 Schematic of the grazing incidence wide angle X-ray scattering (GIWAXS) setup by irradiating a synchrotron X-ray with an incident angle (α_i) relative to the thin film sample, scattering in the xy and z directions resulting in a 2D GIWAXS scattering pattern q_z versus q_x .

The critical angle and penetration depth are dependent on the material. Therefore, for the purpose of this dissertation, I calculated the penetration depth by GIWAXS on FAPbI₃ films as a function of the incident angle α_i .⁹⁰⁻⁹² First, α_c is dependent on δ and β , refractive constants that can be derived from the scattering and absorption properties of the medium, respectively. Equations 2-4 define α_c , δ and β .

$$\alpha_c = \sqrt{2\delta} \quad (2)$$

$$\delta = \frac{n_a r_e \lambda^2}{2\pi} f_1 \quad (3)$$

$$\beta = \frac{n_a r_e \lambda^2}{2\pi} f_2 \quad (4)$$

Where n_a is the number density, r_e is the electron radius, λ is the wavelength of the incident X-ray (13.5 keV equivalent to $\lambda = 0.98 \text{ \AA}$), and f_1 and f_2 are the atomic scattering factors.

The number density defined in Equation 5 depends on the density ρ , in this case 4.1 g/mL for FAPbI₃,⁹² Avogadro's number N_a , and molar mass M_a .

$$n_a = \frac{\rho N_a}{M_a} \quad (5)$$

The atomic scattering factors f_1 and f_2 are calculated following Equation 6, with the values in **Table 3.1.**⁹¹

$$f_1 = \sum_i (Z_i + \Delta f_{1i}) N_i \quad (6)$$

Where Z is the atomic number, N_i the number of atoms per volume unit, Δf_{1i} a correction.

Table 3.1. Atomic scattering factors (⁹³)

	Pb	I	C	N	H
f_1	73.5107	52.9602	6.0067	7.0120	1.00E+00
f_2	9.6752	2.8864	2.97E-03	5.86E-03	3.20E-07

Finally, the penetration depth is calculated from Equation 7 as a function of α_i . For FAPbI₃ thin films, α_c is calculated to be approximately 0.16°.

$$\tau(\alpha_i) = \frac{\sqrt{2}\lambda}{4\pi} \left(\sqrt{(\alpha_i^2 - \alpha_c^2)^2 + 4\beta^2} - (\alpha_i^2 - \alpha_c^2) \right)^{-1/2} \quad (7)$$

Figure 3.5 shows the penetration depth as a function of incident angle for FAPbI₃ thin films for GIWAXS measurements with an energy of 13.5 keV.

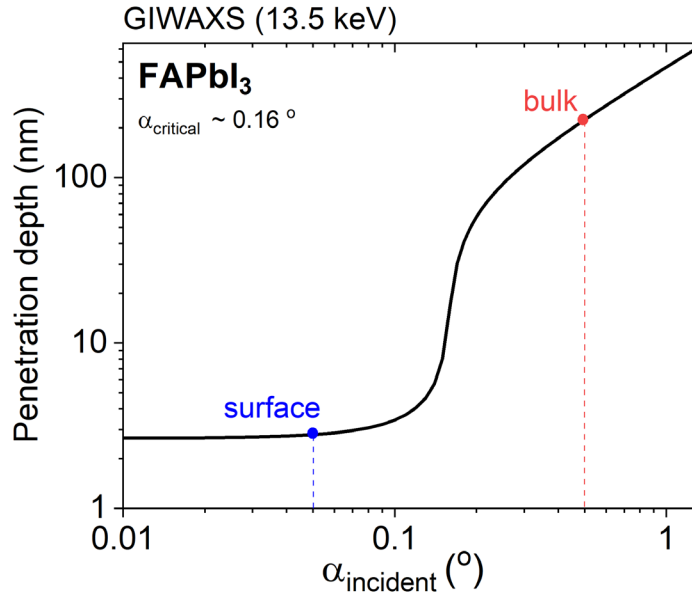


Figure 3.5 Calculated X-ray (13.5 keV) penetration depth as a function of the incident angle (α_i) in FAPbI₃ thin films.

In addition to probing the structure at the surface and bulk with GIWAXS on thin films, GIWAXS has been used to qualitatively describe the orientation of the crystallographic domains in polycrystalline thin films.⁸⁶ The shape and intensity distribution of scattering peaks in the reciprocal scattering patterns (q_z vs q_{xy}/q_r) can be used to describe the orientation of the scattering crystallographic domains.⁸⁶ A film with no preferred orientation or random orientation, such as a powder in diffraction, will result in a ring of uniform intensity, as shown in **Figure 3.6**. In a film with preferred out-of-plane orientation, but isotropic in-plane, the scattering pattern will have spots or arcs of high intensity. The shape of these high-intensity regions will also allow quantitatively comparing the degree of orientation. For example, the defined spot in **Figure 3.6** describes a high degree of crystallographic orientation. Therefore, GIWAXS allows us to compare and learn about thin film orientation. Crystallographic orientation in LHP is investigated in-depth in **Chapter 4** of this dissertation.

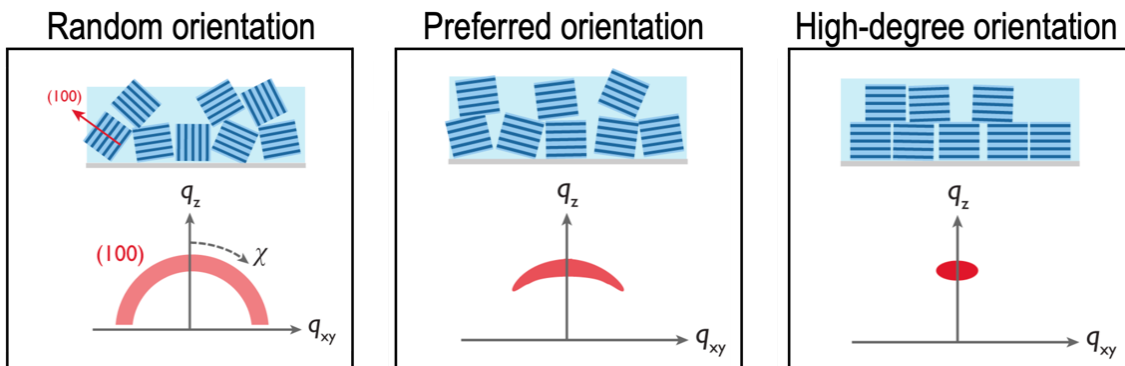


Figure 3.6 Qualitative information on crystallographic orientation from GIWAXS patterns. (left) A complete scattering ring indicative of random orientation. (center) Arc indicative of preferred orientation, and (right) sharp Bragg spot indicative of a high degree of preferred orientation. Figure modified and reproduced with permission from *Chem. Rev.* 2012, 112, 5488-5519. Copyright 2012 American Chemical Society.

The GIWAXS measurements for this dissertation were done at the beamline for Complex Materials Scattering (11-BM), at the National Synchrotron Light Synchrotron II at Brookhaven National Laboratory. An X-ray beam (13.5 keV, $\lambda = 0.918 \text{ \AA}$) with a footprint of 0.2 mm (height) \times 0.05 mm (width) was irradiated on samples in vacuum ($\sim 10^{-5}$ torr) for 10 s with incidence angles of 0.05° , 0.1° , and 0.5° . The samples exposure time was of 20 s, beam divergence was 1 mrad and energy resolution 0.7%. The data were analyzed using the SciAnalysis package provided by the beamline.

3.2.1.1 *In-situ* Humidity Measurements

For *in-situ* GIWAXS with humidity exposure, the LHPs were deposited on glass/ITO or glass/FTO/TiO₂. The incident angles used were 0.1° and 0.5° . Data was taken subsequently for 16 exposed samples. Therefore, the time between measurements of a single sample was around 12 min. In addition, another measurement was done every five points in another spot of the sample to compare and account for sample heterogeneity and discard changes due to sample degradation. The *in-situ* humidity setup is shown in **Figure 3.3**.

3.2.2 X-ray Diffraction

Before the development of synchrotron X-rays, X-rays were discovered in 1895. Later, in 1912, used X-rays to analyze the diffraction of crystals, given their periodicity.⁹⁴ Since then, X-ray diffraction (XRD) is a technique that has been used to determine the structure of crystalline materials that have a periodicity in space.^{87,94} A diffracted beam is composed of a large number of scattered rays; therefore, diffraction is also a scattering phenomenon.⁹⁴ In the same way as for GIWAXS, the scattered X-rays will produce a constructive interference of waves that have an angle of incidence θ to a set of lattice planes that are at a distance d_{hkl} , known as the d-spacing within the lattice planes. The angle at which diffraction occurs is related to the d-spacing of the planes, where h, k, l are Miller indices used to designate the planes within a crystal.^{86,94} The condition of constructive interference is defined by Bragg's law in Equation 8 for an incident X-ray with a certain wavelength λ .⁹⁴

$$n\lambda = 2 \cdot d_{hkl} \cdot \sin\theta \quad (8)$$

Generally, XRD has been used to finely characterize the structure of single-crystals or polycrystalline, such as powders or thin films. Different to the grazing-incidence geometry previously described, powder XRD is generally measured in the Bragg-Brentano geometry. In this geometry, the diffractometer has a constant distance between the sample and detector to measure the same incident and scattered angle θ . From Bragg-Brentano XRD it is not possible to account for and describe orientation. Regarding orientation, a powder has a random orientation of all its crystallites. When measuring thin films, it is not possible to conclude about crystallographic orientation. Though, it is known that orientation affects the diffraction peak intensities and ratios between the different diffraction peaks. From Bragg-Brentano XRD it is not possible to obtain complete information about the structure of polycrystalline thin films.

For this reason, GIWAXS and XRD are complementary to describe the microstructure of LHP thin films.

In this dissertation, Bragg-Brentano XRD was used to study the structural properties of both LHP thin films and powders. For *ex-situ* XRD measurements, a Bruker D8 instrument with a Bragg-Brentano geometry (HZB, Berlin), or a PANalytical Empyrean and PANalytical X'Pert Pro MPD (Georgia Tech, Atlanta) were used. For the results in **Chapter 4**, XRD analysis was done by fitting with the Gaussian distribution and calculating FWHM in OriginPlus software. For the results in **Chapter 5** and **Chapter 6**, a Le Bail analysis was done using the FullProf software, and the structure identification was made using CrystalMaker software.

3.2.2.1 *In-situ* Powder XRD Measurements

In **Chapter 6.2**, for the set of powder LHPs Mixed Cation and Mixed halide, the temperature-dependent phase transitions were measured by *in-situ* XRD. Synchrotron-based *in-situ* XRD was measured at beamline KMC-2 in BESSY II at the Helmholtz Zentrum Berlin (HZB), Germany. The instrument used a Bruker Vantec 2000 area detector. The X-rays had an energy of 8 keV, optimized for the beamline. For the temperature controller, a closed cycle refrigerator of reference TMP-CCR-HXR was used. XRD patterns were taken from 300 K to 20 K in steps of 20 K. This beamline offered both the experimental precision as well as the sample environment to perform such investigations. Powder studies are also important for a better indication of the thermodynamic processes due to a more pronounced crystallization

process, less exposed surfaces, larger probed volume compared to thin film samples, and a better instrumental resolution. Le Bail fittings using the FullProf software were done to calculate the lattice parameters and phase refinement for the samples at 300 K.

3.2.3 *Small Angle X-ray Scattering*

Small angle X-ray Scattering (SAXS), different from WAXS, provides important and unique information on the size and morphology of larger-scale structures. From SAXS measurements, it is possible to learn about inter-particle correlations in non-crystalline systems.⁸⁷ In this dissertation, in **Chapter 4**, SAXS was measured to the LHP precursor solutions to learn about inter-particle correlations in solution previous to LHP thin film formation.

The SAXS measurements were performed on lead bromide solutions using the HZB ASAXS instrument⁹⁵ installed at the four-crystal monochromator beamline (FCM) of the Physikalisch-Technische Bundesanstalt (PTB),⁹⁶ and operated at the BESSY II synchrotron of HZB. The solutions were measured in transmission in flat rectangle-shaped capillaries of 0.1 mm thickness under vacuum conditions using monochromatic X-rays of 10 keV. We used a four-crystal monochromator with Si 111 crystals for monochromatizing. This energy was optimized for the sample's transmission and scattering vector range. Data were collected three times for each sample with 600 s illumination per image. The images did not show any notable differences, implying that the solutions were stable under the chosen conditions. The 2D scattering patterns were azimuthally integrated and corrected for instrumental background and contributions of the sample holder through the BerSAS software.⁹⁷ The SAXS measurements in this dissertation were performed by Dr. Joachim Breternitz, Dr. Armin Hoell, and Professor Susan Schorr from the Helmholtz Zentrum Berlin.

3.3 Elemental Chemistry Characterization

Different from X-ray scattering, elemental chemistry is learned through X-ray absorption techniques. In this case, an X-ray photon is absorbed by an atom, and the excess energy is transferred to an electron which is expelled from the atom, leaving it ionized.⁸⁷ The fluorescent X-ray emission occurs when one of the electrons in an outer shell fills the hole, creating a photon. The Auger electron emission happens when the atom may also relax to its ground state energy by liberating one electron.⁸⁷

3.3.1 *Surface Chemistry by X-ray Photoelectron Spectroscopy*

X-ray photoelectron spectroscopy (XPS) is a surface-sensitive technique used to learn about material's elemental composition, chemical state, and electronic structure. In general, XPS needs an ultra-high vacuum. Soft X-rays are irradiated on a sample, and the photoelectron effect leads to the emission of an electron which is then analyzed by its kinetic energy. A spectrum is obtained as a plot of the number of detected electrons per energy interval versus their kinetic energy.⁹⁸ In particular, each element has a unique spectrum, allowing us to quantify the elemental chemistry of a material. In addition, from peak heights or areas it is possible to identify the chemical states. In addition to the photoelectrons emitted, Auger electrons may also be emitted because of the relaxation of the excited ions remaining after photoemission.⁸⁷

In this dissertation, XPS was used to quantify the elemental chemistry at the surface of LHPs. XPS was measured with a Thermo Scientific K-Alpha system using a monochromatic Al K-alpha X-ray source (1486.6 eV) with a 60° incident angle and a 0° photoemission angle, both measured from the samples' normal vector. The pressure of the chamber was less than $1e^{-7}$ Torr. Survey and high-resolution scans were collected. High-

resolution scans were taken with a step size of 0.100 eV and a dwell time of 50 ms for C1s (20 scans), N1s (16 scans), I3d (3 scans), O1s (20 scans), Pb4f (3 scans), and Cs3d (3 scans). Peak fitting and elemental composition were calculated with the Thermo Scientific Avantage Data System.

3.3.2 Bulk Chemistry by X-ray Fluorescence and Operando X-ray Beam Induced Current

X-ray fluorescence (XRF) is another technique used to learn about the elemental chemistry of a sample. A synchrotron-based high-energy X-ray source is irradiated on the sample, and core electrons are excited, displacing them from their atomic orbital positions. Electrons from higher shells then occupy the vacant positions, and in this process a fluorescent photon is released. These photons have a characteristic energy based on the excited element, therefore, and this signal is measured by the detector in an XRF instrument.⁹⁹ Moreover, XRF has been used as a mapping technique. XRF mapping allows plotting the elemental chemistry and area distribution of a sample. Synchrotron-based XRF uses X-rays with 10 ppm sensitivity at a spatial resolution of 1 μm . XRF mapping is a useful technique for the elemental plotting of thin films such as LHPs.

XRF can be correlated to other methods, such as X-ray beam induced-current (XBIC). Synchrotron-based XRF has been used in parallel to *operando* XBIC in PSCs.⁹⁹ The XRF-XIBC measurements allow to correlate the chemical composition with electrical performance, thereby probing recombination dynamics or changes in photocurrent due to the presence or distribution of certain elements.⁹⁹ In this dissertation, I characterized LHP films by XRF and PSCs by XRF-XBIC. From XRF maps, I quantified the elemental compositions, obtaining values of grams per area, and then compared the molar ratios between the LHP main elements such as Pb, I, and Br. For XRF-XBIC maps, complete PSCs were measured.

These measurements were done at beamline 2-ID-D at the Advanced Photon Source (Argonne National Laboratory). The X-ray energy used was 16.5 keV with a step size of 0.15 μm and 50 ms dwell time. The XRF data was acquired with the backside of the solar cell, the Au facing the incident X-ray beam, and the fluorescence spectrum was collected point-by-point during mapping. XRF data was obtained in the same area of the induced current, giving a direct correlation between both. For data analysis, the MAPS software was used, and the spectrum fitting was used to deconvolute overlapping peaks and backgrounds from fluorescence data. In addition, after a standard calibration, it was possible to quantify in the software the mass concentration in the sample to calculate the ratio between Br:Pb and Cs:Pb accurately. The NIST thin-film standards SRM 1832 and 1833 were used for the calibration of the elemental concentrations.

3.4 Morphology and Optical Properties Characterization

In addition to the X-ray techniques used to characterize the structure and chemistry in LHPs in this dissertation, other secondary techniques were used to characterize the film morphology and to calculate the optical bandgap of these materials.

3.4.1 Scanning Electron Microscopy

Scanning electron microscopy (SEM) is one of the most widely used characterization techniques in PSCs. This tool has been mostly used for the morphological characterization of materials. The most common use is to analyze and control the thickness of the layers and

surface coverage. In LHPs, it has been used to identify the uniformity and homogeneity in the grain sizes.⁹⁹ In SEM, an image is formed by the interaction of the sample and a focused beam of electrons with a voltage between 0.1 and 50 kV. The sample measurement parameters and preparation are important to prevent sample charging. Low voltages are needed, and in some cases, it is needed to metallize the sample with gold or platinum.⁹⁹ In this dissertation, I measured SEM to control the morphology, uniformity, and domain sizes on the LHP thin films. The SEM measurements were done using an SEM Hitachi SU8010 1nm resolution and secondary electron detector at 5keV and 10uA (Georgia Tech, Atlanta).

3.4.2 *UV-VIS Spectroscopy*

UV-VIS spectroscopy is a simple and widely used type of absorption spectroscopy that uses light in the ultraviolet (UV) and visible (VIS) regions of the electromagnetic spectrum. UV-VIS light is used to study the electronic structure of different samples in liquid or solid states (i.e., thin films, powders). The light is irradiated to a sample and collected by transmission or reflection, and the amount of light absorbed is measured. From the absorption spectrum, it is possible to learn about the electronic transitions that occur in the sample, from which it is possible to know the optical bandgap, for example.

The bandgap energy of a semiconductor describes the energy needed to excite an electron from the valence band to the conduction band.¹⁰⁰ From UV-VIS spectra, the optical bandgap of different LHP was calculated. To calculate the bandgap, the tauc-plot method was used by plotting the absorption component versus its energy following the methods described by others.¹⁰⁰ In this dissertation, UV-VIS was measured using a PerkinElmer Lambda 1050 spectrophotometer. The measurements were done on LHP on glass substrates, at room temperature, and air atmosphere.

3.5 Solar Cell Characterization

To evaluate the performance of the fabricated PSCs, their photovoltaic performance and long-term efficiency stability was measured. In addition, impedance spectroscopy measurements were done on solar cells to learn about other electrical properties, such as ionic effects.

3.5.1 Photovoltaic Performance

The performance characteristics of a solar cell device are extracted from a current density-voltage ($J-V$) curve.¹ The $J-V$ curves are obtained by applying a voltage sweep in reverse and forward scan to obtain a current density for each voltage point. The $J-V$ measurement is done under light or dark. Generally, one sun is irradiated (100 mW/cm^2 , AM 1.5G by a solar simulator) to the device to evaluate its solar cell performance. Moreover, sun simulators allow for modifying the light intensity and tuning the light spectrum. The obtained $J-V$ curve allows us to calculate the main solar cell parameters, namely short circuit current (J_{sc}), open circuit voltage (V_{oc}), fill factor (FF), maximum power point (MPP), and power conversion efficiency (PCE). In particular, the FF is calculated as the ratio between the MPP and the power from $J_{sc} \cdot V_{oc}$. The PCE is calculated from the ratio between the MPP and the incoming solar power (100 mW/cm^2), providing a percentage of efficiency.

In this dissertation, the $J-V$ curves of the solar cells in **Chapter 4.1** and **Chapter 6** were measured using a LITOS LITE setup (Fluxim, Switzerland) equipped with a Wavelabs Sinus-70 AAA solar simulator with standard AM1.5 G illumination at room temperature and ambient air. The $J-V$ curves were obtained in the range from 1.4 to -0.5 V with a scan speed of $50 \text{ mV} \cdot \text{s}^{-1}$ from both reverse and forward scan directions. The active area of the device was 0.128 cm^2 , and a black metal mask with an aperture area of 0.0625 cm^2 was used to define the

illuminated area. The stabilized PCE was acquired by measuring the MPP for 180 s. The solar cells in **Chapter 4.2** were measured using a Keithley and Wavelabs solar simulator for devices with an area of 0.1 cm^2 without a mask.

To track long-term device stability, a stabilized MPP was measured under one sun illumination. For the solar cells in **Chapter 4**, the solar cells were aged in a custom-built high-throughput Ageing Setup.¹⁰¹ To track the MPP, a perturb and observe algorithm¹⁰² with a delay time of 1 s and a voltage step-width of 0.01 V was applied. MPP values were recorded every 2 min for all cells automatically. Devices were actively cooled with Peltier elements and always kept at $25 \text{ }^\circ\text{C}$ with active areas touching a heating pad for direct thermal coupling. Aging was performed under a continuous flow of nitrogen in a closed box. No additional encapsulation was utilized. Sunlight with 1000 W/m^2 intensity was provided by a metal-halide lamp using an H_2 filter. The light intensity was actively controlled with the help of a silicon irradiation sensor which itself was calibrated using a Silicon reference cell from Fraunhofer ISE. The test is in accordance with the protocol ISOS-L-1I.¹⁰³ For the solar cells in **Chapter 6.1**, for the long-term stability measurement, LITOS was used, a stress-test platform for degradation analysis (Fluxim, Switzerland). The solar cells were stressed by one sun illumination and introduced a constant flow of air. The power density was measured every 100 s, for 24 hours, without a mask.

Additionally, from the $J-V$ curve, an additional feature that has been widely investigated in PSC was observed, the hysteresis of the $J-V$ curve. The hysteresis is the mismatch between the forward voltage scan (FS, from short circuit to open circuit) with the reverse scan (RS, from open circuit to short circuit) from the $J-V$ curve.¹⁰⁴ Previous LHP studies have shown a unique dependence on the voltage scan direction revealing significantly

different power conversion efficiencies depending on the scanning direction. The origin of this phenomenon is still unclear but generally attributed to slow capacitive current, trapping and de-trapping processes, defects, ion migration, and ferroelectric polarization.¹⁰⁴ In this dissertation, in **Chapter 4**, hysteresis is attributed to ionic effects. Hysteresis was used to quantitatively compare the mismatch between FS and RS, therefore, a hysteresis index was calculated.

3.5.2 *Impedance Spectroscopy*

Impedance spectroscopy is used to analyze the electrical properties of a material as a function of frequency. A small electrical signal is applied to a sample or device, and the resulting current-voltage responses are measured. From the impedance spectra, it is possible to analyze the resistive and capacitive properties of a device. Impedance spectroscopy has been used to analyze the electrical properties in PSCs. However, it has shown to be a challenging characterization given the variety of data interpretations depending on the chosen solar cell equivalent circuit.¹⁰⁵ In **Chapter 4** of this dissertation, the solar cells were analyzed by impedance spectroscopy. The objective was to correlate capacitive properties with ionic effects in PSCs. Impedance measurements were carried out in a PAIOS instrument (Fluxim, Switzerland) on complete solar cells at room temperature under one sun illumination and ambient air. The measurements were performed at different offset voltages from 0 V to the open circuit in 5 steps. The sweep frequency was from 10 MHz to 0.1 Hz, with an amplitude of 10.0 mV. Z-view software was employed to analyze the results and fit the data to the equivalent circuit.

CHAPTER 4. CRYSTALLOGRAPHIC ORIENTATION IN HALIDE PEROVSKITES

This chapter is based on the published articles:

“Solvent and A-site Cation Control Preferred Crystallographic Orientation in Bromine-Based Perovskite Thin Films”, *Chemistry of Materials*, 2023, 35, 11, 4181-4191, by **Juanita Hidalgo**, Yu An, Dariia Yehorova, Ruipeng Li, Joachim Breternitz, Carlo A.R. Perini, Armin Hoell, Pablo P. Boix, Susan Schorr, Joshua S. Kretchmer, and Juan-Pablo Correa-Baena. Reprinted with permission. Copyright 2023 American Chemical Society.

External contribution: The theoretical DFT calculations were developed by the group of Professor Joshua S. Kretchmer from the School of Chemistry and Biochemistry at the Georgia Institute of Technology. The ideas regarding the mechanisms resulted from discussions between me, Prof. Kretchmer, Dariia Yehorova, and Prof. Correa-Baena.

“Moisture-Induced Crystallographic Reorientations and Effects on Charge Carrier Extraction in Metal Halide Perovskite Solar Cells”, *ACS Energy Letters*, 2020, 5, 3526-3534, by **Juanita Hidalgo**, Carlo A.R. Perini, Andrés-Felipe Castro-Mendez, Dennis Jones, Hans Köbler, Barry Lai, Ruipeng Li, Shijing Sun, Antonio Abate, and Juan-Pablo Correa-Baena. Reprinted with permission. Copyright 2020 American Chemical Society.

Preferred crystallographic orientation in polycrystalline films is desirable for efficient charge carrier transport LHP and semiconductors, more generally. However, the mechanisms that determine the preferred orientation of LHPs are still not well understood. This dissertation investigates the factors that affect crystallographic orientation in LHPs. The first part of this chapter shows that the solvent of the precursor solution and organic A-site cation strongly affect the preferred orientation of the deposited Br-based perovskite films. Specifically, the solvent DMSO influences the early stages of crystallization and induces preferred orientation in the deposited films by preventing colloidal particle interactions. Additionally, the MA cation induces a higher degree of preferred orientation than the FA counterpart. This work highlights the important interplay between the solvent and organic A-site cation in determining crystallographic orientation.

To study the structure-property-performance relationship between crystallographic orientation, electric properties, and performance of solar cells, the second part of this chapter evaluates different orientations and their effect on solar cells. Previous studies have shown changes in crystallographic properties due to humidity exposure.^{106,107} Therefore, to evaluate the effect of different crystallographic orientations in LHP films in solar cells, a humidity-induced reorientation treatment was used as a tool to tune orientation in the mixed-cation mixed-halide perovskite $\text{Cs}_{0.05}(\text{MA}_{0.15}\text{FA}_{0.85})\text{Pb}(\text{I}_{0.85}\text{Br}_{0.15})_3$ (CsMAFA). Humidity exposure induces a crystallographic reorientation in the polycrystalline films, which also depends on the amount of organic A-site cation material at the surface. For films with an excess of organic halide, the humidity was shown to induce orientation in the (100) plane contributing to the enhancement of photocurrents and long-term device stability. This work shows the importance of preferred orientation for the electronic properties of LHPs emphasizing charge carrier extraction in photovoltaic devices.

4.1 The Role of the Solvent and A-site Cation

Preferred crystallographic orientation in polycrystalline films is highly desired to control charge carrier transport in organic-inorganic lead halide perovskite solar cells. For example, oriented crystallographic domains have been shown to enhance charge carrier transport¹⁰⁸ and suppress ionic migration¹⁰⁹ in lead halide perovskite films. Therefore, manipulating the degree of crystallographic orientation presents an important design principle.^{86,110,111} Furthermore, organic-inorganic lead bromide perovskites, compared to the more common lead iodide perovskites, have also shown potential for multijunction perovskite solar cells because of their wide bandgap and phase stability.¹¹²⁻¹¹⁴ Beyond solar cells, lead bromide perovskites have been used for light-emitting devices¹¹⁵ and photodetectors.^{116,117} For these reasons, understanding the structure-property relationships of bromine-based perovskites is fundamental to designing better optoelectronic devices. In particular, the underlying mechanisms that dominate crystallographic orientation in lead bromide perovskites are underexplored.

Solvent engineering has been used to control the crystallization kinetics and different properties of perovskite polycrystalline thin films.¹¹⁷⁻¹²² The highest power conversion efficiency in perovskite solar cells has been through solution processing utilizing a precursor solution of a mixture of N,N-dimethylformamide (DMF), and dimethyl sulfoxide (DMSO).¹¹⁸ Differences in coordination between the solvent, DMF or DMSO, with the perovskite precursors salts (e.g., MABr, FABr, PbBr₂) have led to variations in the crystallization process, affecting the film morphology and crystallographic orientation.^{83,122,123} Solvent coordination influences the formation of colloidal particles in solution, which has an important effect on the overall crystallization process and perovskite thin film morphology.^{82,124,125} For example, adding an optimum amount of DMSO slows down crystallization and helps control

crystallinity in halide perovskites.^{118,120,126,127} Instead, DMF coordinates less strongly, leading to a faster and poorly controlled crystallization.^{120,127} The colloids in the precursor solution may agglomerate, forming colloidal particles and intermediate solvent-perovskite phases, all of which have an effect on the crystallized film.^{81,82,124} In particular, iodide-based lead perovskites form numerous types of iodo-plumbate structures in solution and other solvent-perovskite phases both in DMF and DMSO.^{83,121,128} Ray et al. studied and observed important differences in the precursor solution colloids leading to different final structures in Cs-Pb-Br complexes.¹²⁵

In lead halide perovskites APbBr_3 , A can be the inorganic Cs atom or the organic methylammonium (MA) or formamidinium (FA) molecule.^{86,108,110,111,129} The A-site cation has also been shown to play a role in the crystallization behavior of halide perovskite thin films. For example, Petrov et al. showed that FA and MA led to different solvent-halo-plumbate complexes. For the Br-based compositions, they showed that the combination of MABr and PbBr_2 in DMF or DMSO did not form any solvent intermediate phase as it converted directly into MAPbBr_3 perovskite.⁸³ However, in the case of FA, combining FABr and PbBr_2 in DMSO, a solvent intermediate phase $(\text{FA})_2\text{PbBr}_4\text{-DMSO}$ was formed.^{83,117} This suggests that the A-site cation has a very strong influence on the crystallization of thin films. An et al. studied the Cs-FA iodide-bromide compositional space from a pure DMSO precursor solution, showing that the film became more oriented when Cs and Br were added.⁶⁴ In agreement with An, Steele et al.¹²⁹ studied the crystallographic orientation of all-inorganic lead iodide perovskites, where they found that incorporating Br into CsPbI_3 reduced the orthorhombic lattice distortion and led to energetically favored crystallographic orientations. Zheng et al.¹¹⁰ manipulated the crystallographic orientation of lead halide perovskites by incorporating alkali metal cations such as Cs and Rb into the A-site. These different studies have shown that both solvent and composition will influence the orientation. Further, separating the solvent and

composition (A-site cation) effects is important to understand the dominating factors that lead to a high degree of orientation for an optimal material design.

Herein, we investigate the role of the solvent and, importantly, of the organic A-site cation in controlling crystallographic orientation in lead bromide perovskites. To understand polycrystalline film orientation, we start from the early stages of crystallization by analyzing the precursor solutions through small-angle X-ray scattering (SAXS). We study the two organic cations MA and FA, both in DMF and DMSO, to unravel the A-site cation effect in orientation. Crystallographic film orientation is analyzed by grazing-incidence wide-angle X-ray scattering (GIWAXS). We observe an interplay between solvent and A-site cation that dominates the crystallographic orientation in lead bromide perovskites. We observe that DMSO creates a highly oriented film, compared to a more random orientation, when using DMF. For the A-site cation, regardless of the solvent, MAPbBr₃ shows a higher degree of orientation than FAPbBr₃. By calculating the surface energy of the (100) and (110) plane facets, we see that MAPbBr₃ is thermodynamically favored to have the (100) planes oriented parallel to the surface; instead, FAPbBr₃ exhibits a near degeneracy between the (100) and (110) facets, leading to a lower degree of preferred orientation. In addition, we show that the A-site cation, given differences in preferred orientation, does not affect ionic diffusion but does change the ionic density as a function of a bias, as shown in impedance spectroscopy. The latter causes increased hysteresis in solar cells. Our findings provide valuable guidelines for designing lead bromide perovskites with an optimum degree of preferred crystallographic orientation for optimal performance.

4.1.1 Early Stages of Crystallization

To analyze the perovskite precursor solutions, we measured SAXS of MABr-PbBr₂ and FABr-PbBr₂ precursors in DMF and DMSO (1 M). SAXS is a technique widely used to analyze the structure of nanoparticles in solution and their colloidal properties, and reveals information about sizes, distributions, and the interaction of these particles.^{82,130} Flatken et. al introduced SAXS as a technique to reveal the colloidal nature of lead halide perovskites.⁸² Moreover, SAXS allows for the analysis of high concentration solutions in comparison to other techniques such as dynamic light scattering (DLS) and UV-VIS spectroscopy, that necessitate lower concentrations.^{82,124,131} **Figure 4.1** shows our SAXS results and interpretation. In **Figure 4.1A**, the DMF solutions generate clear and strong scattering peaks. In SAXS patterns, the scattering intensity indicates the presence of particles in solution. In addition, the scattering peak maximum results from particle interactions in solution.⁸² This strong particle interaction indicates a quasi-crystalline prearrangement of particles in solution, which will affect the early stages of crystallization.^{82,89} The maximum peak position at q_{max} reveals the mean d spacing from Bragg's law $d = 2\pi/q_{max}$. The d spacing is the distance between the mass centers of interacting colloidal particles. From Figure 1A, we calculate the q_{max} from a Lorentzian fitting and retrieve the d -spacing (fitting in **Figure AS1, Appendix A**). For both A-site cations in DMF there is colloidal particle interaction in solution. The calculated interparticle distance for both FA and MA particles is around 1.85 nm. Flatken et al. have shown a similar SAXS peak when preparing different lead iodide perovskites such as MAPbI₃ and FAPbI₃ in a mixture of DMF and DMSO.^{81,82} However, the pure DMSO precursor solution showed no clear scattering peak (**Figure 4.1A**).

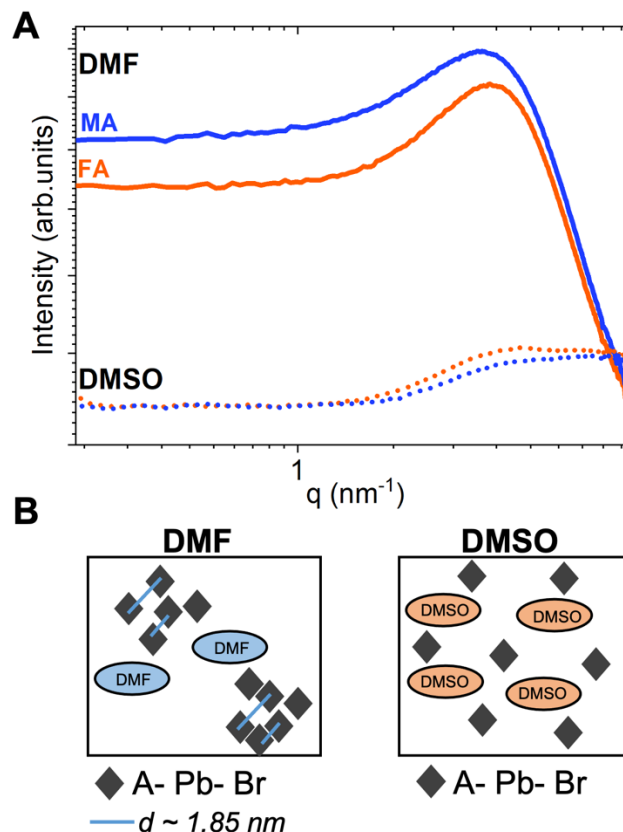


Figure 4.1 Particle interactions in the precursor solution. (A) SAXS data for the four studied systems MAPbBr_3 in DMF or DMSO, and FAPbBr_3 in DMF or DMSO. (B) Schematic of the particle interaction in DMF and DMSO interpreted from SAXS data, A is MA or FA, and d is the interparticle distance.

In comparison to DMF, DMSO prevents the A-Pb-Br interaction as DMSO binds more strongly than DMF to the precursor salts, preventing the A-Pb-Br interaction. This suggests that there is no colloidal particle interaction. In contrast, in DMF, a solvent with weaker coordination, the colloidal particles interact with each other and form clusters.¹²² This is in agreement with the previous work by Ray et al. which showed that due to the strong coordination of DMSO, the particles in solution do not interact with each other, remaining isolated.¹²⁵ This work also showed that DMSO forms colloidal particles one order of magnitude smaller than in DMF.¹²⁵ The schematics in **Figure 4.1B** show the hypothesized differences in particle interaction for DMF and DMSO. The shape and composition of these

particles are unknown but based on the work of Ray et al.¹²⁵ and Flatken et al.⁸¹, we speculate that these are bromo-plumbate octahedra, the result of the interaction between A- Pb- Br in solution. We observe that in the bromide precursor solution, like in iodide perovskites,^{120,122} the colloidal particle interactions in solution are driven by the solvent, while the A-site cation does not show to play a role in the colloidal interactions.

4.1.2 Preferred Crystallographic Orientation

We performed GIWAXS measurements on thin films prepared with DMF and DMSO to examine the effect of different cluster formations arising from the different solvents on the orientation of the thin films. Synchrotron-based GIWAXS has been widely used to analyze the crystallographic orientation and the structure of the lead halide perovskites in thin films and solar cells.^{129,132} First, we study the effect of the solvent of the precursor solution on the crystal phases and crystallographic orientation by comparing the deposition of FAPbBr₃ and MAPbBr₃ in DMF, DMF:DMSO (4:1 volume), and DMSO. The 2D GIWAXS patterns were integrated to provide 1D diffraction patterns that are shown in **Figure AS2**. For all the solvents, MAPbBr₃¹³³ and FAPbBr₃^{36,134} display diffraction peaks corresponding to a cubic symmetry $Pm\bar{3}m$. To identify crystallographic orientations, we analyzed the Debye-Scherrer rings from the GIWAXS patterns in **Figure 4.2**. **Figure 4.2A** shows the 2D GIWAXS for MAPbBr₃. As we change the solvent from DMF to DMSO, we see a clear evolution of the crystallographic orientation. For DMF, we observe a complete Debye-Scherrer ring of the (100) plane at $q \sim 1.06 \pm 0.06 \text{ \AA}^{-1}$, evidence of random orientation as the crystallographic domains scatter X-rays in all angles. The complete ring sharpens into an arc when adding one-fourth of the volume of DMSO, showing a preferred orientation of the crystallographic domains. For pure DMSO, the arc of the (100) plane sharpens further into a high-intensity

Bragg spot, indicating a high degree of preferred orientation. **Figure 4.2B** shows the 2D GIWAXS for FAPbBr₃, where the evolution and degree of orientation differ. For DMF and DMF:DMSO, FAPbBr₃ shows a uniform intensity in all the rings, suggesting the film has no preferred orientation. For pure DMSO, the ring of the (100) plane sharpens into an arc with maximum intensity at $q_r = 0$, increasing the degree of preferred crystallographic orientation from random to preferentially oriented crystallographic domains.

To further analyze and quantify crystallographic orientation, we integrated the azimuthal profile (χ) of the Debye-Scherrer rings of the first two peaks corresponding to the (100) plane at $q_r \sim 1.06 \pm 0.06 \text{ \AA}^{-1}$, and the (110) plane at $q_r \sim 1.4 \pm 0.06 \text{ \AA}^{-1}$. The peak of the azimuthal profile provides information about the direction of the preferred orientation of the planes. Since the grazing-incidence measurements give rise to a missing wedge near the q_x axis due to the curvature of the Ewald sphere, it is important to analyze the orientation of the two planes. We studied the (100) and (110) planes, where the (110) plane complements the quantitative description of orientation. The 100 and 110 Debye-Scherrer rings are integrated from $\chi = -80^\circ$ to 80° , where $\chi = 0^\circ$ is set at $q_r = 0$ (out-of-plane) and $\chi = 90^\circ$ at $q_x = 0$ (in-plane). For MAPbBr₃, we integrated the azimuthal profile of the Debye-Scherrer rings from **Figure 4.2A** into **Figure 4.2C**, and for FAPbBr₃, the azimuthal profiles are integrated from **Figure 4.2B** into **Figure 4.2D**. To understand the dispersion in the preferred orientation of the crystallographic domains, we fit the azimuthal profile peaks into a Pseudo-Voigt or Gaussian function from which we obtain the full width to half maximum (FWHM) and other statistical parameters shown in **Table AS1**. The azimuthal profile for MAPbBr₃ in **Figure 4.2C** shows a peak at 0° of the (100) plane, evidence that these planes are oriented parallel to the substrate. In addition, the azimuthal profile peak of the (110) plane is around 45° , which is consistent with the (100) plane being oriented parallel to the substrate (explanation in **Figure**

AS3). We also observe that the choice of solvent changes the FWHM of the fitted azimuthal peak, as expected from the evolution in the degree of orientation seen in the 2D GIWAXS patterns in **Figure 4.2A**. In MAPbBr₃ in DMF, the (100) peak is broader, and the fitting has a larger error and low R² (Table S1). When DMSO is added (DMF:DMSO and pure DMSO), the azimuthal peaks sharpen, and the raw data fits nicely into the Pseudo Voigt function with a high R² (**Table AS1**). The sharp azimuthal profile peaks indicate a high degree of preferred orientation of the (100) plane parallel to the substrate. In addition, the MAPbBr₃ with DMSO has the lowest FWHM, hence the highest degree of preferred orientation.

In **Figure 4.2D**, we plot the azimuthal profile peaks for FAPbBr₃. Compared to MAPbBr₃, the FAPbBr₃ peaks are all broader and have a higher FWHM, showing a lower degree of preferred orientation. For DMF, the crystallographic domains show dispersion in the integrated data, suggesting a low degree of preferred orientation. The fitted Gaussian peak for DMF has a very low R² and a large error in **Table AS1**. The poor fitting for FAPbBr₃-DMF is attributed to the random orientation of the film. As we added DMSO to the precursor solution, the R² of the fit of the 100 azimuthal peak 0° increased, showing a preferred orientation of crystallographic domains with the (100) plane parallel to the substrate. For FAPbBr₃-DMF:DMSO, the 110 azimuthal profile shows three broad peaks at around ± 45° and 0°, which indicates a lower degree of orientation and a higher dispersion. With pure DMSO, the 100 azimuthal peak sharpens, the 110 azimuthal profile shows two broad peaks at ± 45°, and the data fitting improves, with a higher R² and lower error in **Table AS1**. These changes suggest that pure DMSO induces some preferred orientation, even in FA-based films. These results on preferred crystallographic orientation were corroborated by comparing the ratio in intensity between the 100 and 110 peaks from Bragg Brentano XRD to complement the missing wedge from GIWAXS (**Figure AS4**). In summary, the FWHM of the 100

azimuthal peak shown in **Figure 4.2E** quantifies the dispersion of orientation of the crystallographic domains. MAPbBr₃ films deposited from a pure DMSO precursor solution show the lowest FWHM, evidence of the highest degree of preferred orientation. In contrast, FAPbBr₃ shows a higher FWHM, decreasing the degree of preferred orientation. Additionally, we verified that the preferred orientation was induced by the solvent and was not kinetically determined by the antisolvent addition times. **Figures AS5-6** show the GIWAXS patterns and azimuthal integration of lead bromide perovskite films adding CB as antisolvent at different times during the spin-coating process.

The SAXS results discussed in the previous section suggest that there are interactions between the bromo-plumbate octahedra colloidal particles in DMF, which favor the possible formation of agglomerates in solution. We speculate that these colloidal aggregates could form dispersed and agglomerated nuclei for the crystallization process. This could lead to the random orientation observed in DMF from the GIWAXS measurements, as illustrated in the schematics of **Figure AS7**. The higher degree of random orientation in DMF is observed regardless of cation type, indicative of this solvent-dominated phenomenon. To further understand the origins of preferred crystallographic orientation in lead bromide perovskites, we now discuss why MA and FA impact preferred orientation in pure DMSO, where there are no colloidal interactions. Instead, in DMSO, the octahedra particles and nuclei would be isolated, and the crystallization is slowed down. We also learned from SAXS in **Figure 4.1** that there were no differences between MA and FA in solution. However, the crystallized films in pure DMSO still show differences in orientation. Regardless of the solvent, we observe differences in crystallographic orientation when comparing MAPbBr₃ and FAPbBr₃. For this reason, other underlying forces and mechanisms must lead to differences in orientation for the different A-site cations in lead bromide perovskites.

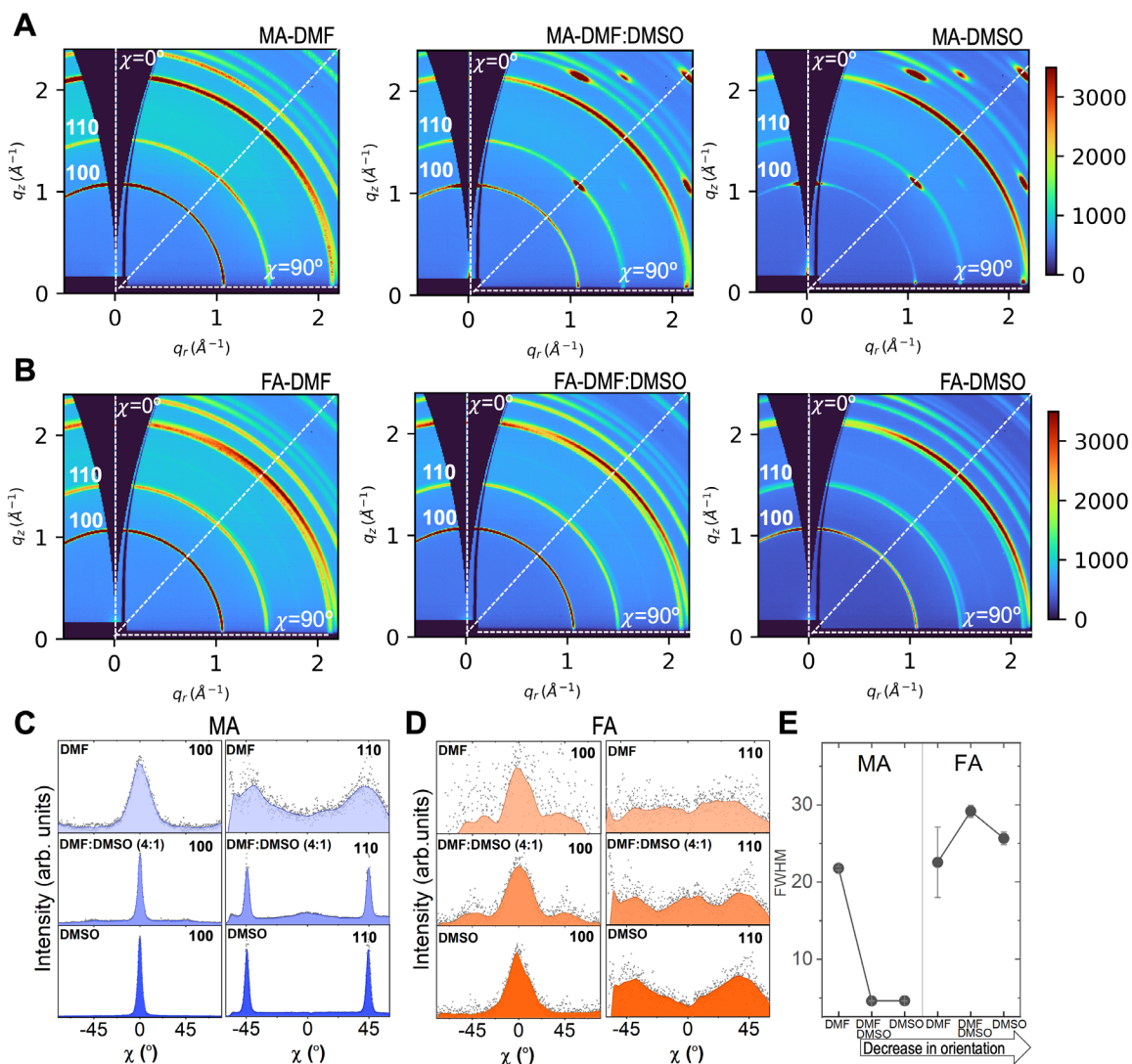


Figure 4.2 Figure Interplay of solvent and A-site cation in the crystallographic orientation of lead bromide films studied by GIWAXS. (A,B) 2D GIWAXS patterns in DMF, DMF:DMSO (4:1 volume), and DMSO for (A) MAPbBr₃ and (B) FAPbBr₃. (C,D) Azimuthal integration profiles of the main Debye-Scherrer rings (100 and 110) as a function of the χ angle from GIWAXS for three solvent systems for (C) MAPbBr₃ and (D) FAPbBr₃. (E) FWHM and error bar of the azimuthal peak for MAPbBr₃ and FAPbBr₃ as a function of the solvent.

4.1.3 Mechanisms for Preferred Orientation

We used periodic DFT to calculate the relative surface energies for MAPbBr₃ and FAPbBr₃ to help explain the difference in crystallographic orientation observed in the GIWAXS measurements arising from the difference in A-site cation. The calculated surface energies for

a representative surface from the {100} and {110} family of planes are presented in **Figure 4.3A**. We considered both PbBr_2 and FABr/MABr termination, but we observed that the termination only leads to a qualitatively negligible variation in the surface energy regardless of A-site cation and surface plane. Therefore, the following qualitative conclusions are discussed regardless of this distinction.

Figure 4.3A shows that the (100) terminated slab is energetically more stable in comparison to the (110) terminated slab for MAPbBr_3 , in agreement with previous calculations. The (100) and (110) FAPbBr_3 have almost equivalent surface energies. The energy differences between the (110) and (100) surfaces for both cations are presented in **Figure 4.3B**. The large energy difference for MA compared to FA agrees with and helps explain the experimentally observed difference in crystallographic orientation. For MA, the (100) surface is energetically more stable and will therefore be the dominant surface that is formed. For FA, the relative degeneracy between the (100) and (110) surfaces imply no thermodynamic driving force to form one surface over the other. Therefore, both surfaces can be easily formed, leading to a higher degree of orientational disorder. The relative difference in surface energies between MAPbBr_3 and FAPbBr_3 surface can be understood by comparing the orientation of the A-site cation in the final surface structures (**Figure 4.3C**) to that in the bulk. In all cases, the organic A-site cation adopts a configuration where its dipole moment is parallel to the surface to minimize the energetic penalty of forming the surface. The difference is that in MAPbBr_3 , the orientation of the A-site cation in the bulk already corresponds to a planar configuration; MAPbBr_3 only exhibits a minor geometric re-organization for both the (100) and (110) surfaces in comparison to the bulk structure associated with a rotation along the C-N bond for the MA cation. Similarly, the FA cation is already planar in the (100) surface and therefore does not reorient significantly. However, the bulk configuration of the FA cation is

perpendicular to the (110) surface plane. Therefore, the FA cations close to the surface significantly reorient upon the formation of the (110) surface, such that they adopt a configuration parallel to the (110) surface. This reorientation leads to an energetic stabilization of the (110) surface and results in the relative energy degeneracy between the (100) and (110) terminations. This planar configuration of the FA cation has been previously observed in the context of FAPbI₃.¹³⁵ While this analysis does not account for the kinetics of surface formation, the presence of two competing surface orientations in FAPbBr₃ provides thermodynamic insight into the increased disorder observed in the GIWAXS measurements (Figure 4.3D).

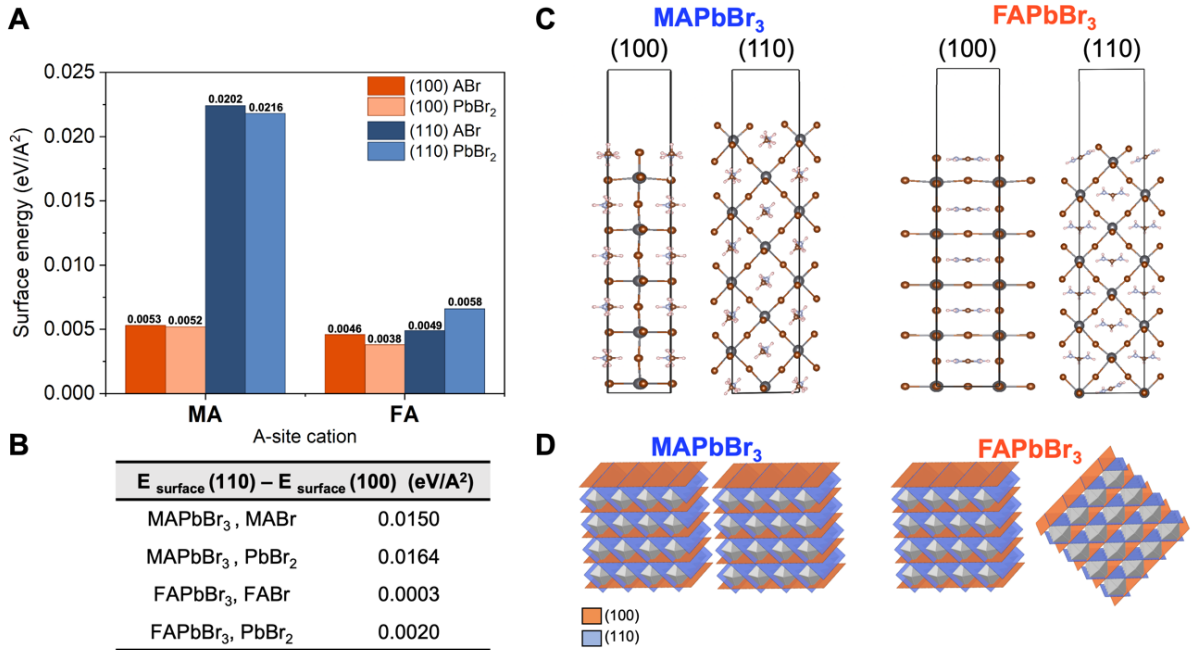


Figure 4.3 Results of the DFT calculation for the representative (100) and (110) surfaces of MAPbBr₃ and FAPbBr₃. (A) Surface energy of the analyzed structures computed for surfaces with PbBr₂ or FABr/MABr termination. (B) Energy difference between the corresponding (110) and (100) surfaces. (C) Representative final structures of the FABr/MABr terminated calculation for MAPbBr₃ and FAPbBr₃. The inorganic lattice of the bottom surface that demonstrates the PbBr₂ phase was frozen throughout the calculation. (D) Pictorial representation of the increased surface disorder due to the presence of two competing surfaces in FAPbBr₃.

4.1.4 Solar Cell Performance and Ionic Movement

Having understood the effect of the A-site cation on preferred crystallographic orientation, we studied how the choice of A-site cation impacts the electric response in perovskite solar cells. We confirmed the same differences in the preferred orientation of the MA and FA lead bromide perovskites on the solar cell substrate (**Figure AS8**). The solar cells had an n-i-p architecture that was described in the experimental section, and it is shown in **Figure 4.4A**. Lead bromide perovskite solar cells exhibit significantly lower efficiency compared to their iodine counterparts due to their wider bandgap and unoptimized contacts.^{63,136,137} However, their large bandgap expands the scope of application into multijunction solar cells or other optoelectronic applications. We measured the $J-V$ characteristics of the solar cells under simulated solar illumination (AM 1.5 G, 100 mW/cm²) to calculate the figures of merit of the solar cells ($J-V$ curves example in **Figure AS9**). We measured the open circuit voltage, short circuit current, fill factor, power conversion efficiency (PCE) from the J-V scan, and the stabilized PCE from the maximum power point tracking (PCE_{MPP}). The statistical distribution of the open circuit voltage is shown in **Figure 4.4B**. The optical bandgap variations (**Figure AS10**) dominate the trends in the open circuit voltage. A larger bandgap for MA relative to FA increases the open circuit voltage and decreases the short circuit current (**Figure AS11**). Given the differences in the bandgap, we cannot attribute the differences in charge carrier transport solely to crystallographic orientation. However, based on previous studies, a better charge carrier transport is expected for an oriented polycrystalline thin film.^{108,110} The other figures of merit of the solar cells, fill factor, and PCE from the reverse scan are reported in the **Appendix A (Figure AS11)**.

Beyond the effect of crystallographic orientation on charge carrier transport in perovskite solar cells, some studies have shown that orientation can influence the pathway of ionic movement. It has been shown that the halide and Pb ions can move along the (110) plane.¹⁰⁹ Hysteresis of the $J-V$ curve in lead halide perovskite solar cells has been attributed to ion migration,¹³⁸ among others.¹³⁹⁻¹⁴¹ Although ionic movement is not solely associated with $J-V$ curve hysteresis,¹⁴² we analyze the hysteresis behavior to get an insight into how crystallographic orientation influences ion migration. Therefore, we calculated the absolute hysteresis index from the PCE to study the effects of ionic movement by comparing the difference between the forward scan (FS) and reverse scan (RS) of the PCE as follows:¹⁴³

$$\text{hysteresis \%} = \frac{|PCE_{RS} - PCE_{FS}|}{PCE_{RS}} \quad (9)$$

The devices made with FAPbBr₃ perovskites show a lower hysteresis than those made with MAPbBr₃. This hysteresis behavior associated with ion migration that is dependent on lead halide perovskite composition is in line with the previous reports.^{139,141,144} In MAPbBr₃, the defect activation energy barrier for ion movement has been calculated to be lower than that of FAPbBr₃, giving rise to more ionic movement, and explaining the larger hysteresis behavior for MAPbBr₃.¹⁴⁴ In addition, the hydrogen bond between the organic A-site cation and the bromine is stronger for FA than MA, limiting the motion of the cation in the case of FAPbBr₃.¹⁴⁴ This could be an additional explanation for the increase in hysteresis in MAPbBr₃ solar cells.

To further understand the role of A-site cation on ionic motion in these materials, we measured impedance spectroscopy under different biases. The resulting Nyquist plots reproduce the characteristic patterns of lead halide perovskite solar cells¹⁴⁵ (see representative spectra in **Figure AS12**). The Nyquist plots were fitted to an equivalent circuit reported

elsewhere (illustrated in **Figure 4.4C**).¹⁴⁶ This circuit includes a resistor (R_{rec+tr}) that couples both the recombination and transport resistances due to the low chemical capacitance of perovskite solar cells and a low-frequency branch with a capacitor (C_{dr}) and resistor (R_{dr}), both related to the ionic nature of the lead halide perovskites. In **Figure 4.4D**, R_{rec+tr} displays negligible variations between MAPbBr₃ and FAPbBr₃ under lower bias values.

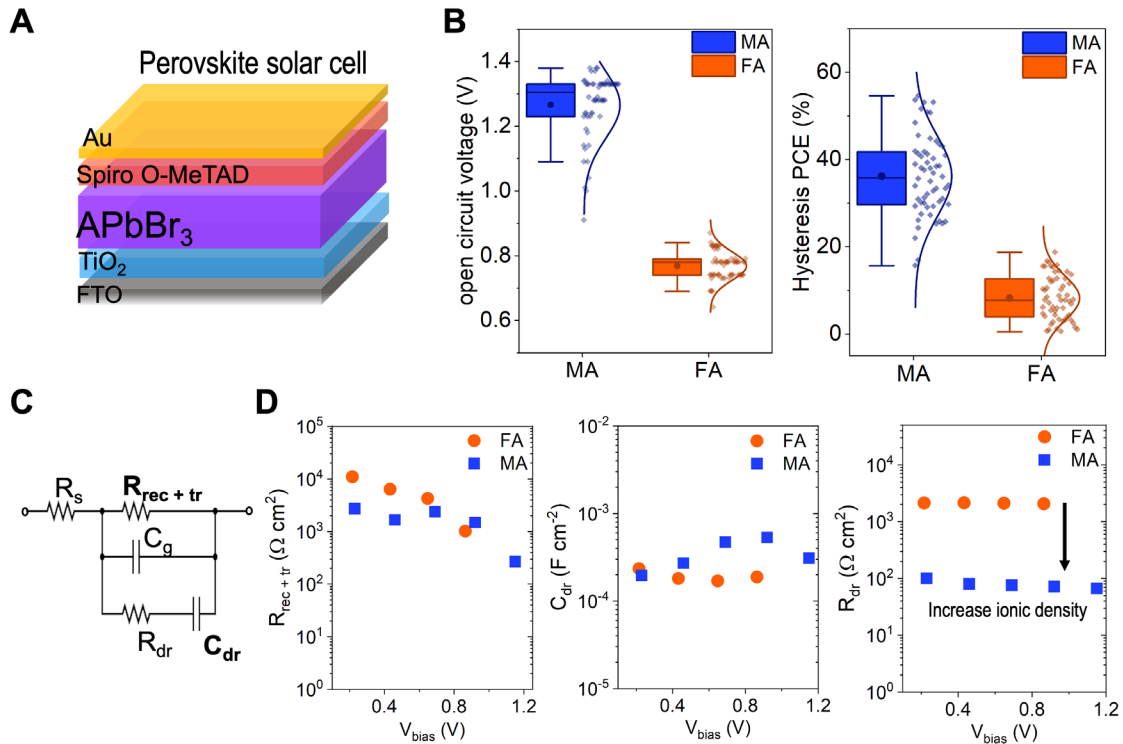


Figure 4.4 Electrical properties of solar cell. **(A)** Perovskite solar cell architecture where **A** in APbBr₃ is MA or FA in DMSO, **(B)** Box plots of the solar cell characterization from J-V curve open circuit voltage, and absolute hysteresis index of the power conversion efficiency (PCE). **(C,D)** Impedance spectroscopy measurements for MAPbBr₃ and FAPbBr₃ solar cells. **(C)** Equivalent circuit used for the analysis of the impedance spectra, **(D)** Recombination and transport resistance for different applied biases (R_{rec+tr}), low-frequency capacitance for different applied biases (C_{dr}), and low-frequency resistor (R_{dr}).

High capacitance values at low-frequency regimes have been a fingerprint of lead halide perovskite solar cells.¹⁴⁶ The origin of this low-frequency capacitance is typically attributed to the mixed ionic-electronic nature of these materials.^{145,147} In the equivalent circuit employed to analyze the results, this capacitance is modeled by a constant phase element C_{dr}

to account for dispersive phenomena, yet with exponent values close to 1. The C_{dr} can be interpreted as an indication of increased ionic density or as higher ionic diffusion.¹⁴⁸ Therefore, a comparative analysis of the C_{dr} is used to understand the ionic differences between MAPbBr₃ and FAPbBr₃, as observed in **Figure 4.4D**. FA has a slightly lower C_{dr} than MA. The slight reduction of C_{dr} can be interpreted as an indication of increased ionic diffusion or higher ionic density in FAPbBr₃. To decouple the effects between ionic density and ionic diffusion, we examined the low-frequency part of the spectrum R_{dr} . The increase of R_{dr} for FAPbBr₃ compared to MAPbBr₃ confirms the higher ionic density of the latter. These variations are in line with the increase of the absolute $J-V$ hysteresis in MAPbBr₃ solar cells (**Figure 4.4B**). These experimental results align with published computational results¹⁴⁴ in which bromide vacancies and interstitials had much lower formation energies and higher densities in MAPbBr₃ than for FAPbBr₃, where the FA cation suppressed ion diffusion.

Analyzing the effect of preferred crystallographic orientation on the ionic effects, we observe that the highly preferentially oriented MAPbBr₃ has the highest ionic density compared to the randomly oriented FAPbBr₃. We suggest that ionic effects could be affected by the crystallographic orientation in lead bromide perovskites. Previous studies have shown the effects of in-plane crystallographic orientation of lead halide perovskites, where it has been observed that preferred orientation leads to a higher movement of ions. Fassel et al. studied the effect of in-plane crystallographic orientation on ionic transport rate from simulations and experimental work.¹⁴⁹ They found that the relative orientation of the crystals affects ionic migration in polycrystalline films; aligned crystals had uniform ion transport, while randomly oriented crystals had varying rates of ionic transport. Further, Eames et al. showed that in perovskite films with vacancy defects, ions have favorable crystallographic planes to move.¹⁵⁰ The halide migrates along the octahedron edge between halide sites.¹⁵⁰ Given that mobile ions

can move in the $\langle 110 \rangle$ family of directions, Flannery et al.¹⁰⁹ observed that ionic movement through the absorber layer is higher if the crystals in a mixed-halide lead halide perovskite film were highly oriented in the (110) plane. While an effect of orientation on charge transport cannot be excluded, we show that increased preferred orientation along the (100) plane does not contribute to an improved ion diffusion. Differences in the ionic contribution are ascribed to an increased ionic density in the highly ordered MAPbBr₃ perovskite.

4.1.5 Conclusions

We studied the effect of the solvent and organic A-site cation on the crystallographic orientation in lead bromide thin films. We showed that there is an interplay between the type of solvent and A-site cation that determines the preferred crystallographic orientation in bromine-based perovskites. Polycrystalline thin films prepared from solutions in DMF solvents exhibit less orientation, whereas films prepared from solutions in DMSO exhibit higher degree of preferred orientation for both FA and MA. Regardless of the solvent, MAPbBr₃ showed a higher degree of preferred orientation compared to FAPbBr₃. Theoretical calculations showed that thermodynamically, MAPbBr₃ is energetically favored to grow along the (100) plane, while in FAPbBr₃ the (100) and (110) surfaces are nearly degenerate in energy, and both are equally favored for growth. In addition, we observed that there are larger ionic movement effects in the highly oriented MAPbBr₃ solar cells. The $J-V$ hysteresis of the solar cells, and impedance spectroscopy results, indicate higher ionic density effects in MAPbBr₃. This work provides new insights on the role of both solvent and A-site cation on the crystallization of thin films.

4.2 Humidity-Induced Crystallographic Reorientations and Effects on Charge Carrier Extraction in Perovskite Solar Cells

To understand the effects of crystallographic orientation on charge carrier extraction in perovskite solar cells, a highly efficient LHP, mixed-cation mixed-halide perovskite $\text{Cs}_{0.05}(\text{MA}_{0.17}\text{FA}_{0.83})_{0.095}\text{Pb}(\text{I}_{0.83}\text{Br}_{0.17})_3$, abbreviated as CsMAFA, was studied.²⁵ The APbX_3 structure has been tailored to include multiple A-site cations (i.e., MA, FA, Cs) and X anions (i.e., I, Br) and to improve the efficiencies of PSCs.^{151,152} CsMAFA is among the most widely used LHP for PSCs. In this composition, a slight PbI_2 excess has been introduced to improve PCEs by reducing non-radiative recombination both in the bulk and at LHP film interfaces.^{153–156} The change in the A:Pb stoichiometric ratio has also been thought to improve stability by reducing the amount of polar organic A-site cation (more hygroscopic) at the LHP surface, which would favor hydroxyl group interactions that accelerate degradation.^{157,158} In contrast, MAPbI_3 solar cells have shown a positive effect on performance caused by humidity in the short term. Exposing MAPbI_3 films to humidity during^{159,160} or immediately after processing^{106,107,161} has been shown to enhance the microscale film morphology, e.g., larger grains, and improvements in solar cell performance. Chiang et al.¹⁰⁶ and Petrus et al.¹⁰⁷ show improved crystallinity in MAPbI_3 after humidity, suggesting improved preferred orientation. Therefore, to study the effect of orientation in highly efficient solar cells, we evaluate humidity-induced changes in the morphology and orientation for a state-of-the-art LHP composition, CsMAFA.

Herein, crystallographic orientation changes due to exposure to humidity and their effects on the electronic properties of solar cells are investigated as a function of different stoichiometric ratios. Changes in the orientation of the LHP films were probed at the surface

and in the bulk using GIWAXS below and above the critical incident angle. Synchrotron-based XRF maps with operando XBIC was used to understand the effects of humidity exposure on elemental composition. This work revealed two main observations: (1) changes in the surface crystallographic orientation versus the bulk for excess Pb films correlate with a decrease in photocurrent and stability of the solar cell, and (2) inducing orientation of the (100) plane to be parallel to the direction of charge carrier transport (i.e., perpendicular to the substrate in a solar cell) leads to a large improvement in photocurrents. This work shows that exposure to humidity induces changes in the orientation of LHP crystals and that such changes, dependent on the film organic A:Pb ratios, have a major impact on charge transport and collection in a solar cell. Humidity-induced reorientation is an example of crystallographic orientation tuning, an important parameter to control and further study to enhance the efficiency and long-term stability in various types of LHPs.

4.2.1 *Morphology of the LHP Thin Films*

To understand crystallographic orientation when exposed to humidity for a highly efficient state-of-the-art LHP, a set of CsMAFA LHPs were fabricated with different organic A:Pb ratios: 9% excess Pb (EL) and 5% excess organics (EO), with no changes in the CsI addition for all stoichiometries. A set of LHP films were exposed to a high relative humidity (RH) environment for 48 hours right after the spin coating and annealing (**Figure 3.2, Chapter 3**). The LHP films were then introduced to a nitrogen environment for two hours. Films exposed to humidity are labeled “H₂O” and those that were not exposed are labeled “w/o H₂O”, with the latter being the control samples.

To investigate LHP film coverage and micro defects, top-view scanning electron microscopy (SEM) images were taken (**Figure 4.5**). The SEM images show a continuous

coverage of the substrate with no visible pinholes and clearly defined grains regardless of processing conditions for all LHP films. A significant increase in the average grain size for the EO films after exposure to moisture is observed from 200 nm to 500 nm. For the EL films exposed to humidity, we observe a relatively unchanged average grain size of around 300 nm. Exposure to humidity has been shown to increase LHP grains for some^{106,107,162}, whereas other studies have shown no changes.^{159,163} In this work, SEM results shows that these discrepancies could be attributed to changes in stoichiometry in the precursor solutions.

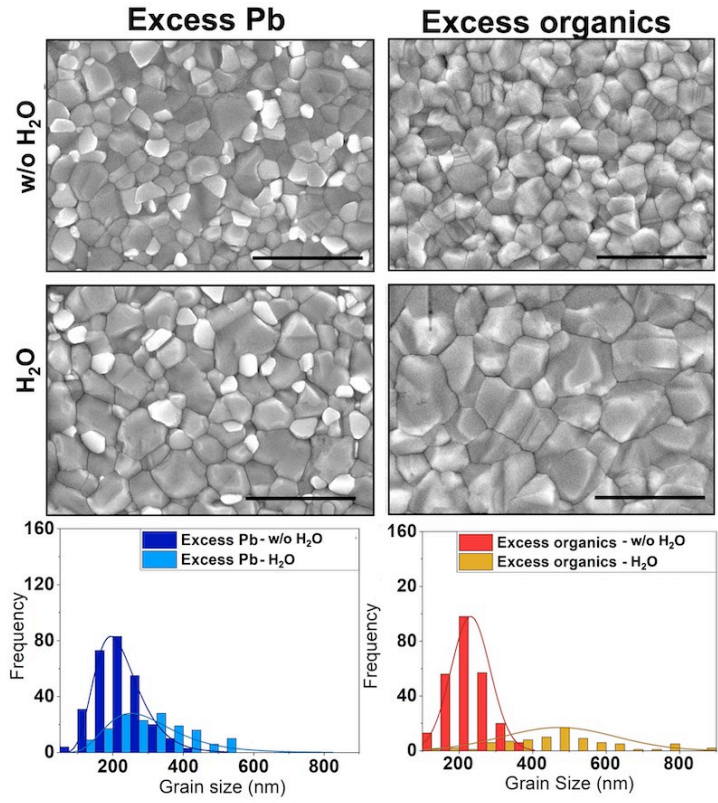


Figure 4.5 SEM images for each studied condition of LHP on top of ITO substrates and the grain size histogram (fitted by a log-normal distribution) from 5 analyzed images per condition. Without humidity exposure (w/o H₂O) and exposed to humidity (H₂O) for 24 hours RH ~70%. Stoichiometry Pb:A ratio is 1.09: 1 for EL, and 0.95: 1 for EO. Scale bar is 1 μm.

The increase in the grain size for the EO films, when exposed to moisture, could be explained by the hygroscopic nature of the organic cations and recrystallization.^{107,158} It is possible that

water molecules have a higher interaction of the hydroxyl group with the hydrogen from the organic cations, triggering a re-arrangement of the molecules that could cause enlarging of the grain size. In contrast, the EL films, where less unreacted organics are present, have potentially less interactions with water molecules and thus less pronounced changes in the polycrystalline microstructure. The latter is in line with theoretical simulations which have suggested that PbI_2 terminated LHPs are more robust to humidity degradation.¹⁵⁸

4.2.2 Elemental Chemistry by XPS

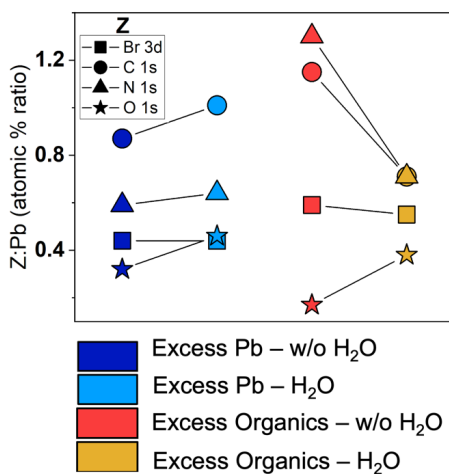


Figure 4.6 Elemental chemistry by XPS surface composition: element (Z) to Pb atomic percentage ratio (Z:Pb) calculated from XPS for Pb 4f, Br 3d (square), C 1s (circle), N 1s (triangle), and O 1s (star) for each of the studied conditions. Without humidity exposure (w/o H₂O) and exposed to humidity (H₂O) for 24 hours RH ~70%. Stoichiometry Pb:A ratio is 1.09: 1 for EL, and 0.95: 1 for EO.

X-ray photoelectron spectroscopy (XPS) was performed to analyze the surface elemental composition (Figure AS13, Table AS2, Appendix A) with values in the theoretical and reported range for CsMAFA.^{25,164} The ratio of Br 3d, C 1s, N 1s, and O 1s with respect to Pb 4f (Element: Pb ratio) were calculated and differences were observed when exposing EL and EO to humidity, as plotted in Figure 4.6. EO has a higher ratio of C 1s and N 1s to Pb 4f than EL, which is correlated to the excess of organic cation at the surface of the film, while

Br 3d has a similar value for both stoichiometries. After humidity exposure we observed that EO film lost N 1s which is hypothesized to correspond to a loss of FA.¹⁶⁴ The C 1s and N 1s peaks decreased simultaneously, possibly caused by that same loss of organic components. The O 1s peak increased due to water presence at the surface, and Br 3d remained constant. For the EL films the N 1s and Br 3D peaks did not change when exposed to humidity, while C 1s and O 1s moderately increased.

4.2.3 Structural Analysis of the LHP Thin Films

To investigate if the changes observed in SEM domain size also impacted the film crystal structure, XRD was measured for all LHP films (**Figure 4.7**). The XRD pattern in **Figure 4.7A** shows the 001 PbI₂ peak only for the EL films, suggesting no PbI₂ for the EO films with or without exposure to humidity (**Figure AS14**). We do not observe hydrated phases on the XRD pattern after exposing the films to humidity, in contrast with the MAPbI₃ perovskite hydrated phases seen in literature when exposed to humidity^{107,157,161} (e.g. monohydrate at 10.5°, and dihydrate phase at around 11.4°).¹⁵⁹ From all the measured XRD patterns (**Figure AS14**), the intensity ratio between the 100:110 LHP peaks (**Figure AS15**) was calculated. The ratio for the EO films was three times larger when exposed to humidity, revealing an increase in orientation of the (100) parallel to the substrate, in agreement with previous reports where orientation changes were prompted by water.^{106,107,165,166} XRD changes in peak intensity suggest a change in crystal orientation triggered by exposure to humidity, in particular, for EO.

For in-depth analysis of the peak positions and broadening, the d-spacing and full width at half maximum (FWHM) from the (100) LHP peak were calculated (**Figure AS16**, **Table AS3**, **Table AS4**). The d-spacing for each composition showed no significant change for the EL films. However, for the EO films, there was a slight increase in d-spacing when

exposed to humidity. The FWHM of the (100) LHP diffraction peak showed an increase for the EL and a large decrease for the EO. These results suggest that the EO LHP films undergo a large change in crystallite size, which agrees with the SEM images (Figure 4.5).

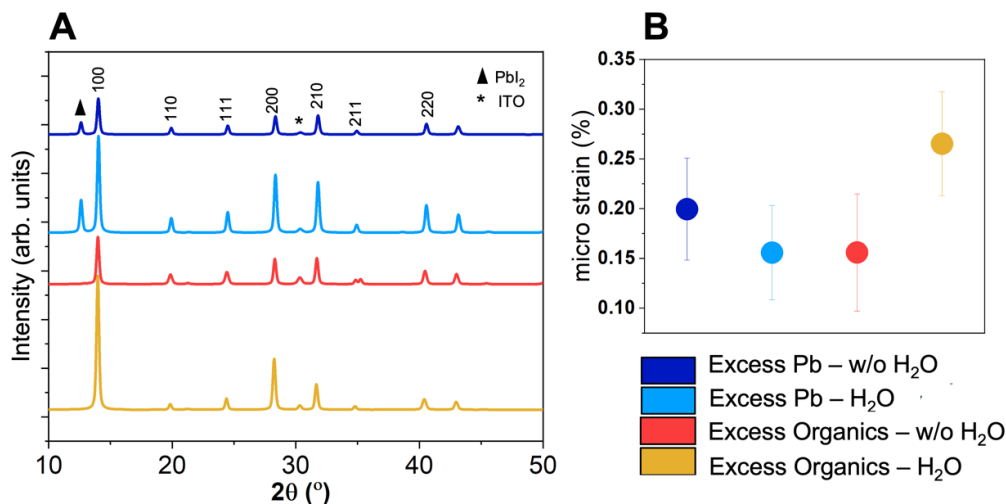


Figure 4.7 Structure of CsMAFA films by XRD. (A) XRD pattern with characteristic simple cubic LHP peaks labeled and (B) micro strain calculated from the Williamson-Hall plot method. The results were calculated from 4 different series of XRD patterns, and the average and standard deviation are shown. Without humidity exposure (w/o H₂O) and exposed to humidity (H₂O) for 24 hours RH ~70%. Stoichiometry Pb:A ratio is 1.09: 1 for EL, and 0.95: 1 for EO.

To extend the FWHM analysis and identify the strain and crystallite size components, a Williamson-Hall plot was created assuming an inhomogeneous strained film (Figure AS17). From this plot, the micro strain (Figure 4.7B) and crystallite domain size (Figure AS18) were calculated (Table AS5, Table AS6). The micro strain for the EO films exposed to humidity increased. A higher strain might be caused by inhomogeneities,¹⁶² such as phase segregation and crystallographic defects in the lattice. However, secondary phases were not detected from XRD. Therefore, it is possible that the increased strain is a product of elemental segregation, which introduces lattice defects and higher micro strain. The EO films showed an increase in the crystallite-size and a decrease in FWHM when the films were exposed to humidity (Figure

AS18). The SEM and XRD characterization techniques showed considerable changes in LHPs microstructure driven by stoichiometry and humidity exposure.

To further understand the structural information of the polycrystalline films, GIWAXS was performed as shown on **Figure 3.4, Chapter 3**. GIWAXS is a technique that has been used on LHPs to understand crystal structures and crystallographic orientation at the surface and bulk of a thin film.^{110,155,167,168} **Figure 4.8A,B** show the diffraction of LHP films with EL or EO with and without exposure to humidity for a grazing incident angle α of 0.5° . The Debye-Scherrer rings at q_r 1.01, 1.42, and 1.74 \AA^{-1} are attributed to the 100, 110, and 111 Bragg peaks, respectively, of the cubic $Pm\bar{3}m$ LHP lattice; the peaks at q_r 0.9, 1.82 and 2.4 \AA^{-1} or the EL samples are attributed to the 001, 011 and 012 planes of the $P\bar{3}m1$ PbI_2 (complete indexing in **Figure AS19**).¹⁶⁹ The LHP films with EL showed almost no changes in crystal orientation after exposure to humidity, while major reorientation was observed in films with EO. The reorientation was visualized from the redistribution of the peak intensity along the GIWAXS diffraction ring at q_r 1.01 and 2.01 \AA^{-1} . To identify the preferred angles of orientation, q_r was fixed at the 100 peak and the variations on intensity were monitored as a function of the azimuthal angle (χ), defined from the vertical to the origin. **Figure 4.8C,D** plot the integrated (100) plane diffraction as a function of χ .

The interaction with water is expected to propagate from the surface to the bulk of the LHP films. To probe structural differences between surface and bulk, the azimuthal distributions were retrieved from two different GIWAXS images acquired below and above the critical angle of the sample. The measurements were performed at incident angles (α) of 0.1° and 0.5° , which provide information about the film's first few nanometers (surface) and the bulk of the film, respectively (**Chapter 3, Grazing Incidence Wide-Angle X-ray Scattering**).

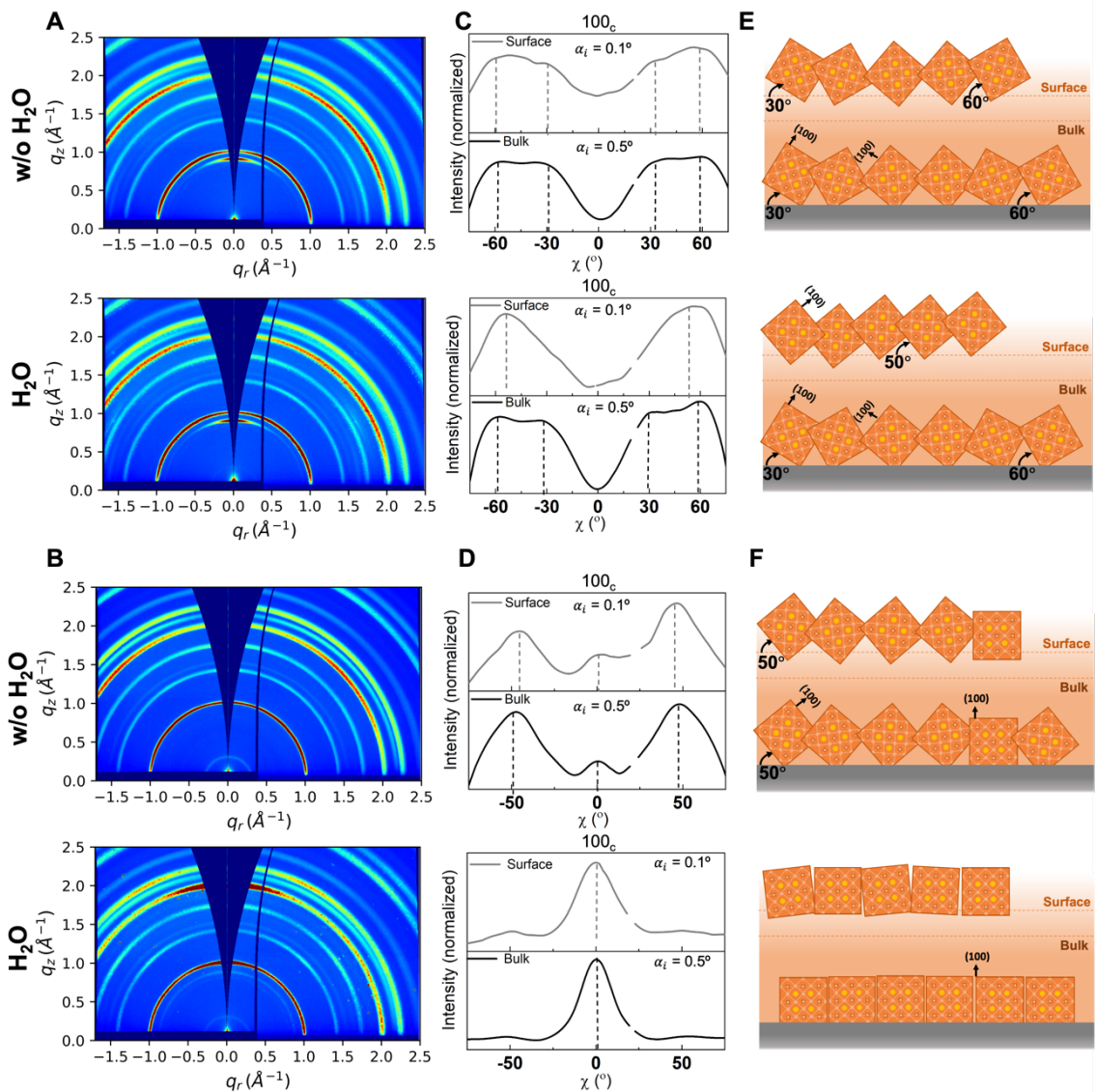


Figure 4.8 GIWAXS with different stoichiometric content without (w/o) exposure to humidity (H₂O) for (A) EL and (B) EO. Integrated intensity plots in the azimuth angle (χ) along the ring at q_r (1.012) corresponding to the plane (001) for a cubic structure at different incident angles α , 0.1° (surface) and 0.5° (bulk) for (C) EL and (D) EO. Schematic of the hypothesized rearrangement of the crystal orientations at the surface and bulk in the (001) plane for (E) EL and (F) EO.

The bulk diffraction of LHP films containing EL showed preferred orientations at $\chi = 30^\circ$ and 60° with and without exposure to humidity. For films without humidity exposure, no significant changes were seen for the surface versus the bulk. For films that were exposed to humidity, the surface orientation changed, and there was a shift toward $\chi = 50^\circ$, while the

bulk maintained its preferred orientations at $\chi = 30^\circ$ and 60° . The schematic in **Figure 4.8E** depicts these orientations.

LHP films with EO followed a markedly different behavior. Both the bulk and surface of these films reoriented after exposure to humidity. Before exposure to humidity crystallites had the (100) plane mainly oriented at $\chi = 50^\circ$, with a minor orientation at $\chi = 0^\circ$. After the films were exposed to humidity, both surface and bulk aligned along $\chi = 0^\circ$. The diffraction at $\chi = 0^\circ$ is generated from planes that are parallel to the substrate. The CsMAFA has a cubic structure, therefore one of the {100} family of planes is perpendicular to the substrate. The azimuthal angle integration of higher order planes for the films are in line with the distribution detailed in **Figure 4.8C** and **D** and are reported in **Figures AS20- 23**. The exposure to humidity influenced the recrystallization in the surface for the EL polycrystalline film and a reorientation of the bulk and surface of the EO films.

4.2.4 *Optical Properties*

To understand the correlation between the structural changes and the optical properties of the material, UV-VIS absorption and steady-state PL were measured (**Figure 4.9**). **Figure 4.9A** shows the PL spectra where the LHP emission peak was detected ranging between 762 nm to 782 nm from EL to EO (both exposed to humidity). In the PL spectra, a red shift was observed with the addition of organics. The optical bandgap in **Figure 4.9B** was calculated from the PL emission peak, where a considerable decrease of 0.01 eV in the bandgap was seen when going from the EL to the EO films. This trend was also seen after exposing to humidity, where bandgaps decreased further by 0.02 eV. Furthermore, **Figure 4.9C** shows the UV-Vis absorption spectra of the films. No significant changes in the absorption were seen for samples

with or without exposure to humidity. However, there were stoichiometry-dependent changes. EO LHPs showed a lower absorption for wavelengths lower than 750 nm. The optical bandgap was calculated from the absorption spectra by the tauc-plot method (**Figure AS24**); results were consistent with the bandgap values from the PL peak positions (**Figure 4.9B**).

Previous studies showed that at high humidity levels, a water-driven halide segregation occurred in parallel to a PL red shift.¹⁷⁰ In this work, a PL red shift was observed for the EO when exposed to humidity. We hypothesize that a decrease in bandgap is related to the loss of Br in the EO film exposed to humidity, which prompts conversion to FAI-rich LHP due to the loss of MA by evaporation and/or segregation of Br from the LHP structure. In addition, the lattice parameter changes seen in the XRD in **Figure AS16** can also be related to changes in Br distribution and concentration. It is possible that as Br is lost, a FAI-rich LHP would have a larger d-spacing and a lower bandgap as shown in the literature.¹⁵¹ Therefore, the observed bandgap shift can be correlated with a loss or redistribution of Br in the LHP.

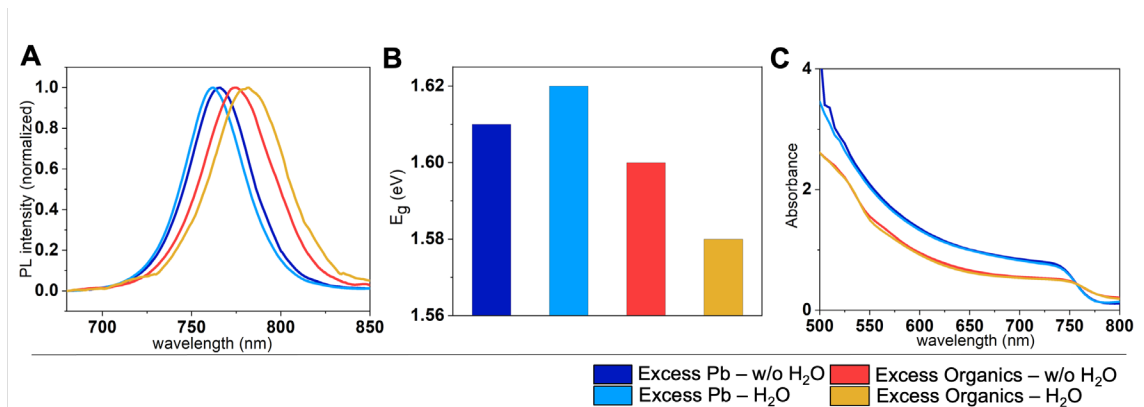


Figure 4.9 Optical measurements: (A) steady state normalized PL spectra for EL and EO LHP deposited over FTO, (B) band gap from the PL emission peak and (C) UV-VIS absorption spectra. Without humidity exposure (w/o H₂O) and exposed to humidity (H₂O) for 24 hours RH ~70%. Stoichiometry Pb:A ratio is 1.09: 1 for EL, and 0.95: 1 for EO.

4.2.5 Perovskite Solar Cell Performance

To study the effects of the humidity-induced crystallographic orientation changes described above on the performance of solar cells, PSCs with n-i-p architecture were fabricated as illustrated in **Figure 2.9, Chapter 2**. The LHP layers were exposed to humidity or kept in a nitrogen glovebox before depositing the Spiro-OMeTAD layer and gold electrode. Solar cell short circuit current density (J_{sc}) and PCE were extracted from current-voltage (J - V) curves and were plotted in box plots in **Figure 4.10A**. The champion J - V curves are shown in **Figure 4.10B**.

For samples without humidity exposure, lower PCE was obtained for the EO samples as compared to the EL counterparts. Open circuit voltage (V_{oc}), fill factor (FF), and J_{sc} values decreased along with the PCE, which was 18% for EL and 12% for EO (**Figure AS25**). The major change occurred in the J_{sc} , where the EL current was more than 21 mA/cm², whereas the J_{sc} for EO was around 15 mA/cm². Numerous studies have reported that excess Pb in LHPs (i.e. MAPbI₃, MAFA, CsMAFA) is beneficial as it improves PCE, charge transport mechanisms, and stability.^{25,153,154} For example, it has been shown that PbI₂ passivates the interfaces by altering the energy level alignment.¹⁵⁴

For samples exposed to humidity, the solar cell performance varied depending on the stoichiometry. The EL solar cells showed small variations in the performance metrics for the exposed films. The devices showed lower champion values for V_{oc} , J_{sc} , FF, and PCE, but the median and mean values were almost unchanged (**Figure AS25**). For the EO solar cells, a significant improvement in overall performance was observed when the LHP layer was exposed to humidity. The improvement was mainly driven by a large increase of 4 mA/cm² in the J_{sc} , showing an overall increase of 4% in the PCE.

In previous studies, excess Pb in the LHP film has acted as a passivation layer, decreasing defects and leading to higher performance and tolerance to humidity.^{107,154,158} We have shown that crystallographic orientation in the surface was modified for the EL thin films (**Figure 4.8**) and that a minor decrease in performance was measured (**Figure 4.10**, EL). This suggests that differences in orientation between bulk and surface in the EL LHPs alter the overall solar cell properties. For MAI-excess films, Petrus et al. showed an improvement in Jsc and PCE upon exposure to humidity for MAI-excess films.¹⁰⁷ We have shown that EO solar cells exhibit an enhancement in performance when exposing the LHP layer to humidity. The highest PCE for the EO solar cells (**Figure 4.10**) correlates to highly oriented (100) plane in the LHP films (see schematics of **Figure 4.8E**). Perpendicular orientation results agree with enhancement of photocurrents and charge carrier transport properties in different GIWAXS reports in PSCs.^{155,171,172} Additionally, the improvement in photocurrents and PCE for the EO films exposed to humidity correlates with the FA loss in the surface (**Figure 4.6**). Having an FA residual layer (as seems to be the case for the unexposed EO films) can lead to lower currents due to this layer being electronically inactive.¹⁵⁴

The improvement in all photovoltaic performance parameters due to exposure to humidity for the EO devices and the changes in the preferred crystallographic orientation motivated the study of long-term changes in PCE. A maximum power point tracking (MPPT) test was done in nitrogen for 170 hours under 1 sun illumination (AM 1.5). The average PCE for 10 pixels per composition is shown in **Figure 4.10C**. On average, a higher stabilized PCE was observed for the EL devices without exposure to humidity and for the EO devices exposed to humidity in **Figure 4.10C** (best pixel results are shown in **Figure AS27**). Solar cells with EO LHP films exposed to humidity showed slower PCE decrease after a week under illumination when compared to the devices with unexposed films. Because crystallographic

orientation in LHPs is one of the largest changes we see in these devices, we hypothesize that a perpendicular crystallographic orientation is desired to enhance photovoltaic performance, and it could also be correlated to stability due to the structural order.

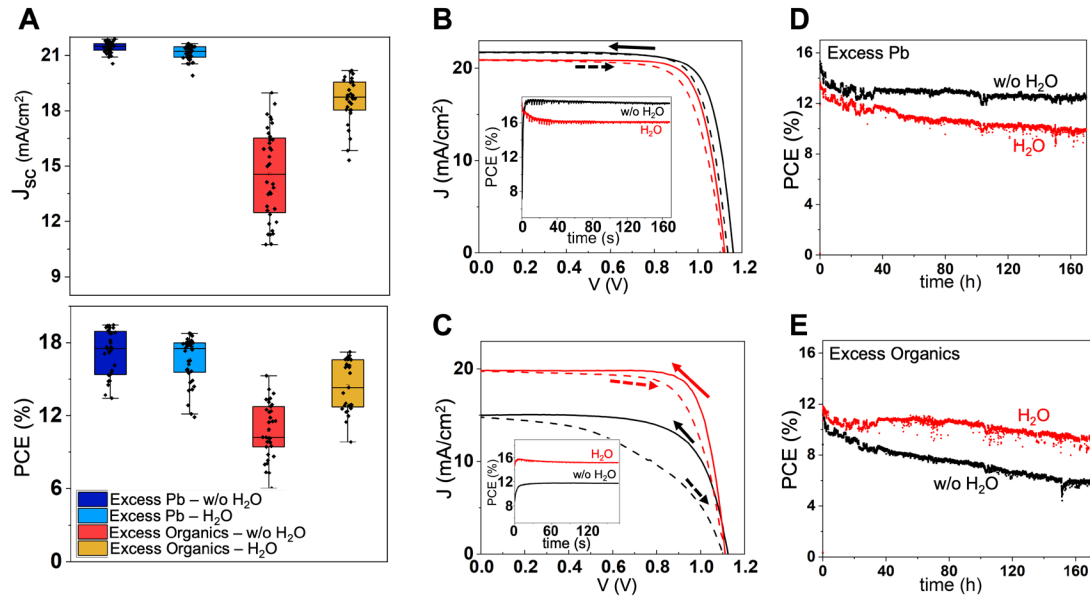


Figure 4.10 Solar cell characterization. (A) Boxplots of J_{sc} , and PCE showing the distribution of all measured devices in a reverse bias for different stoichiometries with or without exposure to humidity J - V curves of the best pixel for (B) EL and (C) EO devices without (w/o) and with exposure to humidity (H_2O). Inset graphs show the maximum power point tracking (MPPT) for 170 s for a random pixel studied (not corresponding to same pixel from J - V curve). (D,E) Average PCE_{MPP} from the stability aging test by maximum power point tracking (MPPT) for 170 hours from a total of 10 pixels for (D)EL (D) and (E) EO. Without humidity exposure (w/o H_2O) and exposed to humidity (H_2O) for 24 hours RH ~70%.

4.2.6 Chemical Composition and Induced Current Mapping

Chemical composition changes due to LHP thin films exposure to humidity were probed by XRF. Correlative XBIC mapping was used to probe the effects of the chemical changes on the electronic properties of the device. These X-rays can penetrate microns allowing for probing complete devices which are typically about 1 μm thick. The combined synchrotron-based XRF-XBIC tool has a resolution of 200 nm.¹⁷³ Therefore, complete devices were characterized to be able to correlate the elemental composition with the current extracted.

XRF elemental maps were plotted for the Br:Pb molar ratio of EL and EO LHP devices as shown in **Figure 4.11A,B**. The LHP films without exposure to humidity showed a homogenous distribution of the halides, with no apparent segregation of elements. However, two small Br rich areas were seen in the EO device. Exposure to humidity led to halide segregation regardless of the stoichiometry. Both high and low intensity Br:Pb ratios (dark blue or intense red spots) were observed in the elemental XRF maps. It has been reported that LHP interaction with water can trigger phase segregation¹⁷⁰ and compositional/stoichiometric changes by breaking hydrogen bonds between the organic cation and PbI_2 , leading to possible diffusion of the MA cation.¹⁵⁷ The Br agglomeration in **Figure 4.11B** for humidity-exposed samples also shows areas that become more iodine rich around the Br-rich areas. This could be due to Br movement towards a specific spot as the films recrystallize, leaving less Br around that Br cluster. In addition, this could help explain the narrower bandgap of the EO films exposed to humidity, as the homogenous part of the film becomes more iodine-rich, which has a narrower bandgap than Br-rich LHPs.

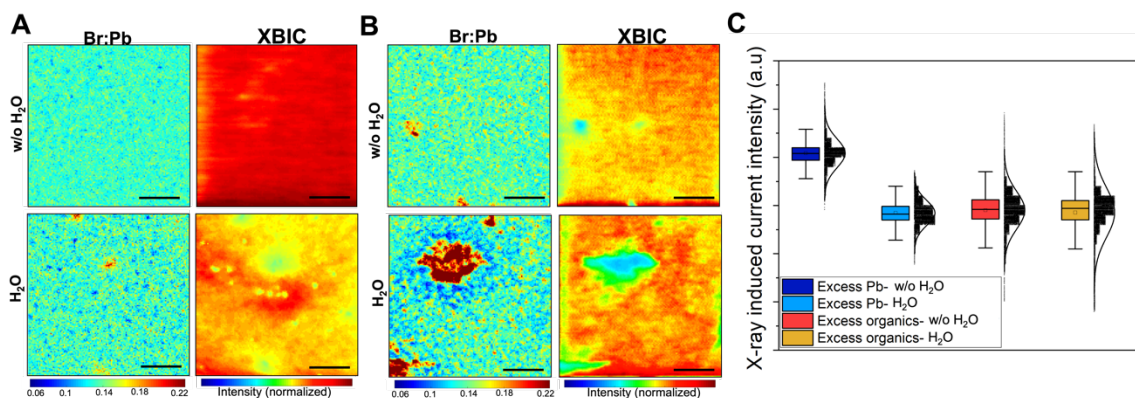


Figure 4.11 XRF for the elemental molar ratio between Br:Pb and XBIC for the different set of solar cells (A) EL and (B) EO, with (H_2O) and without (w/o H_2O) humidity treatment. Scale bar is $5 \mu\text{m}$. (C) Boxplot and normal distribution of the integrated XBIC data for EL and EO solar cells.

The XBIC signal provided insights on the effects of Br agglomeration on charge extraction. In general, the Br agglomerations led to a decrease in XBIC intensity, showing that Br clusters are detrimental to charge carrier collection. XBIC is not particularly sensitive to bandgap changes because the X-ray energies are so high. This makes the technique ideal to rule out current changes due to a wider bandgap of the Br-rich clusters. The low currents were particularly strong for the EO LHP films exposed to humidity. The maps showed a large Br-rich area with a surrounding Br-poor ring and a large decrease in current in the same area was observed. To estimate the total amount of current extracted from these XBIC maps, the induced current intensities were integrated and are plotted in **Figure 4.11**. The integrated currents showed a decrease in the current for the EL sample when it was exposed to humidity. On the other hand, for the EO XBIC maps, there was no change in intensity when exposing the samples to humidity. The decrease in XBIC intensity for humidity exposed EL solar cells agreed with the J_{sc} results, but not for EO devices, as shown in **Figure 4.10** and **Figure AS25**. It is possible that the changes in orientation have a more important role in the extraction of charge carriers than anything else. Despite the detrimental heterogeneities in humidity exposed EO LHPs that led to lower clusters of photocurrents, the photocurrents increased (**Figure 4.10**). The sharpest change shown from the experiments was on the changes of preferred orientation, which is believed to be helping with charge carrier extraction into the selective layers.

4.2.7 Reorientation Mechanism

The mechanisms that drive reorientation in LHP films as a function of stoichiometry are very important to design a more robust and efficient PSC. Here, we suggest that these stoichiometry-dependent changes occurred due to compositional differences between surface

and bulk, leading to diverse humidity interaction pathways. From SEM, we observed that the CsMAFA with EO after humidity exposure showed evidence of what we presume is a coalescence growth process, as we observed small domains coalesce into larger domains (**Figure 4.5**). We hypothesize that this coalescence process depends on the LHP solubility. Given that H₂O is the medium where the domains coalesce, the solubility of the LHP in H₂O affects how much it coalesces; EO has the highest polarity and coalesces the most. The domain size growth is larger in the case of EO compared to EL, given that EO has more organic cations, which are highly hygroscopic.¹⁷⁴ More than polarity, the initial preferred crystallographic orientation can also be important for coalescence since the surface energy associated with each domain boundary varies based on the orientation between contacting faces.^{175,176} The change in domain size for the EO films also happens to be the one with sharper azimuthal peaks, indicating a higher degree of preferred orientation. The domain boundary energy is low for films with a higher degree of preferred orientation; hence the crystallographic domains coalesce more.¹⁷⁵ The proposed mechanism is shown in **Figure 4.12** as follows.

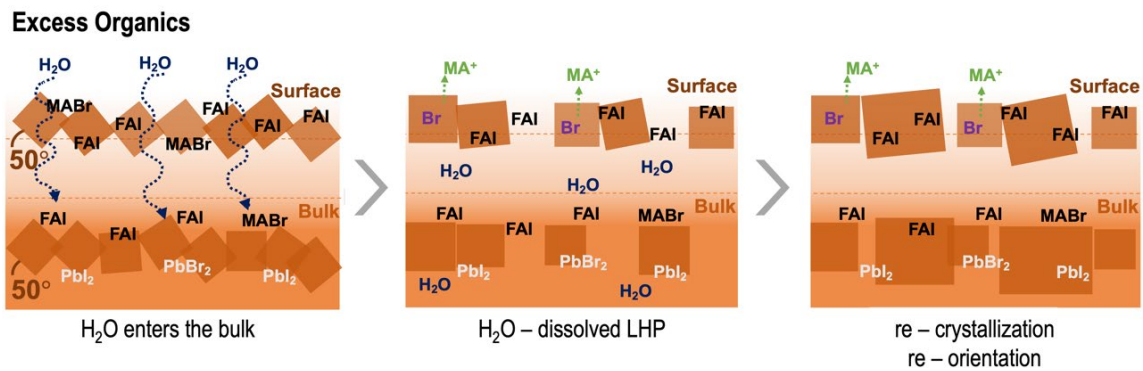


Figure 4.12 Reorientation mechanism in excess organics CsMAFA LHP thin films.

The large excess of organics present in the EO LHP thin film leads to stronger interactions with water that allows for larger diffusion throughout the film, leading to the

dissolution of the LHP in water. This interaction then leads to a recrystallization, triggering the growth of the domains *via* coalescence. Reorientation may be an effect of the domain growth into a thermodynamically preferred facet. Exposing the films to humidity shows a loss of MA and FA, as shown in **Figure 4.6**, and Br segregation occurs in parallel (**Figure 4.11**). This phenomenon is not seen for EL LHP films because of the limited amount of hygroscopic organics available through the film. Therefore, the crystallographic orientation is only affected at the very surface, where some organic material is accumulated.¹⁵⁴

4.2.8 Conclusions

In conclusion, this work shows how crystallographic reorientation due to humidity exposure has a major effect in the electrical properties of LHPs. Importantly, this recrystallization is dependent on the precursor stoichiometry. For excess organics present, even if there is higher micro-strain and halide segregation due to humidity exposure, reorientation plays a dominant role, causing an increase in extracted photocurrents in the reoriented films. In the case of excess Pb, different crystallographic orientations are measured for surface and bulk. This leads to a lower charge transport that translates into low photocurrents and low stabilized efficiencies. This suggests that orientation in the {100} family of planes is fundamental to allow transport through and out of the LHP thin film, yielding a high performing PSC with long-term durability. Polycrystalline preferred orientation tuning can be used as tool to improve charge carrier extraction from the LHP, which then lead to enhanced efficiencies and long-term stability.

4.3 Chapter Conclusions

This chapter shows that the solvent and the A-site cation in LHPs dominate crystallographic orientation. This fundamental understanding was done on Br-based perovskites. Further, a humidity treatment approach was used to induce reorientation via recrystallization, showing that a higher degree of preferred orientation leads to improved charge carrier transport in PSCs. Tuning the degree of crystallographic orientation is a tool to modify and understand the electric properties of LHPs for their use in solar cells, among other applications. In addition, in the first part of this chapter, it was found that the early stages of crystallization are critical for the crystallization process. Further work in the field requires understanding all stages of the crystallization and kinetics to finely control and design the structure, microstructure, morphology, and optoelectronic properties of LHPs.

CHAPTER 5. UNDESIRE PHASE TRANSFORMATIONS IN HALIDE PEROVSKITES

This chapter is based on the submitted article:

“Synergistic Role of Water and Oxygen Leads to Degradation in Formamidinium-Based Halide Perovskites”, *Manuscript under review*, 2023, by **Juanita Hidalgo**, Waldemar Kaiser, Yu An, Ruipeng Li, Zion Oh, Andres-Felipe Castro-Mendez, Diana K. LaFollette, Sanggyun Kim, Barry Lai, Joachim Breternitz, Susan Schorr, Carlo A.R Perini, Edoardo Mosconi, Filippo De Angelis, and Juan-Pablo Correa-Baena.

External contribution: The theoretical DFT calculations were developed by the group of Professor Filippo De Angelis, from the University of Perugia and CNR-ISTM, Italy. The reactions and mechanisms resulted from my discussions with Dr. Waldemar Kaiser.

Formamidinium ($\text{CH}(\text{NH}_2)_2$, FA) metal halide perovskites have emerged as promising materials for solar cell applications due to their exceptional light-harvesting properties, producing high power conversion efficiencies (PCEs) up to 26.08%.¹³ However, one of the most significant challenges is their stability, particularly in the presence of moisture (H_2O) and oxygen (O_2), which can trigger phase transformations to non-perovskite structures during operation.¹⁶ To overcome this challenge, mixed ion perovskites, including $\text{Cs}_x\text{FA}_{1-x}\text{PbI}_3$ (CsFA), have been shown to provide improved stability compared to their single-cation counterparts.^{16,40,47} However, CsFA perovskites also degrade when exposed to ambient air, where the perovskite structure transforms into non-perovskite phases such as the hexagonal FAPbI_3 (2H) and orthorhombic $\delta\text{-CsPbI}_3$ (δCs).^{19,177} Perovskite degradation due to water exposure^{178–182} and photo-oxidation under illumination in oxygen is widely recognized.^{22,183,184} Nonetheless, we lack a clear understanding of the mechanisms that lead to phase instabilities in these FA-rich perovskites due to water and oxygen interactions. Therefore, a fundamental understanding of the mechanisms causing perovskite phase transformations is crucial for developing durable and efficient metal halide perovskites for solar cell applications.

Herein, we investigate the origin of structural phase instability of FA-based perovskites upon exposure to H_2O , in air ($\text{H}_2\text{O}/\text{Air}$) or nitrogen ($\text{H}_2\text{O}/\text{N}_2$), using *in-situ* grazing incidence wide-angle X-ray scattering (GIWAXS). We study the surface chemistry and propose a mechanism to explain phase transformations when the perovskites are exposed to H_2O and O_2 using X-ray photoelectron spectroscopy (XPS) and density functional theory (DFT) calculations. We find that the degradation rate is considerably slower when the perovskite is exposed to H_2O in nitrogen compared to humid air. Our results show that a critical synergy between H_2O and O_2 is needed to accelerate the undesired phase transformations in perovskites. The H_2O molecules dissolve FAI on the perovskite surface, leading to the

volatilization of iodide and FA⁺ cations. In the dark, O₂ may interact with the exposed lead-iodide rich surfaces, oxidizing iodide and forming the thermodynamically favored iodate, IO₃⁻, which bonds to surface Pb ions. Lead (II) iodate, Pb(IO₃)₂, can then volatilize from the surface, leaving PbI₂ vacancies behind and allowing H₂O molecules to infiltrate the crystal structure. The continuous removal of FAI causes a local imbalance between Cs⁺ and FA⁺, destabilizing the CsFA phase and favoring transformation to the 2H and δCs phases. Our study provides structural and atomistic insights of the phase instability in FA-based perovskites when exposed to humid air conditions and provides surface passivation strategies to stabilize the perovskite phase for highly stable and efficient solar cells.

5.1 Structural Phase Transformations

To understand the structural phase transformations in FA-based perovskites, we used *in-situ* GIWAXS, as shown in **Figure 5.1** and **Figure BS1 (Appendix B)** where we exposed CsFA films to a relative humidity of ~100%. Initially, we analyzed the structural phase without H₂O exposure (Le Bail refinement, **Figure BS2, Table BS1**), resulting in a mixed cation (Cs 17% - FA 83%) tetragonal perovskite phase (β) with a space group *P4/mbm*^{19,64} (**Figure 5.1A**). **Figure 5.1B** shows the *in-situ* GIWAXS scattering patterns as a function of time exposed to H₂O/Air for 600 min. In H₂O/Air, the β phase (mixed-cation) transformed into two different phases, namely, the single-cation FAPbI₃ hexagonal phase (2H)^{19,20} and CsPbI₃ orthorhombic phase (δCs)^{37,40} (structures shown in **Figure 5.1A**). The 2H and δCs are both non-perovskite phases given the lack of corner-sharing octahedra. **Figure 5.1C** shows the quantified peak evolution of the integrated area of the main scattering peak of the perovskite (β) and non-perovskite phases (2H, δCs). We observe that δCs forms at around 50 min after exposure to

H₂O/Air, while 2H forms after 200 min of exposure, but at a faster rate. A kinetic model was used to quantify the phase transformation rates, shown in **Figures BS3-4**, where we fit a rate constant b . The negative b for the b-110 peak indicates the loss of the b-perovskite phase in H₂O/Air. The positive b for the 2H and δ Cs peaks reveals the appearance of the non-perovskite phases and a faster formation rate for 2H compared to δ Cs.

To isolate the effect of H₂O from O₂, we performed *in-situ* GIWAXS experiments by exposing the CsFA films to H₂O/N₂, as shown in **Figure 5.1D**. It is important to study the role of H₂O alone, considering that O₂ has been key in the photooxidation of methylammonium lead iodide (MAPbI₃) under illumination.¹⁸⁵⁻¹⁸⁷ Remarkably, when CsFA is exposed to H₂O/N₂, the β phase does not change and a 2H phase does not appear. This is in contrast with the samples exposed to H₂O/Air, which suffered phase transformations after the same exposure time. The peak evolution in **Figure 5.1E** shows a minor decrease of the b-perovskite integrated area from 92 to 85 with no formation of the 2H phase. However, the δ Cs phase still forms with a rate constant b of 1.5, compared to 2.2 in H₂O/Air (**Figure BS4**), confirming a slower δ Cs phase formation.

To isolate the role of oxygen (from air) from that of the water molecule, we exposed the CsFA films to dry air only. Interestingly, from *in-situ* GIWAXS (**Figure 5.1F**) and the time evolution of the main peaks (**Figure 5.1G**), the phase transformations previously seen do not occur. The effects of humidity exposure or dry air are independent of the substrate we use (**Figure BS5**). We identified that the CsFA phase instability is not just due to humidity exposure but is accelerated by O₂. These results are further corroborated by additional analyses of the *in-situ* GIWAXS experiments (**Figures BS5-6**).

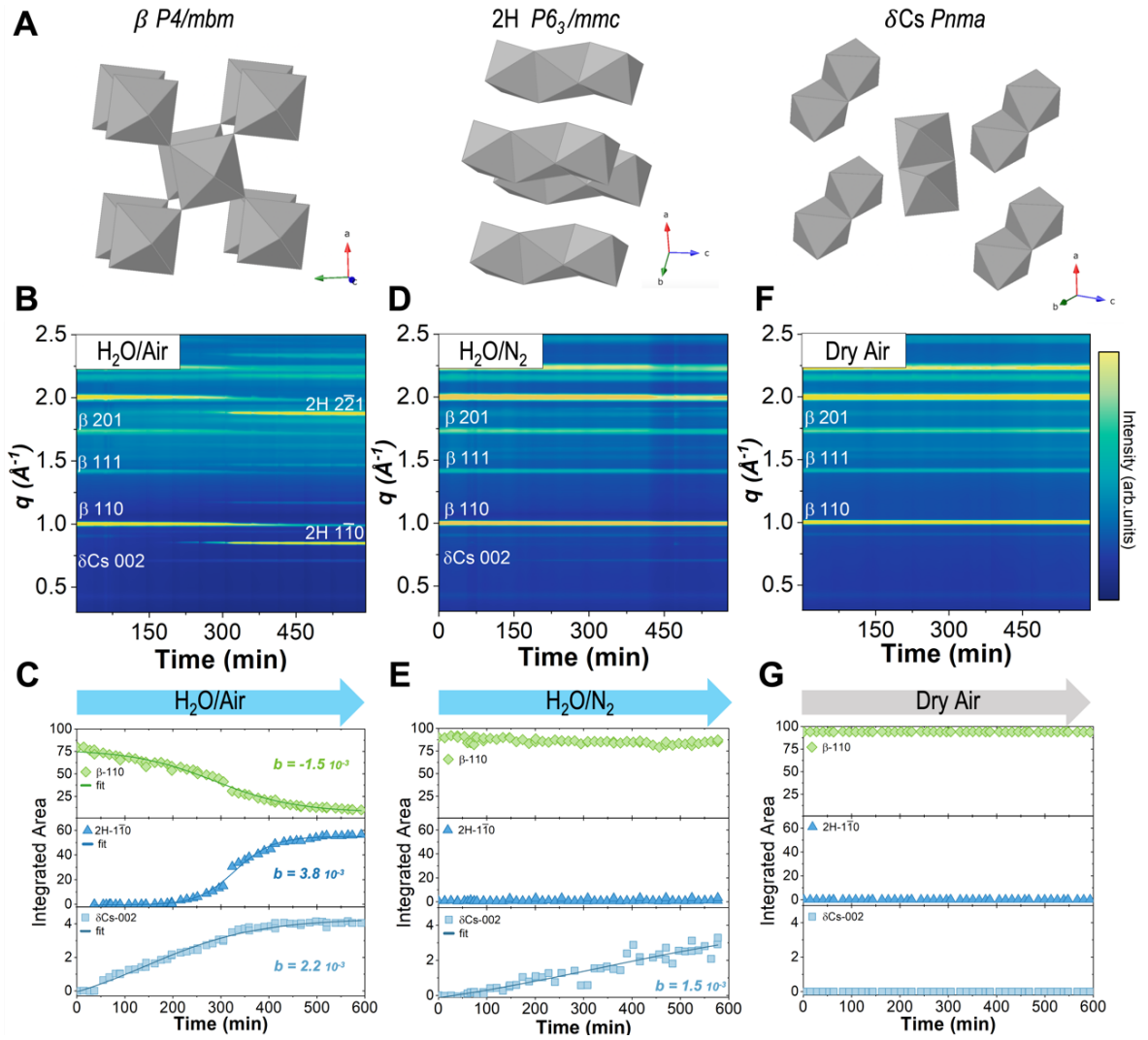


Figure 5.1 Humidity-induced structural phase transformations by *in-situ* GIWAXS. The structural phases analyzed are (A) tetragonal b-perovskite of space group $P4/mbm$ (left), 2H FAPbI₃ hexagonal non-perovskite phase of space group $P6_3/mmc$ (center), and orthorhombic d-CsPbI₃ non-perovskite phase of space group $Pnma$ (right). By *in-situ* GIWAXS we studied the phase transformations of CsFA b-perovskite in (B) H₂O/Air, (D) H₂O/N₂, (F) dry air, and where (C, E, G) are the corresponding integrated areas of the main scattering peak of each phase.

To study the structural changes at the surface of CsFA films exposed to H₂O/Air, we analyzed the *in-situ* GIWAXS with an incident angle below the critical angle (Figure BS7). We observed the same transformation from perovskite into non-perovskites on the surface as in the bulk (Figure 5.1). Further, analyzing the formation of the non-perovskite phases 2H and δ Cs, we calculated a larger rate constant b at the surface (Figure BS7), evidence of a faster

transformation into non-perovskites. In addition, areas with more charging were observed by scanning electron microscopy (**Figure BS8**), suggesting the formation of new phases. The UV-VIS spectroscopy shows a larger bandgap for the CsFA film after H₂O/Air exposure, which may be due to the absorption from the 2H phase (**Figure BS9**).^{20,65} The emission observed from photoluminescence (PL) and carrier lifetime from time-resolved PL (TRPL) are both reduced, as expected with the conversion to non-perovskite phases (**Figure BS9**).

5.2 Surface Chemistry

To investigate the chemical changes at the surface, we performed X-ray photoelectron spectroscopy (XPS) of the CsFA films without exposure and after H₂O/Air exposure (**Figure 5.2**). After exposure to H₂O/Air, the N 1s peak (**Figure 5.2A**, CsFA) decreases by 5.6 % in atomic content (**Tables BS2-3**), evidence of the FA⁺ volatility, as the N 1s peak corresponds to the C=N bond of the FA.⁴⁸ The I 3d peak from iodine decreases by 11.4 % atomic content after exposure to H₂O/Air (**Figure 5.2B**, CsFA), suggesting the loss of FAI at the surface and the additional loss of iodine.¹⁸⁷⁻¹⁸⁹

The exposure of CsFA films to H₂O/Air influences the oxygen signal. An increase in the O 1s peak signal is observed after exposure (**Figure 5.2C**), corresponding to an 18 % atomic content (**Table BS3**). The O 1s peak (Peak 1) is centered at 532.3 eV, suggesting the existence of adsorbed O₂ molecules.⁹⁸ Peak 1 may be attributed to the formation of hydroxides (OH⁻) or carbonates (CO₃²⁻) expected from the exposure to H₂O/Air.¹⁹⁰ The C 1s peaks also suggest carbon-oxygen complexes such as carbonates after H₂O/Air exposure (**Figure BS10**).⁹⁸ The peak assigned to C-C or C-H bonds increases after H₂O/Air exposure, possibly from atmospheric contamination (**Figure BS11**). **Figure 5.2C** also shows a small Peak 2, centered at 530.4 eV, suggesting the formation of Pb-oxides.⁹⁸ **Figure 5.2D** summarizes the

changes in the atomic ratio of iodine, cesium, nitrogen, and oxygen compared to Pb on CsFA films after H₂O/Air exposure, showing the volatilization of nitrogen and iodine, and an increase of oxygen content.

To further understand the chemical surface species after H₂O/Air exposure, we deposited FAI and PbI₂ thin films and characterized their surface chemistries by XPS (**Figure 5.2** FAI, PbI₂, and **Figures BS12-13**). After H₂O/Air exposure, the FAI films show a decrease of the atomic content from the N 1s and I 3d, confirming the volatilization of FAI (**Figure 5.2A,B** FAI, and **Tables BS4-5**). An expected increase in the intensity of the O 1s peak is observed on the FAI films (**Figure 5.2C**, FAI). The FAI films without H₂O exposure show an O 1s peak centered at 532.8 eV in **Figure 5.2C** (FAI), suggesting that atmospheric H₂O and O₂ molecules are adsorbed on FAI films when the samples are mounted in the XPS, confirming the high hydrophilicity of FAI. The deconvolution of the O 1s peak shows a second peak (Peak 2) centered at 530.8 eV, indicating that this peak may result from FA exposure to ambient conditions. Therefore, the O 1s Peak 2 in **Figure 5.2C** (CsFA) can be attributed to either Pb-oxides and to I or FA-oxides. In contrast, the PbI₂ films before and after H₂O/Air exposure do not show changes in Pb 4f (**Figure BS13**) or I 3d (**Figure 5.2B**, PbI₂), and there is no oxygen from the O 1s spectra (**Figure 5.2C**, PbI₂ and **Tables BS6-7**). Analyzing the chemistry changes in the bulk, X-ray fluorescence (XRF) elemental mapping also shows the loss of iodine after H₂O/Air exposure (**Figure BS14**), agreeing with the XPS results (**Figure 5.2B**). Fourier transform infrared spectra (FTIR) showed no oxygen in the vibrational modes of CsFA powders and films (**Figures BS15-16**, **Table BS8**). Thus, we are confident that the H₂O/Air-induced CsFA phase transformations begin at the surface through oxygen interactions with the perovskites.

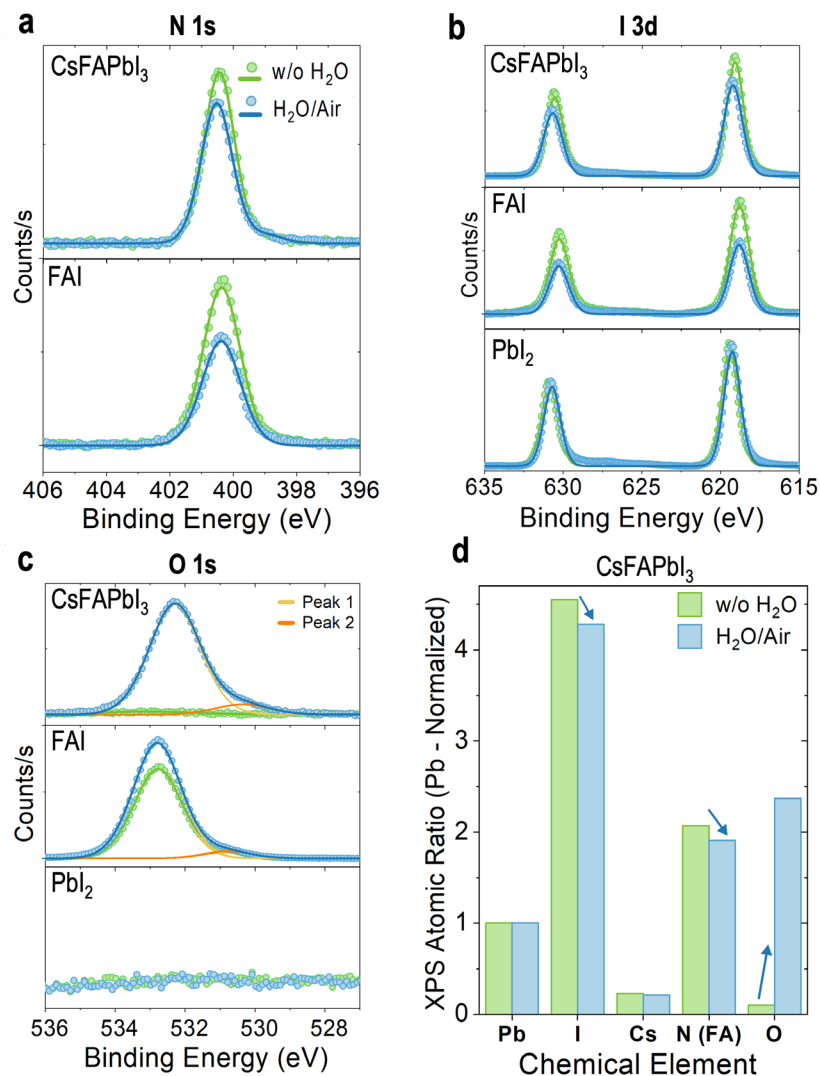


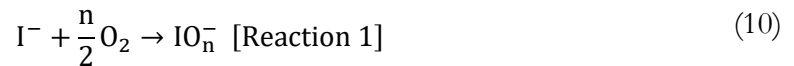
Figure 5.2 Surface chemistry by XPS. XPS spectrum of the peaks: (A) N 1s, (B) I 3d, (C) O 1s of CsFA perovskite, FAI, and PbI₂ films w/o and after H₂O/Air exposure. For the CsFA perovskite films, panel (D) Atomic ratio of Iodine (I), Cesium (Cs), Nitrogen (N, FA), or Oxygen (O) normalized to lead (Pb), w/o and after H₂O/Air exposure. CsFA perovskite films without (w/o) H₂O exposure (green) were fabricated in a nitrogen glovebox and exposed to room atmosphere while mounting the XPS measurement. CsFA films after H₂O/Air exposure (blue) were fabricated in a nitrogen glovebox, exposed to humidity, and then measured.

5.3 Chemical Reaction Mechanism

Previous studies have suggested adverse effects of H₂O on lead-iodide perovskite surfaces leading to the degradation of the material.^{24,177,185,191} Molecular dynamics simulations of

MAPbI₃/H₂O interfaces have shown the fast dissolution of MAI-terminated surfaces, as H₂O molecules break the bond between surface I⁻ and underlying Pb²⁺ ion resulting in the removal of I⁻, accompanied by the desorption of the MA⁺.^{158,192} Despite FA being less polar than MA,¹⁹² the same mechanism is expected to occur on FAI-terminated surfaces. Previous results showed the dissolution of FAPbI₃ with water vapor,¹⁹³ explaining the release of I⁻ and FA⁺ from the CsFA perovskite surface¹⁹⁴ and within the FAI films (**Figure 5.2A,B,D**) after exposure to H₂O/Air.¹⁹³ The removal of CsI or FAI leads to a PbI₂-terminated surface that is more resistant to degradation by water alone.¹⁵⁸

To understand the phase transformation mechanisms, we performed DFT calculations on the interactions of oxygen molecules with the PbI₂-terminated CsFA perovskite surface (**Figure BS17**). The O₂ adsorption is favored at the PbI₂-terminated surface ($E_{\text{ads}} = -0.03$ to -0.22 eV, **Table BS9**) compared to a CsFAI-terminated surface ($E_{\text{ads}} = 0.06$ to 0.36 eV, **Table S10**), while H₂O may further support O₂ adsorption. Note that the PbI₂-terminated surface is made of undercoordinated Pb²⁺, which makes it more hydrophilic than the hydrophobic PbI₂ crystal phase (**Figure 5.2C**) made of fully coordinated Pb²⁺.¹⁹⁵ The direct formation of PbO units from the adsorption of O₂ appears thermodynamically unfavorable, with reaction energies of $+1.09$ eV (**Figure BS18**). Therefore, we consider the oxidation of iodide ions on the surface by O₂ as the starting point, modeled by *reaction 1* (Equation 9). Here, surface iodide changes its oxidation state from -1 to positive values ($-1 + 2 \times n$) while oxygen atoms are in their stable -2 oxidation state. We observe that, as previously suggested,¹⁹⁶ oxygen breaks the Pb–I bonds at the surface, forming a Pb–O–I_{ox}–I⁻ bond network, where I_{ox} is the oxidized iodine and I⁻ is a surface iodide in its negative charge state as shown in **Figure 5.3A**.



Our calculations show positive reaction energies for the formation of hypiodite (IO^-) and periodate (IO_4^-) of 0.13 and 0.14 eV, respectively, while iodite (IO_2^-) is slightly favored by -0.05 eV. Notably, iodate (IO_3^-) with iodide in its +5-oxidation state is strongly thermodynamically favored with a formation energy of -0.97 eV, indicating an irreversible surface degradation. From IO_3^- in *reaction 2* we consider the formation of lead (II) iodate, $\text{Pb}(\text{IO}_3)_2$, at the surface (indicated by *) by oxidizing two adjacent iodide ions sharing bonds with the same Pb surface ion. The formation energy of surface $\text{Pb}(\text{IO}_3)_2$ is $\Delta E = -1.19$ eV (**Figure 5.3B**), which suggests a thermodynamically favorable replacement of a surface PbI_2 unit. Finally, in *reaction 3*, we compute the removal of surface $\text{Pb}(\text{IO}_3)_2$ leaving a PbI_2 vacancy (**Figure 5.3B**).¹⁹⁷ We predict an energy of -0.77 eV for *reaction 3*, significantly more favorable than the direct removal of a PbI_2 unit from a non-oxidized surface ($\Delta E = 0.07$ eV, **Figure BS19**).



We note that the interaction of O_2 with water molecules lowers the π^* orbitals of O_2 acting as accepting orbitals in oxidation reactions (**Table BS10**), while hydration of perovskite surfaces raises the energies of the iodide-based valence band edge (**Figure BS20**), which results in more facile oxidation of surface iodide. These results suggest that O_2 can modify PbI_2 -terminated surfaces by oxidizing iodide to iodate species and creating PbI_2 vacancies. These vacancies may allow H_2O molecules to enter the structure and dissolve the next FAI layers in an iterative process.

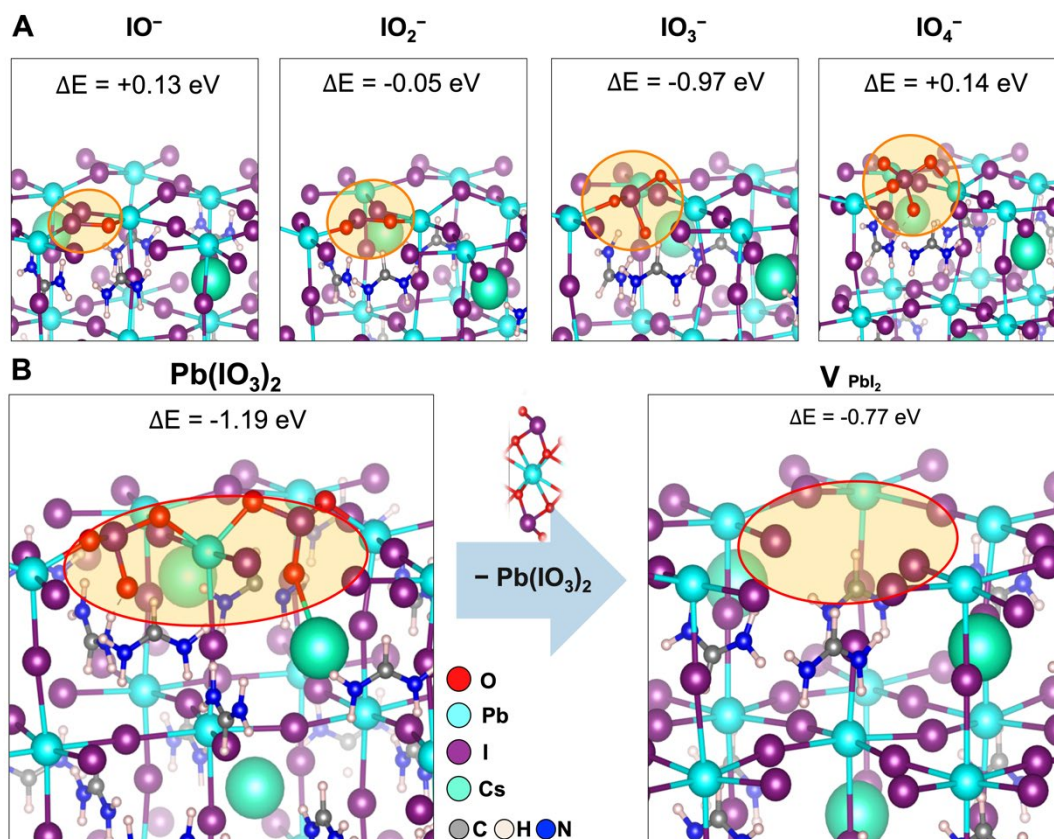


Figure 5.3 DFT calculation of iodide oxidation and superoxide formation on the perovskite surface. Panel (A) visualizes the formation of IO_n^- species upon oxidation of surface iodide ions [Rx. 1]; from left to right: hypoiodite, IO^- ; iodite, IO_2^- ; iodate, IO_3^- ; and periodate, IO_4^- . All oxidized species are explicitly highlighted, and reaction energies are given (see computational methods for details). (B) Reaction mechanism [Rx. 2 and 3] of (left) lead (II) iodate, $\text{Pb}(\text{IO}_3)_2$, formation by consumption of oxygen molecules, and (right) removal of $\text{Pb}(\text{IO}_3)_2$ resulting in a surface vacancy V_{PbI_2} . The following color code is used for the atomic representations: purple, I; cyan, Pb; blue, N; green, Cs; gray, C; white, H; red, O.

Our experimental and theoretical analyses suggest that first, the $\text{H}_2\text{O}/\text{Air}$ atmosphere dissolves the surface of CsFA perovskite and causes a loss in FA at the surface, likely increasing the relative amount of Cs relative to FA. Previous studies have shown that the CsFA perovskite phase becomes thermodynamically unstable when exceeding a Cs fraction of 0.2 (FA below 0.8).^{32,40} We note that the studied composition of $\text{Cs}_{0.17}\text{FA}_{0.83}$ is on the upper limit of Cs-molar content to form a single-phase perovskite.^{19,32} The loss of FAI may easily shift the composition into the thermodynamically unstable phase by increasing the ratio between Cs:FA, favoring the segregation into non-perovskite phases. Iodide vacancies created by H_2O

may further accelerate the phase transitions.¹⁸¹ Additionally, previous studies have highlighted the role of superoxide on perovskite degradation under light irradiation.^{22,187,188,190} Room light during the *in-situ* GIWAXS measurements can only lead to a negligible amount of free charge carriers (**Figure BS21**), likely insufficient to create a superoxide. However, under light irradiation, reactive superoxide species may accelerate perovskite phase transformations in H₂O or dry air (discussion in **Appendix B.6.5, Figures BS22-25**).

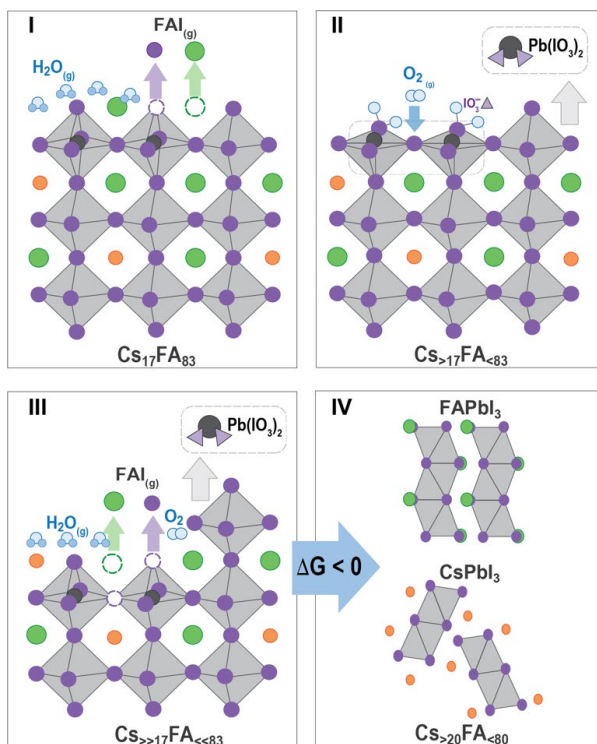


Figure 5.4 Surface and bulk mechanism when CsFA is exposed to H₂O/Air. (I) H₂O is adsorbed on the CsFA surface, promoting the loss of FA and I (g). Surface vacancies are created leading to preferential oxygen binding sites, favoring the oxidation of iodide and energetically favorable (II) formation of Pb(IO₃)₂, which will (III) create a PbI₂ vacancy. Surface vacancies and the loss of FAI will lead to faster phase segregation and (IV) phase transformations from mixed-cation perovskite into single-cation non-perovskite phases.

A proposed mechanism for the role of chemistry on phase transformations during exposure to H₂O/Air is shown in **Figure 5.4**. First (I), water molecules dissolve FAI at FAI-rich perovskite surfaces, creating PbI₂-rich surface regions. Second (II), O₂ molecules are adsorbed and oxidize surface iodide, resulting in iodate species at the surface. Third (III), lead

iodate can subsequently leave the surface, leaving PbI_2 vacancies on the surface, which act as hotspots for further FAI dissolution by H_2O . Fourth (IV), the loss of FA changes the Cs:FA molar ratio beyond the thermodynamically stable region, forming single-cation non-perovskite phases. We emphasize that the structural phase transformations in $\text{H}_2\text{O}/\text{Air}$ are initiated at the surfaces. Thus, chemical surface treatments, such as reducing undercoordinated Pb ions at the surface, should reduce interaction with H_2O and O_2 , likely improving phase stabilization.

5.4 Conclusions

Exposing mixed-cation CsFA perovskites to $\text{H}_2\text{O}/\text{Air}$ leads to undesired structural phase transformations, unlike the slower degradation observed in $\text{H}_2\text{O}/\text{N}_2$ and little to no degradation in dry air. When exposed to $\text{H}_2\text{O}/\text{N}_2$, the CsFA perovskite degrades slower by dissolving FAI molecules from the surface. However, in the presence of both H_2O and air, after the dissolution of the FAI molecules, O_2 from air oxidizes surface iodide ions, forming lead (II) iodate, which is a volatile species. This further causes the formation of PbI_2 vacancies, which act as hotspots for H_2O to enter the structure and dissolve more FAI molecules. This results in the loss of FAI molecules in an iterative process. This alteration in the local Cs:FA ratio goes beyond the energetically stable region, leading to a thermodynamic force that drives the phase transformation from perovskite to non-perovskite phases. This phase transformation process starts at the surface, where H_2O and O_2 react with surface ions. Our fundamental understanding of *in-situ* structural phase transformations at the bulk, coupled with insights into surface chemistry and reaction mechanisms provides a foundation for designing durable and efficient solar cell materials.

CHAPTER 6. PREVENTING PHASE TRANSFORMATIONS IN HALIDE PEROVSKITES

This chapter is based on the following articles:

“Bulky Cation Hinders Undesired Secondary Phases in FAPbI₃ Perovskite Solar Cells”, *Accepted to Materials Today*, 2023, by **Juanita Hidalgo**, Lahoucine Atourki, Ruipeng Li, Andres-Felipe Castro-Mendez, Sanggyun Kim, Emmet A. Sherman, Alexander S. Bieber, Meng-ju Sher, Lea Nienhaus, Carlo A.R. Perini, Juan-Pablo Correa-Baena.

“Synergistic Role of Water and Oxygen Leads to Degradation in Formamidinium-Based Halide Perovskites”, *Manuscript under review*, 2023, by **Juanita Hidalgo**, Waldemar Kaiser, Yu An, Ruipeng Li, Zion Oh, Andres-Felipe Castro-Mendez, Diana K. LaFollette, Sanggyun Kim, Barry Lai, Joachim Breternitz, Susan Schorr, Carlo A.R. Perini, Edoardo Mosconi, Filippo De Angelis, and Juan-Pablo Correa-Baena.

“Br-Induced Suppression of Low-Temperature Phase Transitions in Mixed Cation Mixed Halide Perovskites”, *Under Preparation*, 2023, by **Juanita Hidalgo**, Joachim Breternitz, Daniel Toebbens, Juan-Pablo Correa-Baena, Susan Schorr.

The major drawback to the commercialization of PSCs is their lack of long-term stability. Especially, the instability of the perovskite phase is detrimental to the device's performance. The first PSCs were fabricated using MAPbI₃¹⁴; however, due to the low thermal stability of the MA cation,¹⁹⁸ and ease to humidity and photodegradation of this material,^{24,184} the durability is in the range of hundreds of hours without encapsulation methods.¹⁹⁹ Different approaches have been made to improve structural and performance long-term stability in LHPs. As mentioned in earlier chapters, mixing A-site cations and X-site halides has been widely used to improve the stability of these materials, leading to the complete replacement of the MA cation by FA. FA has shown better thermal stability than MA, but the structural phase stability is still an issue (**Chapter 2**, Polymorphism). This chapter investigates two strategies to stabilize the FA-based perovskite phase. First, a phenyl bulky salt, phenethylammonium iodide (PEAI), is investigated as a hydrophobic protection layer by forming a low-dimensional (LD) RP phase structure on top of the 3D FA-based LHP. Second, this chapter studies the effect of adding Cs and Br into FAPbI₃ on the stability of the perovskite phase by analyzing the structural phase transitions at low temperatures.

6.1 The Role of PEA I

Low dimensional (LD) Ruddlesden-Popper structures or bulky cations have been added to the surface of 3D lead halide perovskites (LHPs) to improve the stability and efficiency of perovskite solar cells (PSCs).^{200–203} These bulky cations create a thin LD layer on the surfaces known as the “capping layer”,²⁰⁴ which can improve the moisture resistance^{205,206} and reduce non-radiative recombination at the interfaces, ultimately increasing the solar cell's power conversion efficiencies (PCE).^{204,207–209} However, most studies have only focused on the crystal structure of the LD layer and neglected the changes induced at the surface and bulk of the 3D

film, which is crucial to understanding how these surface treatments lead to improved performance in PSCs.

To create LD structures on the surface of 3D LHPs, bulky organic cations such as phenethylammonium (PEA^+) and butylammonium (BA^+) have been used.^{210,211} These cations are hydrophobic and moisture-resistant, which can provide stability to the LHP and interfaces.^{201,212–214} Bulky cations also reduce the polar surface on LHP, improving moisture resistivity.^{205,206} In addition, these LD structures can reduce the non-radiative recombination at interfaces by preventing recombination, boosting the fermi-level splitting and open circuit voltages (V_{oc}) in PSCs.^{204,207–209}

While the LD-3D capping layer improves some optoelectronic properties, the 3D LHP primarily absorbs and transports charge carriers in PSC.²¹⁰ Formamidinium lead iodide perovskite (FAPbI_3 , FAPI) is an excellent candidate as the bulk 3D film due to its bandgap of around 1.48 eV, which helps maximize the potential PCE to be extracted in a single-junction solar cell.²¹⁵ However, the FAPI perovskite cubic phase is unstable, given that at room temperature, it quickly transforms into the non-perovskite hexagonal phase known as 2H.^{215,216} Different additives have been used to stabilize the FAPI perovskite cubic phase and achieve high efficiencies, such as Cs.^{206,217–219} However, the role of treated interfaces with bulky cations in stabilizing the FAPI perovskite, without additives, is not well understood.

Herein, we investigate the effects of adding a LD PEAI layer into a pure FAPI and mixed-cation CsFA perovskite to understand how the LD capping layer alone is responsible for enhanced perovskite phase stability and PCE. First, to analyze the pure FAPI, we use synchrotron-based GIWAXS, time-resolved photoluminescence (trPL), and time-resolved THz spectroscopy (THz) to study the impact of the capping layer on the structure and carrier

dynamics. We reveal how the bulky cation hinders the structural conversion of the cubic FAPbI_3 perovskite into non-perovskite phases both on the surface and in the bulk. We fabricate FAPI solar cells with and without a PEAI capping layer and measure the photovoltaic parameters. Adding 5 mg/mL of PEAI on top of the 3D FAPI prevents the formation of undesired non-perovskite phases and improves solar cell performance. While our study analyzes the structure at the surface and bulk of FAPI treated with PEAI, the same analysis can be applied to other bulky cations and LHPs to improve performance and phase stability by tailoring the device interfaces. Second, to analyze the mixed-cation CsFA, we also show that surface treatments using a hydrophobic top layer of PEAI effectively stabilize the surface, resulting in strongly increased perovskite phase stability when exposed to H_2O and air. Solar cells made of CsFA-PEAI films have stable power conversion efficiencies even after exposure to H_2O and air. Our study provides structural and atomistic insights into the CsFA perovskite phase instability under humid air conditions and derives surface passivation strategies to stabilize the perovskite phase for stable and efficient solar cells.

6.1.1 PEAI on Pure FAPI

We study the effect of a LD capping layer on the structure at the surface and bulk of FAPI. As shown in **Figure 6.1A**, we first deposit FAPI by spin-coating and annealing the films at $150\text{ }^\circ\text{C}$ to form a black cubic FAPI perovskite (structural details in **Chapter 3**). In the second step, the PEAI is added via dynamic spin-coating 1 mg/mL or 5 mg/mL of PEAI in 2-propanol. We suggest that adding PEAI will form a LD capping layer, as shown in the schematic of **Figure 6.1B**. For PEAI, the LD layer is expected to be a RP phase, an array of corner-sharing octahedra divided by the bulky cation PEA with the chemical formula PEA_2PbI_4 . The influence of the structural changes of the LD-3D FAPI on solar cell

performance is evaluated by fabricating n-i-p devices with the architecture shown in **Figure 6.1C**.

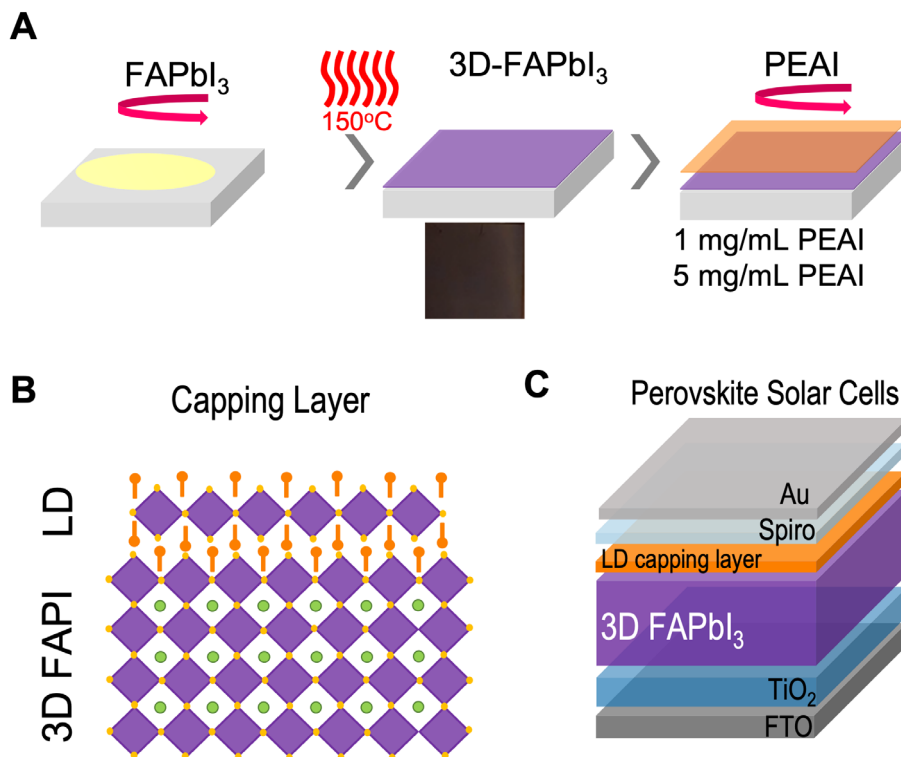


Figure 6.1 FAPI-PEAI experimental design. (A) Schematic representation of the preparation of PEAI-treated FAPI films by spin coating PEAI as a post-deposition process after FAPI annealing. (B) Schematic showing the suggested structure at the surface and bulk after PEAI deposition into the 3D FAPI perovskite. (C) The solar cell device architecture adopted in this study.

Surface engineering in LHPs has contributed to the rapid development of PSCs.²²⁰ Interfacial treatments have improved surface defect passivation in PSCs. However, surface treatments can also impact the structure of the bulk, which is often neglected. Therefore, it is important to study structure-property relationships at the surface and in the bulk in LHP films treated with LD layers. Using GIWAXS it is possible to obtain crystallographic information from the surface and the bulk. By measuring GIWAXS with different X-ray incident angles (α_i), we can tune the X-ray penetration depth as discussed in **Chapter 3 (Figure 3.5)**.^{90–92} For

an incident 13.5 keV X-ray, and FAPI films, $\alpha_i = 0.05^\circ$ penetrates around 3 nm and $\alpha_i = 0.5^\circ$ around 225 nm. Given that the FAPI films have a thickness of approximately 500 nm, we probe the surface for $\alpha_i = 0.05^\circ$ and the bulk for $\alpha_i = 0.5^\circ$.

6.1.1.1 Structural Analysis: Surface vs. Bulk

First, we analyze the structure of the untreated FAPI films in **Figure 6.2**. In the 2D GIWAXS in **Figure 6.2A**, the Debye-Scherrer rings of the perovskite phase have a high intensity and some brightness variations throughout the ring, revealing a random orientation in the surface and bulk. To ease comparing the presence and ratio of crystallographic phases in the film, the 2D GIWAXS pattern is integrated to obtain a 1D circular average diffraction pattern (**Figure CS1**). We subtract the amorphous background from the circular average patterns and normalize the diffraction data with the 100 cubic FAPI peak at $q_r = 1 \text{ \AA}^{-1}$ in **Figure 6.2B**. From a detailed phase analysis, most of the peaks in the diffraction pattern correspond to a cubic FAPI perovskite, both at the surface and bulk (**Figure CS1**). Additionally, in **Figure 6.2B** we observe diffraction peaks below $q_r = 1 \text{ \AA}^{-1}$ corresponding to secondary FAPI hexagonal polytypes from $q_r = 0.75 \text{ \AA}^{-1}$ to $q_r = 0.95 \text{ \AA}^{-1}$ (simulated diffraction patterns in **Figure CS2**).²²¹ The most common and predominant FAPI hexagonal polytype is 2H.²¹⁵ The 2H 110-peak at $q_r = 0.85 \text{ \AA}^{-1}$ in **Figure 6.2B** shows a higher relative intensity at the surface than in the bulk, indicating a larger presence of the 2H at the surface. At the bulk, the (110) plane of the non-perovskite 2H phase shows preferential orientation perpendicular to the surface. Additional peaks appear in the diffraction pattern of FAPI, at $q_r = 0.82 \text{ \AA}^{-1}$ and $q_r = 0.91 \text{ \AA}^{-1}$. We suggest that these two peaks correspond to the formation of other hexagonal polytypes different than 2H (labeled “H”), such as 4H or 6H.²²² However, not all the peaks from the simulated patterns of 4H and 6H are present. Hexagonal polytypes have been shown to be

intermediate phases as the metastable FAPI cubic phase¹⁹ converts into the 2H phase.²²² Therefore, we hypothesize that different hexagonal polytypes of a greater number, up to 11H, could originate those peaks. In **Figure 6.2B**, the scattering pattern is normalized to the main FAPI cubic perovskite 100 peak, given that the signal comes from different probed volumes. For untreated FAPI films, without the addition of PEAI, there are no peaks from $q_r = 0.25 \text{ \AA}^{-1}$ to $q_r = 0.5 \text{ \AA}^{-1}$ in **Figure 6.2B**, which are assigned to LD PEAI phases. The schematic in **Figure 6.2C** summarizes the distribution of the different phases in the film as highlighted by GIWAXS.

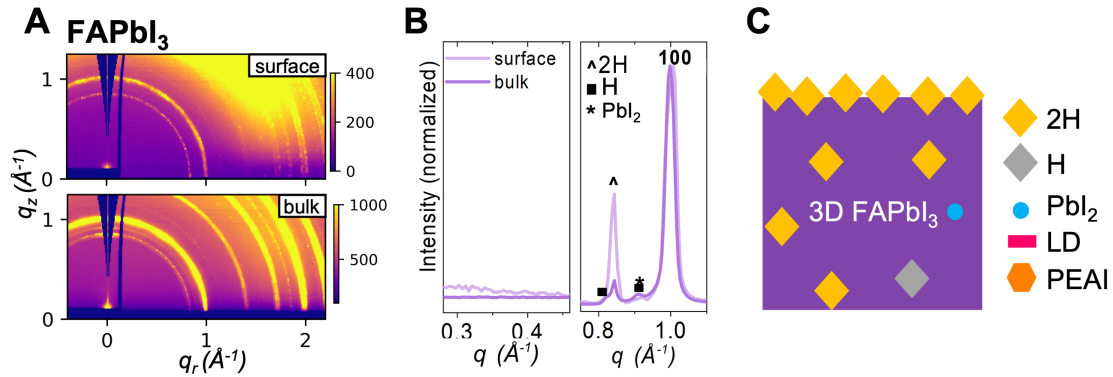


Figure 6.2 GIWAXS analysis of the untreated FAPI films. (A) 2D pattern at two different incident angles 0.05° for the surface, 0.5° for the bulk. (B) circular average showing the ranges where LD PEAI-based, hexagonal polytypes, and perovskite peaks are expected. (C) Schematic of crystallographic phases observed at the surface and bulk of FAPI. The legend of the non-perovskite phases is shown in the schematics. FAPbI₃ films were exposed to ambient air for measurements.

Having characterized the crystallographic phases in the untreated FAPI layer, we move to observe the structural changes when treating FAPI with 1 mg/mL of PEAI. **Figure 6.3** shows the structural changes of FAPI coated with 1 mg/mL PEAI. The 2D GIWAXS plots in **Figure 6.3A** reveal a random orientation of the perovskite phase in the films. The LD PEAI₂PbI₄ main peak^{223–226} is observed from $q_r = 0.25 \text{ \AA}^{-1}$ to $q_r = 0.45 \text{ \AA}^{-1}$ in **Figure 6.3B** (simulated structure in **Figure CS3**). We observe in **Figure 6.3B** the appearance of PEAI₂PbI₄

at the surface but not in the bulk, suggesting that the PEAI combines with PbI_6 corner-sharing octahedra to form a LD layer only at the surface. In **Figure 6.3B** we also observe two low-intensity peaks corresponding to non-perovskite hexagonal phases. The 2H phase and other hexagonal polytypes H are visible at the surface and in the bulk. Moreover, in **Figure 6.3B**, we observe an additional peak next to the 100 FAPI peak, slightly above $q_r = 1 \text{ \AA}^{-1}$. This peak could correspond to another hexagonal polytype, such as 6H²²¹ (**Figures CS2**). To summarize, **Figure 6.3C** shows the phases in the 3D film treated with 1 mg/mL PEAI. A LD capping layer is formed by adding 1 mg/mL of PEAI to 3D FAPI. The capping layer hinders the formation of non-perovskite phases in 3D FAPI.

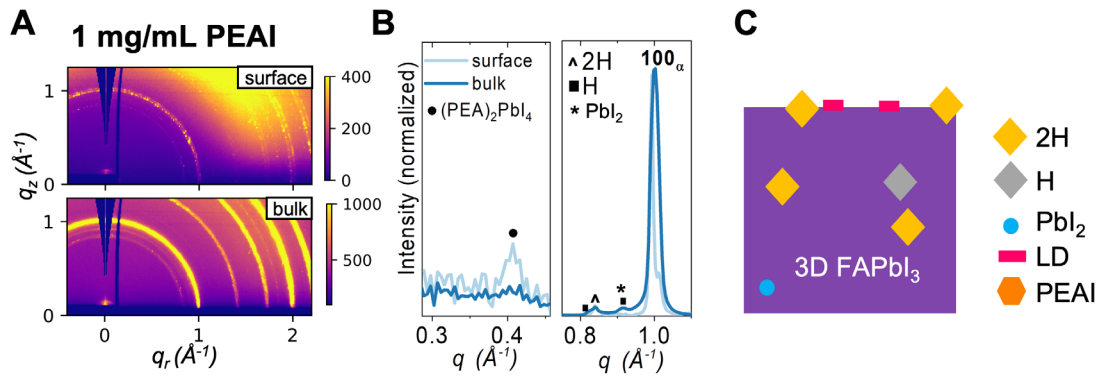


Figure 6.3 GIWAXS analysis of the 1 mg/mL PEAI-treated FAPI. (A) 2D GIWAXS pattern at two different incident angles 0.05° for the surface, 0.5° for the bulk. (B) Circular average showing the ranges where LD PEAI-based, hexagonal polytypes, and perovskite peaks are present. (C) Schematic of crystallographic phases in the FAPbI_3 surface and bulk. The legend of the non-perovskite phases is shown in the schematics. FAPbI_3 films were exposed to ambient air for measurements.

Building on this understanding, we increase the amount of PEAI added to 5 mg/mL to further prevent the formation of non-perovskite hexagonal polytypes in the FAPI film. The changes in the structure at the surface and bulk are presented in **Figure 6.4**. Analogously to the case of the untreated FAPI and of FAPI treated with 1 mg/mL of PEAI, **Figure 6.4A** show evidence of randomly oriented FAPI domains in the films treated with 5 mg/mL of PEAI. In **Figure 6.4B**, we observe the details in the circular average diffraction patterns

(complete patterns in **Figure CS5**). In **Figure 6.4B**, from $q_r = 0.25 \text{ \AA}^{-1}$ to $q_r = 0.45 \text{ \AA}^{-1}$, we observe a peak corresponding to PEAI at the surface.²⁰⁹ This PEAI layer can contribute to the passivation of defects, as seen before by Jing et al.²⁰⁹ Lower concentrations of PEAI, such as 1 mg/mL shown in **Figure 6.3**, do not show the PEAI peak. The latter is because less amount of PEAI fully results in full conversion to the LD PEA_2PbI_4 ,²²⁷ whereas higher amounts also convert to PEA_2PbI_4 but not completely. In addition, by adding 5 mg/mL of PEAI, we observe that the LD PEA_2PbI_4 is visible both at the surface and in the bulk. The presence of LD phases at the surface suggests a capping layer, as proposed in **Figure 6.1B**. The scattering intensity from the non-perovskite peaks, 2H and other H phases, is reduced compared to the untreated FAPI and FAPI treated with 1 mg/mL of PEAI (**Figure 6.2B** and **Figure 6.3B**). We hypothesize that the PEAI and the PEA_2PbI_4 capping layer prevent the transformation of the FAPI cubic perovskite into non-perovskite phases, as shown in **Figure 6.4C**.

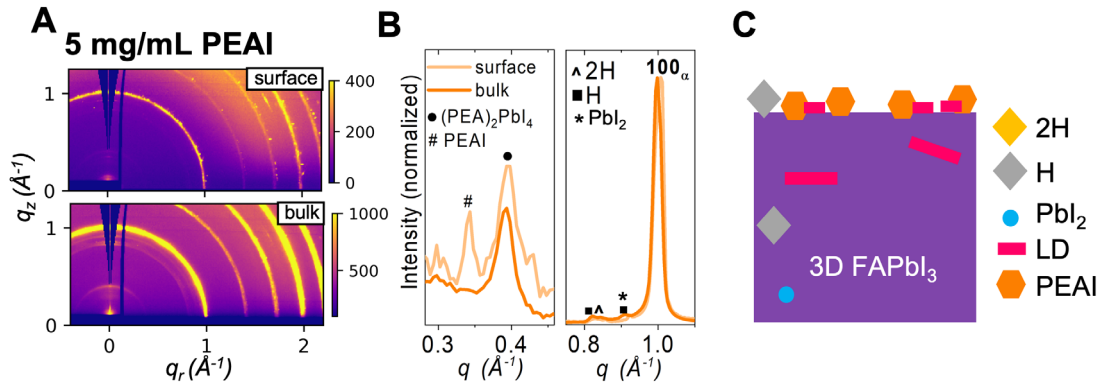


Figure 6.4 GIWAXS analysis of the 5 mg/mL PEAI-treated FAPI. (A) 2D GIWAXS pattern at two different incident angles 0.05° for the surface, 0.5° for the bulk. (B) circular average showing the ranges where LD PEAI-based, hexagonal polytypes, and perovskite peaks are present. (C) schematic of crystallographic phases in the FAPbI_3 surface and bulk. The legend of the non-perovskite phases is shown in the schematics. FAPbI_3 films exposed to ambient air for measurements.

Overall, we observe that the appearance of secondary hexagonal phases starts at the surface (**Figure CS6**). Adding PEAI leads to the formation of a LD capping layer, which

hinders the conversion into non-perovskite phases in the bulk of the 3D film. When adding 1 mg/mL of PEAI, we observe the formation of a LD capping layer at the surface. However, when adding 5 mg/mL of PEAI, the bulk is also transformed into a LD-3D, suggesting that the concentration of PEAI influences the crystal structure of the perovskite material. A higher concentration of PEAI leads to a more significant crystal transformation of the crystal structure since more material is added and this LD material can diffuse at grain boundaries,²²⁷ forming the 2D-LD in the bulk.

6.1.1.2 Surface Chemistry

To investigate the chemical interaction between PEAI and the 3D perovskite at the surface, we performed XPS analysis. The C 1s and the N 1s elemental scans reveal the presence of PEA cations at the surface upon treatment of the FAPI film, accompanied by a decrease in the Pb 4f signal in **Figure 6.5**. **Figure 6.5A** shows the C 1s spectrum of the FAPI perovskite films, where two major peaks are observed. The two peaks correspond to the C–C (284.8 eV) and C=N (288.5 eV) bonds. The C=N bond indicates the presence of the FA cation, as shown previously in other works.^{228,229} By adding PEAI, the intensity of the C=N peak decreases, and the intensity of the C–C bonds increases, indicating the presence of PEA cations at the surface. From the C 1s XPS spectra, in the PEAI-treated FAPI samples, the co-existence of FA and PEA agrees with the results from GIWAXS that indicate a 2D-3D mixture at the surface, as suggested from the structural GIWAXS results in **Figure 6.3** and **Figure 6.4**. In addition, from the C 1s spectra we observe a third small peak around 287 eV, assigned to a C–N single bond.⁹⁸ This peak intensity agrees with the amount of PEAI added at the surface, since it is more evident for 5 mg/mL compared to 1 mg/mL. The C=N (401.5 eV) bond, characteristic of FA, is also observed in the N 1s spectrum of the FAPI films in **Figure 6.5B**, showing the

highest intensity in pure FAPI films. As the PEAI is added, the intensity of C=N decreases. In the N 1s spectrum, we also observe the peak assigned to the C–N (402.5 eV) bond, which is characteristic of PEA. The Pb spectrum (**Figure 6.5C**) shows the Pb 4f lines at 138.1 and 143 eV. Quantifying all elemental composition at the surface (**Table CS1**) supports the above explanation. We analyze the film morphology by SEM (**Figure CS7**), showing no visible changes in the FAPI surface when adding PEAI.

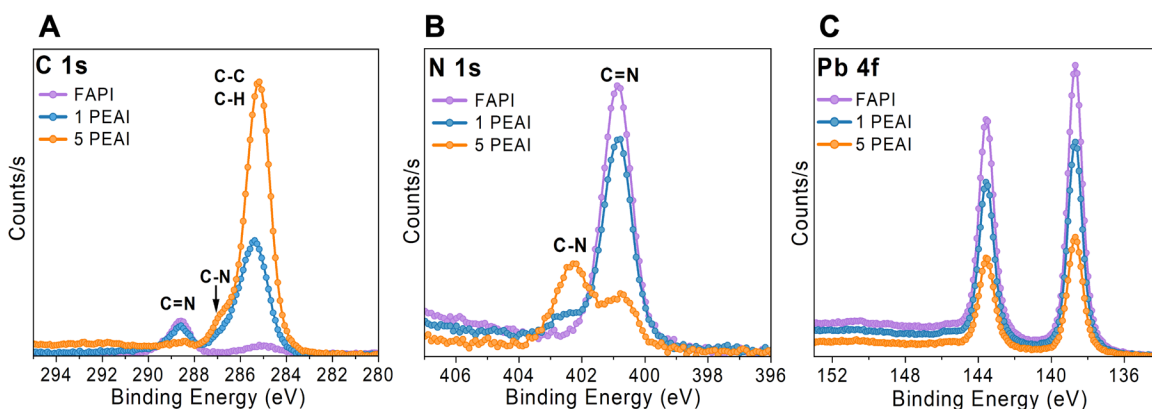


Figure 6.5 Surface chemistry by XPS on FAPI films treated with PEAI. (A) C 1s, (B) N 1s, and (C) Pb 4f spectra. 1 mg/mL PEAI is labeled “1 PEAI” and 5 mg/mL PEAI is labeled “5 PEAI”. FAPbI₃ films were exposed to ambient air for measurements.

6.1.1.3 Optoelectronic Properties

We use photoluminescence (PL) spectroscopy to understand how the optical properties of the FAPI thin films are affected by the structural changes induced by PEAI (**Figure 6.6A**). The untreated FAPI shows broad emission with low intensity in the 500-800 nm wavelength range, which is expected for a degraded FAPI perovskite after exposure to air.²³⁰ The PL evolution from nitrogen to air is shown in **Figure CS8**. After air exposure, it is evident that the broad emission is a result of degradation (**Figure CS9**). This degradation corresponds to undesired hexagonal phases observed in GIWAXS (**Figure 6.2**). The films treated with PEAI (1 mg/mL

and 5 mg/mL) show narrow emission peaks centered around 800 nm. Air degradation is hindered when the FAPI is covered with PEAI. Emission in the 1 mg/mL PEAI-treated films is centered at 797 nm. The position of the PL maximum is at 812 nm in the 5 mg/mL PEAI samples.

Time-resolved photoluminescence (trPL) was used to measure carrier lifetimes in the deposited films (**Figure 6.6B**). Longer carrier lifetimes may be linked to reduced non-radiative recombination pathways. The relatively fast decay component is commonly assigned to charge carrier trapping by defects at the surface and grain boundaries of the films.²³¹ The slower decay components are instead attributed to charge carrier recombination in the bulk.^{231,232} The trPL of the degraded FAPI is shown in **Figure 6.6B**. FAPI shows a very fast initial trPL decay, which is consistent with the presence of secondary phases and with degradation progressing from the surface. PEAI treated films show slower decays, suggesting reduced defect density at the surface of the films. Defect recombination is slowest for the films treated with 5 mg/mL PEAI.

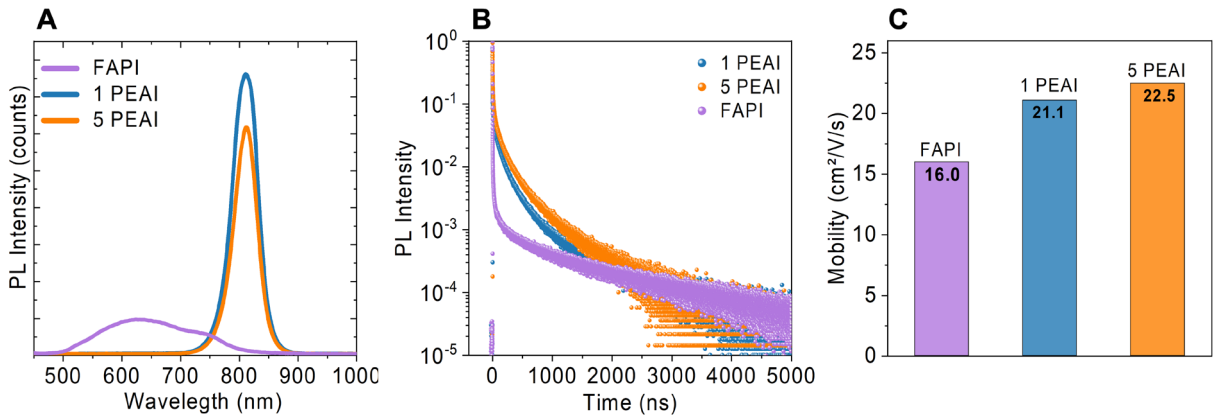


Figure 6.6 The effect of PEAI concentrations on (A) PL emission and (B) trPL carrier lifetime. (C) Charge carrier mobilities from THz. 1 mg/mL PEAI is labeled “1 PEAI” and 5 mg/mL PEAI is labeled “5 PEAI”. FAPbI₃ films were exposed to ambient air for measurements.

To study the effect of PEAI addition and annealing on the charge carrier mobility in the bulk (**Figure 6.6C**), we performed the carrier transport measurements using time-resolved THz spectroscopy (**Figure CS10**). Upon excitation, the change of THz transmission (ΔT) reflects the photoconductivity of the sample. ΔT increases with excitation fluences because of the higher excited carrier density and hence higher photoconductivity. At even higher excitation densities, carrier-carrier interactions reduce the measured carrier mobility and enhance higher-order recombination processes (bimolecular and Auger recombination). We use the THz transmission change at $t = 0$ and assume that the density of charge carriers is equal to the density of the absorbed photons (roughly $1 \times 10^{19} \text{ cm}^{-3}$ at the lowest laser fluence). We calculate the carrier mobility using Equation 13, where μ_{THz} is the carrier mobility at THz frequencies, T_0 is the initial THz transmission through an unexcited film, $Z_0 = 377 \Omega$ is the impedance of air, N_{photon} is the incident photon flux, q is the elementary charge, n_{SiO_2} is the index of refraction of the quartz substrate at THz frequencies.²³³

$$\mu_{THz} = \frac{-\Delta T}{T_0} \frac{Z_0}{N_{photon} q (1 + n_{SiO_2})} \quad (13)$$

The THz photoconductivity measurements show that an untreated FAPI film suffers from lower charge carrier mobilities than those samples treated with PEAI (**Figure 6.6C**). FAPI films exhibit mobilities calculated to be around $16 \text{ cm}^2/(\text{V}\cdot\text{s})$. The carrier mobility of the untreated FAPI sample is lower than other literature reports,^{234,235} but we note that THz mobility is a strong function of excited laser power and that due to the unstable nature of FAPI, some degradation could occur in the measurement. Upon addition of PEAI, the carrier mobility at the lowest excitation fluence increases significantly by 31% and 42% for the 1 mg/mL and 5 mg/mL PEAI samples, respectively. The highest mobility measured in these samples is for FAPI treated with 5 mg/mL PEAI sample at $22.5 \pm 0.3 \text{ cm}^2/(\text{V}\cdot\text{s})$. This dataset

shows that the PEAI addition at 5 mg/mL helps retain the improved electronic properties provided by passivation.

6.1.1.4 FAPI Perovskite Solar Cells

To understand the effect of PEAI addition on the performance of a complete solar cell, we fabricated devices based the architecture in **Figure 6.1C**. The V_{OC} and PCE for the treated and untreated devices are summarized in **Figure 6.7A,B**. The V_{OC} increases from an average of 0.99 V, for the untreated FAPI to an average of 1.08 V for all PEAI-treated devices. Based on the data discussed above, most of the improvements seen in V_{OC} may be due to the structural preservation of the FAPI perovskite phase with PEAI deposition. However, it is also possible that defect passivation is occurring concurrently.^{235–237}

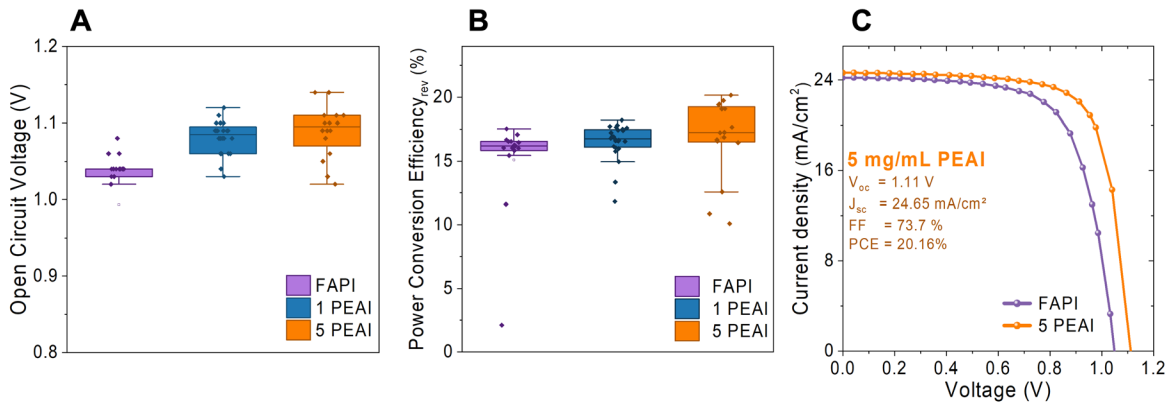


Figure 6.7 FAPI Solar Cells. (A) Open circuit voltage (V_{OC}) and (B) PCE for solar cells with FAPI untreated and treated with PEAI. The data points are plotted in boxplots which show the median (central line) and the lower and upper quartiles (25% and 75%) (bottom and top lines of the box, respectively). (C) J - V curves of a high-performing device of the FAPI untreated and treated with 5 mg/mL of PEAI. FAPbI₃ films were exposed to ambient air for measurements.

The J_{SC} and FF increased on average from 22.6 mA/cm² and 65.3%, respectively, when untreated FAPI, to 23.11 mA/cm² and 66.5% when treated with 5 mg/mL of PEA (**Figure CS11** and **Figure CS12** for 10 mg/mL). The increased J_{SC} and FF are consistent with hindered

degradation of FAPI into the 2H phase and enhanced mobilities (see THz in **Figure 6.6C**). The highest V_{OC} obtained in this work was 1.14 V via 5 mg/mL of PEAI added, around 91% of the Shockley–Queisser limit V_{OC} (1.25 V). The best device in this work had an efficiency of 20.2 % and stabilized PCE of 19.0 %, which is among the highest reported PCE for pure FAPI solar cells.²³⁸ The J - V curve of the highest efficiency device treated with 5 mg/mL of PEAI, compared to the untreated FAPI is shown in **Figure 6.7C**.

6.1.2 PEAI on CsFA Improves H₂O Stability

In **Chapter 5**, I studied the mechanism of the undesired phase transformations of the (Cs_{0.17}FA_{0.83})PbI₃ (CsFA) perovskite under H₂O and air exposure. In this chapter, to understand the role of surface blockers, capping layers, or surface passivators on phase transformations at the interface under H₂O exposure.^{239,240} We evaluate the effect of 5 mg/mL PEAI spin coated on a CsFA perovskite film (PEAI-treated).^{135,209} DFT calculations show a substantial reduction in H₂O adsorption energies at the aromatic PEA (**Figure 6.8A**), resulting in hydrophobic protection that can reduce the dissolution of FAI-rich surfaces (**Figure CS13**).

We analyzed the structural phase transformations by *in-situ* GIWAXS in H₂O/Air (Methods in **Chapter 3**). **Figure 6.8B** shows the peak evolution of the main perovskite (i.e. β -CsFA) and non-perovskite phases (i.e. 2H and δ Cs) as a function of exposure time to H₂O/Air. The main 110 β -perovskite peak does not change in H₂O/Air after 600 min of exposure, suggesting that the PEAI layer prevents H₂O and O₂ interaction at the surface compared to the untreated films in H₂O/Air (**Chapter 5, Figure 5.1B,C**). Films treated with PEAI show a slight presence of 2H phase (**Figure 6.8B**), which decreases as a function of time (**Figure CS14**). The δ Cs phase forms when exposed to H₂O/Air, but three times slower

than the untreated films (Chapter 5, Figure 5.1C) when comparing the rate constant b (Figure CS15). Figure 6.8C shows the 2D GIWAXS after the final exposure to H₂O/Air. For the PEAI-treated films, the β -perovskite 110 Debye Scherrer ring has a high intensity at the bulk and surface. We also observe rings that we assigned to low-dimensional (LD) PEA phases, as expected.²²⁷ The pristine CsFA films in Figure 6.8C show that the primary phases non-perovskites 2H and δ Cs.

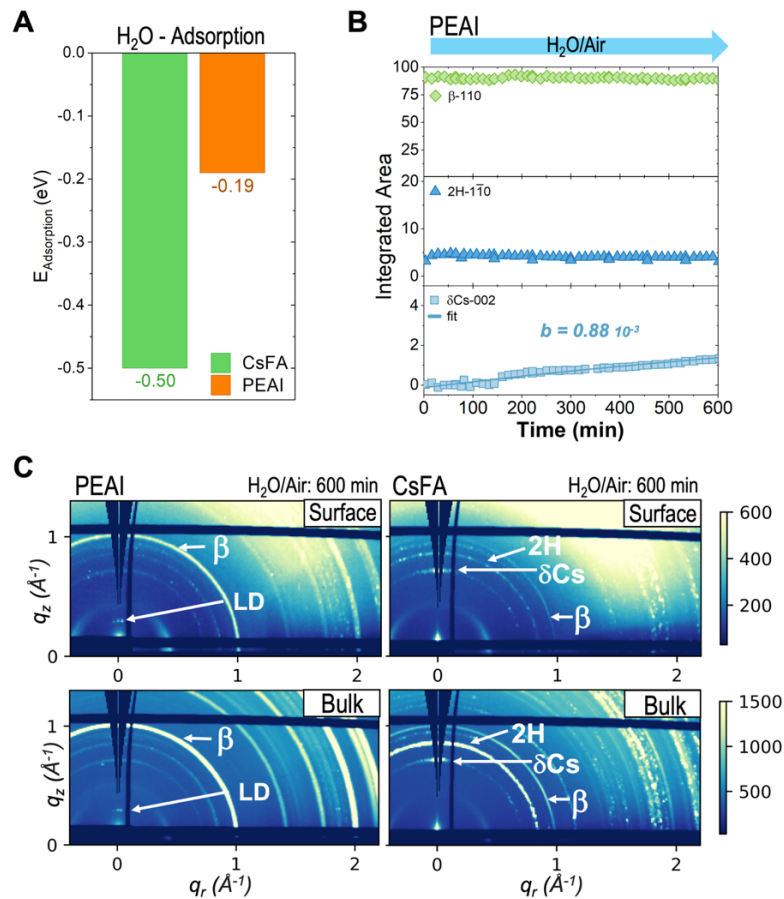


Figure 6.8 PEAI layer to stabilize the CsFAPbI₃ (CsFA) perovskite in H₂O/Air. Panel (A) shows H₂O adsorption energy on a CsFA surface and CsFA-PEAI surface calculated by DFT. From GIWAXS measurements in Figure CS14, (B) is the integrated area of the main scattering peak of each phase in H₂O/Air, and (C) the 2D GIWAXS patterns from the surface and bulk measurements after 600 min exposed to H₂O/Air for the (left) PEAI-treated CsFA films, and (right) untreated-CsFA.

We assessed the long-term stability under operating conditions of solar cells under one sun illumination in dry air (**Figure 6.9D**). Our results show an 85% decrease after 13 hours in the untreated film solar cells. The PEAI-treated solar cells decreased only 30% from their initial PCE after 25 hours, showing a slower degradation, which further suggests an increased robustness to the exposure to H₂O/Air (**Figure CS18**). In contrast, the solar cells exposed to dry nitrogen showed no degradation (**Figure CS19**), suggesting that oxygen in air is key to the degradation of the solar cells.

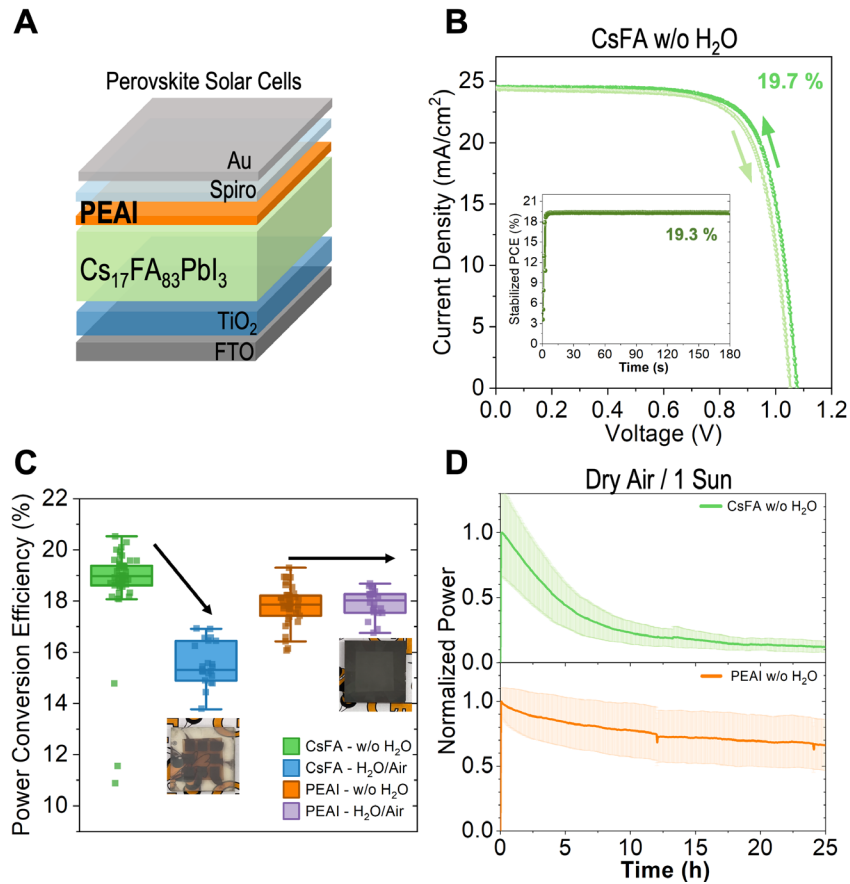


Figure 6.9 The effect of PEAI layer on perovskite solar cells with (A) n-i-p architecture. We evaluated the solar cell performance. Panel (B) shows the current density-voltage curve and stabilized PCE of a high-efficiency device, and (C) shows the statistics of the PCE in box plots for the CsFA-untreated and PEAI-treated, w/o and with H₂O exposure. The inset pictures show the device after H₂O/Air exposure before depositing the Spiro-OMeTAD and Au layers. We evaluated the long-term stability by tracking the maximum power point of 16 devices under the stress of one sun and constant electrical measurement. We plot (D) the average and normalized power, equivalent to PCE, of the measurements done at 25 °C, dry air, and one sun illumination.

6.1.3 The Role of PEAI Conclusions

In summary, Chapter 6.1 examined the role of bulky PEAI interacting with the FAPI and CsFA perovskites at the surface and bulk. On pure FAPI, we found that by adding 5 mg/mL of PEAI, a thin capping layer forms on top of the FAPI perovskite that improves the efficiency of the perovskite phase and reduces the formation of non-perovskite hexagonal phases. Non-perovskite phases have been correlated to poor optoelectronic properties, lower device performance, and a decrease in performance. The increased charge carrier mobility and lifetime observed with the addition of PEAI are linked to the improved perovskite phase purity of FAPI, as shown through structural phase analysis using GIWAXS. Increasing the amount of PEAI deposited at the surface can enhance the stability of the surface treatment. Adding a thin capping layer has been demonstrated to improve the open-circuit voltage (V_{oc}) and efficiency of FAPI solar cells. Later, we 5 mg/mL of PEAI into another type of perovskite, a mixed-cation CsFA. In this case, we also use the PEAI hydrophobic layer for surface passivation, preventing structural phase transformations and maintaining solar cell performance even after exposure to H_2O and air. The fundamental understanding of *in-situ* structural phase transformations at the bulk, coupled with insights into surface chemistry and reaction mechanisms provides a foundation for designing durable and efficient solar cell materials.

6.2 The Role of Br at Low Temperatures

Mixed-cation mixed-halide lead halide perovskites (LHP) have emerged as promising materials for solar energy conversion.²⁵ Specifically, formamidinium(FA)-rich compositions have demonstrated higher thermal stability and an optimal bandgap for single-junction solar cells.¹⁵ Compositional mixing has been employed to achieve optimal optoelectronic properties and

stability.^{16,152} However, it is crucial to unravel the structural phases across a wide range of operating temperatures, including very low temperatures relevant to space applications, to ensure the proper functioning and stability of these materials. The most common and efficient compositions include mixing cesium (Cs) and FA in the A-site, as well as iodine (I) and bromine (Br) in the X-site, resulting in (Cs,FA)Pb(I,Br)₃ LHP compositions. A knowledge gap exists on a complete phase diagram for both mixed-cation and mixed-halide compositions. In this work, we aim to construct a low-temperature phase diagram for (Cs,FA) mixed halide (I,Br) lead perovskites.

Previous studies have reported low-temperature phase diagrams for single-ion compositions such as FAPbI₃,¹⁹ CsPbI₃,²⁴¹ FAPbBr₃,³⁶ and CsPbBr₃.²⁴² Generally, perovskites exhibit a cubic (α) phase at high temperatures above a certain threshold. As the temperature decreases, the perovskite structure undergoes phase transitions from cubic to tetragonal (β) and then from tetragonal to orthorhombic (γ). Phase diagrams have also been studied for single-cation/mixed-halide or mixed-cation/single-halide compositions. For instance, Lehman et al. investigated and presented the temperature phase diagram for MAPb(I,Br)₃ compositions, highlighting the two phase transitions.²⁴³ Nasstrom et al. reported the high-temperature phase diagram for CsPb(I,Br)₃, observing different phase transitions during heating and cooling.³⁸ Other studies focused on the phase diagram for the mixed-cation (Cs,FA) iodide-based perovskite, revealing a solubility limit of the Cs:FA ratio to form a pure perovskite phase.^{32,40} The phase transitions of cubic-tetragonal-orthorhombic were reported for (Cs,FA)PbI₃ compositions.

In the case of pure Br compositions, it has been demonstrated that Cs substitution in FAPbBr₃ perovskite suppresses the orthorhombic phase transition by revealing a geometric

frustration associated with the orientations of FA molecules.²⁴⁴ The suppression of the orthorhombic phase has also been observed in mixed cation MA-dimethylammonium (DMA) lead bromide perovskites (MA,DMA)PbBr₃.^{245,246} This suppression was attributed to the greater disorder of the organic cations in the mixed samples, leading to higher symmetry and less distortion of the inorganic framework. The improved structural stability also enhanced their photodetection capabilities.²⁴⁶ Despite the knowledge from studying phase transitions in various cation and halide combinations, a complete structure phase diagram for the widely-used and highly efficient LHPs (Cs,FA)Pb(I,Br)₃ is still lacking.

Herein, we study the structure of FA-based LHP compositions Cs_yFA_{1-y}Pb(Br_xI_{1-x})₃ by a low-temperature *in-situ* synchrotron powder X-ray diffraction (XRD) at temperatures ranging from 300 K down to 23 K. The focus was on FA-rich and I-rich compositions to maintain a low bandgap suitable for single-junction solar cells. Findings reveal that as Br replaces I in the mixed-cation LHP compositions, the orthorhombic phase transition is suppressed. Additionally, the inclusion of Br eliminates secondary non-perovskite phases. We construct three halide-dependent temperature phase diagrams for different Cs concentrations, demonstrating that adding Br stabilizes the higher symmetry perovskite structure and prevents the formation of non-perovskite phases. This fundamental understanding of the structure provides a basis for designing and developing more resilient and efficient materials capable of functioning under a wide range of extreme temperature conditions. Understanding the material's structure across the entire temperature range is paramount.

6.2.1 *Properties and Structure at Room Temperature and 300 K*

To investigate the low-temperature phase transitions for different FA-based lead halide perovskite (LHP) compositions, we selected a mixed-cation and mixed-halide compositional

space by adding Cs as A-site cation and Br as X-site halide, resulting in the compositions $\text{Cs}_y\text{FA}_{1-y}\text{Pb}(\text{Br}_x\text{I}_{1-x})_3$, shown in **Figure 6.10A**. The low-temperature phase transitions for the LHP compositions were analyzed by cooling down the powders from 300 K down to 23 K. The studied compositions were selected to keep an FA-rich composition with an ideal bandgap for single-junction solar cells.^{15,19,47} The lower limit of Cs and Br was 5 % molar. The selected upper limit for Cs was 17 % molar, given that it is known that its thermodynamic limit to form a single-phase perovskite, when mixed with FA, is around 20 % molar. Some studies have shown this limit is around 20 %, ⁴⁴ while others have reported this value to be less than 15 %.^{32,40,247} Therefore, we chose 17%, targeting a single-phase perovskite formation. The upper limit chosen for Br was 17 %, keeping an I-based composition and equaling the maximum added percent of Cs. We synthesized the powders by evaporating the solvents from a precursor solution in gamma-butyrolactone (GBL) and dimethyl formamide (DMF) with a volume 2:1 between the solvents, respectively. The evaporation was carried out at 170 °C for two hours, and the powders were then ground for analysis.

To analyze the optoelectronic properties of the synthesized materials, we measured UV-VIS absorption spectroscopy (at room temperature), from which we employed the tauc-plot method to calculate the optical bandgap (**Figure CS20**).¹⁰⁰ **Figure 6.10B** shows the optical bandgap calculated for every studied composition. The lowest experimental bandgap is 1.42 eV for the pure FAPbI_3 , which is close but lower than other reported values from calculations (1.51 eV).⁶³ This confirms the ideality of the FAPbI_3 bandgap as it absorbs in the range to achieve the maximum theoretical power conversion efficiency for single-junction solar cells according to the Shockley-Queisser limit.¹¹ However, pure FAPbI_3 is unstable at room temperature in an ambient atmosphere, transforming fast into a yellow powder with a

hexagonal structure, identified here as 2H. For this reason, pure FAPbI₃ is not further analyzed in this work. The bandgap increased as Cs and Br were added to the FAPbI₃ perovskite (Figure 6.10B).

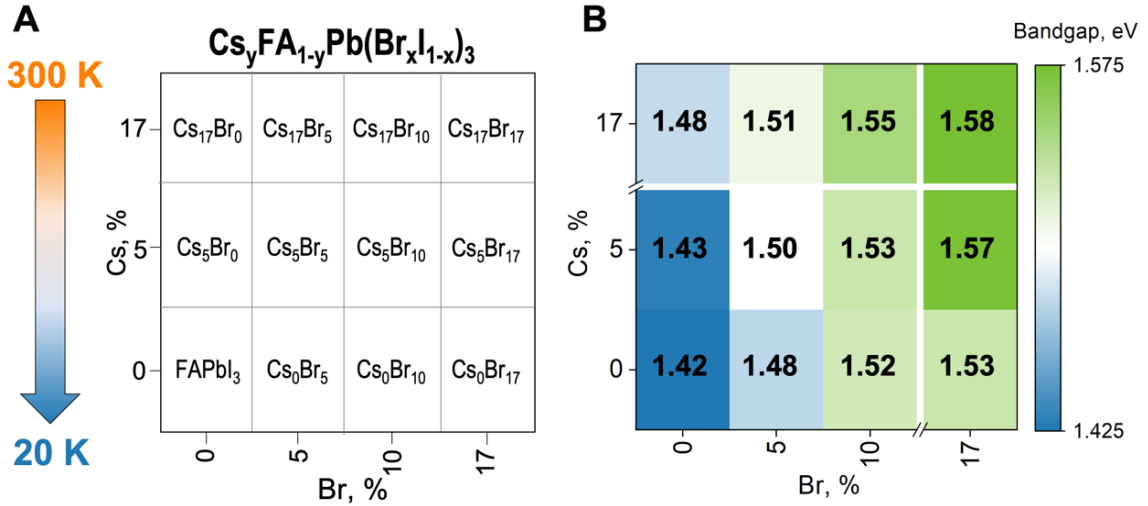


Figure 6.10 Mixed-cation and mixed-halide perovskite compositions of study. (A) Selected compositions to study the *in-situ* phase transitions from 300 K to 23 K, (B) Bandgap from UV-VIS at room temperature.

We observe that adding Br increases the bandgap further compared to the Cs addition. It has been demonstrated that the bandgap and lattice parameters of semiconducting materials correlate with the effective anion radius of the halides, in this case, Br.⁶² Whereas the A-site cation does not participate in the band edge states, it does influence the room temperature optical properties indirectly through changes to the structure of the octahedral arrangement.^{246,248} In this work, the largest bandgap of 1.58 eV is observed for the upper limit of both Cs and Br for the Cs₁₇Br₁₇ composition. We highlight that one of the main advantages of lead halide perovskites is their property tunability through compositional engineering, as we evidence here on bandgap tunability when we add Cs and Br. In this case, the range of studied compositions have a bandgap from 1.43 eV to 1.58 eV, remaining in an ideal range for high-efficiency single-junction perovskite solar cells.

To study the structure of these LHPs, we performed powder X-ray diffraction (XRD), as shown in **Figure 6.11A**. First, we analyzed in detail the structures at 300 K by Le Bail refinements (**Figure CS21-23, Table CS2**), before cooling down the powders. From this initial analysis, we identified the structural phases present in each composition, as shown in **Figure 6.11B**. The structure of the perovskite phase at 300 K corresponds to either a cubic α phase of space group $Pm\bar{3}m$ (identified as α and orange square) or to a tetragonal β phase of space group $P4/mbm$ (identified as β and a green rectangle). For compositions without Br, adding 5 % or 17 % of Cs to FAPbI₃ leads to an initial tetragonal β phase at 300 K. Adding Br to the Cs₁₇ perovskite also shows an initial β structure. Moreover, adding Br to all the other studied perovskite compositions leads to a cubic perovskite structure. The structure of pure FAPbI₃ has been reported to be cubic α at 300 K.¹⁹ Replacing the FA in the A-site by Cs tilts the octahedra, leading to a decrease in symmetry from cubic to tetragonal. However, replacing the I in by Br on the X-site maintains the cubic structure.

Beyond the perovskite structural analysis, we also identified secondary non-perovskite phases from the powder XRD patterns. Perovskite phases are defined by their corner-sharing octahedra, while non-perovskite have either face- or edge-sharing octahedra. In the case of FAPbI₃, the hexagonal structure 2H is a face-sharing octahedra structure with space group $P6_3/mmc$.²⁰ Pure CsPbI₃ shows a non-perovskite structure thermodynamically stable at 300 K, adopting an orthorhombic $Pnma$ edge-sharing structure known as δ_{Cs} .⁶⁸ Mixing FA and Cs has led to a more stable perovskite phase.^{32,40} However, the single-cation CsPbI₃ or FAPbI₃ can segregate into their non-perovskite phases. Furthermore, there are other numerous intermediate hexagonal non-perovskite phases between the corner-sharing and the pure face-sharing, known as 4H or 6H.^{20,42} These hexagonal polytypes have been shown to be present

when having mixed-halide. These polytypes have both some corner-sharing and face-sharing octahedra in their structure. Analyzing the powder XRD patterns, we observe that initially, at 300 K, some compositions have secondary phases such as hexagonal polytypes (H, hexagons in **Figure 6.11B**) and δ_{Cs} (triangles in **Figure 6.11B**). All compositions without Cs (0 %) show some type of hexagonal polytype, specifically due to their characteristic diffraction peaks between 8 and 12 ° in 2θ of the diffraction pattern (**Figure 6.11A**). Adding 5 % of Cs forms a secondary phase δ_{Cs} without any Br, hexagonal polytypes for 5 % of Br, and no secondary phases when having both Cs 5 % and Br 10 % and 17 %. Further, all Cs 17 % compositions show the presence of the δ_{Cs} non-perovskite phase (**Figure 6.11A**). In general, Cs 5 % with Br 10 % or 17 % (Cs_5Br_{10} , Cs_5Br_{17}) are cubic perovskites without any secondary phases.

From the powder XRD at 300 K and the Le Bail analysis, we plot the unit cell volume in **Figure 6.11C**. Tetragonal structures have different lattice parameters, $a = b \neq c$. In the case for the cubic structure, the lattice parameters are all equal $a = b = c$. The volume for the tetragonal structure is significantly larger, given that the value of a and b is around 8.96 Å, increasing the overall volume of the tetragonal unit cell. For the cubic unit cell volumes, we observe that the volume decreases as Cs and Br are added. This is in line with what was expected, given that a smaller size cation, Cs, is replacing the larger cation FA. In parallel, the halide I is being replaced by a smaller ion, Br. Given the replacement by both smaller-size ions, the overall cubic unit cell volume is expected to decrease.

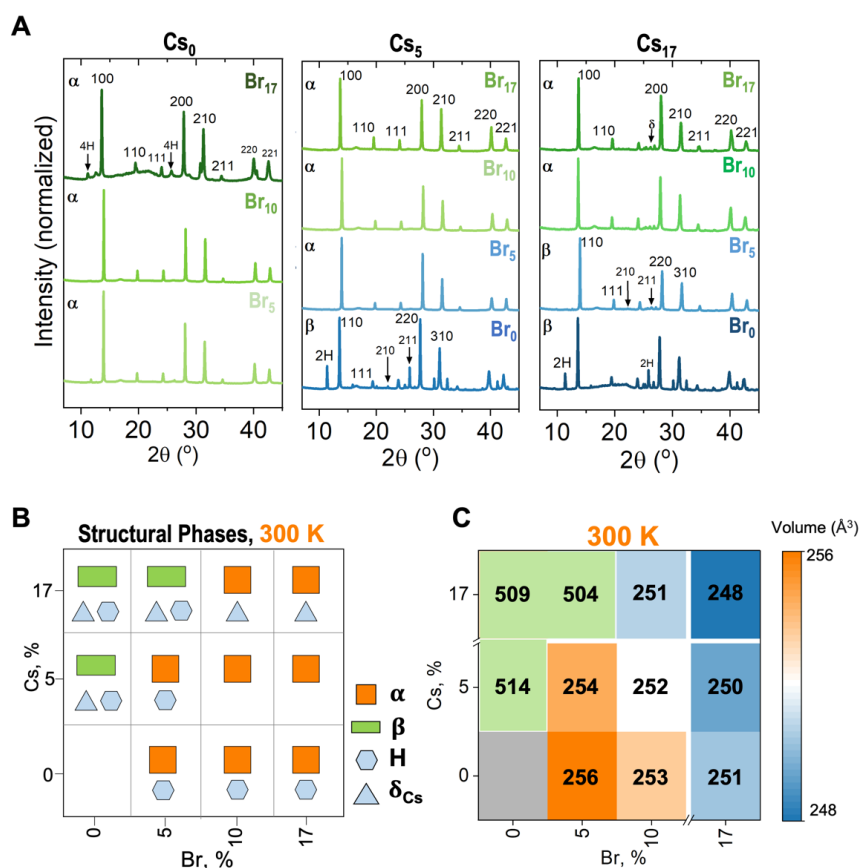


Figure 6.11 Structure from powder XRD at 300 K. (A) XRD patterns for different Cs-Br concentrations for the $(\text{Cs,FA})\text{Pb}(\text{I,Br})_3$ compositions at 300 K and vacuum, (B) Structural phases from Le Bail refinements, (C) Calculated unit cell volume for the $(\text{Cs,FA})\text{Pb}(\text{I,Br})_3$ compositions at 300 K.

6.2.2 $(\text{Cs,FA})\text{Pb}(\text{I,Br})_3$ Temperature Phase Diagram

A low-temperature phase diagram for the $(\text{Cs,FA})\text{Pb}(\text{I,Br})_3$ compositional space was created from *in-situ* powder XRD by cooling the materials from 300 K to 23 K in steps of 20 K (Figures CS24-26). From a general phase analysis, by plotting the diffraction pattern as a function of temperature (Figure CS27), we identified the phase transition temperatures as new diffraction peaks appeared. These phase transition temperatures for all compositions are shown in Table CS3. To show the overall mixed-cation and mixed-halide temperature phase diagram, we divided it into three, for three Cs molar preents, 0 %, 5 %, and 17 % (Figure 6.12). Therefore, each temperature phase diagram is shown as a function of Br molar %.

For 0 % and 5 % of Br, there are two low-temperature phase transitions, from α to β slightly above 250 K, and from β to γ around 150 K (**Figure 6.12A**). These two phase transitions have been reported for mixed-cation (Cs,FA), pure iodide,⁴⁰ for mixed-cation (MA,FA),^{249,250} and all single-cation and single-halide compositions.^{19,36,241,242} Generally, it is expected for the perovskite to decrease its symmetry as it is cooled down, evidenced by the tilting of the corner-sharing octahedra from cubic to tetragonal and from tetragonal to orthorhombic. These transitions are also foreseen since as the temperature decreases, the organic cations move slower and influence the octahedra tilting due to less movement. Moreover, when increasing the Br content to 10 % and 17 % ($\text{Cs}_0\text{Br}_{10}$, $\text{Cs}_0\text{Br}_{17}$), we observe only one phase transition from cubic α to tetragonal β in the studied range (300 K – 20 K). This represents higher stability of the tetragonal phase without the sudden transition to orthorhombic, meaning more stable tilting in the octahedra. With respect to secondary phases, without Cs incorporated into the FAPbI_3 , in all cases (Cs_0), we observe the presence of non-perovskite hexagonal phases (H), in **Figure CS28**. **Figure 6.12B** shows the temperature phase diagram for Cs 5 % molar (Cs_5Br_x). Without any added Br, Cs_5Br_0 , we observe that the phase at 300 K is β tetragonal. We observe one phase transition from β to γ at 150 K. Adding any amount of Br, from 5 % to 17 % to the Cs_5 perovskite leads to an initial cubic α phase, indicating a higher perovskite symmetry at 300 K. Cooling down these Cs_5Br_x perovskites leads to one phase transitions from α to β slightly above 250 K, similar to the Cs_0 set. However, for all Cs_5Br_x compositions, adding Br hinders the transition from β to γ , indicating better stability of the tetragonal phase and a higher perovskite symmetry at low temperatures such as 23 K. In general, when adding 5 % of Cs, no secondary phases are observed (**Figures CS28-29**).

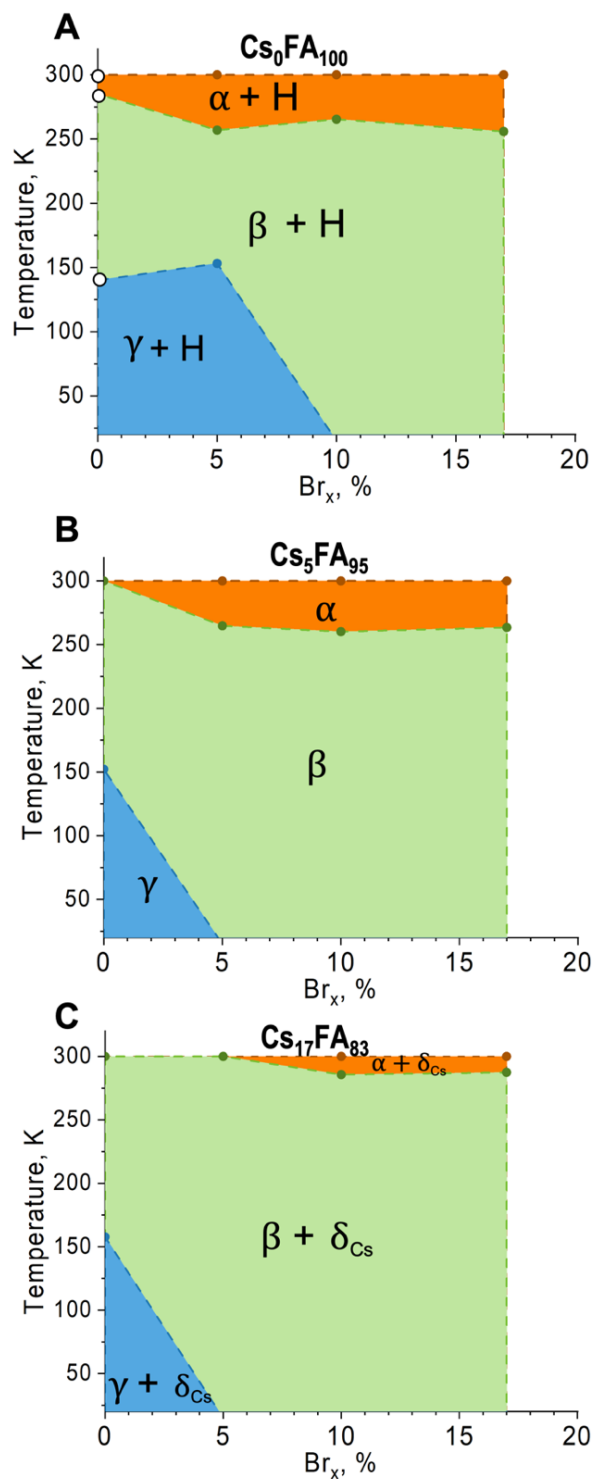


Figure 6.12 Composition – Temperature phase diagram for the $Cs_yFA_{1-y}Pb(Br_xI_{1-x})_3$ mixed-halide mixed-cation lead halide perovskites. (A) without Cs (Cs_0Br_x) as a function of Br_x , (B) Cs 5% (Cs_5Br_x) as a function of Br_x , (C) Cs 17% ($Cs_{17}Br_x$) as a function of Br_x .

Figure 6.12C shows the temperature phase diagram for the case of Cs 17 % ($\text{Cs}_{17}\text{Br}_x$). Analogous to Cs 5 %, without Br ($\text{Cs}_{17}\text{Br}_0$), the mixed-cation perovskite adopts a tetragonal structure at 300 K. This composition shows a phase transition from β to γ at around 150 K. At 300 K, adding Br 5 % ($\text{Cs}_{17}\text{Br}_5$) retains the tetragonal structure of the perovskite. Remarkably, this composition shows no phase transitions in the studied range from 300 K to 23 K; the β perovskite is stable down to very low temperatures. Adding Br 10 % and Br 17 % ($\text{Cs}_{17}\text{Br}_{10}$, $\text{Cs}_{17}\text{Br}_{17}$) leads to an initial cubic α perovskite that will then transition to a tetragonal β at around 270 K. This transition temperature is around 30 K higher than the transition from α to β for lower or no Cs content (Cs 5 %, Cs 0 %).

Equivalent to having Cs 5 %, for Cs 17 %, we observe that adding Br suppresses the phase transition from β to γ all the way to 23 K. Therefore, adding Br improves the stability and symmetry of the perovskite structure at very low temperatures. Regarding the secondary phases, all compositions with Cs 17 % show a minor peak corresponding to the non-perovskite orthorhombic phase of CsPbI_3 , δ_{Cs} (**Figure CS29**). It is known that this non-perovskite is photoinactive and unwanted for solar cell applications.¹⁶

6.2.3 Br addition Improves Stability at Low Temperatures

We evaluated the low-temperature phase transitions for a mixed cation (Cs,FA) and mixed-halide (I,Br) perovskite, as shown in **Figure 6.10A**. In **Figure 6.12**, we presented the three-phase diagrams to compare different ratios of mixed-cation and mixed-halide. These phase diagrams reveal that the addition of Br to mixed-cation (Cs,FA) compositions stabilizes the perovskite β phase over a wide temperature range, from approximately 260 K down to 23 K. This stabilization prevents significant structural changes, symmetry variations, and octahedral

that occur in the γ phase.²⁵¹ **Figure 6.13** illustrates two compositions, Cs_5Br_0 (**Figure 6.13A**) without Br and $\text{Cs}_5\text{Br}_{17}$ (**Figure 6.13B**) with 17 % Br. The complete set of temperature-dependent diffraction patterns can be found in **Figures CS24-26**. In **Figure 6.13A**, the perovskite phase starts as β at 300 K, with characteristic peaks around 22° and 26.5° corresponding to the 210 and 211 Bragg peaks. For Cs_5Br_0 , a new peak appears around 23.2° at 167 K, indicating the presence of a γ phase. In contrast, **Figure 6.13B** shows that when adding 17 % of Br, the perovskite initially adopts a cubic α structure. As the temperature is lowered, β peaks appear at ~ 267 K, and no γ -peak is observed down to 23 K. Furthermore, $\text{Cs}_5\text{Br}_{17}$ does not exhibit any diffraction peaks attributed to secondary phases, maintaining a pure perovskite structure from 300 to 23 K.

The observed phase transitions and structural behavior in mixed-cation mixed-halide perovskites differ from those reported in single-cation or single-halide systems. Adding Br to single-cation iodide compositions, such as $\text{MAPb}(\text{I},\text{Br})_3$ ²⁴³ or $\text{CsPb}(\text{I},\text{Br})_3$,³⁸ has resulted in a transition from β to γ phase. Similarly, in mixed-cation and single-halide systems, such as $(\text{Cs},\text{FA})\text{PbI}_3$, the transition to γ phase has been reported in the range of miscibility.¹⁹ Remarkably, in $(\text{Cs},\text{FA})\text{PbBr}_3$, Cs substitution has been shown to suppress phase transitions at lower temperatures.²⁴⁴ Motzur et al. attributed this phase stability to local compressive strain caused by Cs substitution, overriding the orientation driven by the organic–organic interactions and disrupting changes in low-temperature phase transitions. They highlighted the sensitivity of organic–organic interactions in FAPbBr_3 , explaining the advantages of Cs incorporation in halide perovskites. Other studies have also reported the suppression of phase transition by incorporating Cs in MAPbBr_3 , attributed to compressive chemical pressure.²⁵¹ Similarly, Ray et al. suppressed the orthorhombic phase of MAPbBr_3 by adding DMA and

forming a mixed-cation (MA,DMA)PbBr₃ perovskite.²⁴⁶ This suppression was attributed to increased disorder of organic cations and a less distorted inorganic framework.²⁵² Building upon this understanding, we suggest that the addition of Cs and Br to the FAPbI₃ perovskite, forming a (Cs,FA)Pb(I,Br)₃ framework compresses the structure, as evidenced by smaller lattice parameters, affecting the interactions between organic cations and increasing disorder.

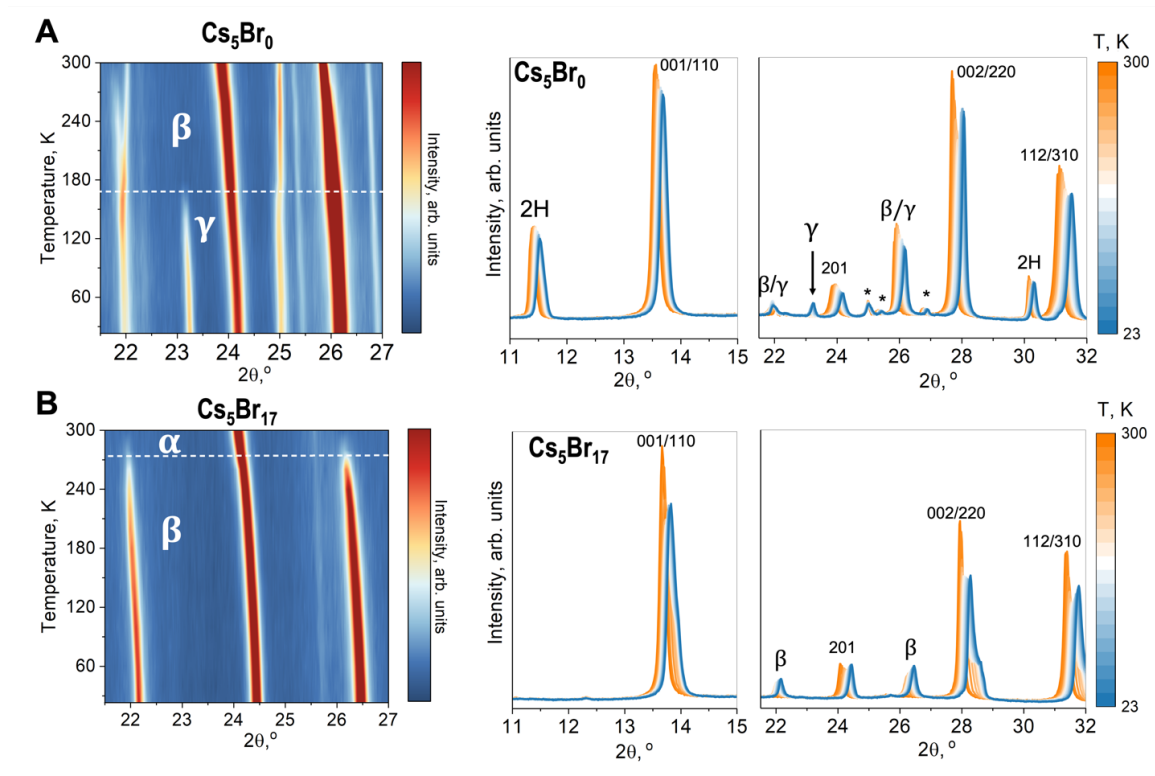


Figure 6.13 The effect of adding Br into the (Cs,FA)PbI₃ lead halide perovskites by *in-situ* X-ray diffraction in a Cs 5% composition. (left) Temperature versus diffraction plot from 21.5–27°, and (right) one-dimensional diffraction patterns in two ranges of 2θ, from 11–15° and 21.5–32°. (A) Cs 5%, and no Br (0%), (B) Cs 5% adding Br 17%.

6.2.4 Conclusions

In conclusion, this work investigates the temperature-dependent phase transitions for a mixed-cation and mixed-halide perovskites. We measured *in-situ* powder XRD to create temperature phase diagrams for different concentrations of Cs and Br in (Cs,FA)Pb(I,Br)₃ perovskites. By

replacing I with Br, we found that the transition from a tetragonal to orthorhombic phase at low temperatures (below 150 K) was suppressed, resulting in a more symmetrical perovskite structure with potential applications at low-temperature settings. When Cs was not present, we observed the formation of non-perovskite hexagonal phases. However, the addition of Cs and Br prevented the formation of the hexagonal structures. It is important to note that the inclusion of 17 % Cs resulted in the formation of the secondary non-perovskite orthorhombic δ -CsPbI₃ phase. From these findings, it can be concluded that adding Br enhances the stability of the perovskite over a wider temperature range, which is advantageous for low-temperature applications. Although the introduction of Br increases the bandgap of the perovskite, which reduces the number of absorbed photons, the overall structure becomes more robust and contributes to long-term stability. To gain a complete understanding of how the crystal structure behaves across the entire temperature range, further investigations focusing on the fundamental structural aspects are essential.

CHAPTER 7. CONCLUSIONS AND OUTLOOK

The overarching goal of this dissertation is to address the instability challenges of lead halide perovskites (LHPs) by understanding the effects of structural changes on properties of halide perovskites and their performance in solar cells. X-ray synchrotron-based characterization techniques were used to study structure-property relationships of LHPs. Specifically, the effects of internal and external factors on the structural properties of formamidinium (FA)-based LHPs compositions were explored. This dissertation provides a new understanding of the factors and mechanisms that dominate the structure and properties of LHPs and provides a basis for the future design of materials with optimal properties.

7.1 Insights and Opportunities: Crystallization and Facet Properties

Chapter 4 investigated crystallographic orientation in lead bromide perovskites. It was shown that the solvent of the precursor solution and organic A-site cation strongly affect the preferred orientation of the deposited perovskite thin films. The solvent DMSO influenced the early stages of crystallization and induced preferred orientation in the deposited films by preventing colloidal particle interactions. The methylammonium A-site cation induced a higher degree of preferred orientation than the formamidinium counterpart. Density functional theory calculations showed that the facet surface energies had an effect in determining the preferred orientation. The lower surface energy of the (100) plane facets in methylammonium-based perovskites, compared to the (110) planes, was the reason for a higher degree of preferred orientation. In contrast, in formamidinium-based compositions, the surface energy of the (100) and (110) facets were similar, leading to a lower degree of preferred orientation. Further, **Chapter 4** showed how differences in polycrystalline

orientation influenced charge transport properties in perovskite solar cells, where a high degree of preferred orientation is beneficial.

This chapter has revealed that solvent-precursor interactions are key in determining the final perovskite microstructure. Such interactions have been underexplored, and there are still unanswered questions regarding the overall crystallization process of polycrystalline LHP thin films. In particular, the solution needs to be characterized in-depth, giving more importance to the nucleation and growth processes that dominate the film formation. Future work should focus on a more in-depth understanding of the precursor solution chemistry and the colloidal formation, nature, structure, and influence on the nucleation of these films (I, **Figure 7.1**). Perovskite colloids are important in forming polycrystalline thin films and in forming nano crystals and quantum dots, which have shown great potential in LHP solar cells and other light-emitting applications.

Additionally, this dissertation identified differences in surface energy for different facets depending on LHP composition. The surface energies led to differences in crystallographic orientation along a specific direction. These results highlight the importance of LHP facet properties and the need for facet engineering to optimize the material's properties. Future work should cover understanding and optimizing the synthesis to control facets in LHP (II, **Figure 7.1**), broadening their applications. Facet importance has been recently identified as a field of work in the in-depth understanding and control of LHPs.²⁵³ A recent *Science* publication highlighted the facet role in the degradation of FAPbI₃, showing that the (111) plane is more robust to degradation.¹⁸

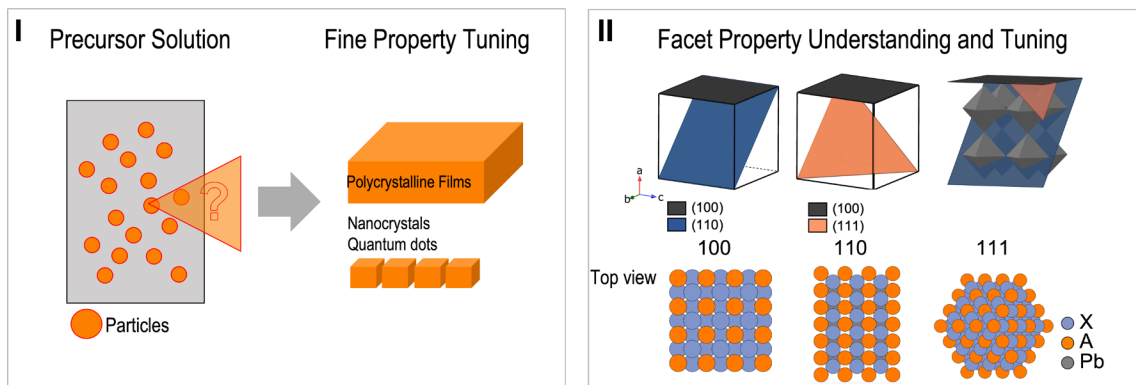


Figure 7.1 Future work for in-depth and further understanding of: (I) The early stages of crystallization to control the structure and properties of polycrystalline films, nanocrystals, and or quantum dots of LHPs, and (II) the LHP facet properties and synthesis optimization for optimal design.

7.2 Insights and Opportunities: Perovskites and Non-Perovskites

Chapter 5 studied the mechanisms that trigger the $\text{Cs}_{0.17}\text{FA}_{0.83}\text{PbI}_3$ (CsFA) perovskite instability when exposed to humidity (water, H_2O) and air (oxygen). The CsFA perovskite has shown remarkable progress in photovoltaic applications with high power conversion efficiencies. However, to achieve large-scale deployment of this technology, efficiencies must be complemented by long-term durability. The latter is limited by external factors, such as exposure to humidity and air, which lead to the rapid degradation of the perovskite phase and devices. **Chapter 5** studied the mechanisms causing the CsFA perovskite phase degradation under water and oxygen exposure through *in-situ* X-ray scattering, X-ray photoelectron spectroscopy, and first-principles calculations. A phase transformation pathway was unraveled, triggered by a surface reaction pathway involving the dissolution of FAI by water, and iodide oxidation by oxygen, driving the Cs:FA ratio into thermodynamically unstable regions, leading to undesired phase transformations. It was found that the synergy of water and oxygen is key to initializing the undesired and irreversible degradation in these FA-based lead iodide perovskites. This challenges the common perception from the halide perovskite

community that humidity (water molecules) is the culprit for the degradation of these high-performance materials. Understanding the mechanisms that lead to perovskite instability is the first step to designing a more robust and efficient material. For example, future work in the field should continue to investigate different methods of encapsulation, not only hydrophobic but also oxygen-blocking barriers.

On the other hand, this dissertation showed the mechanisms of phase transformation of FA-based structures from perovskite into non-perovskite phases, which is undesired for solar cell applications. It is widely known that the hexagonal FAPbI_3 , non-perovskite, is a degradation product from the perovskite phase. However, the properties of this hexagonal phase have yet to be widely studied. From the results of this dissertation (Appendix B), the absorption spectra of hexagonal FAPbI_3 showed an exciton peak (**Figure 7.2**). The non-perovskite material has distinct optical properties from the perovskite phase, which could be exploited in new application spaces. There is an opportunity to investigate further the synthesis, structural control, and properties of the hexagonal FAPbI_3 (**Figure 7.2**).

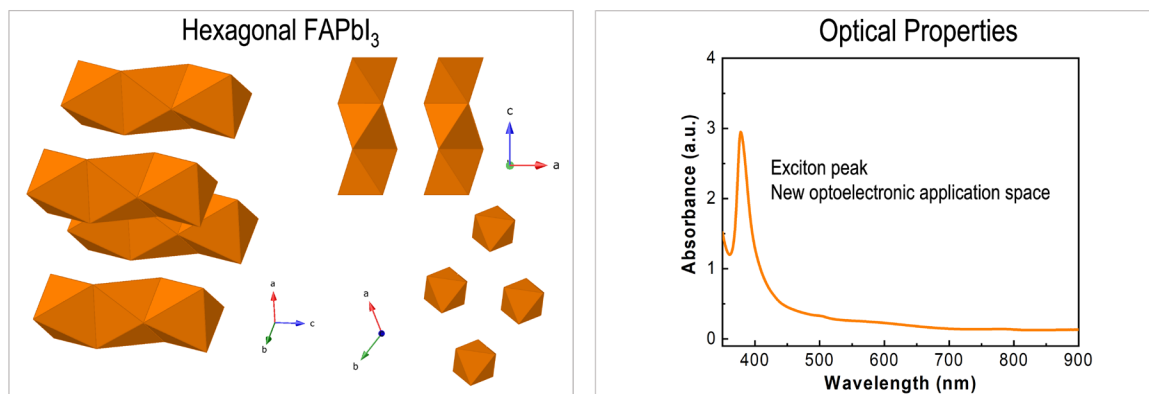


Figure 7.2 The non-perovskite hexagonal FAPbI_3 structure and opportunity to investigate its structural, optical, and electronic properties further, into a new application space.

7.3 Insights and Opportunities: Strategies to Stabilize the Perovskite

As a continuation of **Chapter 5**, **Chapter 6.1** investigated the effect of using a hydrophobic molecule, phenethylammonium iodide (PEAI), as a surface treatment to stabilize FA-based perovskites. Through grazing-incidence wide-angle X-ray Scattering, the surface and bulk structure were examined, observing that films without surface treatments predominantly consisted of hexagonal FAPbI₃ phases. Adding 5 mg/mL of PEA I hindered the undesired structural phase transformations from perovskites into non-perovskites. Thus, PEA I led to a more stable material, regardless of exposure to oxygen or water molecules. Preventing undesired phase transformations through PEA I surface treatments improved power conversion efficiency in perovskite solar cells. These enhanced efficiencies were also linked to increased charge carrier mobility and lifetimes.

Addressing the need for stabilizing the perovskite phase in LHPs to achieve long-term stability and performance is a critical area of research. Therefore, it is important to explore and understand additional stabilization strategies. **Chapter 6.2** investigated the insights into phase stabilization by incorporating Br into FA-base lead iodide perovskites. Preliminary results (not presented in this dissertation) show that adding Br into the FA-based lead iodide perovskites stabilizes the perovskite when exposed to humidity and air (*in-situ* humidity GIWAXS on **Figure 7.3**). **Figure 7.3** shows that adding Br into the CsFA perovskite (i.e., Cs_{0.17}FA_{0.83}Pb(I_{0.83}Br_{0.17})₃) or surface treatment with a Br-based cation such as octyl ammonium bromide (OABr), prevent the undesired phase transformations when exposed to humidity and air. However, the underlying mechanisms and role of Br on phase stabilization are still under explored. Therefore, future work in the structure-property relationships of LHPs should focus on understanding the role of Br, which will contribute to further optimization efforts.

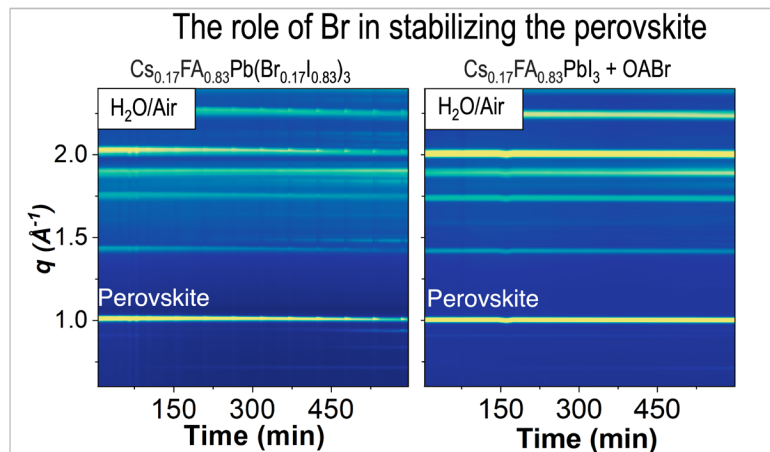


Figure 7.3 Adding Br to the CsFA perovskite has shown to stabilize the perovskite phase when exposed to H₂O/Air. Future work should focus in understanding the role of Br in stabilizing the perovskite phase.

7.4 Insights and Opportunities in Advanced Characterization

There are still challenges in the field of lead halide perovskites that need to be addressed to improve their stability and enable their commercialization. Understanding the relationship between structure, properties, and performance of LHPs is crucial. Recent advances in materials characterizations have provided insights into the atomic-, nano-, and micro-scales of these materials, as presented in this dissertation.

This dissertation employed various advanced characterization methods, including *high-throughput, in-situ* (i.e., grazing-incidence wide-angle X-ray scattering), and *operando* (i.e., X-ray beam-induced current) techniques. **Figure 7.4** summarizes the experimental methods used in this dissertation to understand the chemistry-structure-property relationships enabling optimal device performance. Combined with theoretical calculations, these experimental methods were used to unravel the chemical and structural mechanisms occurring at both the bulk and surface of LHPs. However, future research is needed, and more *in-situ* and *operando* techniques are necessary to understand and correlate the structure and performance of LHPs fully.

Operando measurements are essential as they allow for continuous observations of the material while it is exposed to stressors, as in real-life operations, providing insights into the dynamic changes that occur and their impact on performance. This dynamic perspective may reveal different correlations compared to static equilibrium measurements.

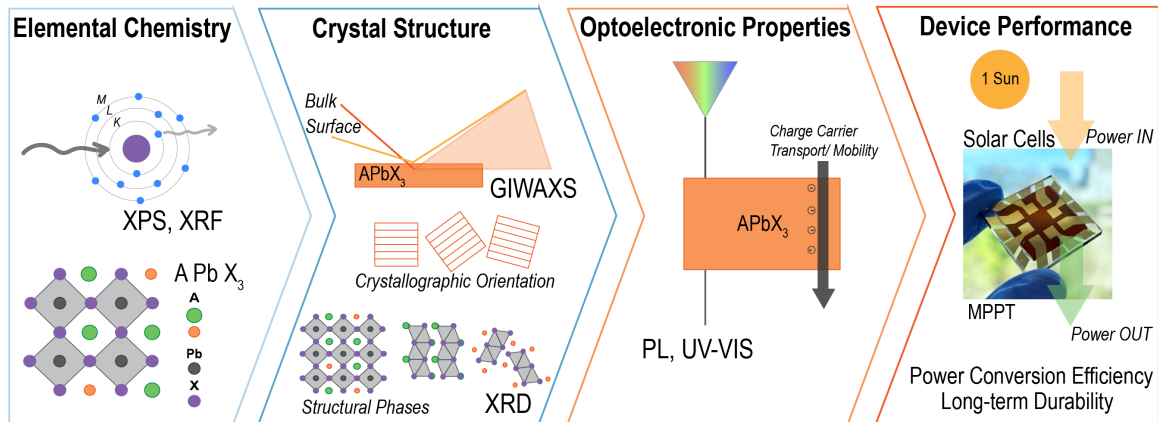


Figure 7.4 Summary schematic of the experimental methods used in this dissertation to understand the chemistry–structure–property–performance relationships in LHPs for solar cells.

The understanding gained from studying LHPs in this dissertation can also be extended to other energy materials beyond perovskites. Energy materials often exhibit structural phase variations and surface effects that significantly influence their properties and performance. Therefore, the approach and characterization methods used in this dissertation can be extrapolated to investigate structure-property-performance relationships in other energy material systems. This broader understanding of energy materials will contribute to developing new energy conversion systems and aid in addressing the global energy crisis.

APPENDIX A. SUPPORTING INFORMATION:

CRYSTALLOGRAPHIC ORIENTATION

A.1 Solvent and A-site Cation Role

A.1.1 Theoretical Calculations Methods

The DFT calculations were done completely by Dariia Yehorova and Professor Joshua S. Kretchmer from the School of Chemistry and Biochemistry at the Georgia Institute of Technology.

The surface energies, γ , of FAPbBr₃ and MAPbBr₃ with different surface orientations were calculated using the following definition:

$$\gamma = \frac{(E_{slab} - NE_{bulk})}{2A} \text{ [AS. 1]}$$

where E_{slab} is the total energy the slab, E_{bulk} is the energy of a unit cell in the bulk of the film, N is the number of formula units within the slab, and A is the area of the surface. A slab is given by a finite number of layers of the material system that are fully periodic in x and y , and isolated from a periodic image in the z direction by a vacuum gap. E_{slab} and E_{bulk} were computed with periodic DFT using Quantum Espresso.^{254,255} Pseudopotentials were given by the projector-augmented wave (PAW) method and used with the Perdew–Burke–Ernzerhof functional in the generalized gradient approximation. The kinetic energy cutoff for the wavefunction was set to 80 Ry, and a corresponding energy cutoff for the charge density was set to 800 Ry. A Monkhorst–Pack k -point grids of $4 \times 4 \times 4$ and $4 \times 4 \times 1$ were chosen for the Brillouin zone sampling of the bulk and the slab calculations, respectively. The super-cell

for the bulk calculation consisted of a single unit cell. Variable cell optimization was performed on each bulk unit cell prior to the surface construction. Each super-cell for the surface calculations was constructed with a 30 Å thick slab and 15 Å vacuum gap. A geometry optimization with a fixed cell volume and shape was performed for each slab. All slabs were constructed with a complete number of perovskite formula units, resulting in two different terminations for the bottom and top surfaces. The surface energy for each termination was computed by freezing one of the surfaces in accordance with the procedure described previously.²⁵⁶ One surface layer of the inorganic substructure composed of 1 Pb and 3 Br atoms was frozen in each slab, while the nuclei of the opposing surface was allowed to relax freely. All cations were set to rotate freely to account for the presence of the variety of cation orientations in the structure and its mobile nature. Due to the asymmetry introduced by the cation structure to the unit cell, cation orientation relative to the inorganic lattice and the surface was shown to break the degeneracy within a single family of planes.²⁵⁶ In this study, we use the lowest energy surfaces as representative structures of the {100} and {110} families of planes. The chosen cation orientations also agree with the structures reported in the literature.^{256,257}

A.1.2 Early Stages of Crystallization

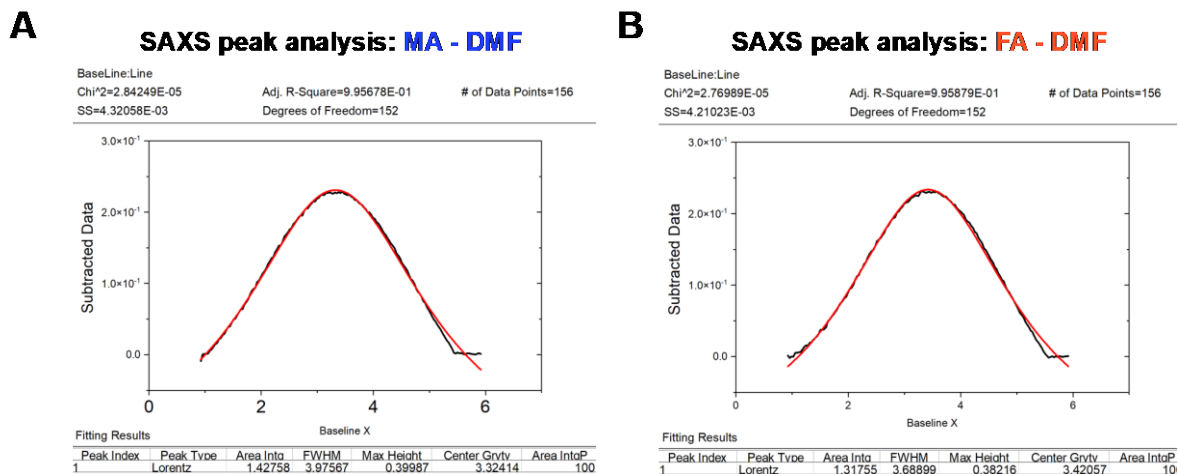


Figure AS1. SAXS peak fitting for A) MAPbBr₃ and B) FAPbBr₃ in DMF (Lorentz function). The Integrated area, FWHM, maximum height, and center of the peak (Center Grvty) are shown.

A.1.3 Structural Analysis

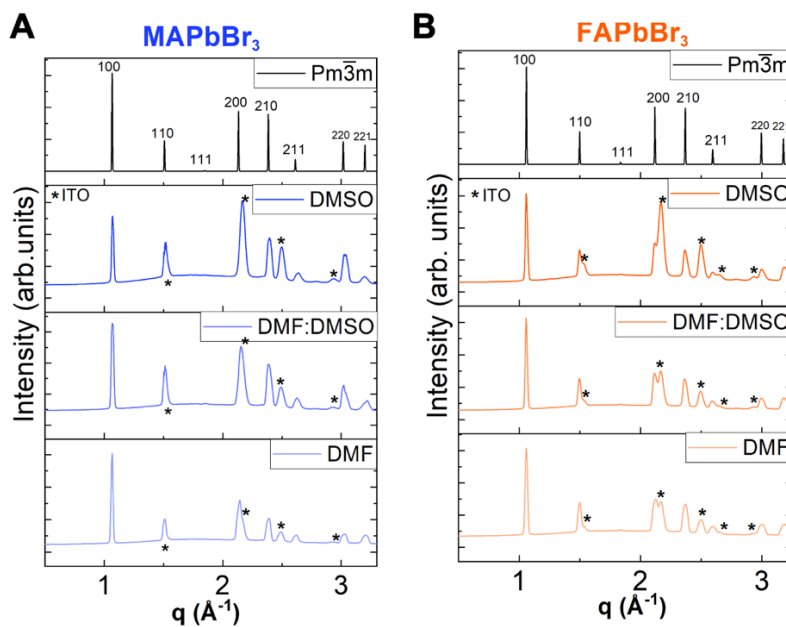


Figure AS2. GIWAXS integrated circular average diffraction patterns for A) MAPbBr₃ and B) FAPbBr₃ deposited from different solvents (DMF, DMF:DMSO 4:1 v/v, DMSO). The perovskite was deposited on glass/ITO substrates, and the * indicates the ITO diffraction peaks.

Note: Figure AS2 shows the 1D GIWAXS diffraction patterns. The ITO substrate plays an important role since the main ITO diffraction peaks overlap with the 110 and 200 peaks of

MAPbBr₃ and FAPbBr₃. It is important to know that there is no peak split but an overlap of the main ITO peak with the perovskite, and similar happens with other ITO peaks.

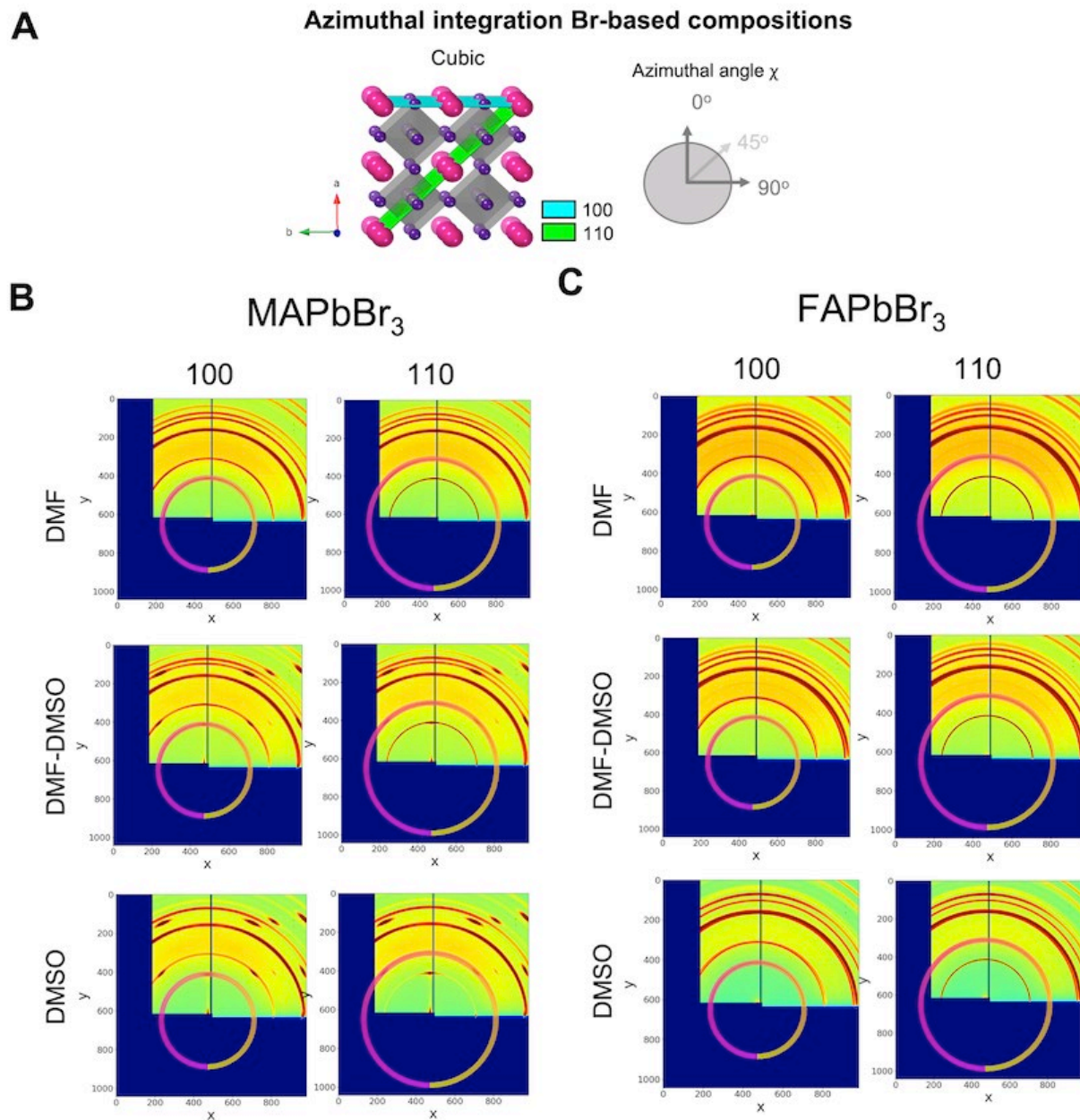


Figure AS3. GIWAXS azimuthal ring that is integrated into the azimuthal profiles in Figure 2 of the main text. A) shows the crystal structure, planes, and reference on the azimuthal profile angles. The azimuthal integration is done to the 100 and 110 Debye-Scherrer rings for B) MAPbBr₃ and C) FAPbBr₃.

Table AS1. Azimuthal integration peak fitting parameters.

100 Azimuthal Peak				
MA				
<i>Solvent</i>	FWHM	error	Height	R ² fit
DMF	21.8	0.223	3473	0.974
DMF:DMSO 4:1	4.61	0.043	9353	0.989
DMSO	4.6	0.015	11032	9.998
FA				
<i>Solvent</i>	FWHM	error	Height	R ² fit
DMF	22.54	4.55	170	N/A
DMF:DMSO 4:1	29.16	0.78	831	0.777
DMSO	25.65	0.83	678	0.863

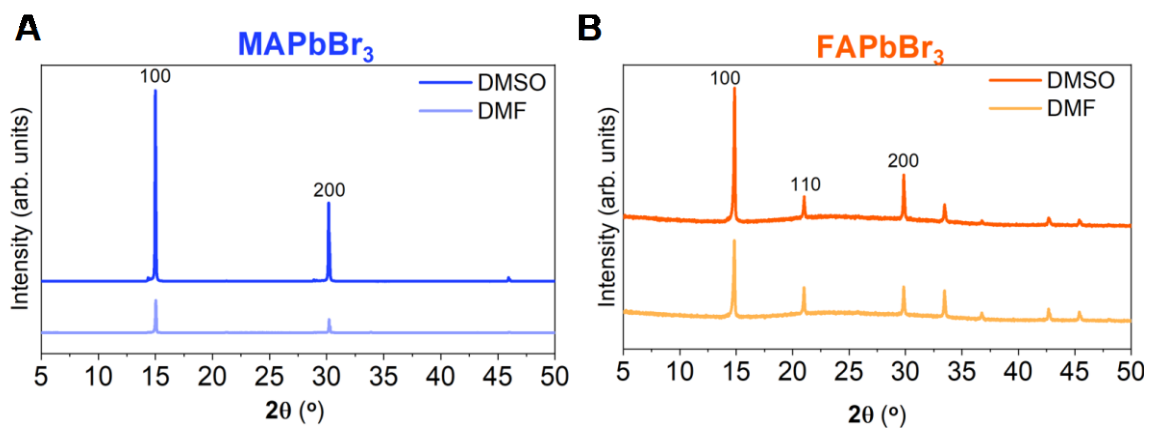


Figure AS4. XRD of the deposited thin films in glass, in DMF and DMSO for A) MAPbBr₃ B) FAPbBr₃

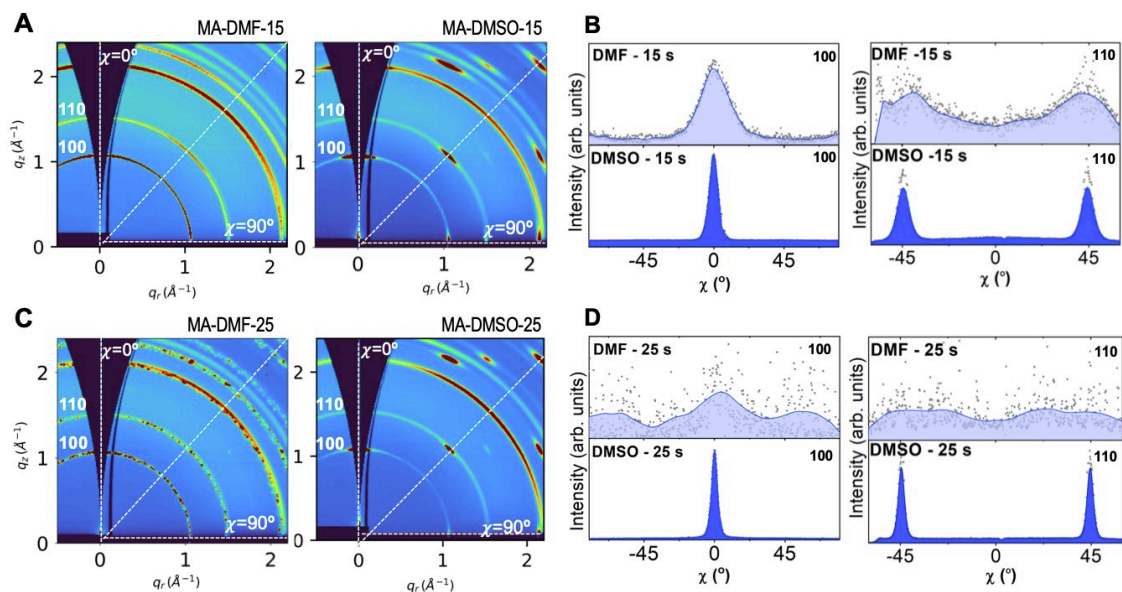


Figure AS5. MAPbBr₃ perovskite by adding chlorobenzene (CB) at different times in the spin-coating process. A) 15 s for DMF and DMSO, B) Azimuthal integration profiles of the main Debye-Scherrer rings (100) and (110) as a function of χ angle from GIWAXS for DMF or DMSO. C) 25 s form DMF and DMSO, D) Azimuthal integration profiles of the main Debye-Scherrer rings (100) and (110) as a function of χ angle from GIWAXS for DMF or DMSO.

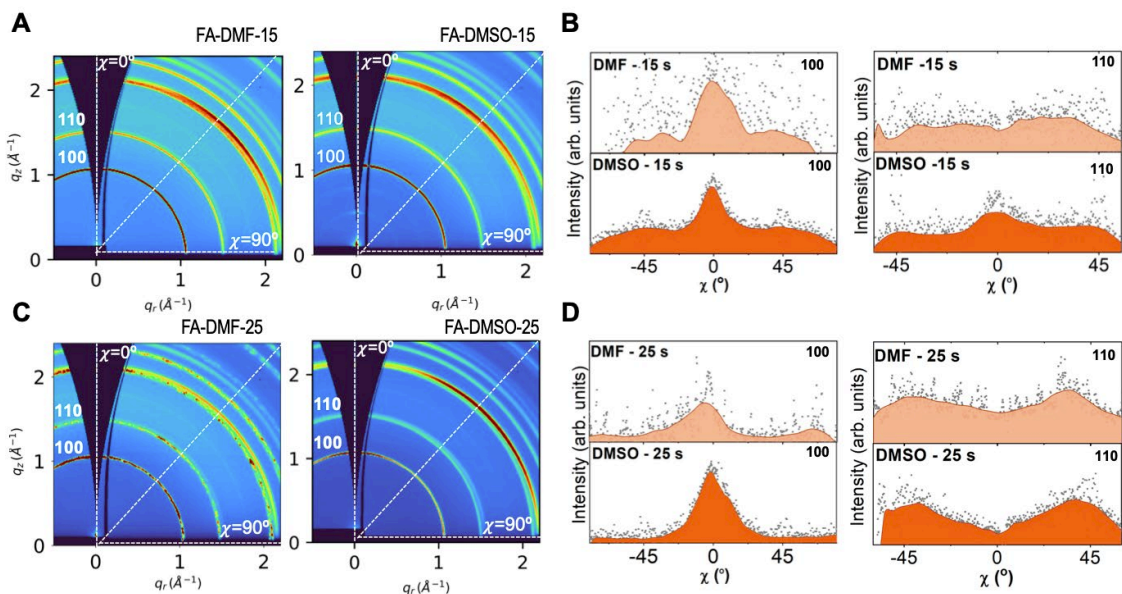


Figure AS6. FAPbBr₃ perovskite by adding chlorobenzene (CB) at different times in the spin-coating process. A) 15 s for DMF and DMSO, B) Azimuthal integration profiles of the main Debye-Scherrer rings (100) and (110) as a function of χ angle from GIWAXS for DMF or DMSO. C) 25 s form DMF and DMSO, D) Azimuthal integration profiles of the main Debye-Scherrer rings (100) and (110) as a function of χ angle from GIWAXS for DMF or DMSO.

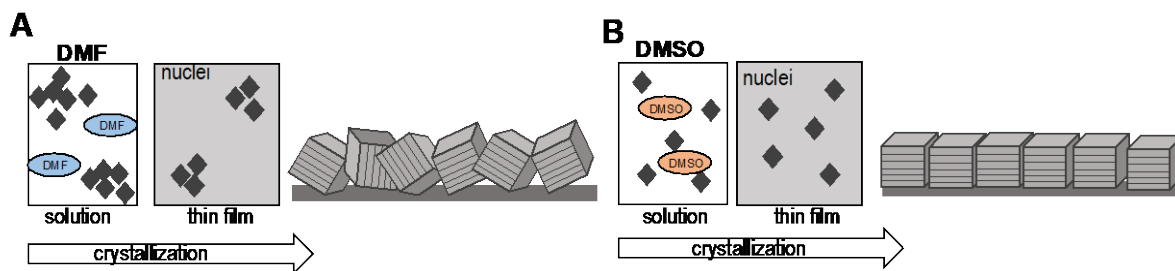


Figure AS7. Schematics on the crystallographic orientation by different solvents. A) DMF leads to random orientation, while B) DMSO leads to a high degree of orientation.

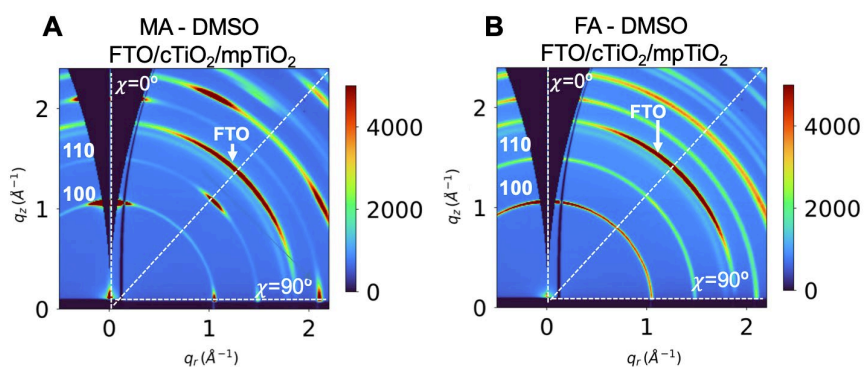


Figure AS8. Substrate effect on crystallographic orientation, films deposited on FTO/ compact TiO₂ (cTiO₂)/ mesoporous TiO₂ (mpTiO₂) layer for A) MAPbBr₃ in DMSO, B) FAPbBr₃ in DMSO.

A.1.4 Perovskite Solar Cells

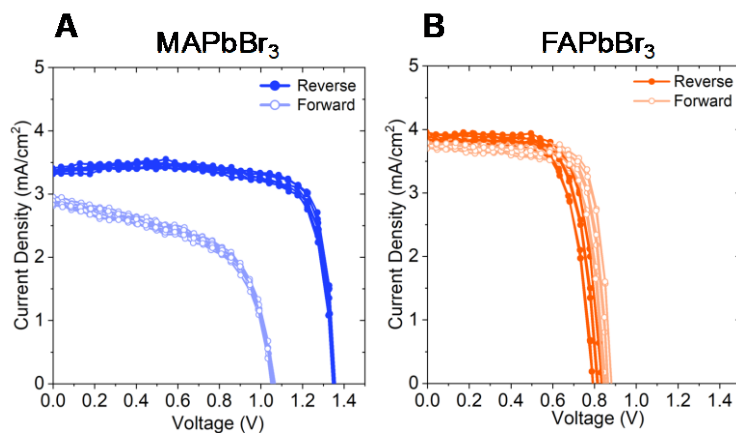


Figure AS9. Representative current J-V curves for 7 devices of A) MAPbBr₃ and B) FAPbBr₃

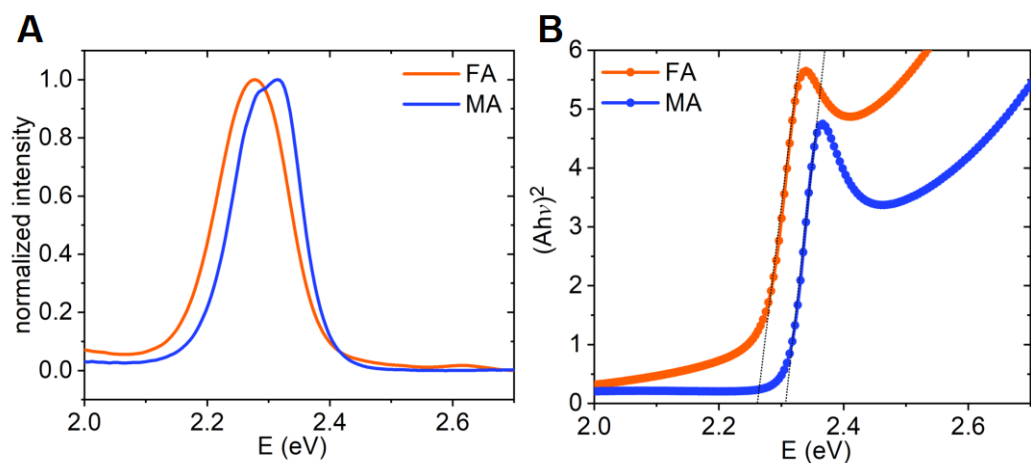


Figure AS10. Optical properties of the lead bromide thin films deposited on glass, MA is MAPbBr₃ and FA is FAPbBr₃. A) Photoluminescence spectra, and B) Absorption spectra from UV-VIS spectroscopy.

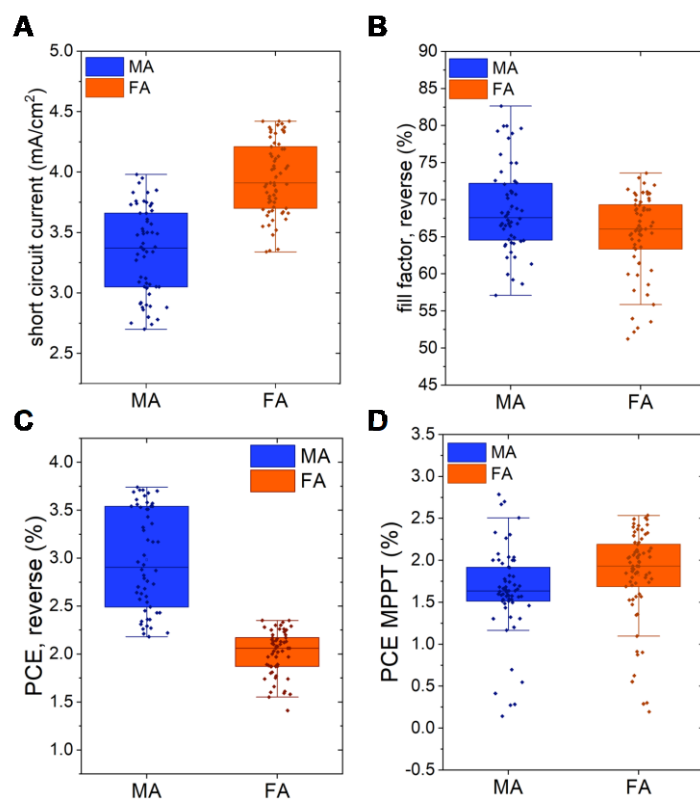


Figure AS11. Lead bromide perovskite solar cell parameters MA: MAPbBr₃ and FA: FAPbBr₃. A) Short circuit current, from reverse scan. B) Fill factor, from reverse scan. C) Power conversion efficiency, from reverse scan, D) stabilized power conversion efficiency from the maximum power point tracking.

A.1.5 Impedance Spectroscopy

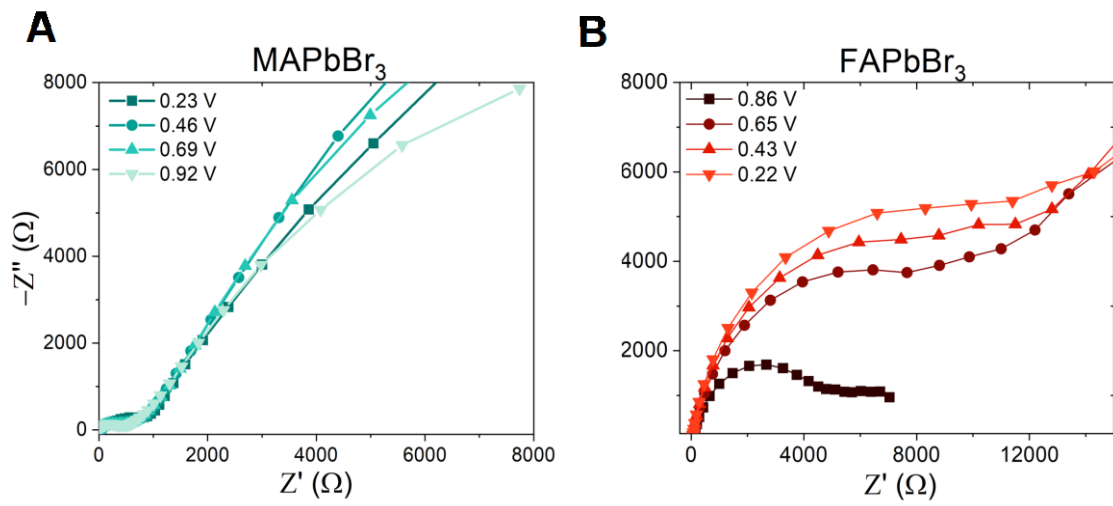


Figure AS12. Impedance Nyquist plots for the perovskites A) MAPbBr₃ and B) FAPbBr₃.

A.2 Crystallographic Reorientation

A.2.1 Surface Chemistry by XPS

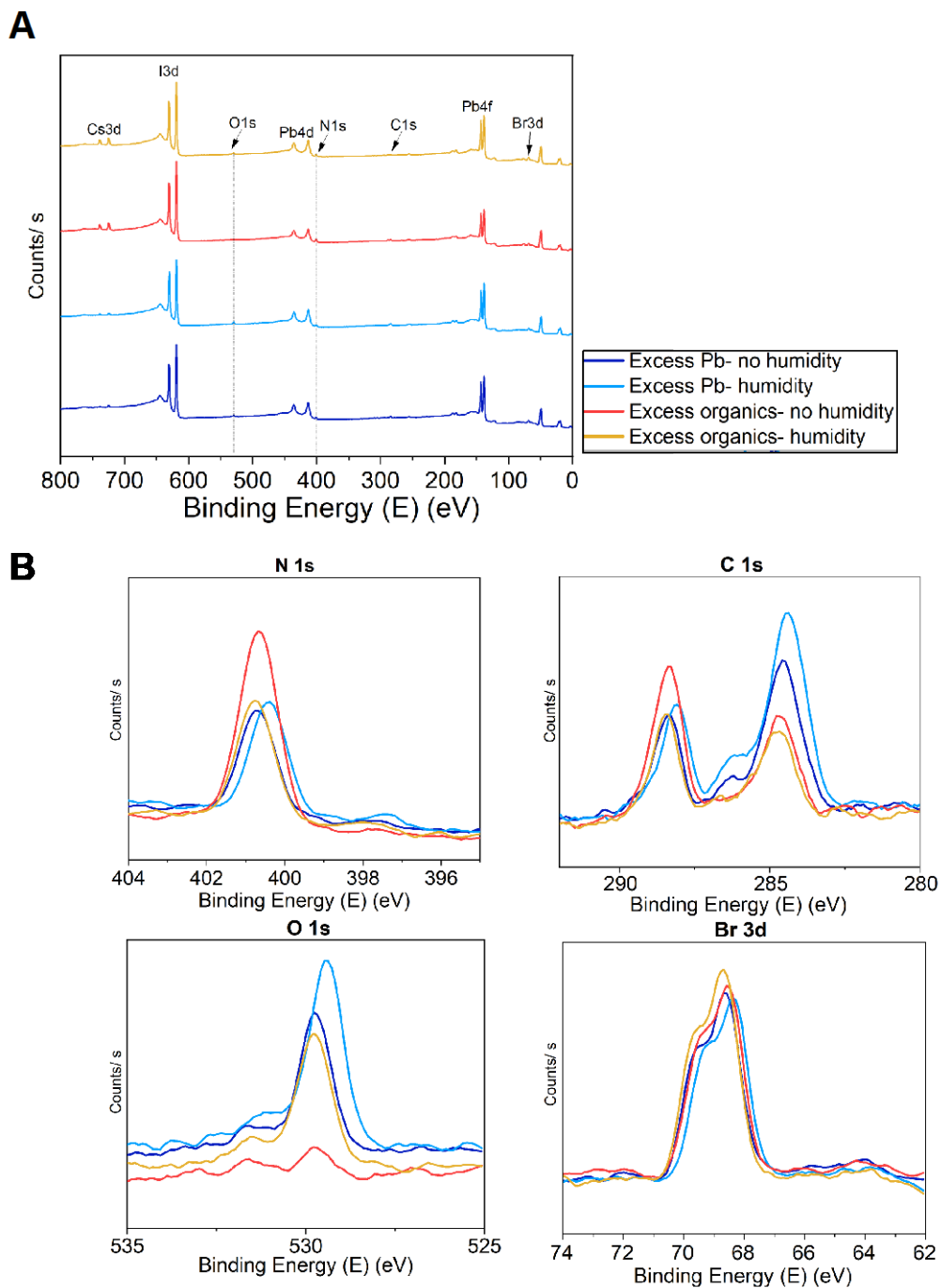


Figure AS13. XPS A) overview spectra and B) zoom into the N 1s, C 1s, O 1s, and Br 3d peaks.

Table AS2. Analyzed peaks from XPS: atomic percentage in sample for element to Pb ratio (Z:Pb)

Z: Pb	Excess Pb- no humidity	Excess Pb- humidity	Excess organics- no humidity	Excess organics- humidity
I 3d	2.14	1.93	2.91	2.18
Br 3d	0.44	0.44	0.59	0.55
C 1s	0.87	1.01	1.15	0.71
N 1s	0.59	0.64	1.3	0.71
O 1s	0.32	0.46	0.17	0.38
Cs 3d	0.06	0.06	0.26	0.2

A.2.2 Structure Analysis by XRD

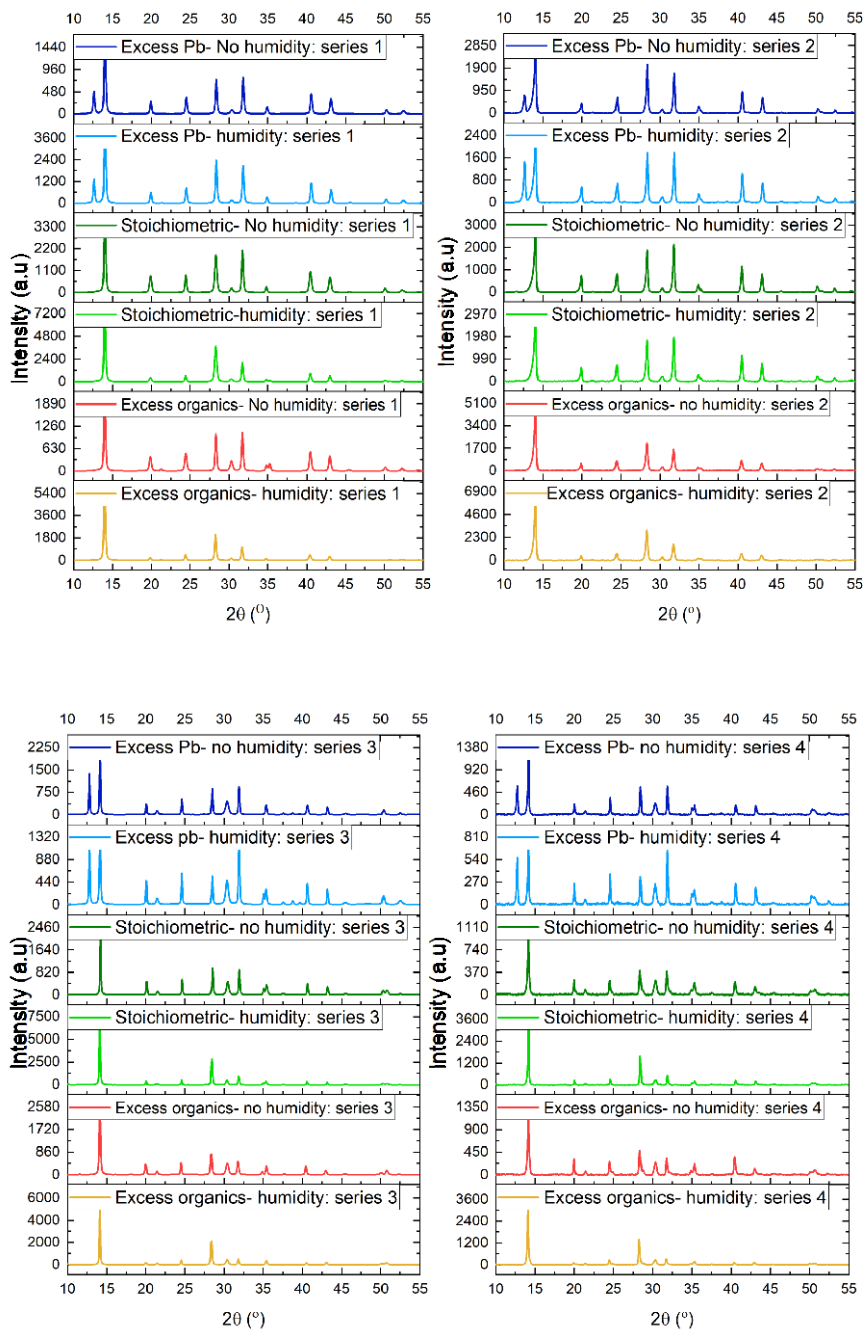


Figure AS14. Complete set of XRD pattern for 4 different series (different batches) for the different stoichiometries and treatments studied. Stoichiometric refers to 1:1 stoichiometry between A:Pb.

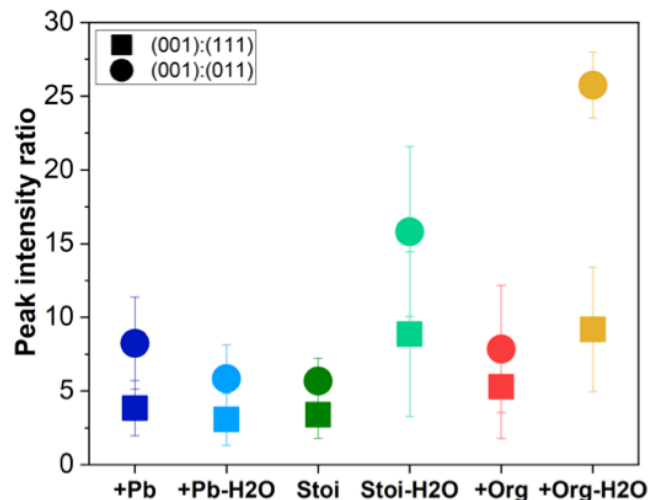


Figure AS15. Peak intensity ratio between 001 peak with 011 – circle- and 111- square, for the studied conditions where humidity treatment is H₂O. (+Pb equals EL in the main chapter, +Org equals EO in the main chapter, Stoi refers to 1:1 stoichiometry between A:Pb)

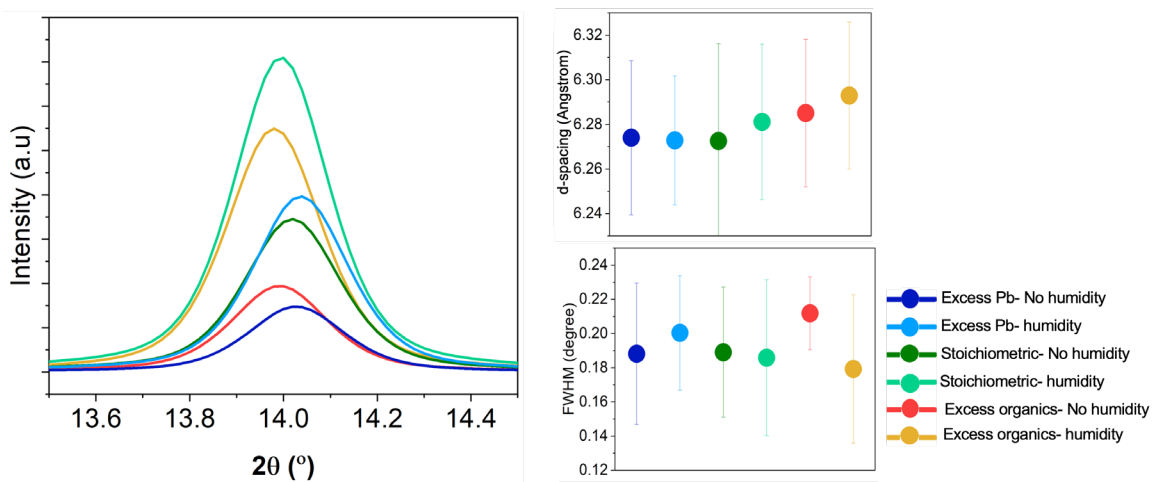


Figure AS16. XRD 001 peak with calculated d-spacing and FWHM for each studied condition (stoichiometry and humidity treatment). Stoichiometric refers to 1:1 stoichiometry between A:Pb.

Table AS3. Full width half maximum for the 100 peak for the complete set.

FWHM 100	Series 1	Series 2	Series 3	Series 4	Average	Error
Excess Pb- No humidity	0.23576	0.20761	0.16572	0.14363	0.19	0.04
Excess Pb- humidity	0.23512	0.19817	0.21251	0.1558	0.2	0.03
Stoichiometric-no humidity	0.23594	0.19111	0.14263	0.18648	0.19	0.04
Stoichiometric- humidity	0.23569	0.20923	0.16565	0.13284	0.19	0.05
Excess organics- no humidity	0.23668	0.21352	0.21262	0.18461	0.21	0.02
Excess organics- humidity	0.22471	0.20801	0.14123	0.14313	0.18	0.04

Table AS4. Lattice parameter (d-spacing) for the (100) peak for the complete set.

d-spacing (100)	Series 1	Series 2	Series 3	Series 4	Average	Error
Excess Pb- No humidity	6.309	6.298	6.242	6.247	6.274	0.035
Excess Pb- humidity	6.3	6.295	6.243	6.253	6.273	0.029
Stoichiometric-no humidity	6.309	6.302	6.214	6.265	6.273	0.044
Stoichiometric- humidity	6.318	6.303	6.254	6.249	6.281	0.035
Excess organics- no humidity	6.318	6.307	6.248	6.267	6.285	0.033
Excess organics- humidity	6.327	6.309	6.251	6.285	6.293	0.033

Williamson-Hall plot equation (Gaussian):

$$B\cos\theta = \left(\frac{k\lambda}{L}\right) + \varepsilon C\sin\theta \text{ [AS. 2]}$$

Where k is 0.9, C is 4, L is the crystallite size and ε the strain.²⁵⁸ B is the experimental FWHM for the selected peak. The Williamson-Hall plot is done by plotting $B\cos\theta$ versus $C\sin\theta$ for the 6 predominant perovskite peaks, where a linear relationship is observed, and the strain and crystallite size are extracted from the slope and y-intercept from the linear fitting. For gaussian-fitted peaks, all the terms need to be squared (i.e. $B^2\cos^2\theta$ and $C^2\sin^2\theta$) in order to obtain the appropriate fitting and interpretation.²⁵⁸ It is important to note that Williamson-hall plots are not accurate for quantitative analysis due to the unknown instrumental broadening; however, they are useful for understanding relative behaviors.

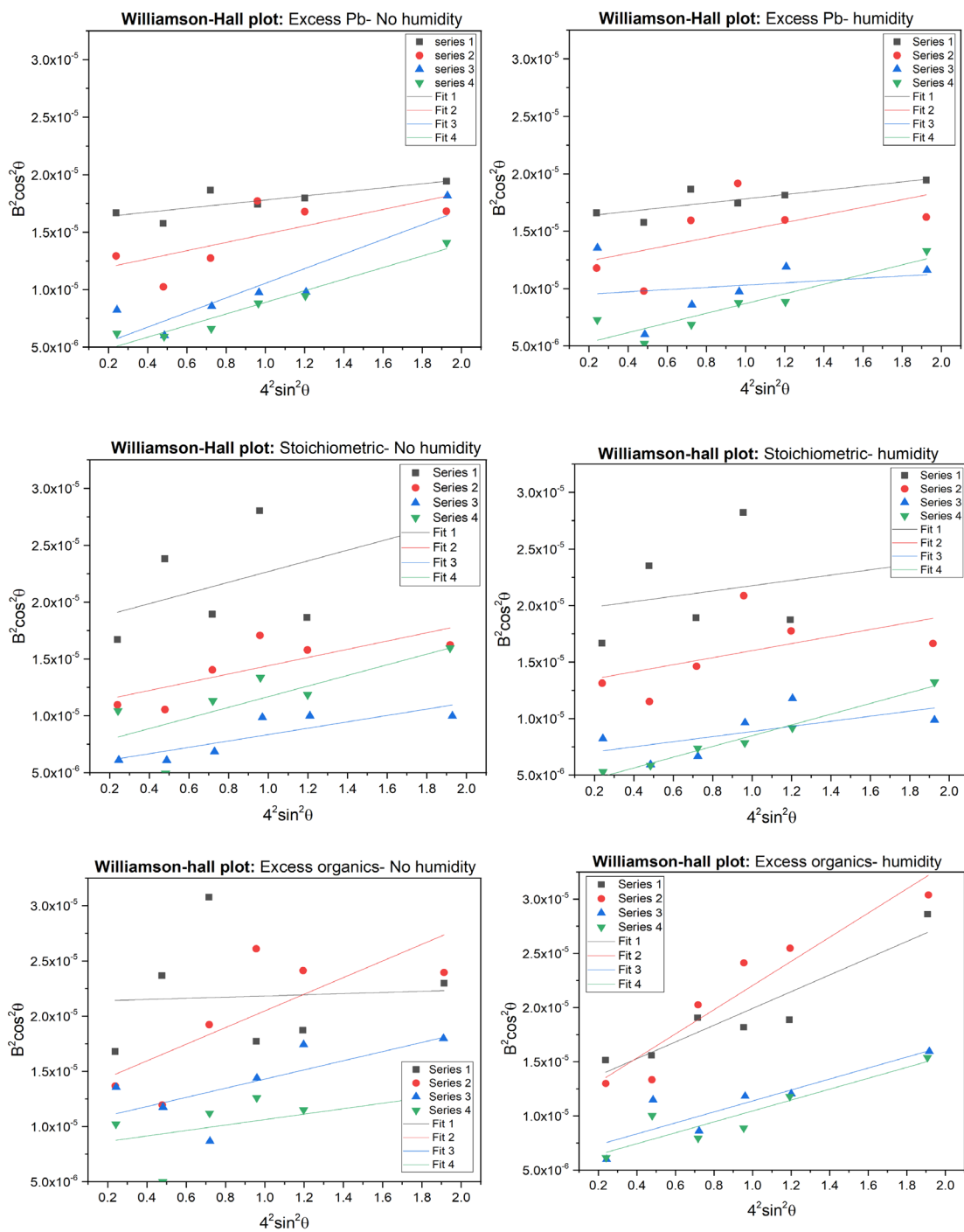


Figure AS17. Williamson-Hall plots for each stoichiometry, with and without humidity treatment for each of the XRD series for a Gaussian peak fitting. Peaks for the fitting were 100 ~14°, 110 ~19°, 111 ~24°, 200 ~28°, 210 ~32°, 220 ~40°.

Table AS5. From Williamson-Hall plot- slope m , y-intercept b , and R^2 values from linear fitting

m (slope)	Series 1	Series 2	Series 3	Series 4
Excess Pb- No humidity	1.77E-06	3.58E-06	6.36E-06	5.04E-06
Excess Pb- humidity	1.84E-06	3.34E-06	9.83E-07	4.22E-06
Stoichiometric-no humidity	4.71E-06	3.62E-06	2.80E-06	4.68E-06
Stoichiometric- humidity	2.35E-06	3.11E-06	2.26E-06	4.76E-06
Excess organics- no humidity	5.30E-07	3.62E-06	4.15E-06	2.47E-06
Excess organics- humidity	7.73E-06	1.12E-05	5.06E-06	5.03E-06

b (y-intercept)	Series 1	Series 2	Series 3	Series 4
Excess Pb- No humidity	1.60E-05	1.12E-05	4.20E-06	3.86E-06
Excess Pb- humidity	1.60E-05	1.17E-05	9.32E-06	4.48E-06
Stoichiometric-no humidity	1.80E-05	1.08E-05	5.54E-06	7.00E-06
Stoichiometric- humidity	1.94E-05	1.29E-05	6.60E-06	3.73E-06
Excess organics- no humidity	2.13E-05	1.08E-05	1.02E-05	8.16E-06
Excess organics- humidity	1.22E-05	1.09E-05	6.32E-06	5.42E-06

R²	Series 1	Series 2	Series 3	Series 4
Excess Pb- No humidity	63.50%	51.30%	82.40%	94.40%
Excess Pb- humidity	66.10%	34.40%	4.70%	83.30%
Stoichiometric-no humidity	32.70%	60.20%	70.50%	57.20%
Stoichiometric- humidity	10.90%	30.10%	38.20%	98.40%
Excess organics- no humidity	0.40%	60.20%	49.00%	27.80%
Excess organics- humidity	88.10%	90.90%	78.80%	84.20%

Table AS6. Calculated micro-strain from the Williamson-Hall plot values.

micro-strain	Series 1	Series 2	Series 3	Series 4	Average	Error
Excess Pb- No humidity	0.00133	0.00189	0.00252	0.00224	0.20%	0.05%
Excess Pb- humidity	0.00136	0.00183	0.00099	0.00205	0.16%	0.05%
Stoichiometric-no humidity	0.00217	0.0019	0.00167	0.00216	0.20%	0.02%
Stoichiometric- humidity	0.00153	0.00176	0.0015	0.00218	0.18%	0.03%
Excess organics- no humidity	0.00073	0.0019	0.00204	0.00157	0.16%	0.06%
Excess organics- humidity	0.00278	0.00334	0.00225	0.00224	0.27%	0.05%

Table AS7. Calculated crystallite size from the Williamson-Hall plot values.

crystallite size (nm)	Series 1	Series 2	Series 3	Series 4	Average	Error
Excess Pb- No humidity	34.63	41.33	67.67	70.59	53.55	18.23
Excess Pb- humidity	34.67	40.46	45.4	65.51	46.51	13.4
Stoichiometric-no humidity	32.69	42.22	58.88	52.38	46.54	11.5
Stoichiometric- humidity	31.46	38.59	53.95	71.74	48.94	17.86
Excess organics- no humidity	30.03	42.22	43.49	48.52	41.07	7.84
Excess organics- humidity	39.7	42.02	55.15	59.53	49.1	9.73

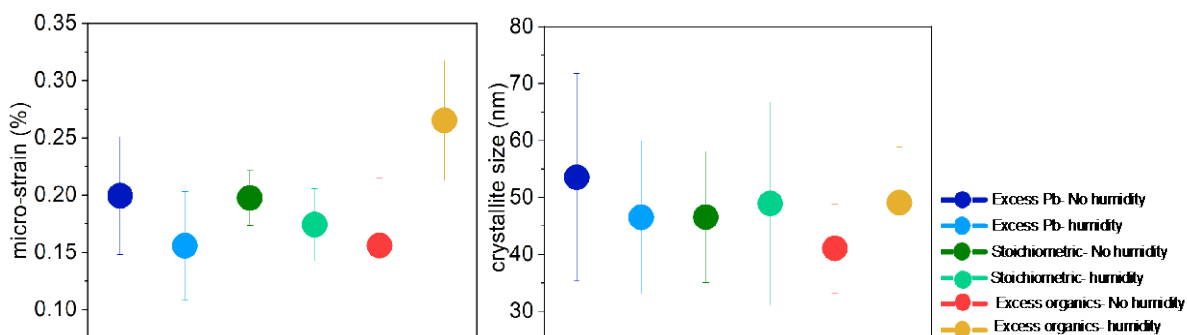


Figure AS18. Micro-strain for the complete set of stoichiometries and crystallite size from Williamson-Hall plot calculated for each stoichiometry without and with humidity treatment.

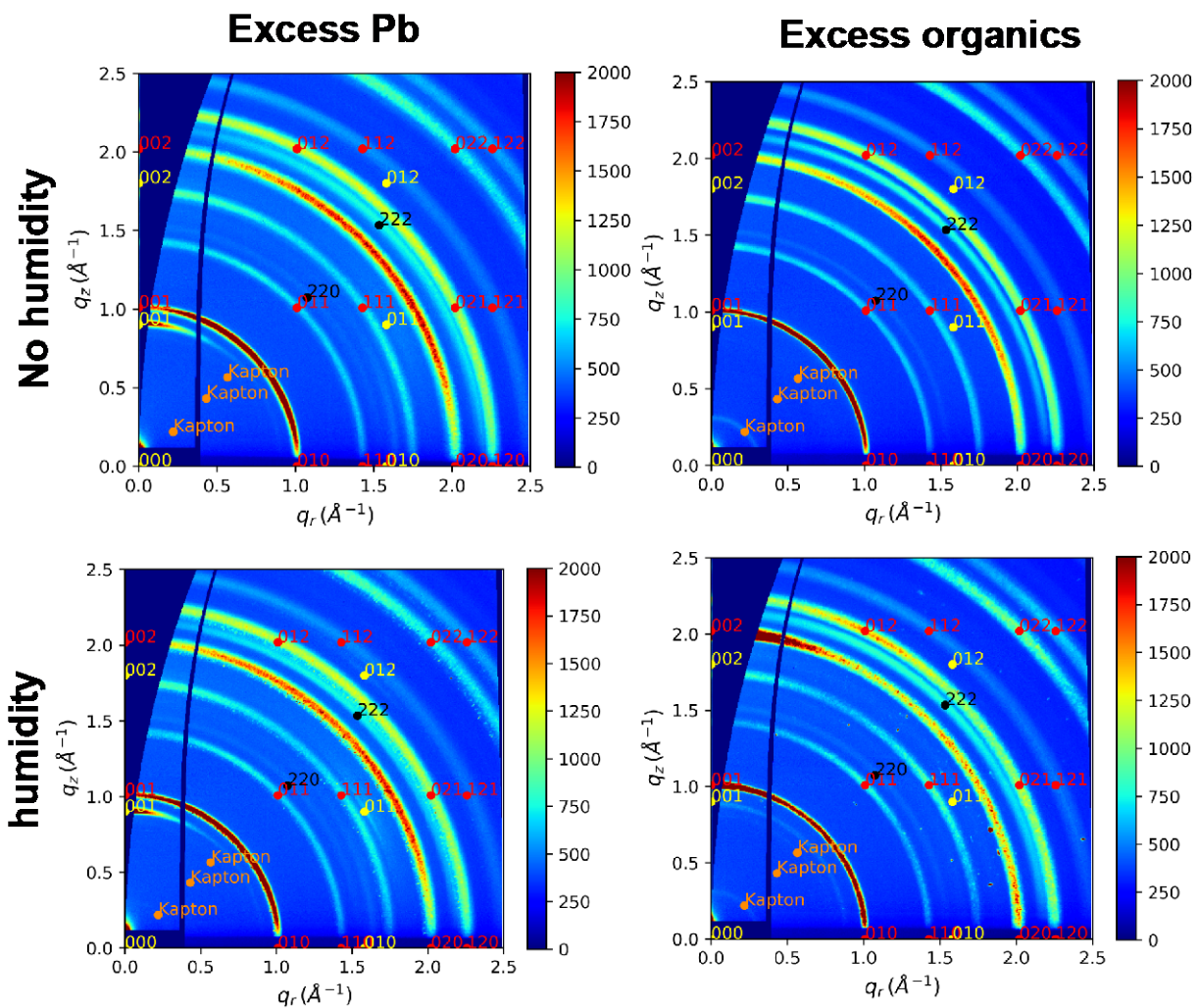


Figure AS19. GIWAXS images with complete indexing of a cubic perovskite (red), PbI_2 (yellow), ITO (black), Kapton (orange)

PbI₂ 001

q = 0.9076
dq = 0.0481

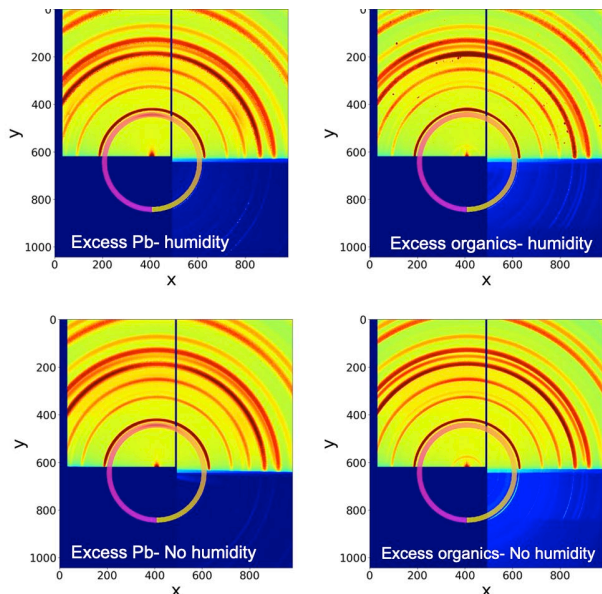
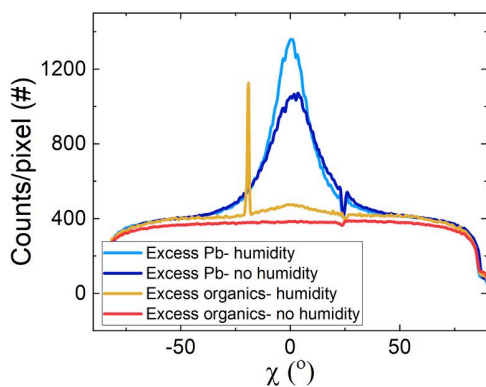


Figure AS20. Integrated for the azimuthal angle (χ) for the PbI₂ 001 peak (it is highlighted in the patterns the integration area for the angular representation of the peaks at a same q, in a x-y coordinate plot) (0.5° impinging angle α_i)

CsMAFA 100

q = 1.01285
dq = 0.05715

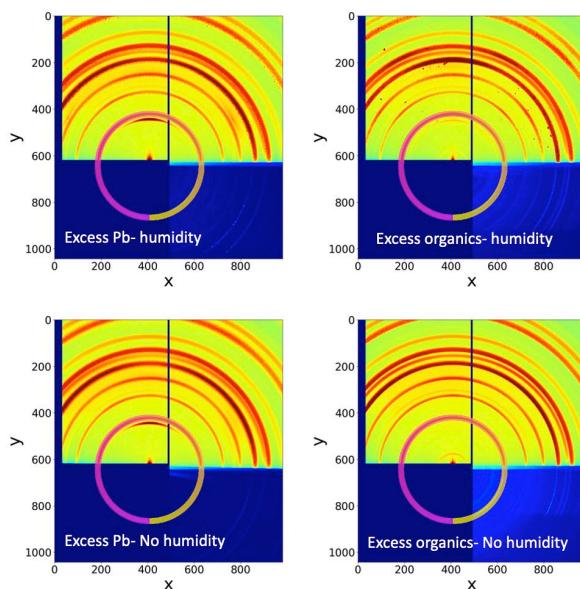
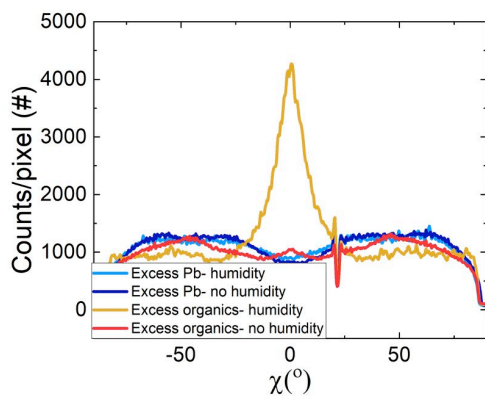


Figure AS21. Integrated for the azimuthal angle (χ) for the CsMAFA 100 peak (it is highlighted in the patterns the integration area for the angular representation of the peaks at a same q, in a x-y coordinate plot) (0.5° impinging angle α_i)

CsMAFA 110

$q = 1.42295$
 $dq = 0.07305$

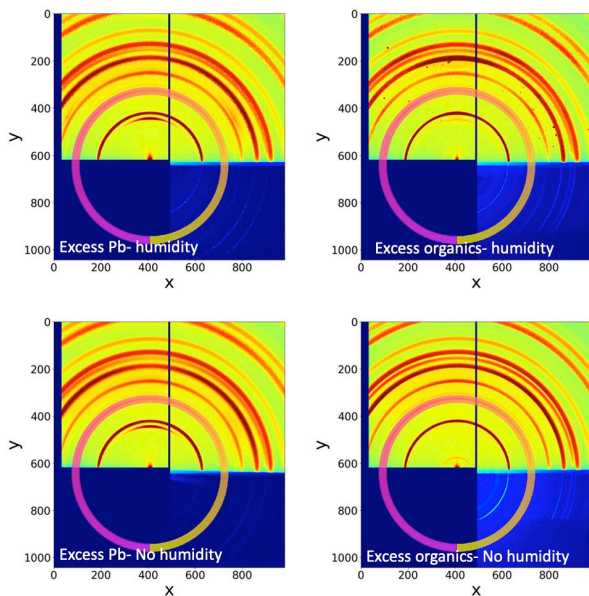
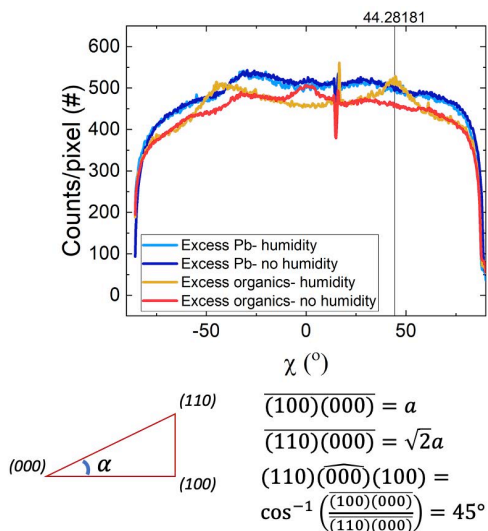


Figure AS22. Integrated for the azimuthal angle (χ) for the CsMAFA 110 peak (it is highlighted in the patterns the integration area for the angular representation of the peaks at a same q , in a x-y coordinate plot) (0.5° impinging angle α_i). Calculation shows that orientation of $\sim 45^\circ$ corresponds to the orientation of 0° at 100 (in Figure AS21).

CsMAFA 111

$q = 1.74$
 $dq = 0.06$

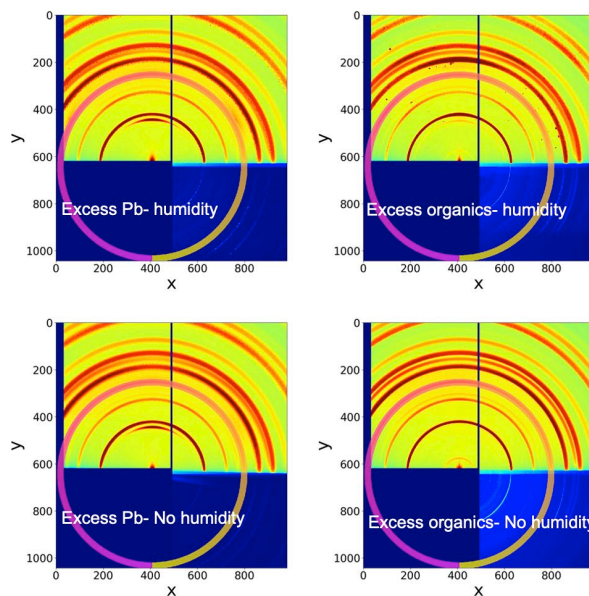
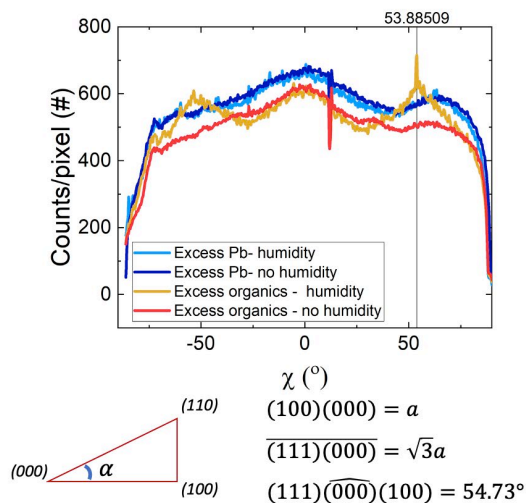


Figure AS23. Integrated for the azimuthal angle (χ) for the CsMAFA 111 peak (it is highlighted in the patterns the integration area for the angular representation of the peaks at a same q , in a x-y coordinate plot) (0.5° impinging angle). Calculation shows that orientation of $\sim 54^\circ$ corresponds to the orientation of 0° at 100 (in Figure AS21)

A.2.4 Optical Properties

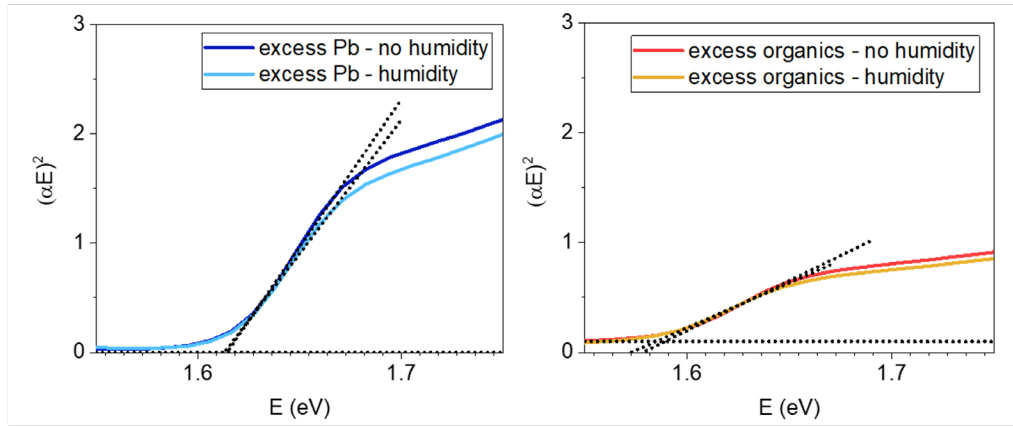


Figure AS24. Tauc-plots for a direct bandgap semiconductor calculated from the UV-Vis absorption data for each composition: Excess Pb and excess organics.

A.2.5. Perovskite Solar Cells

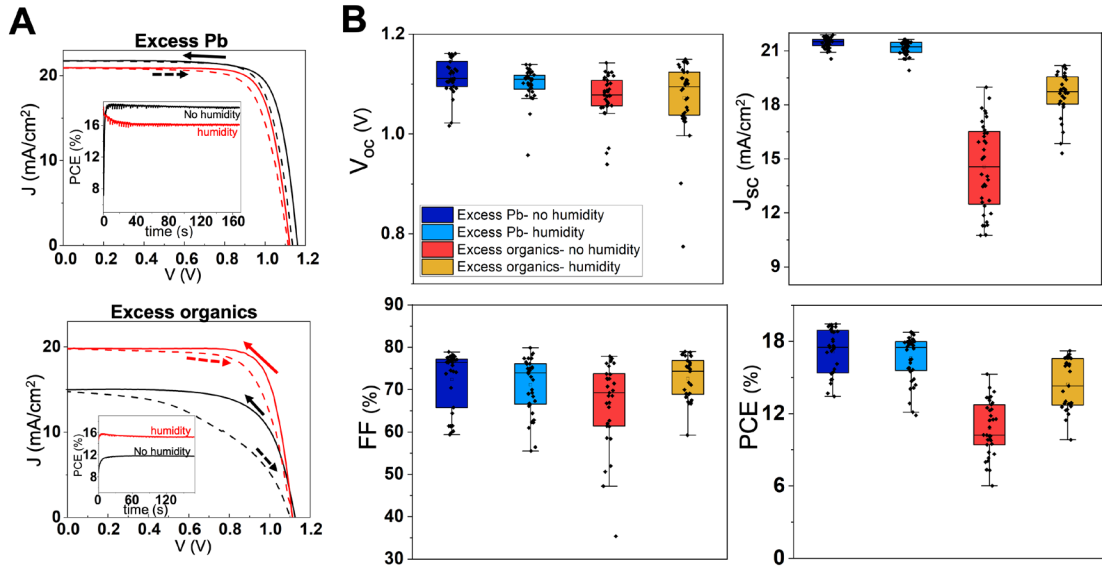


Figure AS25. Solar cell characterization A) J-V curves of the best pixel for each studied condition. Inset graphs show the maximum power point tracking (MPPT) for 170 s to a random pixel studied (not corresponding to same pixel of JV curve). B) Box plots of V_{oc} , J_{sc} , FF and PCE.

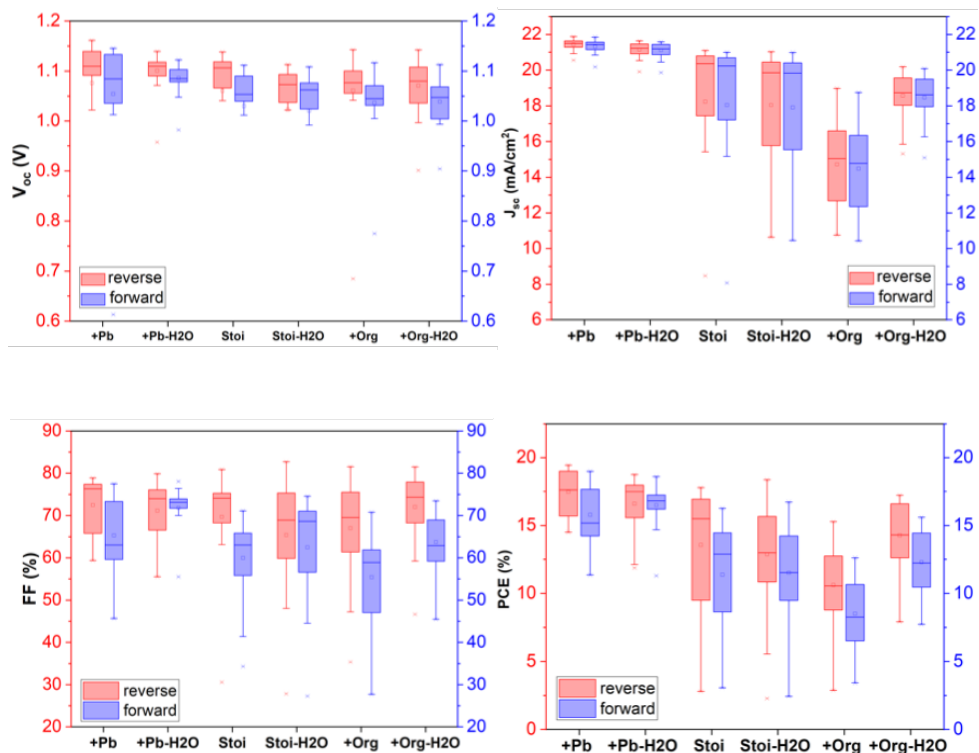


Figure AS26. Solar cell characterization box plots for the studied conditions for the reverse (red) and forward (blue) scans: V_{oc} , J_{sc} , FF and PCE.

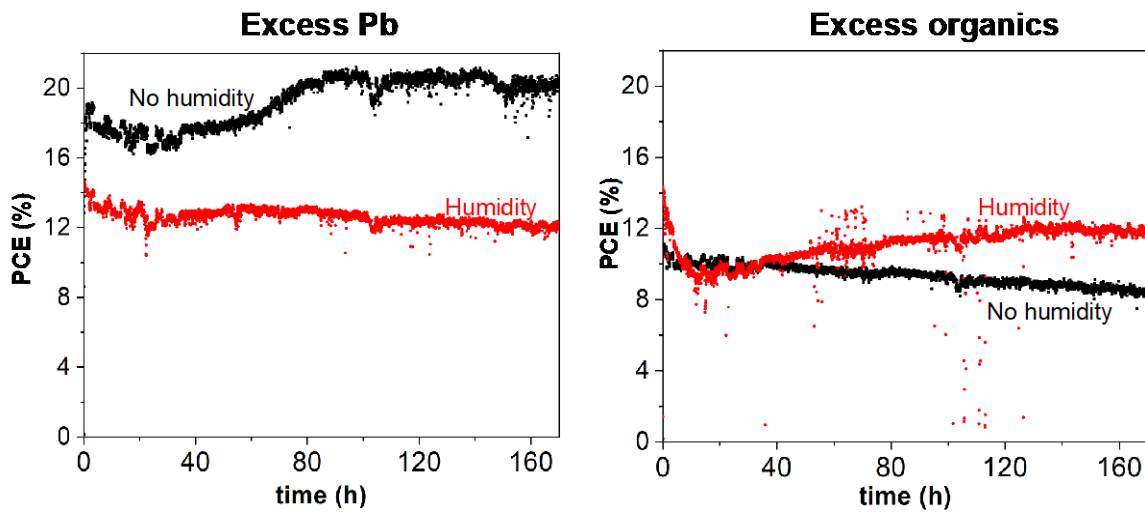


Figure AS27. Stability measurement of PCE obtained from continuous MPPT for 170 h for the champion pixel measured.

APPENDIX B. SUPPORTING INFORMATION: UNDESIRE PHASE TRANSFORMATIONS IN HALIDE PEROVSKITES

B.1 Experimental Details

Powder Synthesis for Characterization

CsI (Sigma Aldrich), FAI (TCI), and PbI₂ (TCI) powders were mixed in 3 mL of gamma butyrolactone (GBL, TCI) and dimethyl formamide (DMF, TCI) with a volume ratio of 2:1 to form a 0.5M solution of Cs_{0.17}FA_{0.83}PbI₃, with 5% molar excess of PbI₂. The solution was mixed for 1 hour at 50 °C. After, the solution was evaporated in a petri-dish at 170 °C until dried and annealed for 1 hour at the same temperature.

FAI and PbI₂ Thin Films

FAI powder (Great Solar) or PbI₂ powder (TCI) were mixed in dimethyl formamide (DMF) and dimethyl sulfoxide (DMSO) with a volume ratio of 2:1 volume ratio to form a 1.2 M solution of FAI or PbI₂. The solution was deposited via spin coating on glass substrates following the same deposition method of CsFA perovskite (1000 rpm for 10 s, and 6000 rpm for 20 s). Chlorobenzene was added as antisolvent 5 s before the end of the second spin coating step. The films were annealed at 100 °C for 15 min.

B.2 GIWAXS Characterization Setup

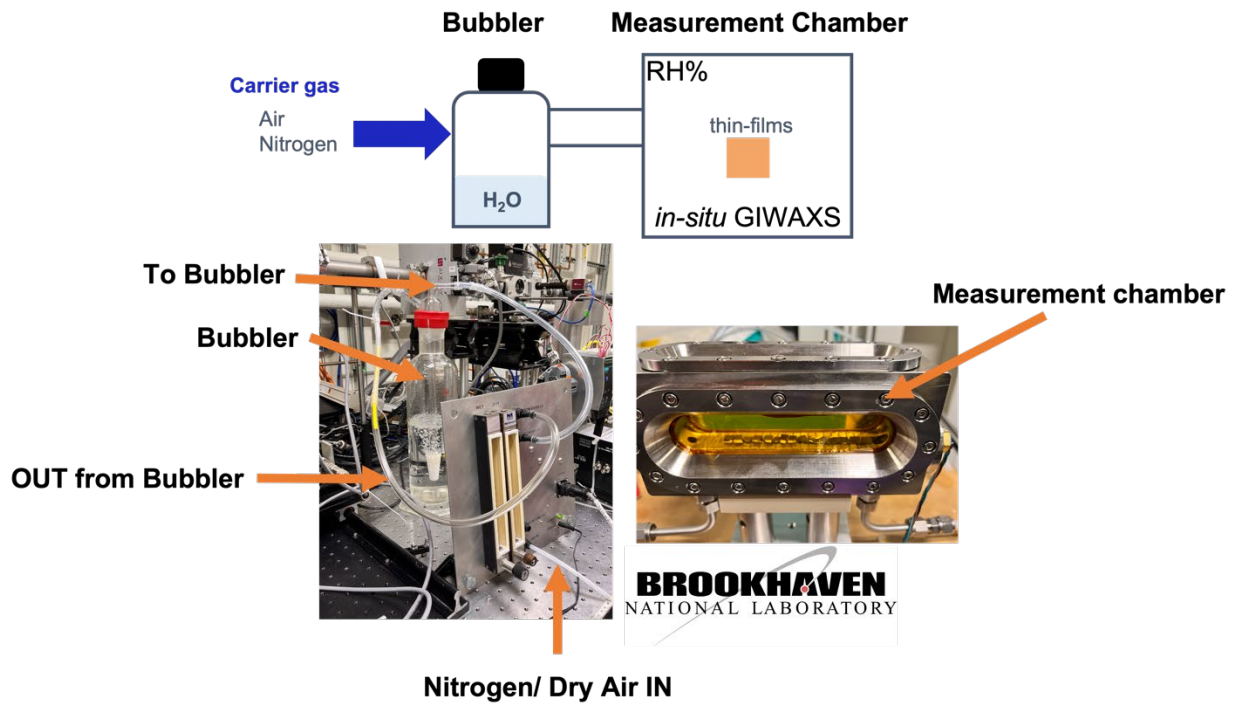


Figure BS1. Experimental setup for the *in-situ* relative humidity GIWAXS measurements

B.3 Structural Phase Transformations

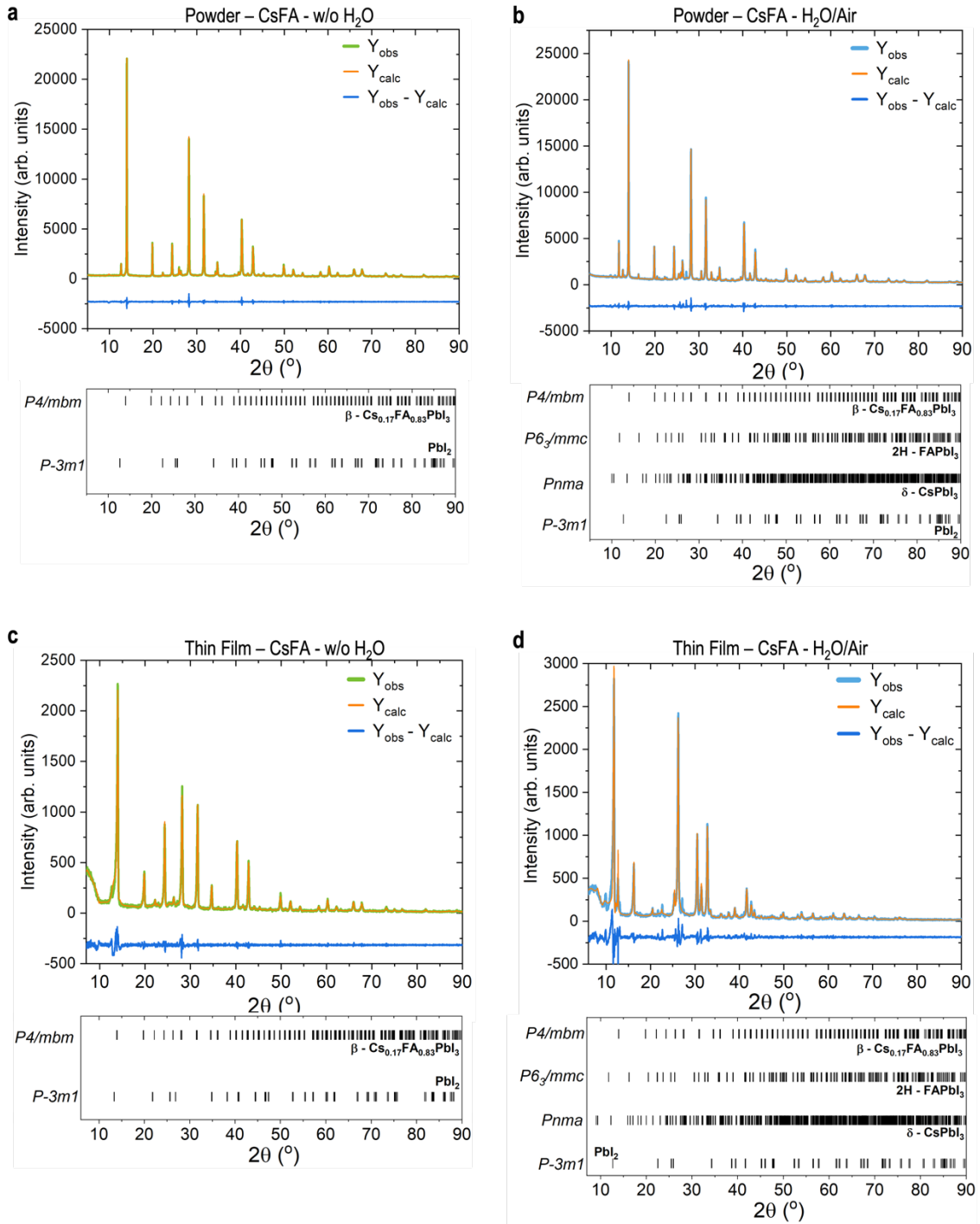


Figure BS2. Le Bail analysis of powder diffraction and thin-film diffraction data. a) $\text{Cs}_{0.17}\text{FA}_{0.83}\text{PbI}_3$ powders without (w/o) H_2O exposure, and b) powders exposed *ex-situ* to $\text{H}_2\text{O}/\text{Air}$ with high relative humidity of 80% for 24 hours c) $\text{Cs}_{0.17}\text{FA}_{0.83}\text{PbI}_3$ thin films without (w/o) H_2O exposure, and d) exposed *ex-situ* to $\text{H}_2\text{O}/\text{Air}$ with high relative humidity of 80% for 20 hours.

Table BS1. Lattice parameters from LeBail analysis in Fig. BS2

Phase	Space group	Lattice parameters						Chi ²
		a / Å	b / Å	c / Å	alpha /°	beta /°	gamma /°	
Thin Film w/o H₂O								
1. Perovskite	<i>P4/mbm</i>	8.95	8.95	6.36	90	90	90	1.29
2. PbI ₂	<i>P$\bar{3}$m1</i>	4.7	4.7	6.63	90	90	120	
Thin Film H₂O/Air								
1. Perovskite	<i>P4/mbm</i>	8.95	8.95	6.34	90	90	90	
2. 2H	<i>P6₃/mmc</i>	8.68	8.68	7.94	90	90	120	3.03
3. delta-Cs	<i>Pnma</i>	10.76	3.93	19.54	90	90	90	
4. PbI ₂	<i>P$\bar{3}$m1</i>	4.56	4.56	6.99	90	90	120	
Powder w/o H₂O								
1. Perovskite	<i>P4/mbm</i>	8.95	8.95	6.33	90	90	90	1.64
2. PbI ₂	<i>P$\bar{3}$m1</i>	4.56	4.56	6.99	90	90	120	
Powder H₂O/Air								
1. Perovskite	<i>P4/mbm</i>	8.95	8.95	6.34	90	90	90	
2. 2H	<i>P6₃/mmc</i>	8.68	8.68	7.93	90	90	120	2.62
3. delta-Cs	<i>Pnma</i>	10.37	4.17	16.92	90	90	90	
4. PbI ₂	<i>P$\bar{3}$m1</i>	4.56	4.56	6.99	90	90	120	

To quantitatively compare the degradation rate of CsFA perovskite, we integrated the area of the main scattering peak for each phase. For the β -perovskite, we integrated the 110 peak at $q_r \sim 1 \pm 0.05 \text{ \AA}^{-1}$. For the 2H phase, we integrated the $1\bar{1}0$ peak at $q_r \sim 0.84 \pm 0.02 \text{ \AA}^{-1}$. For the δ Cs phase, we integrated the 002 peak at $q_r \sim 0.7 \pm 0.05 \text{ \AA}^{-1}$ given that the main 212 peak of δ Cs at $q_r \sim 1.8 \text{ \AA}^{-1}$ overlaps with other phases. The integrated area was plotted in **Figure 5.1**

of the main text. To further compare the phase transformation rate, we normalized the integrated area (α) for each phase as shown in **Figure BS3a**. We observe that the main β -perovskite phase is lost when exposed to H₂O/Air, compared to a more stable phase in H₂O/N₂. We fitted the phase transformation data into a sigmoidal Boltzmann function, observing a high R² value, hence a better fitting for the perovskite transformation in H₂O/Air. In addition, the lowest $d\alpha$ value from the Boltzmann fitting in **Figure BS3a** for the transformation in H₂O/Air confirms the faster decrease. Additionally, we linearize the data with a logarithmic function $[-\ln(1 - \alpha)]^{1/2}$ used in other crystal transformation studies^{259,260} to calculate a time constant b that corresponds to the slope of the fitted linear function. In the case of the β 110 peak in **Figure S3b** we observe a b of -1.5 for the phase transformation in H₂O/Air compared to -0.5 in H₂O/N₂. However, the fitting in H₂O/N₂ has a higher error. In sum, we quantify the faster loss of β -perovskite phase in H₂O/Air.

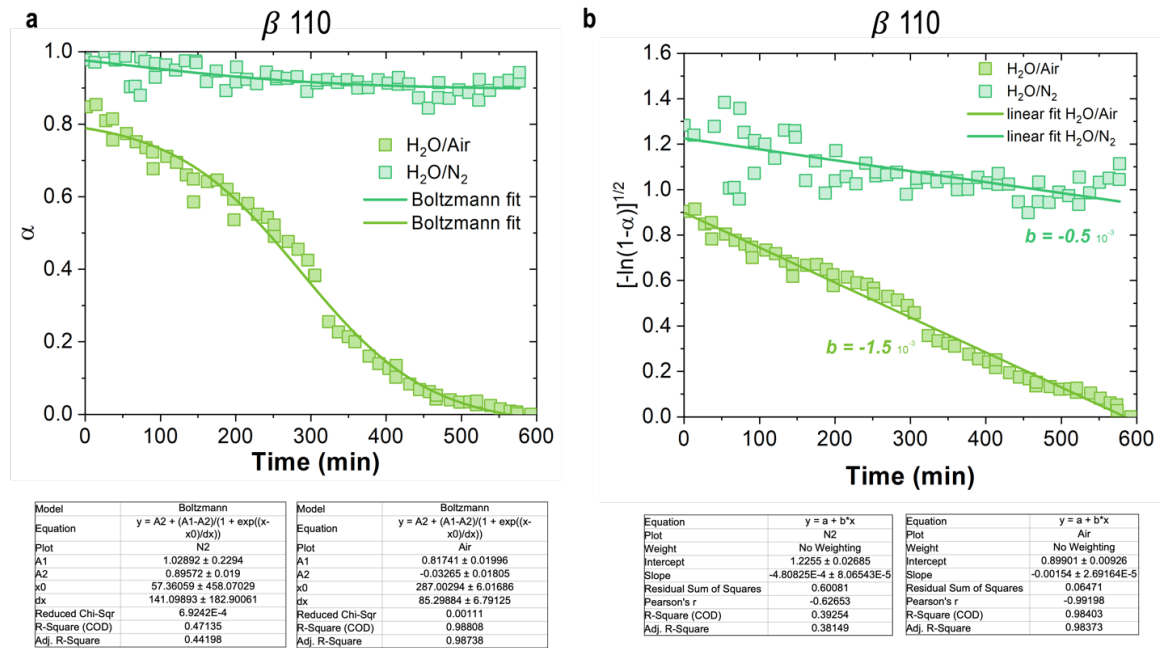


Figure BS3. 110 peak evolutions from the integrated area of the β -CsFA perovskite, normalized into α , and fitted to a) Boltzmann sigmoidal function. b) Fitted into a linear logarithmic model.

We do the same analysis for the formation of the non-perovskite phases 2H and δ Cs by normalizing the integrated area (α) and plotting it as a function of time for the different studied conditions: **Figure BS4a** 2H phase in H₂O/Air, **Figure BS4b** 2H phase in H₂O/N₂, **Figure BS4c** δ Cs in H₂O/Air, and **Figure BS4d** δ Cs in H₂O/N₂. The non-perovskite phases in H₂O/Air form faster, showing a better Boltzmann fitting and a lower $d\alpha$ value from the fitting. Remarkably, **Figure BS4b** shows no formation of the 2H phase in H₂O/N₂. For this reason, there is no Boltzmann nor linear fitting for the data. To compare the non-perovskite phase formation under the same condition, we compared the normalized linearized data. **Figure BS4e** shows how 2H phase forms at a faster rate with a slope, time constant b , higher than for the δ Cs phase.

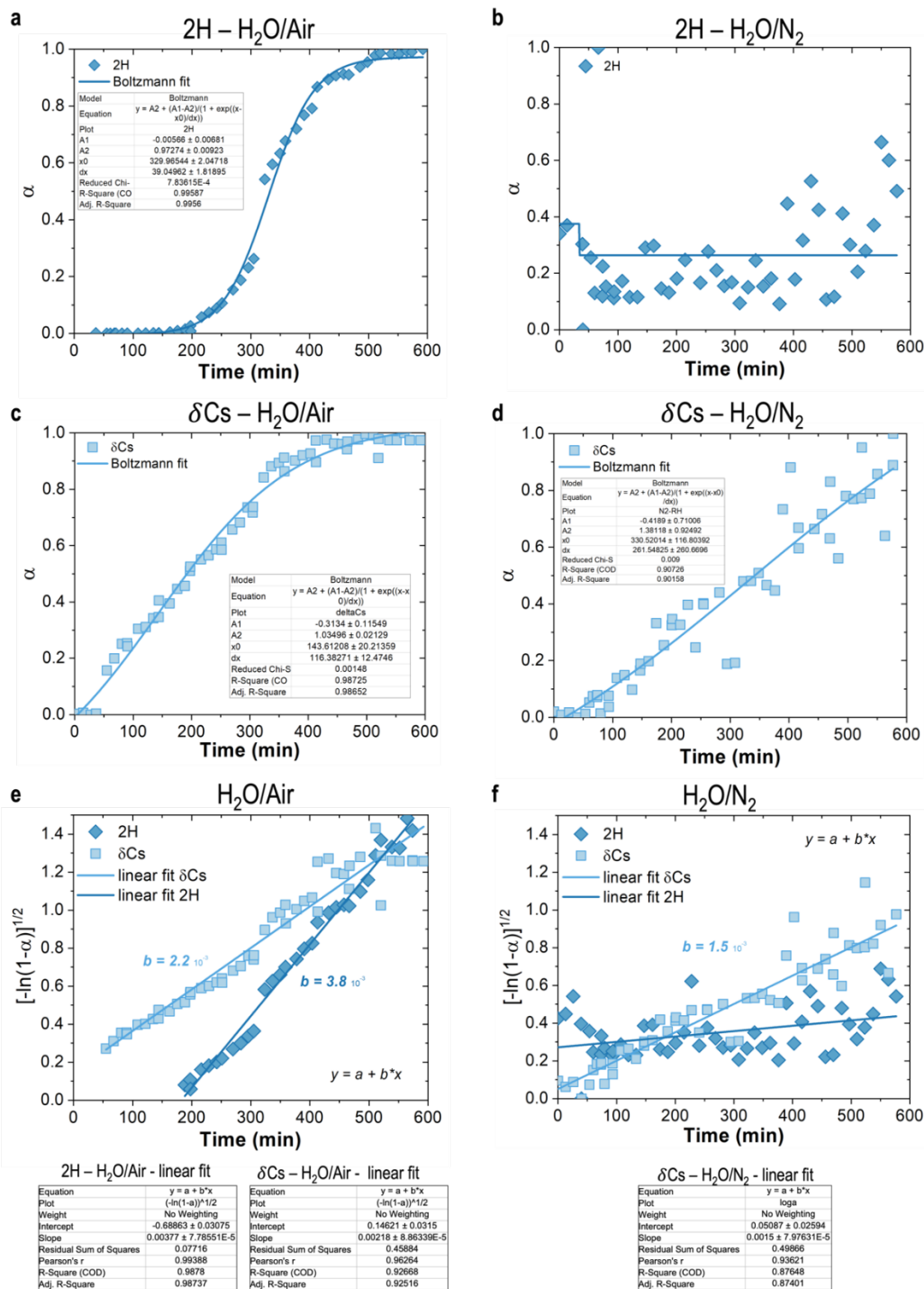


Figure BS4. Peak evolution from integrated area normalized into α and fitted to a Boltzmann sigmoidal function a) 2H peak in H₂O/Air, b) 2H peak in H₂O/N₂, c) δ Cs peak in H₂O/Air, d) δ Cs peak in H₂O/N₂. Data fitted into a linear logarithmic function to compare the evolution and calculate time constant (b) in e) H₂O/Air and f) H₂O/N₂.

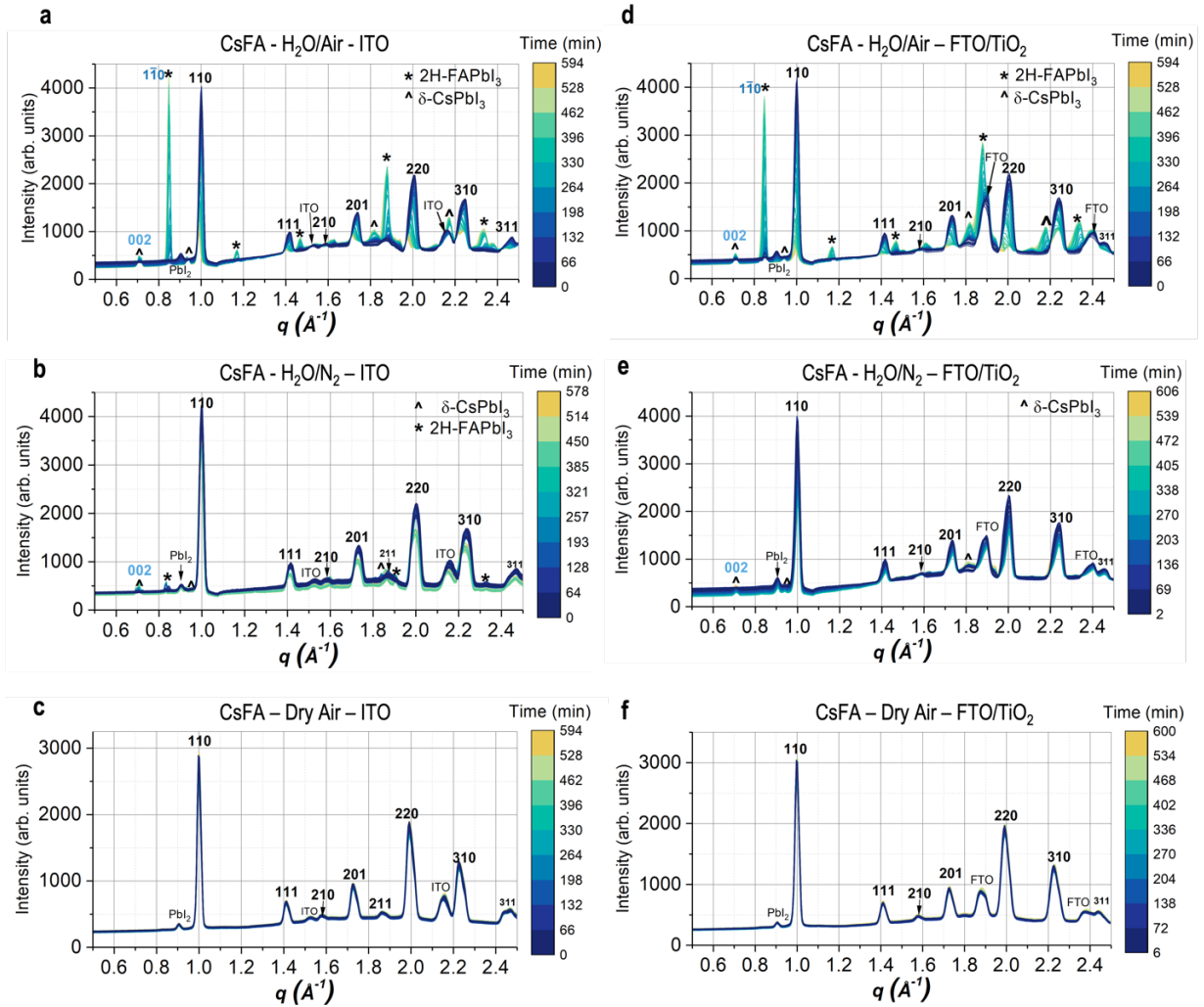


Figure BS5. Integrated circular average from *in-situ* relative humidity for different substrates and exposure conditions a) H₂O/Air on ITO, b) H₂O/Nitrogen on ITO, c) Dry Air on ITO, d) H₂O/Air on FTO and compact and mesoporous TiO₂ layers, e) H₂O/Nitrogen on FTO and compact and mesoporous TiO₂ layers, d) Dry Air on FTO and TiO₂ layers. Bragg peaks are labeled for the β -perovskite phase.

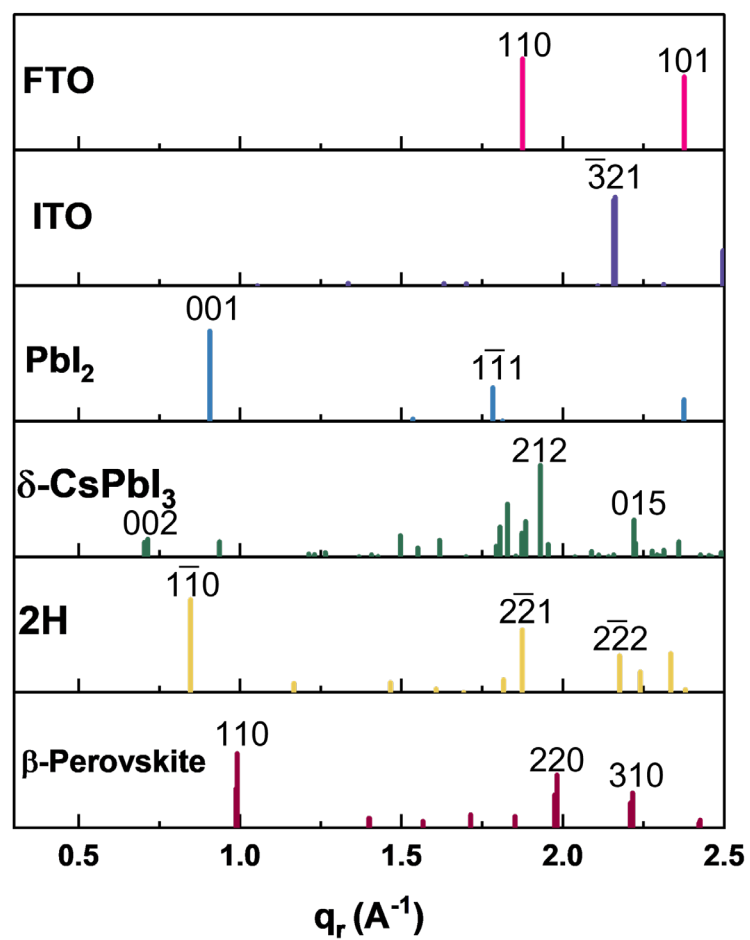


Figure BS6. Peaks from simulated diffraction patterns of the main phases observed in the studied lead halide perovskites: FTO, ITO, PbI₂, orthorhombic δ -CsPbI₃, hexagonal 2H-FAPbI₃, and tetragonal β -perovskite Cs_{0.17}FA_{0.83}PbI₃.

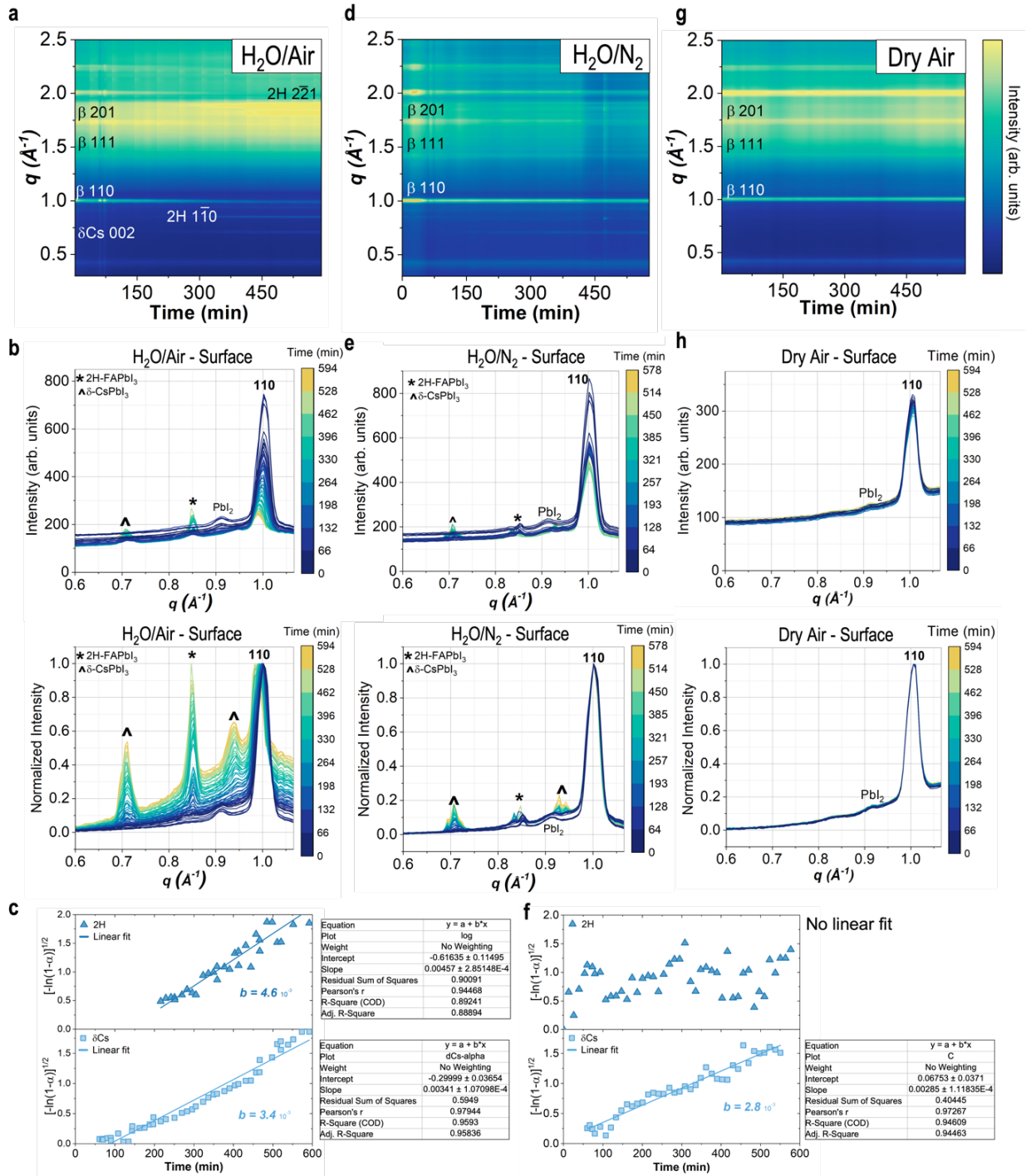


Figure BS7. Structural phase analysis at the surface (GIWAXS incident angle of 0.1° , beyond the critical point for perovskites) by *in-situ* GIWAXS. a, b, c) CsFA films exposed to $\text{H}_2\text{O}/\text{Air}$, d, e, f) $\text{H}_2\text{O}/\text{N}_2$, and g, h) Dry air. a, d, g) *In-situ* scattering vector as a function of time of exposure, b) zoom-in plot of the circular average scattering pattern as a function of time of exposure, and the normalized-intensity plot, and c, f) the peak evolution of the 2H and δCs phases, following the procedure from Figs. S3 and S4, and calculating the time constant b .

Note on surface analysis: The surface GIWAXS is obtained from varying the X-ray incident angle, from 0.5° for bulk to 0.1° for surface. The critical angle for FAPbI₃ has been reported at approximately 0.16° ,²⁶¹ meaning that below we are probing only some tenths of nanometers of layer, while above, we increase to hundreds of nanometers. Given that our film has a thickness of around 500nm, the 0.5° probes the “bulk” and 0.1° probes the “surface. Herein, we observe surface phase transformations for CsFA films exposed to H₂O/Air and to H₂O/N₂. The time constant b shows a higher value at the surface compared to bulk (**Figure BS4**), indicating that the non-perovskite phases form faster on the surface than bulk. By comparing 2H with δ Cs in H₂O/Air, 2H phase forms faster.

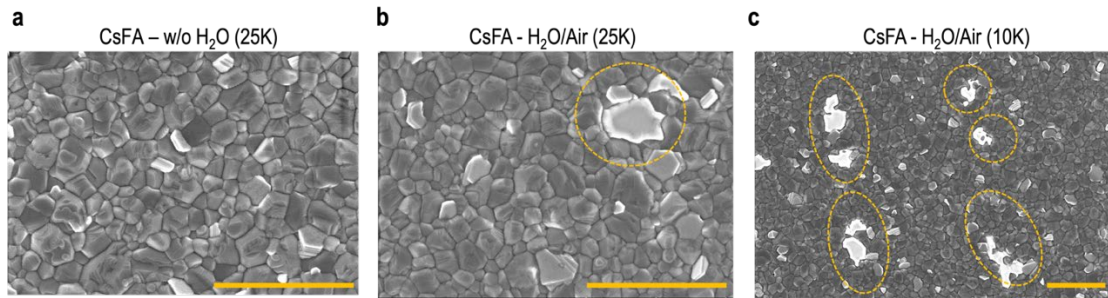


Figure BS8. Morphology from SEM in a) Cs_{0.17}FA_{0.83}PbI₃ (CsFA) thin films w/o H₂O exposure, and b,c) after exposed *ex-situ* to H₂O/Air relative humidity 80% for 20 hours. The scale bar is 2 micrometers. The SEM measurements were done in vacuum, but the samples were exposed to air from the glovebox to the SEM instrument.

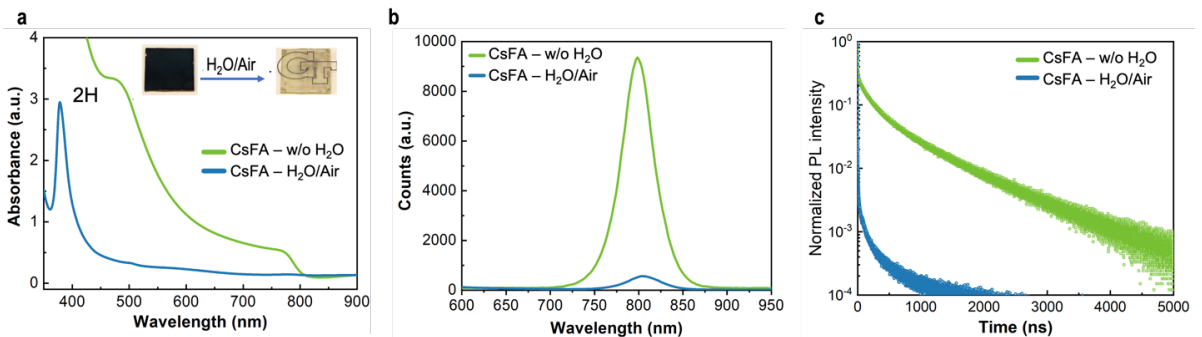


Figure BS9. Optical properties of the Cs_{0.17}FA_{0.83}PbI₃ (CsFA) exposed to H₂O/Air with relative humidity 80% for 20 hours. a) Absorption from UV-VIS spectroscopy, b) steady state PL, and c) trPL with normalized PL intensity. The measurements were done in ambient atmosphere, therefore, exposed to ambient air. (green) CsFA w/o H₂O exposure, (blue) after exposure to H₂O/Air.

B.4 Surface Chemistry

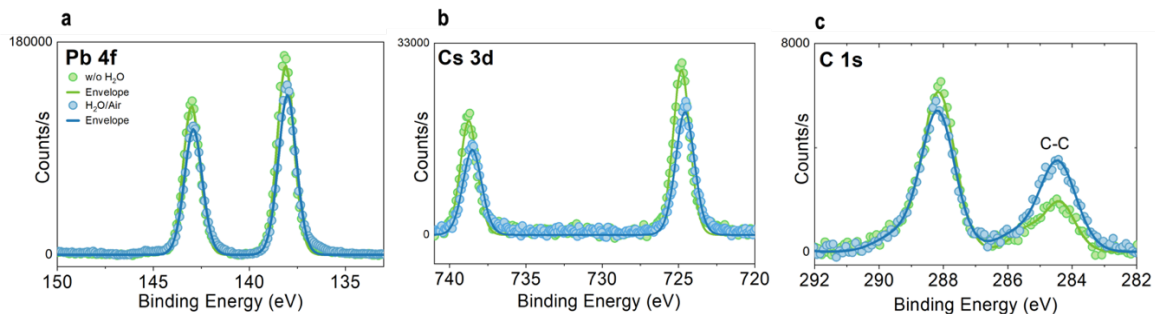


Figure BS10. XPS spectra of $\text{Cs}_{0.17}\text{FA}_{0.83}\text{PbI}_3$ (CsFA) films w/o exposure to H_2O . The films were deposited inside of nitrogen glovebox but exposed few minutes to air while transferring to the XPS instrument. XPS measurement was in vacuum. a) Pb 4f, b) Cs 3d, c) C 1s.

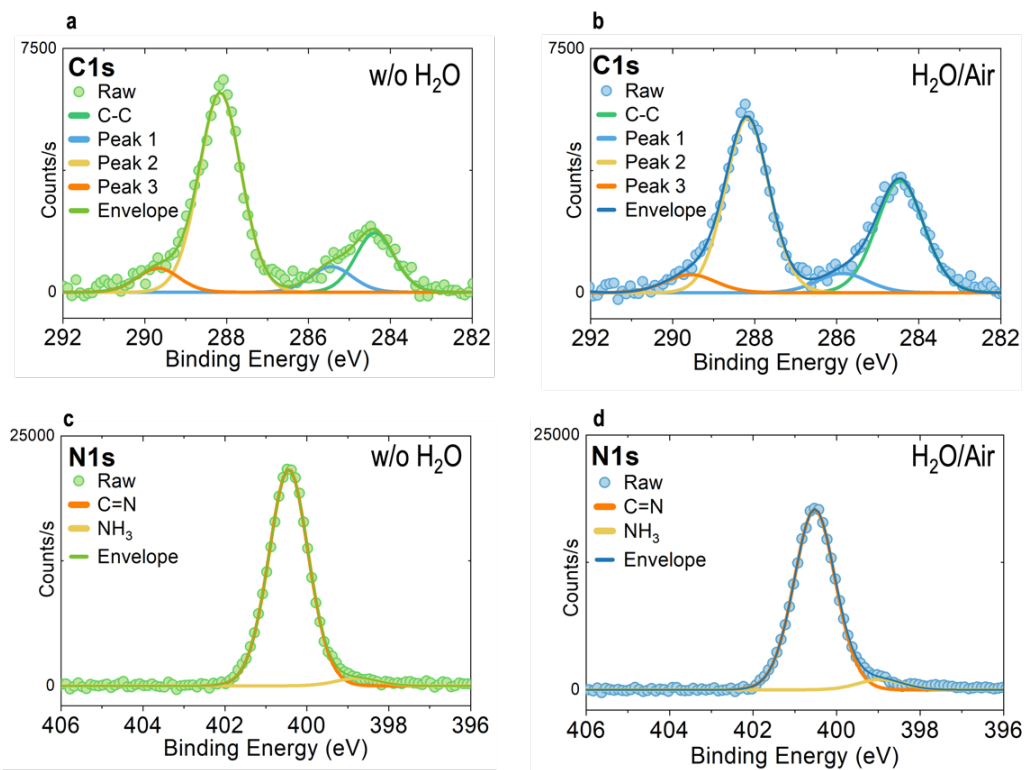


Figure BS11. XPS spectra of $\text{Cs}_{0.17}\text{FA}_{0.83}\text{PbI}_3$ (CsFA) exposed *ex-situ* to $\text{H}_2\text{O}/\text{Air}$ with relative humidity of 80% for 20 hours and peak deconvolution for a) C 1s w/o H_2O exposure, b) C 1s $\text{H}_2\text{O}/\text{Air}$ exposure, c) N 1s w/o H_2O exposure, d) N 1s $\text{H}_2\text{O}/\text{Air}$ exposure.

Table BS2. XPS convoluted peaks details and atomic percent for Cs_{0.17}FA_{0.83}PbI₃ w/o exposure to H₂O

CsFAPbI₃ - w/o H₂O					
	Name	BE eV	FWHM eV	Area (P) CPS.eV	Atomic %
C 1s	C-C	284.37	1.12	2221.37	2.84%
	Peak 1	285.44	1.21	1038.77	1.33%
	Peak 2	288.16	1.21	8075.49	10.18%
	Peak 3	289.68	1.21	978.11	1.25%
N 1s	C=N	400.44	1.14	26751.59	21.77%
	NH3	398.76	1.24	1030.11	0.83%
O 1s	Peak 1	533.1	3.37	2085.32	1.08%
I 3d	I3d5 Scan A	619.09	1.31	741127.39	47.79%
	I3d3 Scan A	630.56	1.31	513604.64	0.00%
Pb 4f	Pb4f7 Scan A	138.13	0.99	174414.28	10.51%
	Pb4f5 Scan A	143.03	0.99	137147.45	0.00%
Cs 3d	Cs3d5 Scan A	724.82	1.3	40130.21	2.42%
	Cs3d3 Scan A	738.75	1.31	27800.64	0.00%

Table BS3. XPS convoluted peaks details and atomic percent for Cs_{0.17}FA_{0.83}PbI₃ exposed to H₂O/Air

CsFAPbI ₃ - H ₂ O/Air					
	Name	BE eV	FWHM eV	Area (P) CPS.eV	Atomic %
C 1s	C-C	284.45	1.36	5096.07	5.71%
	Peak 1	285.86	1.46	936.78	1.05%
	Peak 2	288.18	1.26	7362.1	8.27%
	Peak 3	289.56	1.46	878.29	0.99%
N 1s	C=N	400.52	1.17	22404.59	16.19%
	NH3	398.94	1.26	1404.33	1.01%
O 1s	Peak 1	532.29	1.72	39460.16	18.30%
	Peak 2	530.37	1.82	3891.3	1.80%
I 3d	I3d5 Scan A	619.22	1.4	635074.14	36.38%
	I3d3 Scan A	630.68	1.41	440109.26	0.00%
Pb 4f	Pb4f7 Scan A	138.04	1.04	155980	8.49%
	Pb4f5 Scan A	142.94	1.04	122651.99	0.00%
Cs 3d	Cs3d5 Scan A	724.58	1.45	33320.34	1.79%
	Cs3d3 Scan A	738.52	1.45	23082.88	0.00%

Note on XPS measurements: XPS was performed under an ultra-high vacuum instrument. In addition, the samples were exposed for a few seconds between the transfer from a nitrogen glovebox to the measurement setup. We note that these measurements were done *ex-situ*, therefore, there was no possibility of measuring XPS to samples exposed to H₂O/N₂, nor only exposed to dry air. The *in-situ* setup was only for the GIWAXS measurements to study the structural phase transformations.

Figure BS10c shows the C1s peaks. The peak at ~ 284.5 eV from the C–C and C–H bonds. Two minor peaks resulted from the peak deconvolution (**Figure S11a-b**) that may be attributed to other C–N complexes.^{48,98} The peak at ~ 288.16 eV, peak 2, is principally attributed to C=N bond from FA. After H₂O/Air exposure, Peak 1, corresponding to C–C, C–H, or C–N bonds increases intensity, indicating other carbon species forming at the surface, such as carbonates, possibly from atmospheric contamination (**Figure BS11**). After H₂O/Air exposure, Peak 2, the C=N peak intensity decreases, in line with the FA⁺ loss. However, the atomic percentage attributed to Peak 2 decreases only 2% compared to the 5.6 % decrease in from the nitrogen from the N1s spectra (**Tables BS2-3**). For this reason, we also attribute Peak 2 from the C1s spectra in **Figure BS11b**, after H₂O/Air exposure, to Carbon-Oxygen complexes such as carbonates or carboxyls, that have a binding energy from 288 to 291 eV.⁹⁸

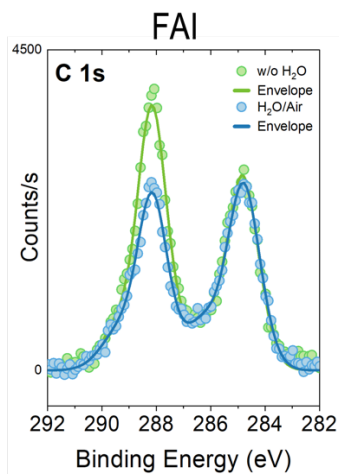


Figure BS12. XPS of FAI thin films deposited in a nitrogen glovebox and exposed for few minutes to air before in the transfer to XPS instrument w/o H₂O exposure or exposed to H₂O/Air with a relative humidity of 80% for 20 hours. Spectra of the C 1s.

Table BS4. XPS convoluted peaks details and atomic percent for FAI films w/o H₂O exposure

FAI w/o H ₂ O					
	Name	BE eV	FWHM eV	Area (P) CPS.eV	Atomic %
	C-C	284.83	1.39	4073.14	5.79
C 1s	Peak 1	286.41	1.49	957.17	1.36
	C=N	288.16	1.29	5146.65	7.33
	Peak 2	289.53	1.29	745.49	1.06
	N 1s	C=N	400.37	1.4	17927.23
O 1s	Peak 1	532.78	1.62	94305.83	55.47
	Peak 2	530.8	1.59	6906.38	4.06
I 3d	I3d5 Scan A	618.8	1.49	117297.44	8.51
	I3d3 Scan A	630.26	1.49	81287.66	0

Table BS5. XPS convoluted peaks details and atomic percent for FAI thin films exposed to H₂O/Air

FAI - H ₂ O/Air					
	Name	BE eV	FWHM eV	Area (P) CPS.eV	Atomic %
	C-C	284.79	1.43	3997.97	5.36
C 1s	Peak 1	286.33	1.52	1017.77	1.37
	C=N	288.15	1.33	3480.2	4.67
	Peak 2	289.47	1.52	770.96	1.04
	N 1s	C=N	400.38	1.44	12185
O 1s	Peak 1	532.8	1.62	122020.69	67.71
	Peak 2	530.8	1.6	7659.7	4.24
I 3d	I3d5 Scan A	618.83	1.47	74209.34	5.08
	I3d3 Scan A	630.29	1.47	51427.41	0

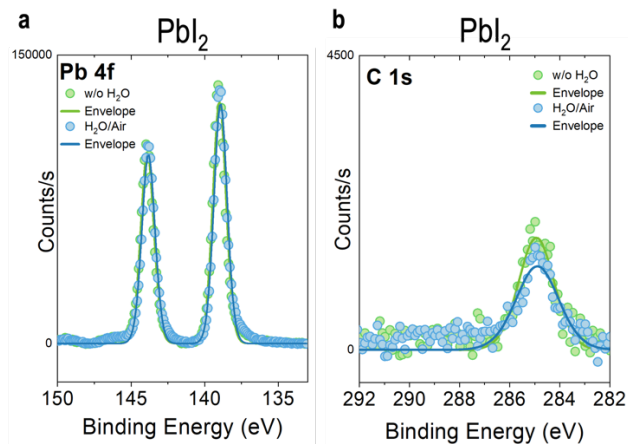


Figure BS13. XPS of PbI_2 thin films deposited in a nitrogen glovebox and exposed for few minutes to air before in the transfer to XPS instrument w/o H_2O exposure or exposed to $\text{H}_2\text{O}/\text{Air}$ with a relative humidity of 80% for 20 hours. a) Pb 4f, b) C 1s.

Table BS6. XPS convoluted peaks details and atomic percent for PbI_2 films w/o H_2O exposure

PbI ₂ w/o H ₂ O					
	Name	BE eV	FWHM eV	Area (P) CPS.eV	Atomic %
C 1s	C-C	284.93	1.68	3119.31	11.58
I 3d	I3d5 Scan A	619.9	1.26	331536.1	62.95
	I3d3 Scan A	631.36	1.26	229756.02	0
Pb 4f	Pb4f7 Scan A	139.01	1.05	143537.9	25.47
	Pb4f5 Scan A	143.91	1.05	112868.37	0

Table BS7. XPS convoluted peaks details and atomic percent for PbI₂ thin films exposed to H₂O/Air

PbI₂ - H₂O/Air					
	Name	BE eV	FWHM eV	Area (P) CPS.eV	Atomic %
C 1s	C-C	284.89	2.01	2789.37	10.58
I 3d	I3d5 Scan A	619.75	1.24	327731.4	63.57
	I3d3 Scan A	631.21	1.25	227119.34	0
Pb 4f	Pb4f7 Scan A	138.92	1.05	142544.16	25.84
	Pb4f5 Scan A	143.82	1.05	112086.96	0

B.5 Bulk Chemistry

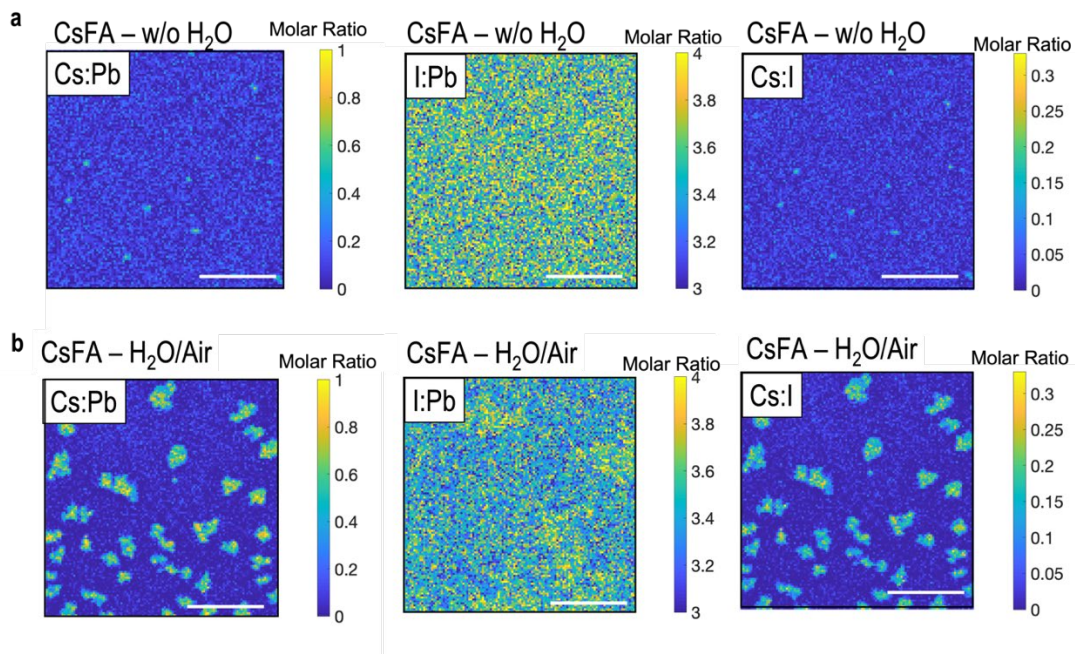


Figure BS14. X-ray fluorescence (XRF) maps of the molar ratios between Cs, Pb, and I in $\text{Cs}_{0.17}\text{FA}_{0.83}\text{PbI}_3$ (CsFA) thin films a) without (w/o) H_2O exposure. The samples were exposed to air before the measurement in a helium-vented chamber. b) after *ex-situ* exposure to H_2O /Air with relative humidity 80% for 20 hours. The measurement was in a helium-vented chamber. The scale bar is $10\mu\text{m}$.

Note on XRF: XRF measurements were done to CsFA films on glass to prevent fluorescence signal from the ITO. It is important to highlight that the characteristic X-ray fluorescence emission energies of Cs and I are close in energy and overlap. For this reason, even if we quantify the mass and molar values with a standard, there is loss of accuracy due to the low and overlapped energies.

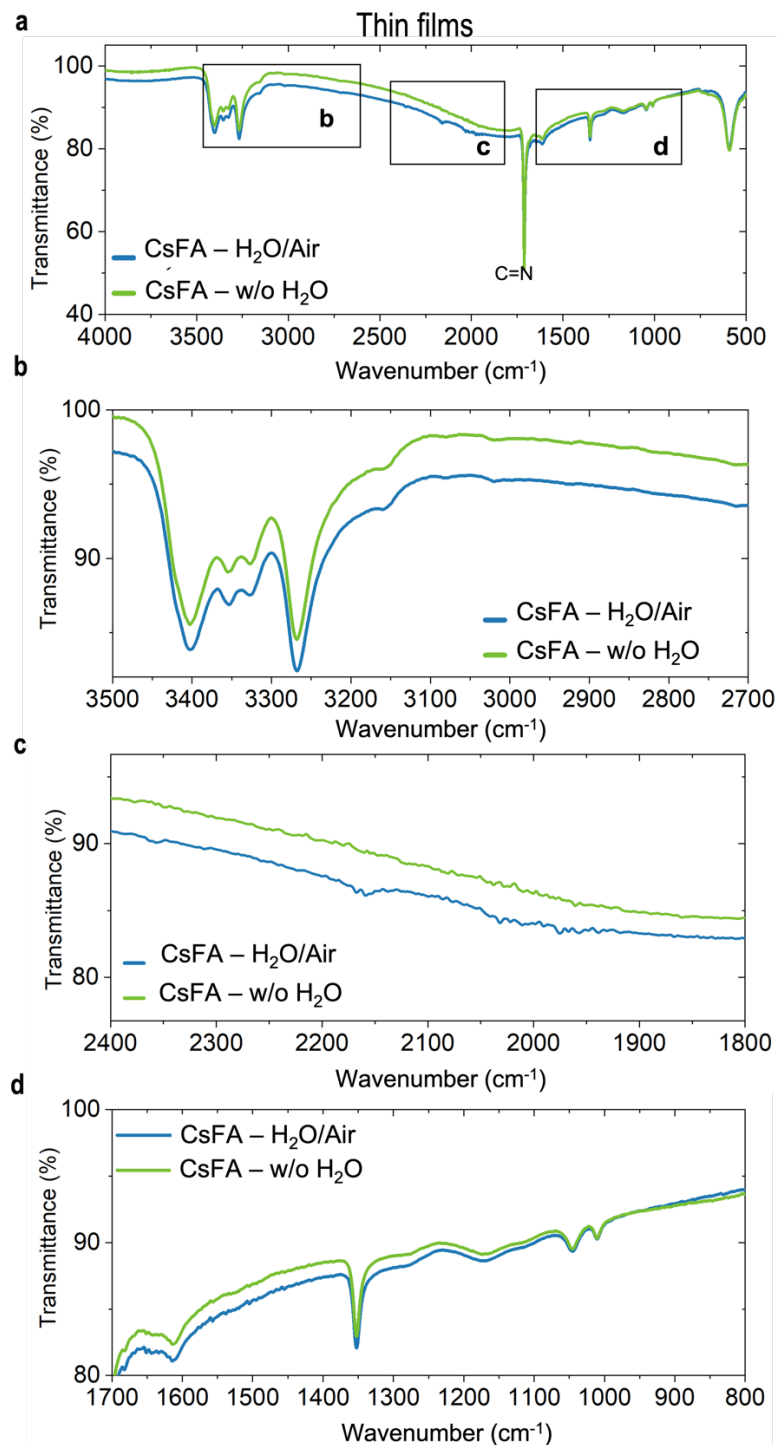


Figure BS15. FTIR $\text{Cs}_{0.17}\text{FA}_{0.83}\text{PbI}_3$ thin films (CsFA). (green) Without (w/o) H_2O exposure deposited, and synthesized in a nitrogen glovebox, and measured in air. (blue) CsFA films after *ex-situ* exposure to $\text{H}_2\text{O}/\text{Air}$ with relative humidity 80% for 20 hours.

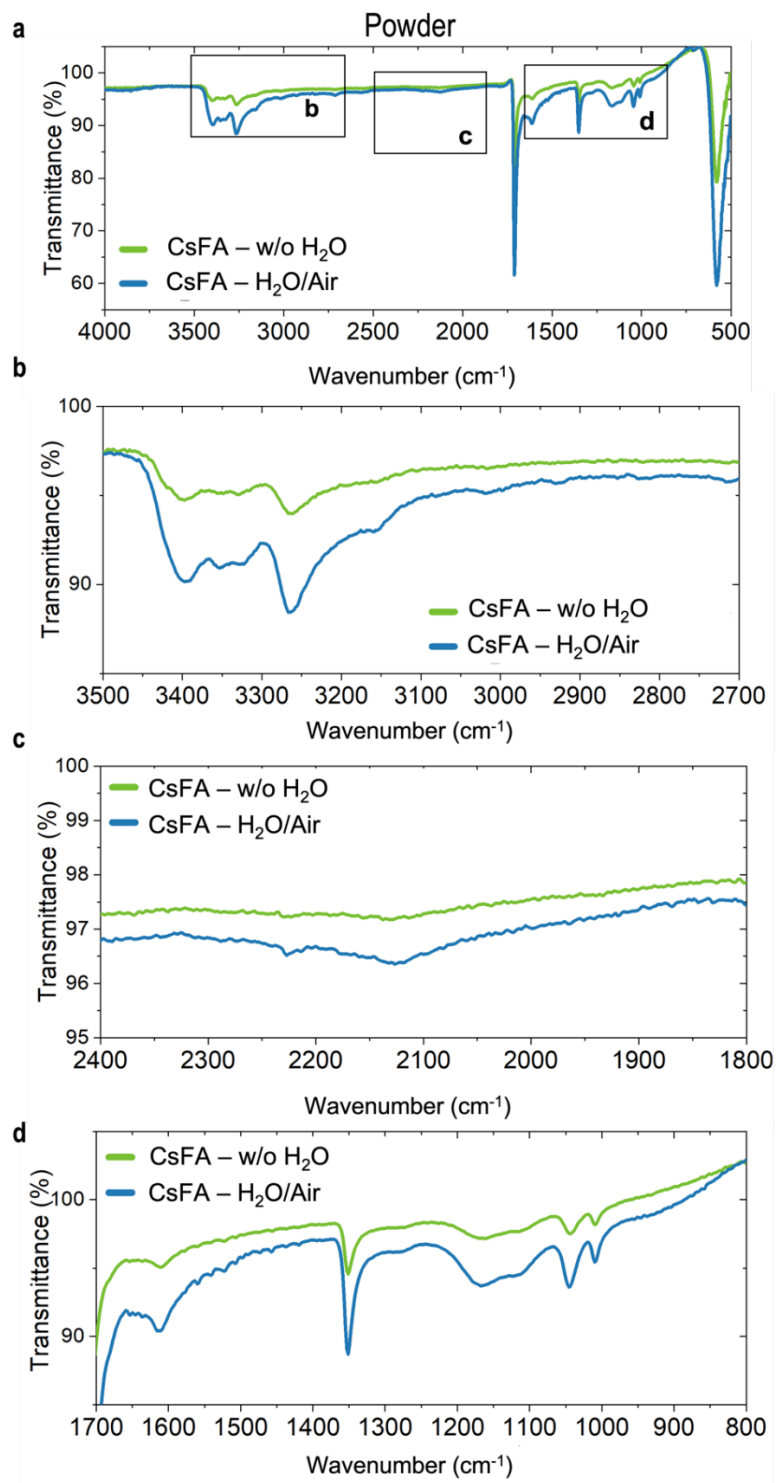


Figure BS16. FTIR Cs_{0.17}FA_{0.83}PbI₃ powders (CsFA). (green) Without (w/o) H₂O exposure, deposited, and synthesized in a nitrogen glovebox, and measured in nitrogen glovebox without air exposure. (blue) CsFA films after *ex-situ* exposure to H₂O/Air with relative humidity 80% for 20 hours.

Table BS8. FTIR peaks and assignment for powders and thin films. ²⁶²⁻²⁶⁵

Wavenumber (cm ⁻¹)		Peak Assignment
Powder	Thin Films	
3400	3403	N-H stretches
3352	3353	
3324	3325	
3264	3267	Symmetric NH ₃ ⁺ stretch
3156	3156	Asymmetric NH ₃ ⁺ stretch
1708	1705	C=N stretch Symmetric
1600	1610	Skeletal C-C, C-N bending
1350	1352	
1275	1270	
1167	1172	
1043	1047	
1007	1010	
579	595.9	

B.6 DFT Calculations

The DFT calculations were entirely done by Dr. Waldemar Keiser, supervised by Professor Filippo De Angelis, from the CNR-SCITEC, Italy.

B.6.1 Surface Models and Computational Details

Density functional theory (DFT) calculations of the interaction of oxygen and water molecules with perovskite surfaces were performed within the Quantum Espresso software package.²⁵⁴ Geometry optimization of the slab models were performed using the PBE exchange-correlation functional²⁶⁶ with plane-wave basis set cutoffs for the smooth part of the wave functions and augmented electronic density expansions of 40 and 320 Ry, respectively. Dispersion interactions are captured within the DFT-D3 scheme.²⁶⁷ Electron-ion interactions are described by ultrasoft, scalar-relativistic pseudo-potentials with electrons from O, N, and C 2s, 2p; H 1s; I 5s, 5p; Cs 5s, 5p, 6s; and Pb 6s, 6p, and 5d shells explicitly included in the calculations. The cell is generated starting from the β -phase of FAPbI₃²⁶⁸, with subsequent replacing of 6 of 32 FA⁺ by Cs⁺ cations within a 2×2×2 supercell, resulting in a Cs_{0.19}FA_{0.81}PbI₃ composition. Subsequent geometry and cell optimization, keeping angles fixed, are performed before generation of the slab models. The PbI₂- and Cs_xFA_{1-x}I-terminated perovskite slab models were made of 5 inorganic layers and of 3 inorganic layers, respectively, as shown in **Figure BS17**. A vacuum region of at least 15 Å was added on top of each surface. For the calculation of water adsorption on PEA cations, we created a PEA₂PbI₄ slab model made of 2 inorganic layers with PEAI-termination and >15 Å vacuum within a 2×2 supercell along a and b direction, using experimental cell parameters.²⁶⁹ In all calculations, the Brillouin zone is sampled at Γ -point.

B.6.2 Modeling of Reactions

Rx.1: The formation energies of oxidized iodide species, IO_n^- , are calculated as follows:

$$\Delta E = E(\text{slab} + \text{IO}_n^-) - E(\text{slab}) - \frac{n}{2} E(\text{O}_2)$$

where $E(\text{slab} + \text{IO}_n^-)$ is the energy of the surface model containing the IO_n^- , $E(\text{slab})$ is the energy of the pristine slab, and $E(\text{O}_2)$ is the energy of an oxygen molecule.

Rx.2: The formation energy of lead(II) iodate, $\text{Pb}(\text{IO}_3)_2$, is calculated as follows:

$$\Delta E = E(\text{slab} + \text{Pb}(\text{IO}_3)_2) - E(\text{slab}) - 3E(\text{O}_2)$$

where $E(\text{slab} + \text{Pb}(\text{IO}_3)_2)$ is the energy of the surface model containing the $\text{Pb}(\text{IO}_3)_2$.

Rx.3: The formation energies of a PbI_2 vacancy upon removal of a $\text{Pb}(\text{IO}_3)_2$ unit is calculated as follows:

$$\Delta E = E(\text{def.}) - E(\text{slab} + \text{Pb}(\text{IO}_3)_2) + \mu(\text{Pb}(\text{IO}_3)_2)$$

where $E(\text{def.})$ is the defective surface the PbI_2 vacancy, and $\mu(\text{Pb}(\text{IO}_3)_2)$ is the chemical potential of lead (II) iodate. To obtain the chemical potential, we calculated the energy of a bulk lead (II) iodate²⁷⁰ available at CCDC 1635205. Geometry optimization of the lead (II) iodate phase were done using high $8 \times 8 \times 1$ k-point sampling and D3 corrections at the PBE level of theory.

B.6.3 DFT Model of Hydration

DFT calculations of the oxygen molecular orbitals are performed using the Gaussian09 program package.²⁷¹ Geometry optimization in water was done using the C-PCM model²⁷² using explicit solvation by four water molecules. All quantities are calculated employing the hybrid B3LYP functional²⁷³ along with 6-311g** basis set and D3 corrections.

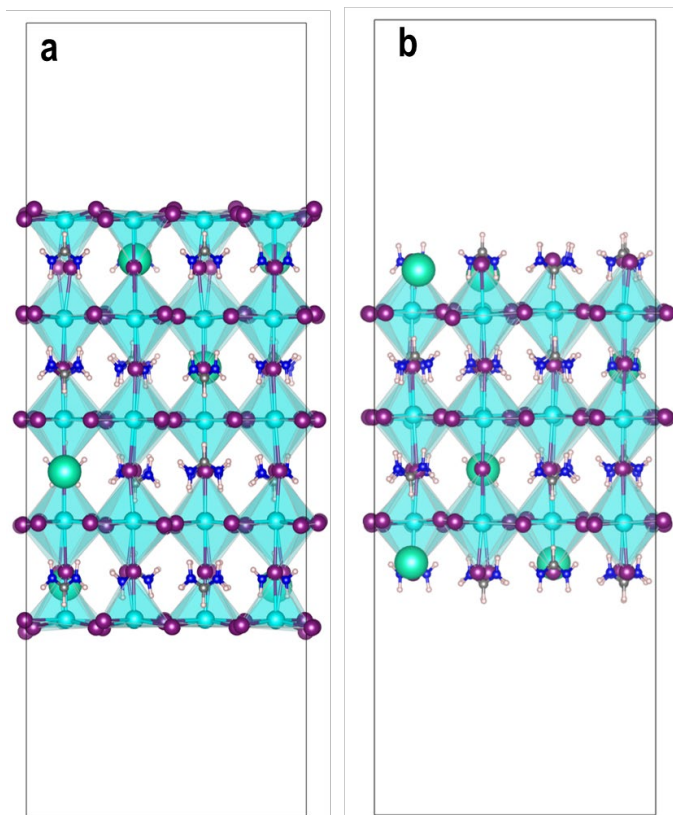


Figure BS17. Surface models of $\text{Cs}_{0.2}\text{FA}_{0.8}\text{PbI}_3$ with a) PbI_2 -termination and b) CsFAI-termination. Following color code is used for the atomic representations: purple, I; cyan, Pb; blue, N; green, Cs; gray, C; white, H.

Table BS9. Adsorption energy of O_2 on PbI_2 - and CsFAI-terminated perovskite surfaces, see Figure S17. Values in parentheses are given without D3 corrections. ^a The hydrated PbI_2 -terminated slab was used as reference to calculate the O_2 adsorption energy.

Surface	Adsorption Site	Adsorption energy / eV
PbI_2 -terminated	Pb	-0.17 (-0.05)
	Cs top site	-0.22 (-0.05)
	FA top site	-0.03 (-0.04)
	V_I	-0.21 (-0.09)
	Hydrated ^a	-0.31 (0.07)
CsFAI-terminated	Cs top site	0.34 (0.27)
	FA top site	0.06 (0.11)

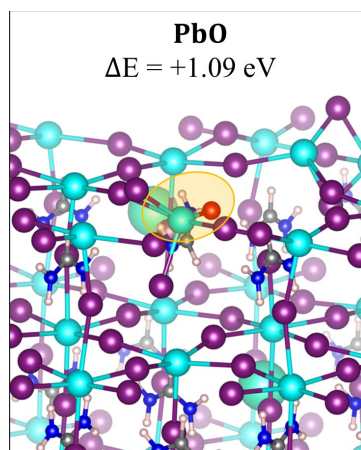


Figure BS18. DFT calculation of PbO formation at a defective PbI₂-terminated surface. An oxygen atom is placed at an iodide vacancy and bonded to Pb as initial setup. The relaxed geometry shows a reaction energy of +1.09 eV, being thermodynamically unfavorable.

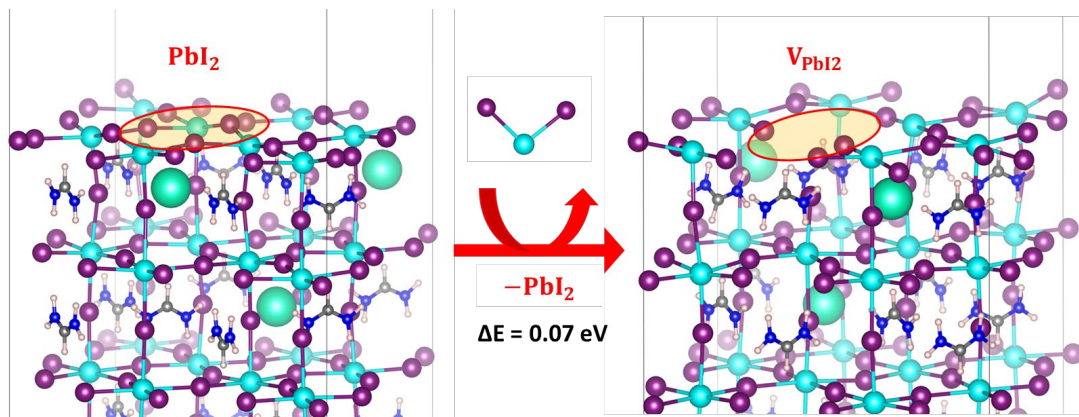


Figure BS19. DFT calculation of PbI₂ vacancy formation: (left) pristine PbI₂-terminated surface, (right) defective surface containing a PbI₂ vacancy. The reaction occurs by removal of a PbI₂ unit from the surface, showing positive reaction energy of 0.07 eV. Following color code is used for the atomic representations: purple, I; cyan, Pb; blue, N; green, Cs; gray, C; white, H.

Table BS10. Energy of π^* orbitals of molecular oxygen in vacuum and hydrated on the B3LYP/6-311G** level of theory with empirical D3 corrections. Effect of water is modeled by placing 4 water molecules next to the oxygen and the use of an implicit solvation model in Gaussian09 (see computational details).

Environment	Orbital energy / eV
Vacuum	-3.185
Water	0.99163783

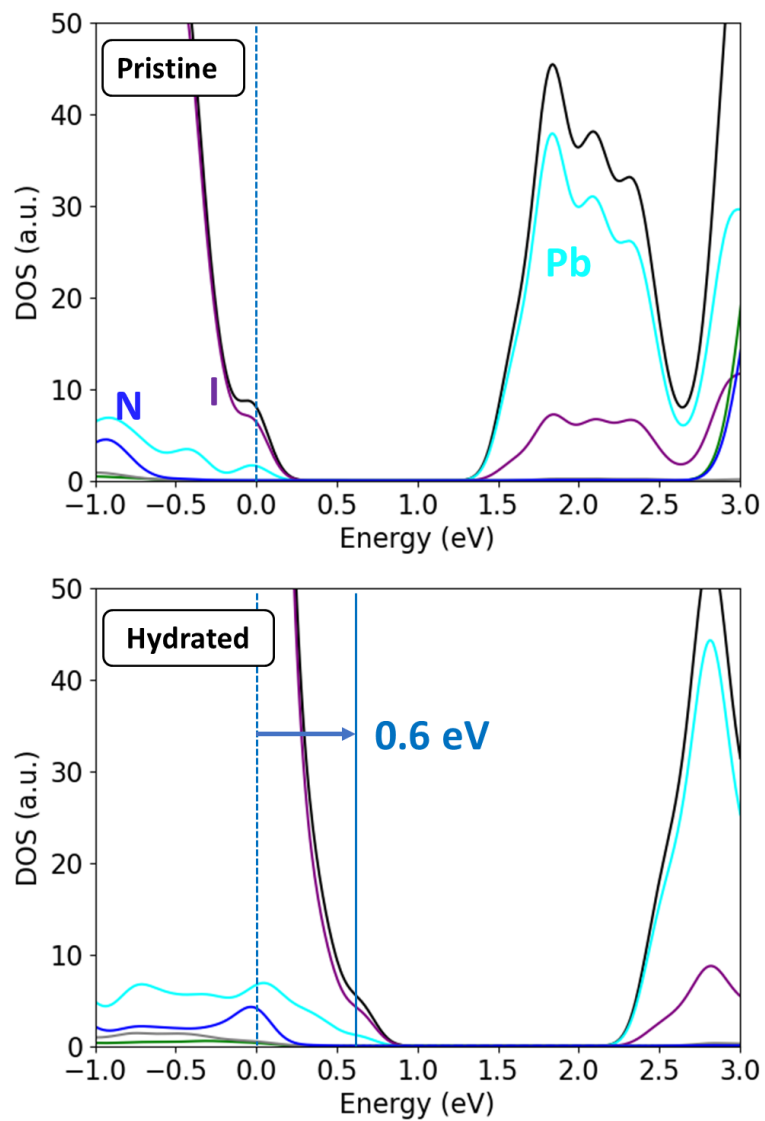


Figure BS20. Density of states (DOS) of the perovskite slab for the pristine and hydrated surface. All DOS are aligned at the C 2s peak of a bulk FA cation, and energies are referenced to the VBM of the pristine surface. The shift in VBM is explicitly highlighted in the lower panel. Following color code is used for the atomic representations: purple, I; cyan, Pb; blue, N; green, Cs; gray, C; white, H.

B.6.5 DFT Superoxide Formation

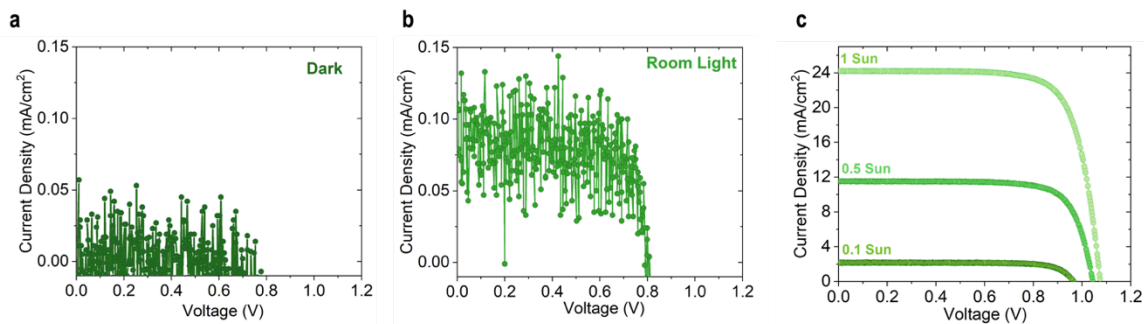
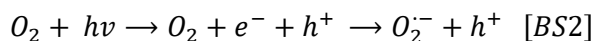
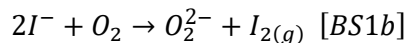
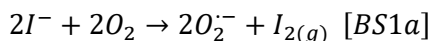


Figure BS21. Current-voltage curves of a $\text{Cs}_{0.17}\text{FA}_{0.83}\text{PbI}_3$ solar cell of the architecture shown in Fig.5d of the main text, untreated. a) Dark, b) room light of the laboratory where the measurement was done, non-quantified, c) comparison of different sun-light intensities: 0.1 sun, 0.5 sun, and 1 sun with intensity AM 1.5.

The current-voltage characteristic of a CsFA perovskite solar cell at room light shows how for a low-intensity, not quantified, room light the device creates a photocurrent and photovoltage. Free charge carriers can be generated from a regular source of light. In addition, we show in **Figure BS21** how the current density and voltage changes as a function of light-intensity, quantified by 1 sun of illumination AM1.5.

We performed DFT calculations of superoxide formation in $\text{H}_2\text{O}/\text{Air}$ and from mobile ions. Recent studies raised the importance of superoxide in perovskite degradation from photooxidation.^{22,187,188,274} Here, we consider potential superoxide ($\text{O}_2^{\bullet-}$) and peroxide (O_2^{2-}) formation mechanisms from mobile iodine ions (Rx: *BS1a* and *BS1b*) and from light (Rx: *BS2*):



Reaction S1 is considered at the FAI-terminated surface, where oxygen molecules are adsorbed on iodide vacancies, forming molecular iodine I_2 by superoxide or peroxide formation, see

Figure BS22. DFT calculations predict a formation energy of +0.81 eV for *Reaction S1a*, being thermodynamically unfavorable in dark. For the formation of peroxide, we obtain a reduced formation energy of +0.65 eV, while the optimized structure shows a deprotonated FA cation by peroxide, resulting in HOO⁻. However, both processes are thermodynamically unfavorable, suggesting a reduced relevance of iodine oxidation via superoxide/peroxide formation.

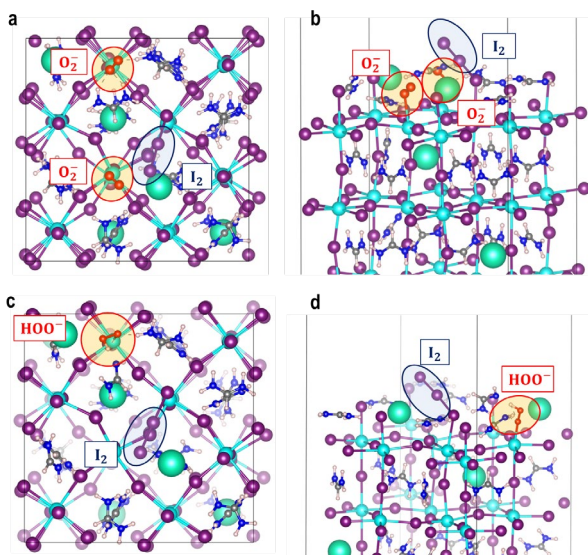


Figure BS22. Top and side view of the FAI-terminated perovskite surface with oxidized iodine, I₂, via (a,b) superoxide [reaction 1a] and (c,d) peroxide formation [reaction 1b]. Following color code is used for the atomic representations: purple, I; cyan, Pb; blue, N; green, Cs; gray, C; white, H.

Reaction BS2 starts from O₂ adsorption on the surface, followed by the photoexcitation of the perovskite at light, and subsequent electron transfer from the perovskite to the O₂, resulting in O₂^{•-} as shown in **Figure BS23**. The superoxide formation energy from reaction [BS2] is modeled in line with literature²² using the following equation:

$$E_{\text{react}}([2]) = E(\text{slab} + \text{O}_2^{\bullet-}) - E(\text{O}_2) - E(\text{slab}^-) + E_{\text{gap}}$$

where $E(\text{slab} + \text{O}_2^{\bullet-})$ is the total energy of the CsFA perovskite slab containing the adsorbed superoxide O₂^{•-}; $E(\text{O}_2)$ is the energy of an isolated O₂ molecule; $E(\text{slab}^-)$ is the energy of the

CsFA perovskite slab in excited state with charge -1; E_{gap} is the band gap of the CsFA perovskite to generate the charge carriers.

Regular room light creates a small photo-current and photo-voltage in a CsFA perovskite solar cell (**Figure BS21**), thus *reaction BS2* is more likely in explicit illumination at 1 sun intensity. We explicitly consider *reaction BS2* at different $\text{CS}_{0.2}\text{FA}_{0.8}\text{PbI}_3$ surfaces. Considering the electronic structure of the pristine surface in **Figure BS24**, the unoccupied π^* orbital of the adsorbed O_2 is close to the conduction band of the perovskite surface. On the hydrated surface in **Figure BS24b**, H_2O molecules enhance O_2 adsorption, $E_{\text{ads}} = -0.31$ eV, and introduce a striking shift of the π^* orbital from 1.44 eV to 0.44 eV above the valence band maximum (VBM) as seen the hydrated one. H_2O molecules strongly bond with undercoordinated surface Pb ions, resulting in an upshift of VBM by 0.58 eV. Moreover, the enhanced O_2 attraction yields a stabilization of the π^* orbital by 0.42 eV. Interestingly, O_2 adsorbed at defects such as V_I^+ ($E_{\text{ads}} = -0.21$ eV) results in a comparable shift of the unoccupied π^* orbital with respect to the VBM, mainly due to the downshift of the π^* orbital by 0.72 eV (Defect in **Figure BS24**).

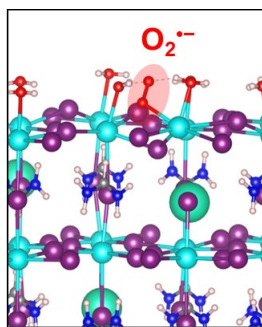
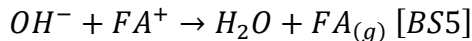
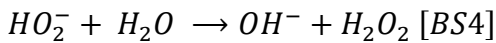
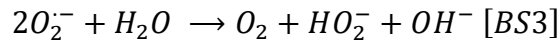


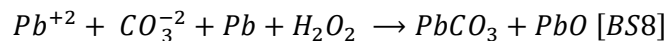
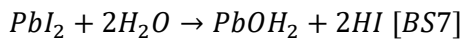
Figure BS23. Light induced superoxide at the hydrated PbI_2 -terminated perovskite surface [reaction 2]. Following color code is used for the atomic representations: purple, I; cyan, Pb; blue, N; green, Cs; gray, C; white, H.

Finally, we computed the superoxide formation energies from the above mechanisms. The formation of superoxide by I₂ release, *reaction BS1*, shows a large energy of 0.81 eV, higher than the energies of *reaction BS2* seen in **Figure BS25**. Upon illumination, we observe similar energies for O₂^{•-} formation at the pristine and at the defective surfaces. In contrast, we obtain a substantial reduction in O₂^{•-} formation energy to 0.39 eV at the hydrated surface, which can be attributed to the stabilization of O₂^{•-} by hydrogen bonding with H₂O molecules. Consequently, the low formation energy suggests an increased superoxide yield at the hydrated CsFA perovskite surface compared to the pristine dry surface under light illumination.

We hypothesize on subsequent reactions driven by superoxide in a H₂O/Air atmosphere. O₂^{•-} reacts with adsorbed water molecules to form hydroperoxyl, HO₂⁻, and hydroxyl radicals, OH⁻ [Rx:BS3].²⁷⁵ These oxygen species catalyze further reactions with water, forming hydrogen peroxide, H₂O₂, among other products [Rx: BS4].^{187,189} Reactive species, such as OH⁻, rapidly deprotonate the FA⁺ [Rx: BS5].



In addition to the chemical reactions described in the text, we consider other reactive species in the air such as CO₂, we show a possible chemical reaction of CO₂ with water [Rx: BS6] that leads to the formation of carbonates. Other reactions associated with Pb species are shown in [Rx: BS6 - BS8].



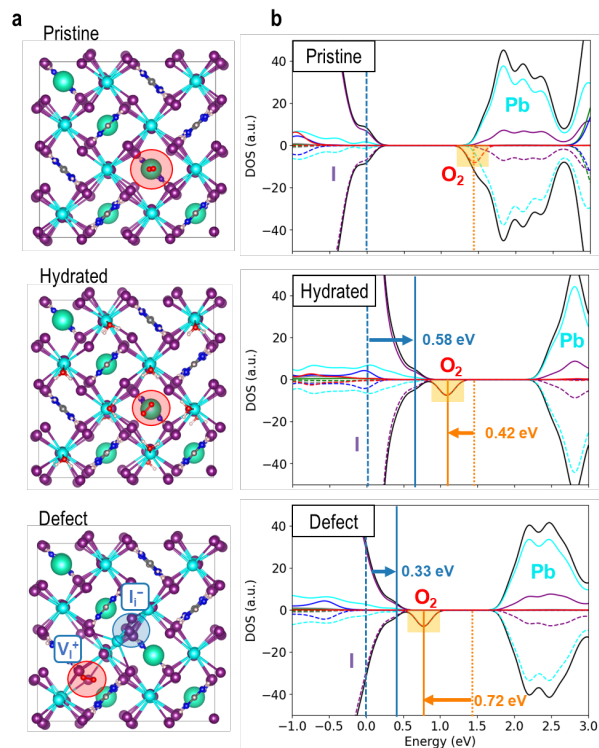


Figure BS24. a) Top view of the PbI₂-terminated perovskite surface after O₂ adsorption on the (top) pristine, (middle) hydrated, and (bottom) defective surface on an iodide vacancy site. The adsorbed O₂ molecule is highlighted by a red circle. b) Density of states (DOS) from spin-polarized DFT calculations for the pristine, hydrated, and defective surfaces after O₂ adsorption. The unoccupied π^* orbitals of the O₂ molecule are explicitly highlighted. All DOS are aligned at the C 2s peak of a bulk FA cation, and energies are referenced to the VBM of the pristine surface.

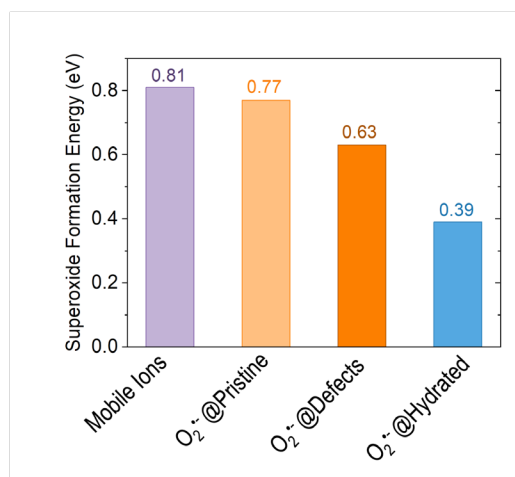


Figure BS25. Superoxide formation energies from mobile ions [Rx. BS1] and from light irradiation of the pristine, defective, and hydrated CsFA perovskite surface [Rx. BS2].

APPENDIX C. SUPPORTING INFORMATION: PREVENTING PHASE TRANSFORMATIONS IN HALIDE PEROVSKITES

C.1 PEAI in FAPI

C.1.1 Structural Analysis

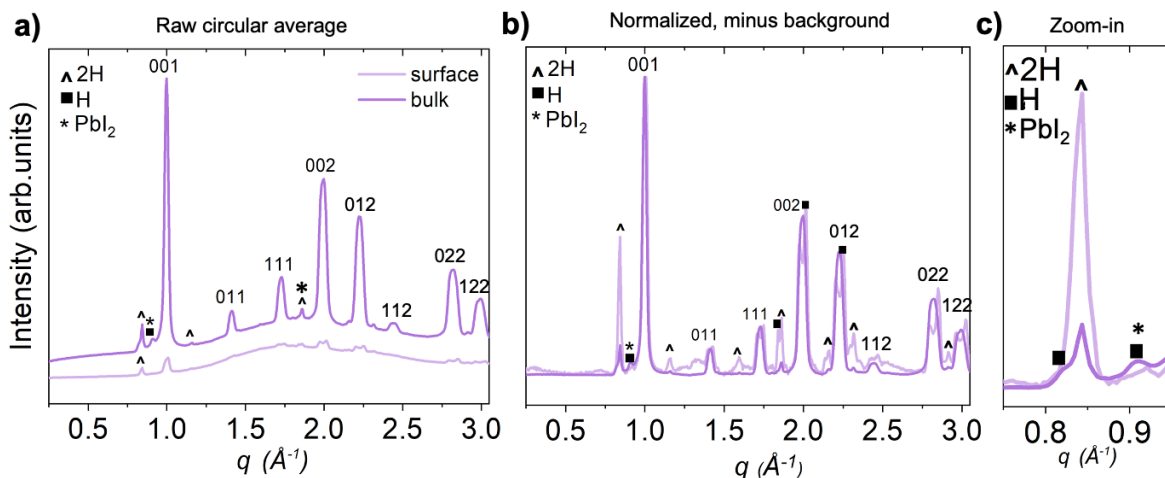


Figure CS1. 3D FAPbI₃. Circular average diffraction pattern at the surface and bulk. a) Raw circular average b) normalized and minus background, c) zoom-in into the hexagonal polytypes region. The hkl peaks labeled in all patterns correspond to the cubic FAPbI₃ perovskite of space group $Pm-3m$.

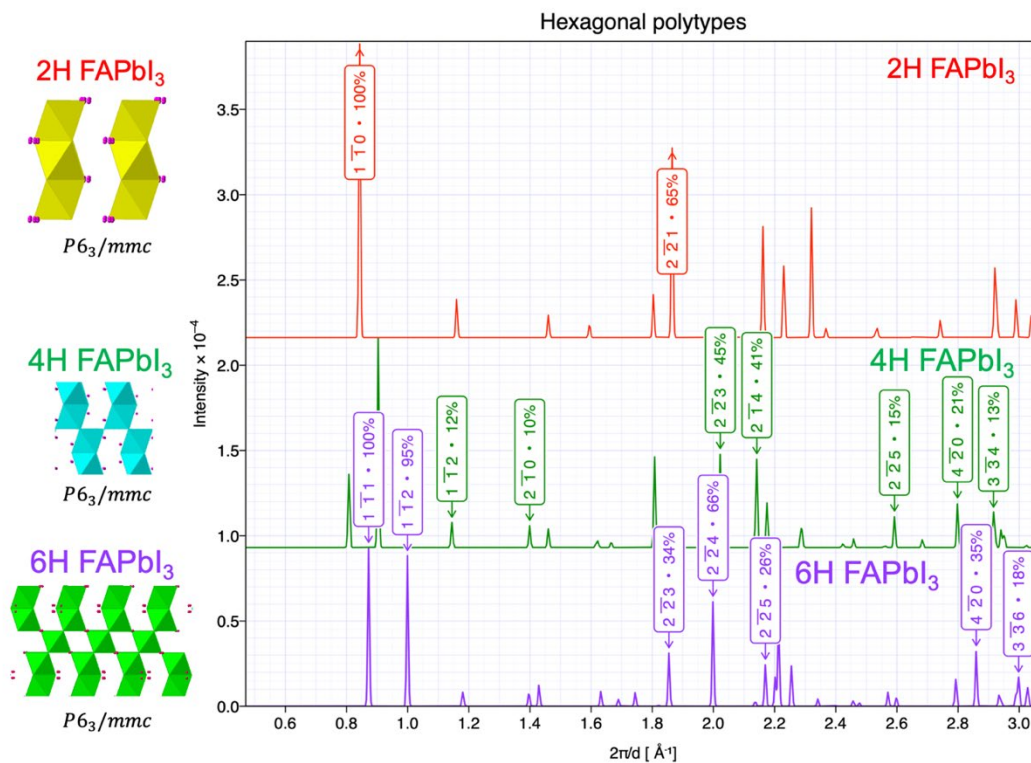


Figure CS2. Simulated diffraction patterns of the FAPbI₃ hexagonal polytypes. Diffraction peaks are labeled with its relative diffraction intensity. cif files were taken from the work by Gratia et al.²²¹

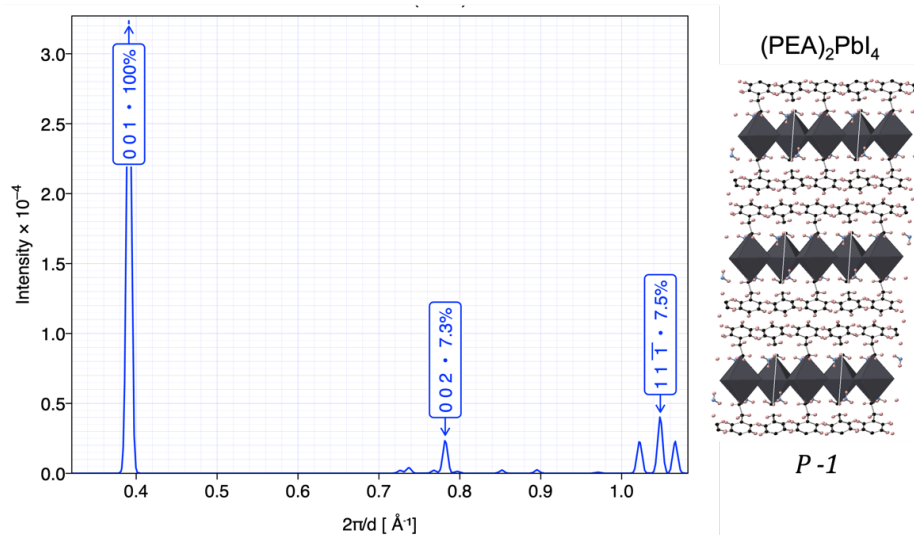


Figure CS3. Simulated diffraction patterns of the (PEA)₂PbI₄ phase. cif files were found on the NMSE database²²⁶ taken from published works.^{276,277}

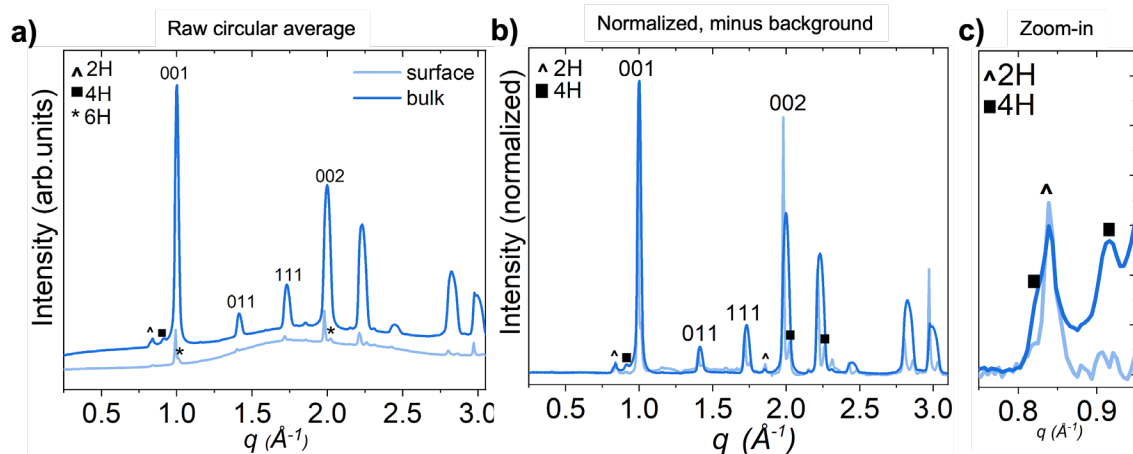


Figure CS4. Circular average diffraction pattern at the surface and bulk 1mg/mL of PEAI + 3D FAPbI₃. a) Raw circular average b) normalized and minus background, c) zoom-in into the hexagonal polytypes region. The *hkl* peaks labeled in all patterns correspond to the cubic FAPbI₃ perovskite of space group *Pm-3m*.

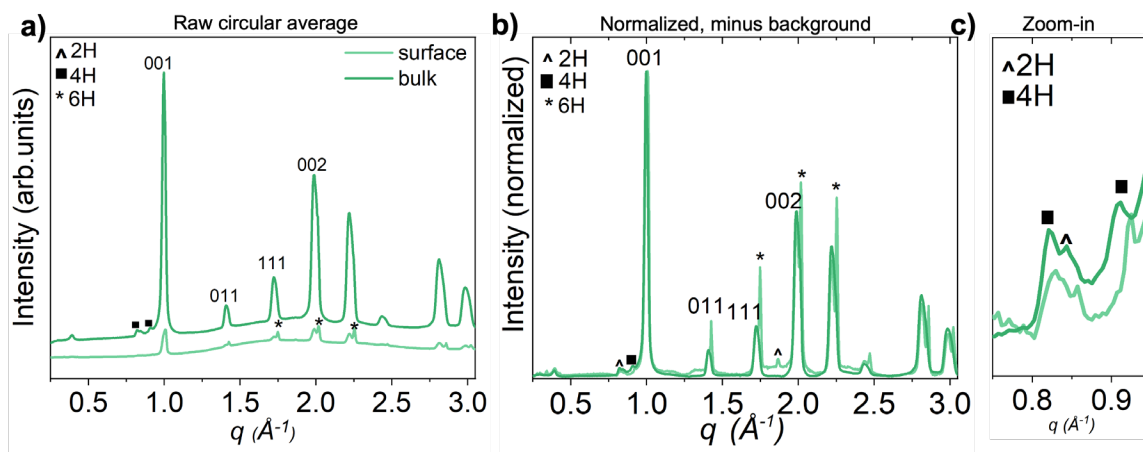


Figure CS5. Circular average diffraction pattern at the surface and bulk 5mg/mL of PEAI + 3D FAPbI₃. a) Raw circular average b) normalized and minus background, c) zoom-in into the hexagonal polytypes region. The *hkl* peaks labeled in all patterns correspond to the cubic FAPbI₃ perovskite of space group *Pm-3m*.

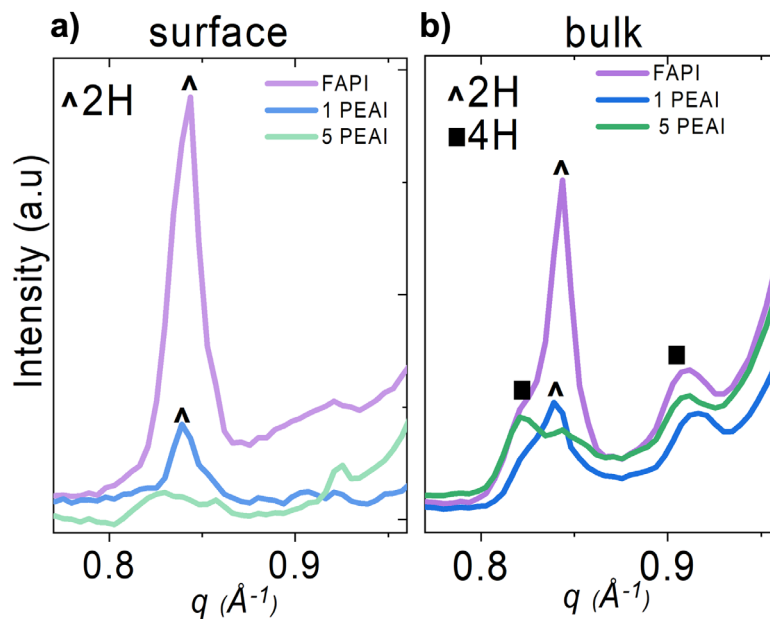


Figure CS6. Overall comparison of the hexagonal polytype region at the surface and bulk.

In the circular average diffraction patterns in **Figures CS2-4**, we observe double peaks for the GIWAXS corresponding to the surface ($\alpha_i=0.05$). These double peaks could be attributed to hexagonal polytypes such as 4H and or 6H, labeled as H in the figures. The most notable splits are observed at the surface, in agreement with the phases observed from the zoom-in regions of the hexagonal polytypes.

C.1.2 Surface Morphology and XPS

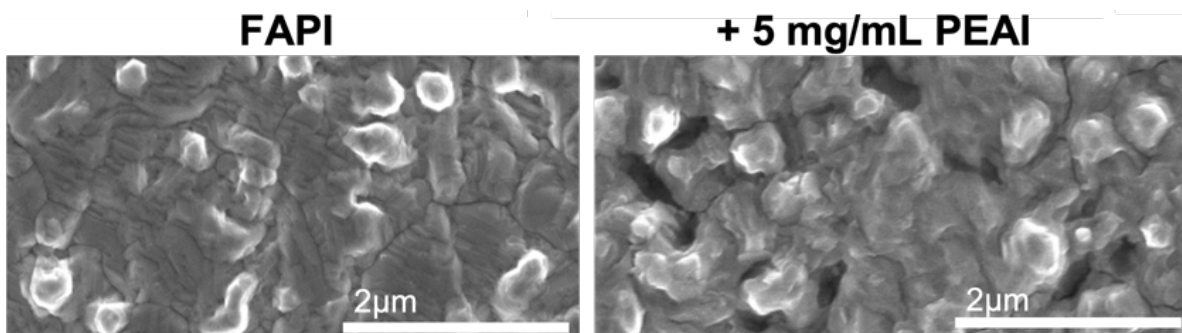


Figure CS7. Surface scanning electron microscopy (SEM) images of pristine, FAPI films treated with 5mg/mL PEAI-treated.

Table CS1. Stoichiometry at the surface in all samples. The amounts of each perovskite component have been normalized to Pb in the table to ease relative comparison of the surface compositions.

	N (PEA)	N (FA)	Pb	I	FA+PEA
FAPI	0	0.99	1	4.14	0.99
1 PEAI	0.22	1.07	1	4.25	1.29
5 PEAI	1.76	0.51	1	5.27	2.28

The morphology of the films is characterized by SEM. **Figure CS7** shows the surface morphology of pure-FAPI and FAPI treated by adding 5mg/mL of PEAI. The film's surface becomes more blurred after PEAI addition indicating increased charging, possibly induced by the formation of an insulating overlayer.

C.1.3 Photoluminescence and THz

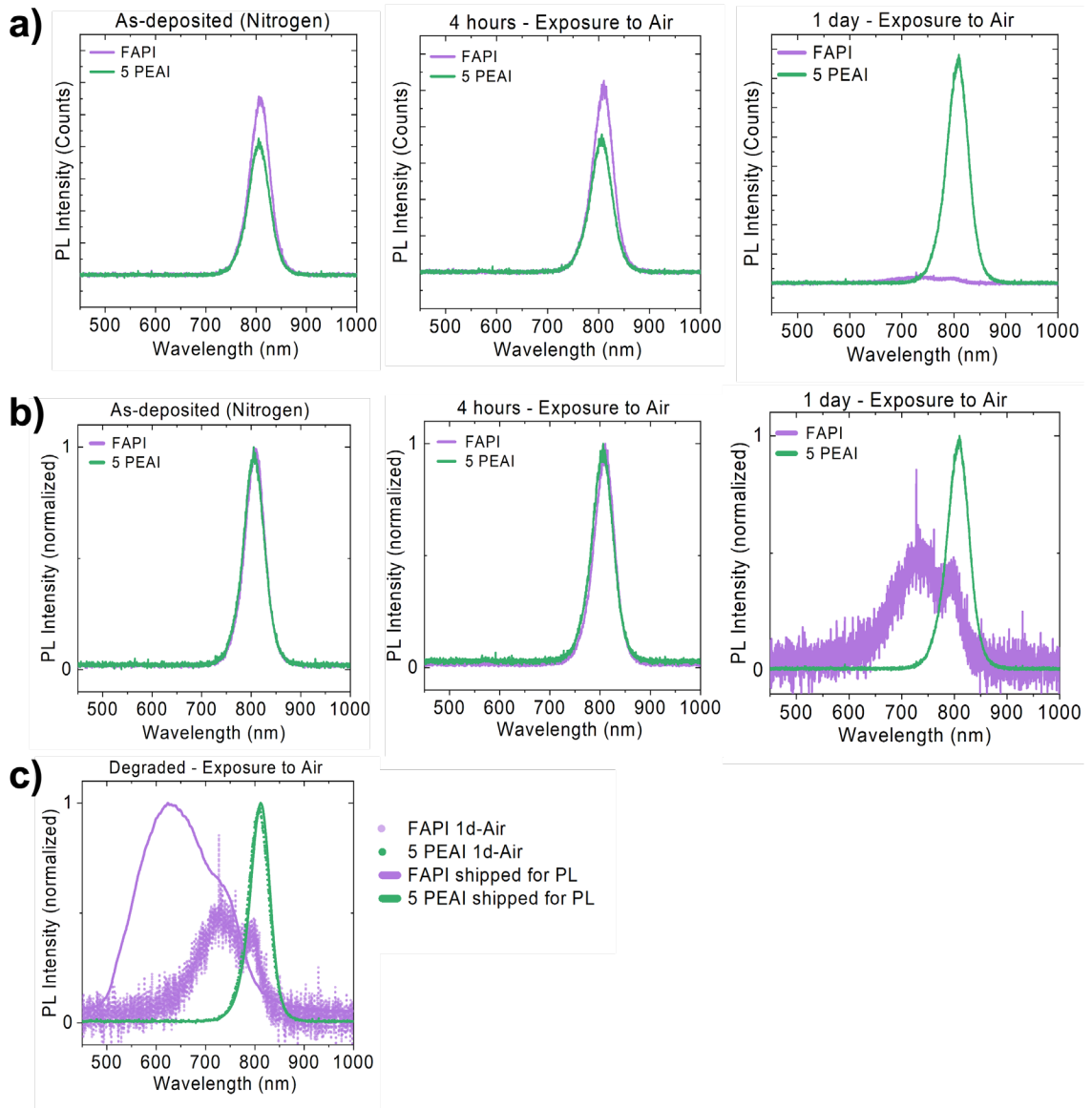


Figure CS8. PL evolution from nitrogen to air for 1) As-deposited films, measured PL inside nitrogen glovebox. 2) After 3 days of deposition and exposed 4 hours to air, 3) After 3 days of deposition and exposed 1 day to air. a) Non-normalized PL intensity, b) Normalized PL intensity, c) Comparison of normalized data with the PL data plotted in the main Chapter 6. The samples in the main text were measured after around 1 week of deposition, plus shipping, and handling in air.

Air Exposure

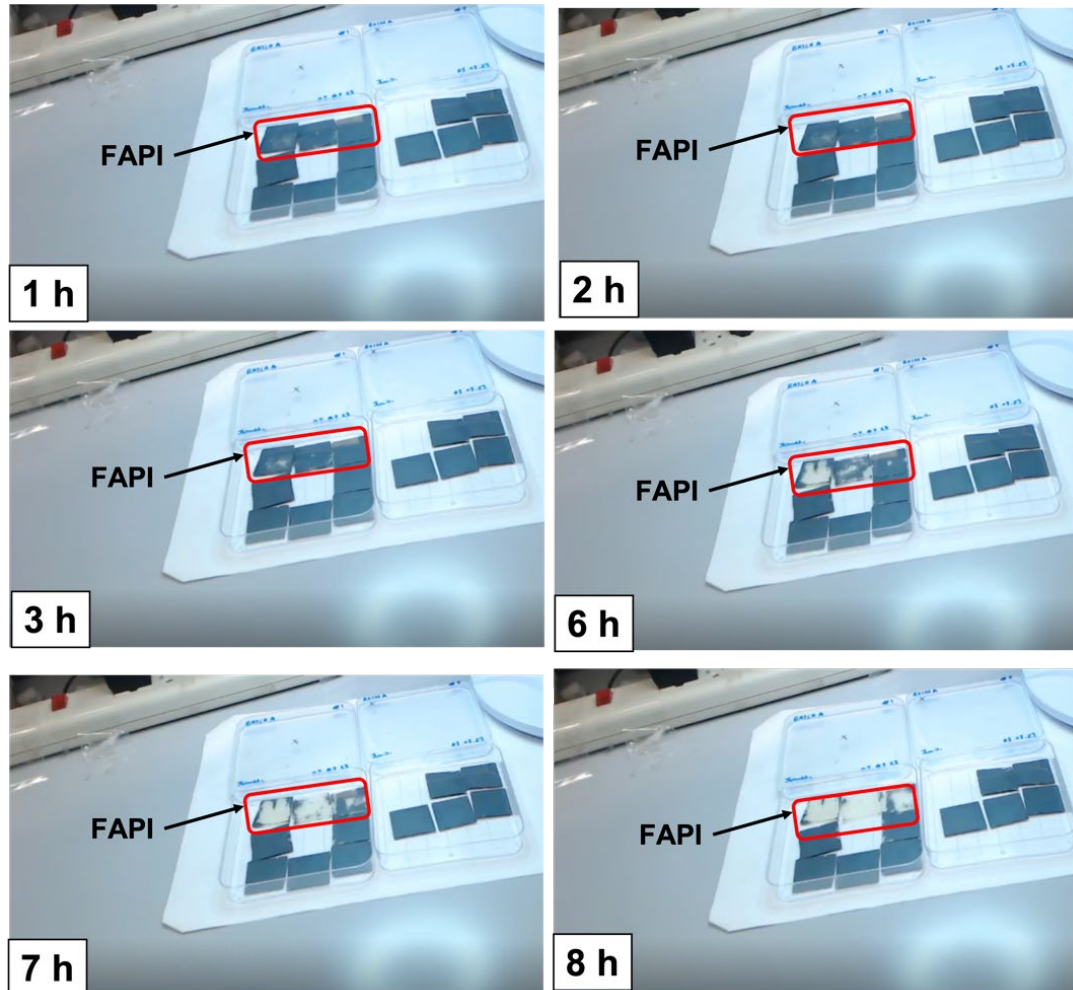


Figure CS9. Air-induced degradation in FAPI films. The exposure to air was done 3 days after deposition and storage in the nitrogen glovebox.

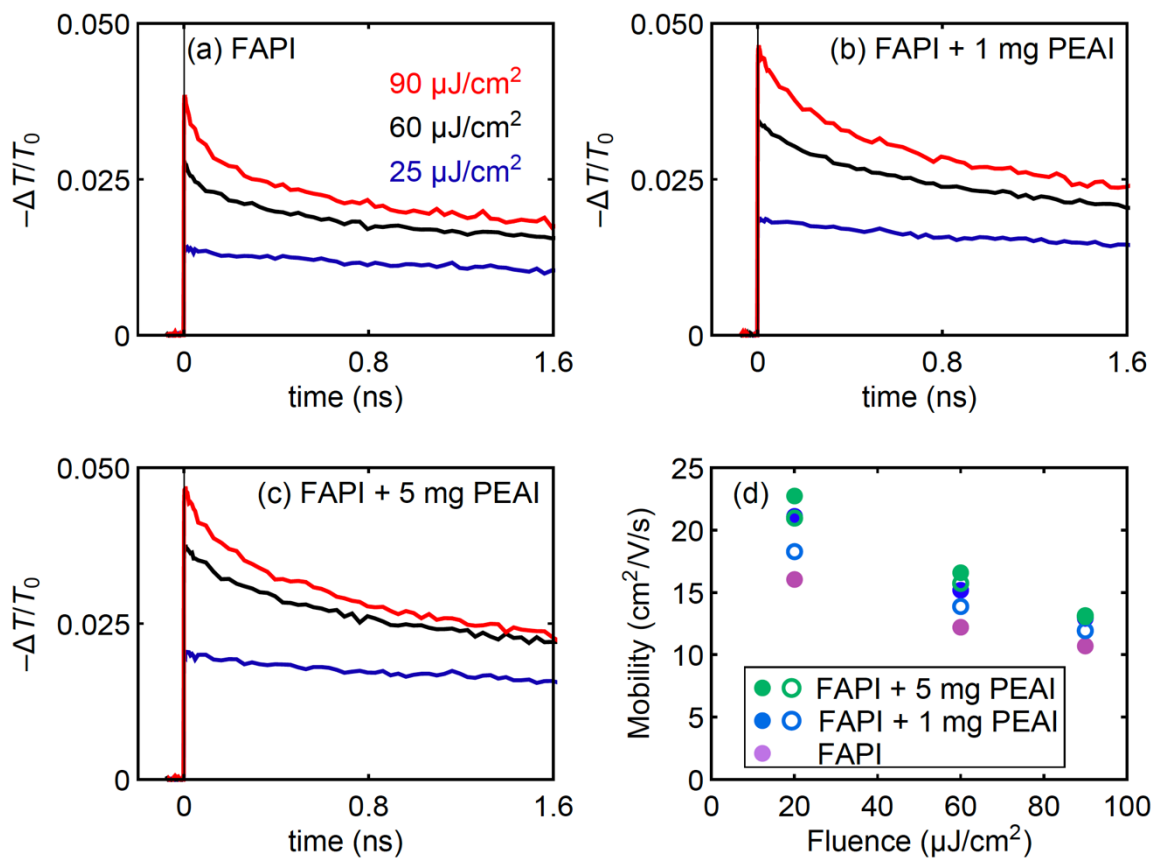


Figure CS10. Time-resolved THz photoconductivity measurements of FAPI, FAPI + 1mg PEAI, and FAPI + 5 mg PEAI. Charge carrier mobilities for FAPI (purple), FAPI + 1mg PEAI (blue), and FAPI + 5mg PEAI (green). Data for annealed samples are shown as open circles. Carrier mobilities at each excitation fluences are calculated from the initial THz transmission changes. The addition of PEAI improves carrier mobility, and upon annealing the carrier mobility reduces.

C.1.4 FAPI Perovskite Solar Cells

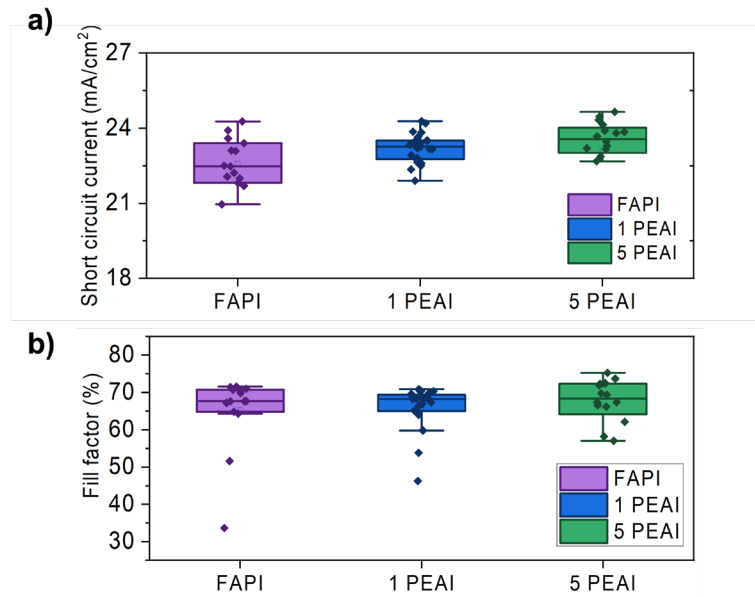


Figure CS11. FAPI solar cells. a) Short circuit current and b) Fill factor for untreated FAPI and treated with PEAI solar cells under simulated AM 1.5 irradiance. The data points are plotted in boxplots which show the median (central line) and the median of the upper and lower halves of the data (top and bottom lines of the box, respectively).

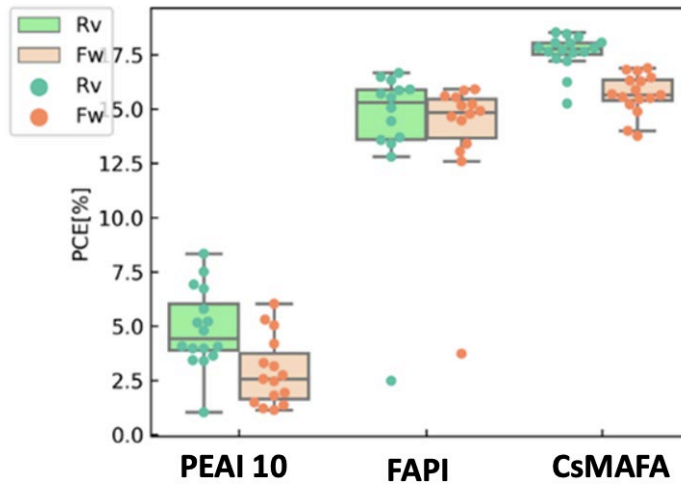


Figure CS12. Perovskite solar cells PCE box plots. Different concentrations of PEAI were tested, such as 10 mg/mL of PEAI (PEAI 10). A different 3D composition without passivation was also fabricated, triple-cation double-halide $\text{Cs}_{0.05}(\text{MA}_{0.17}\text{FA}_{0.83})\text{FAPb}(\text{I}_{0.83}\text{Br}_{0.17})_3$ (CsMAFA).

C.2 PEAI on CsFA: Humidity Exposure

C.2.1 DFT Calculations

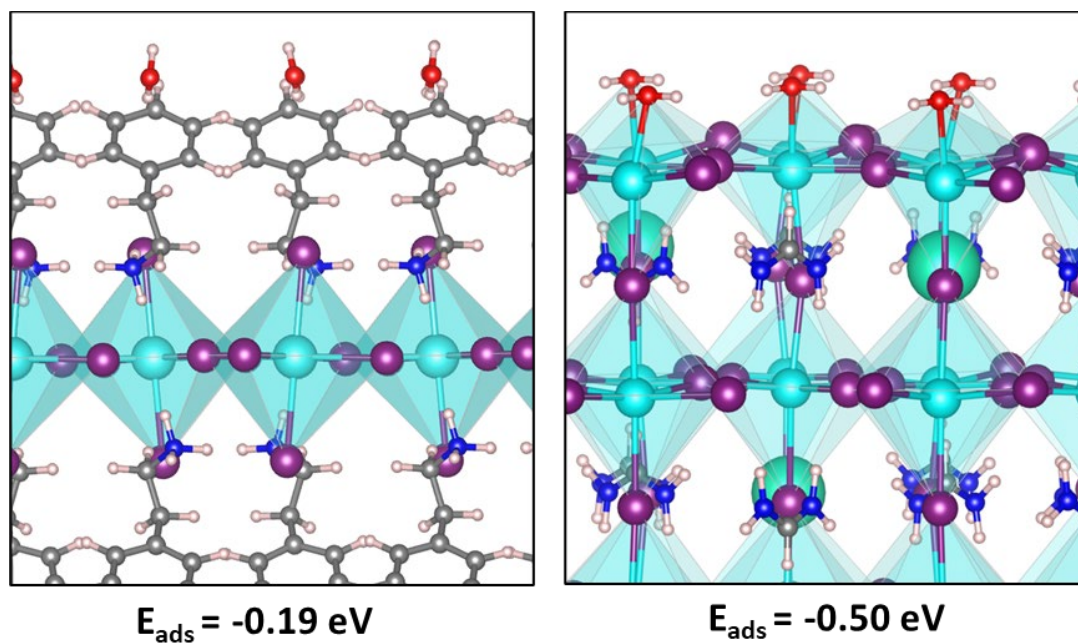


Figure CS13. Water molecule adsorption on the (left) PEAI-terminated surface of a two-dimensional PEA_2PbI_4 perovskite, and (right) PbI_2 -terminated surface of the considered CsFA perovskite. Adsorption energies are given, normalized per water molecule.

C.2.2 *In-situ* humidity by GIWAXS

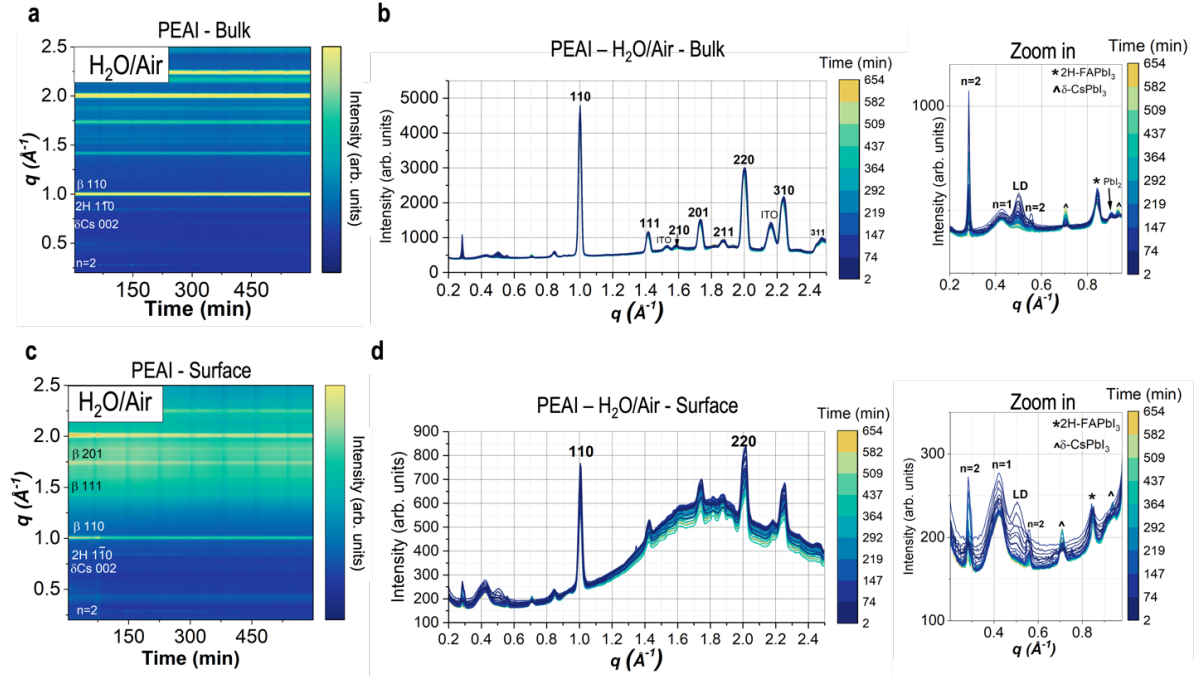


Figure CS14. *In-situ* GIWAXS in H₂O/Air of PEAI-treated samples. Bulk (incident angle 0.5°) a) scattering vector as a function of time exposed to H₂O/Air bulk, b) integrated circular average of the diffraction at the bulk (incident angle 0.5°) and zoom in the PEAI and low-dimensional (LD) phases region bulk. Surface (incident angle 0.1°) c) scattering vector as a function of time exposed to H₂O/Air surface, d) integrated circular average of the diffraction at the surface (incident angle 0.1°) and zoom in the PEAI and low-dimensional (LD) phases region surface.

Note on *in-situ* GIWAXS with PEAI: We observe differences between the surface and bulk measurements. At the surface, there is more n=1 Ruddlesden popper phase (PEA₂PbI₄), while at the bulk it converts into n=2 or other LD PEA-phases.

We analyzed the evolution of the main peaks following the procedure done for **Figure BS3-4 (Appendix B)**, but in this case for the PEAI-treated devices exposed to H₂O/Air in **Figure CS16**. We point out that the non-perovskite phase 2H decreases as a function of time exposed to H₂O/Air. This may be correlated to another mechanism occurring in parallel to

the exposure to H₂O and O₂, of the reaction of the 2H phase with PEAI to form a LD Ruddsden-Popper phase.

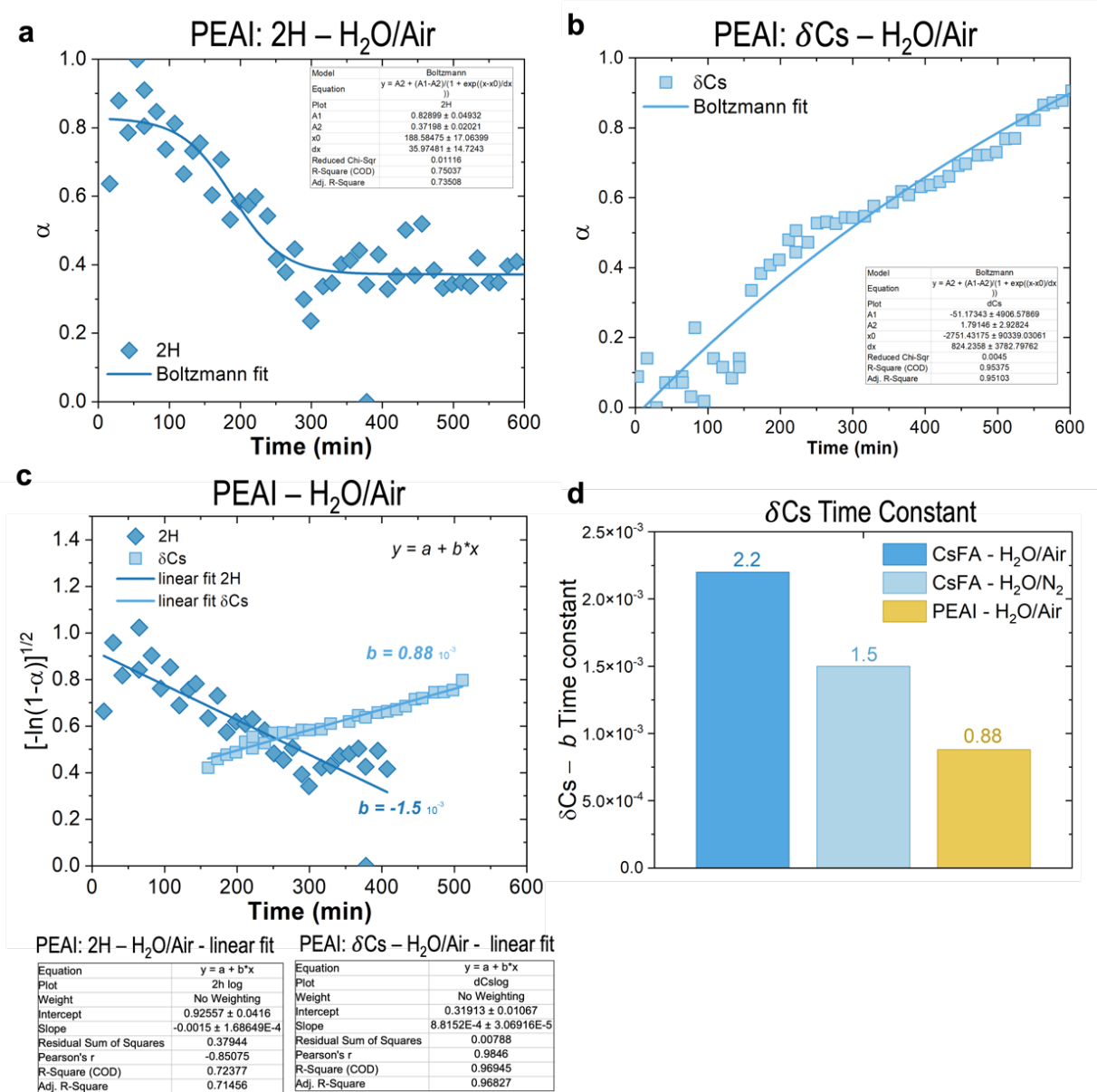


Figure CS15. Peak evolution from integrated area normalized into α and fitted to a Boltzmann sigmoidal function a) PEAI-treated 2H peak in H₂O/Air, b) PEAI-treated δ Cs peak in H₂O/Air. Data fitted into a linear logarithmic function to compare the evolution and calculate time constant (b) for c) PEAI-treated films in H₂O/Air.

C.2.3 CsFA Perovskite Solar Cells

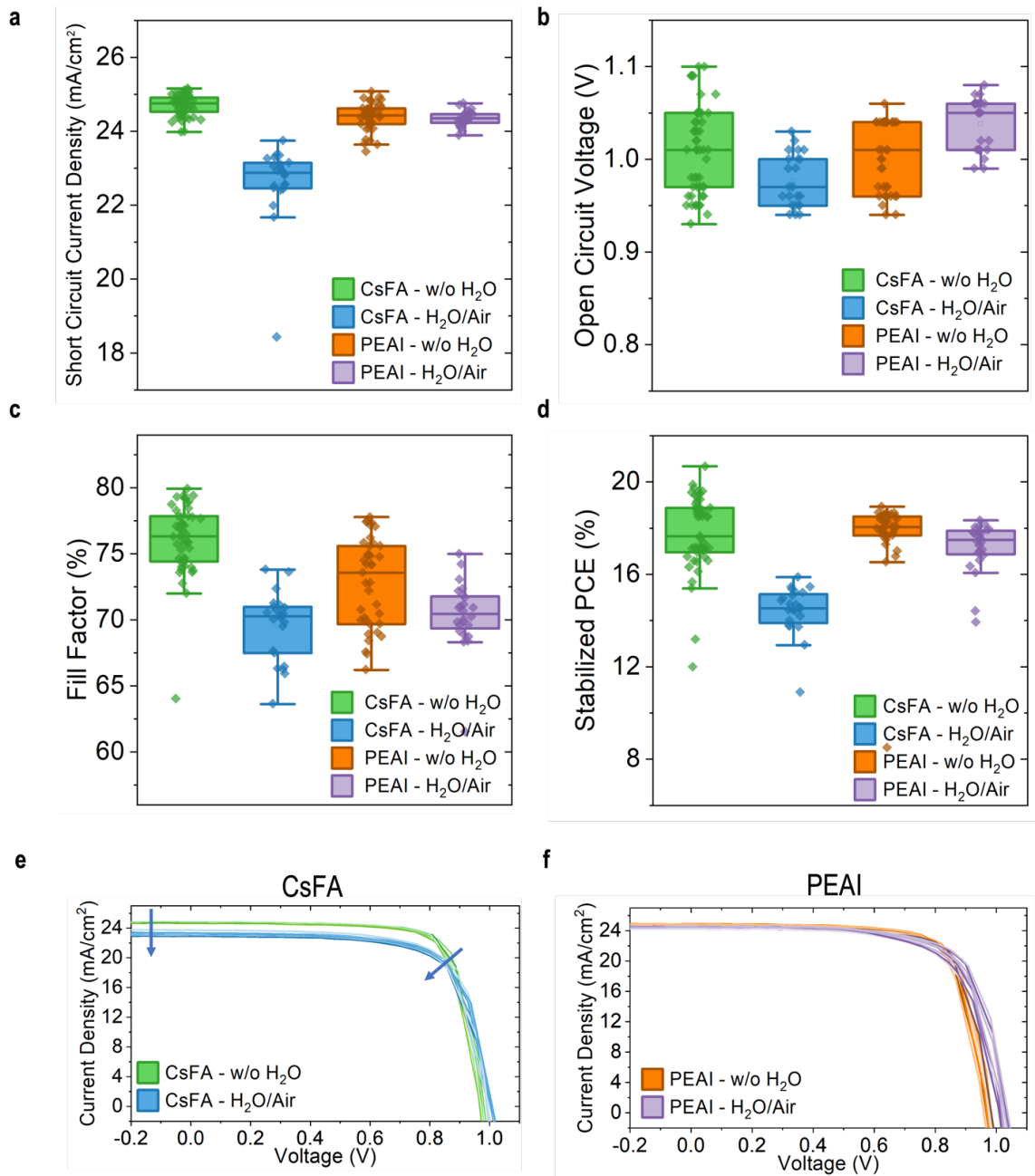


Figure CS16. Solar cells result for the untreated CsFA perovskites, without (w/o) H₂O exposure, after CsFA is *ex-situ* exposed to H₂O/Air, and for PEAI-treated w/o H₂O exposure and after *ex-situ* H₂O/Air exposure. H₂O exposure is done before the Spiro-OMeTAD and Au layers. Figures of merit show: a) Short-circuit current density, b) open circuit voltage, c) fill factor, d) stabilized power conversion efficiency (PCE). Example of current density-voltage curves for e) untreated CsFA and f) PEAI-treated devices without and with H₂O/Air exposure.

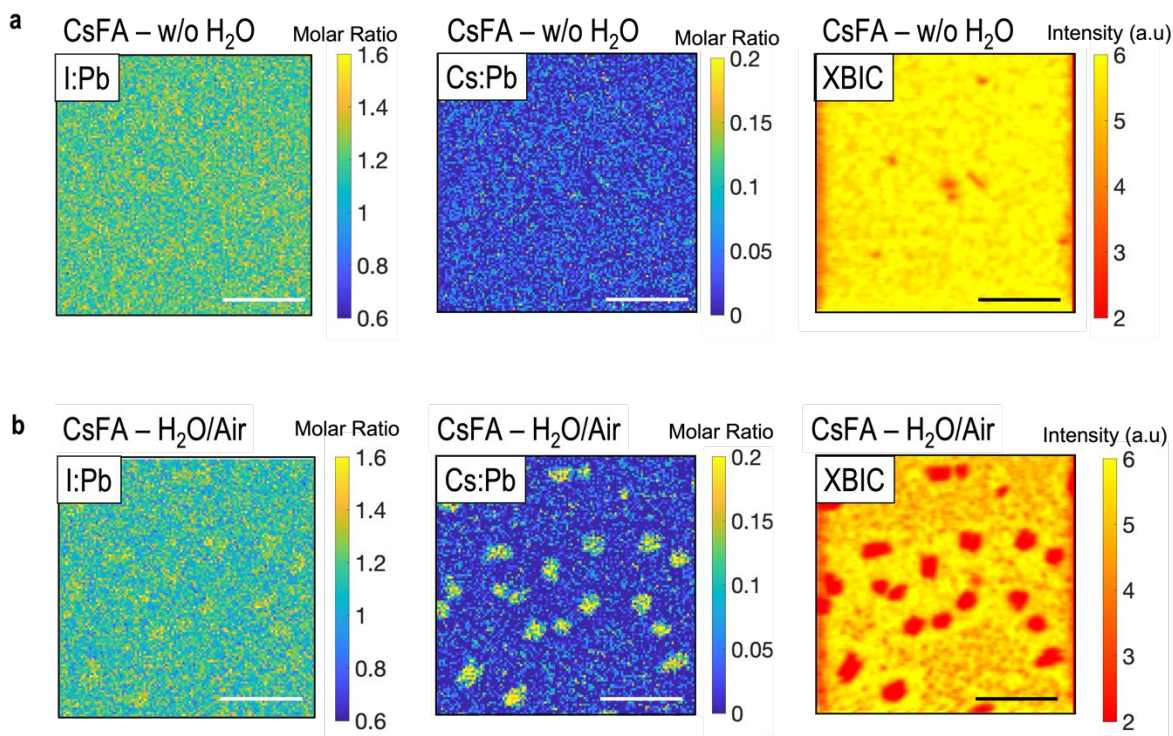


Figure CS17. X-ray fluorescence (XRF) with correlative X-ray beam-induced current (XBIC) done on complete $\text{Cs}_{0.17}\text{FA}_{0.83}\text{PbI}_3$ solar cell devices. a) Without (w/o) H_2O exposure. The samples were exposed to air before the measurement, and the experiment was done in a helium-vented chamber. and b) after *ex-situ* exposure to $\text{H}_2\text{O}/\text{Air}$ with relative humidity 80% for 20 hours. The measurements were done in a Helium-vented chamber. (I:Pb) denotes the calculated molar ratio iodine to lead from mass per area data. (Cs:Pb) denotes the molar ratio cesium to lead. The scale bar is $10\mu\text{m}$.

XRF with correlative XBIC was performed to complete perovskite solar cells (see schematic in **Figure 6.9** in **Chapter 6**). The exposure to H_2O was done *ex-situ* during fabrication, as specified on the additional online methods. From the XRF measurements we obtain and quantify a mass per area value, which we later convert to a molar value to compare the molar ratio between I:Pb and Cs:Pb. It is important to consider that these values are comparable but not quantitatively accurate, given that the top layers of Spiro-OMeTAD, and Au, will affect the fluorescence signal. The main result from XRF-XBIC is the appearance of Cs-rich clusters that are correlated with a decrease in induced current. We also observe a relative decrease in I:Pb ratio after $\text{H}_2\text{O}/\text{Air}$ exposure, in line with the XRF results in **Figure BS14**.

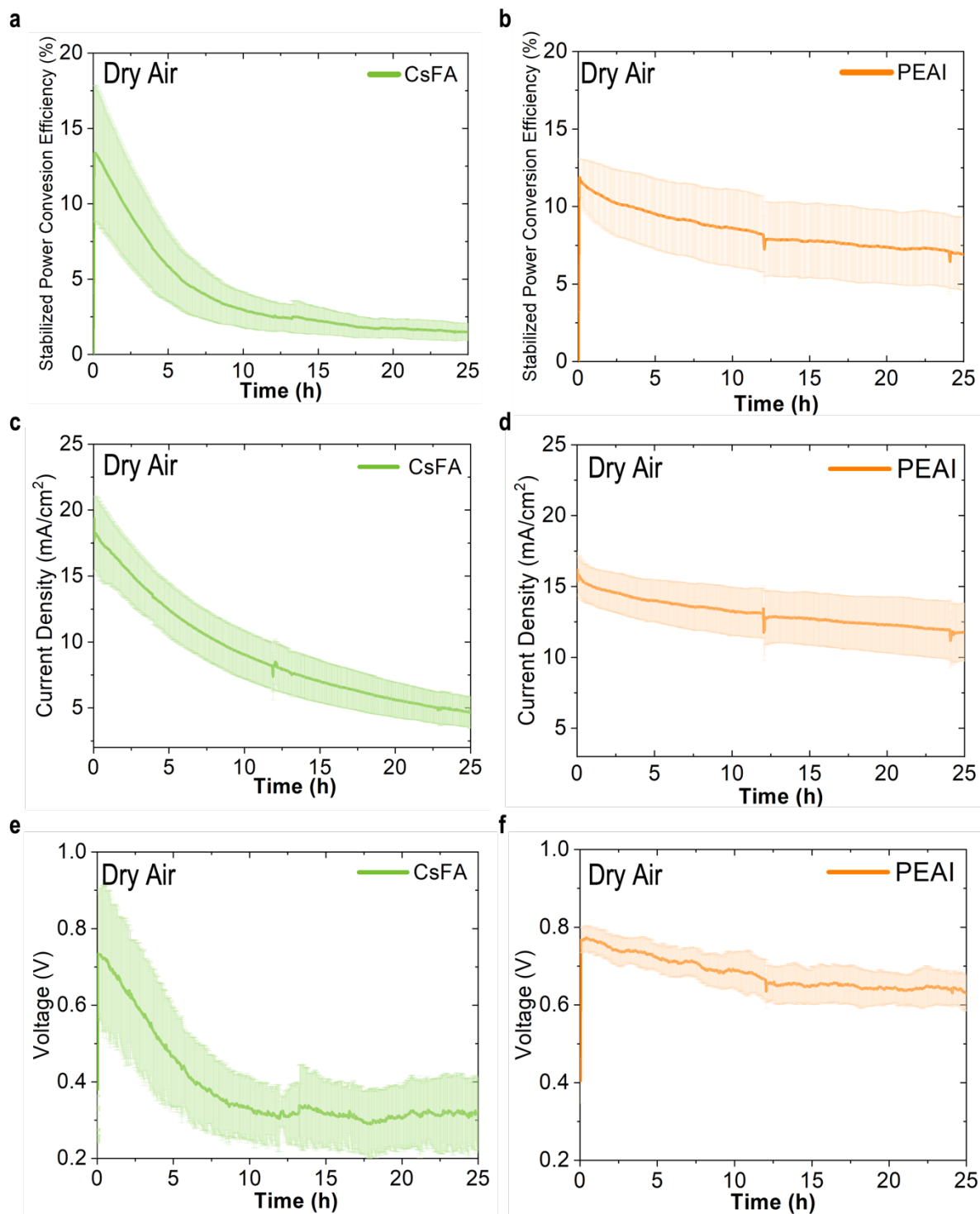


Figure CS18. Long-term stability of the solar cells of $\text{Cs}_{0.17}\text{FA}_{0.83}\text{PbI}_3$ without and with a top layer of PEAI stressed constantly over one-sun illumination in dry air. The results show the average (bold line) of 16 devices with an area of 0.128 cm^2 , and the standard deviation (light line). a,b) Stabilized power conversion efficiency (%) as a function of time in a) CsFA perovskite solar cell, and b) with PEAI-treated. c,d) Current-density as a function of time in c) CsFA perovskite solar cell, d) PEAI-treated. e,f) Voltage as a function of time in a) CsFA perovskite solar cell, and f) PEAI-treated.

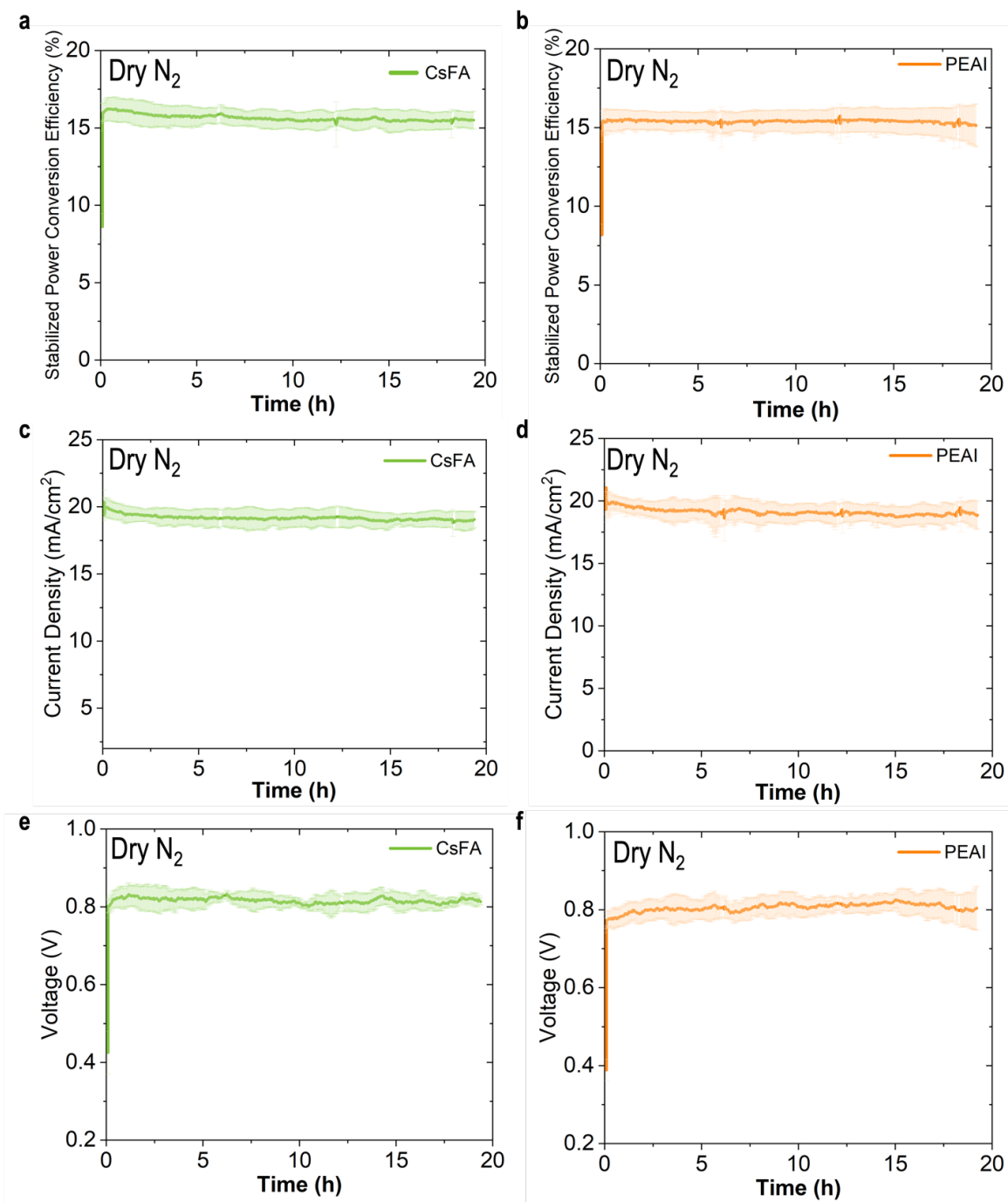


Figure CS19. Long-term stability of the solar cells of $Cs_{0.17}FA_{0.83}PbI_3$ without and with a top layer of PEAI stressed constantly over one-sun illumination in dry nitrogen (N_2). The results show the average (bold line) of 8 devices with an area of 0.128 cm^2 , and the standard deviation (light line). a,b) Stabilized power conversion efficiency (%) as a function of time in a) CsFA perovskite solar cell, and b) with PEAI-treated. c,d) Current-density as a function of time in c) CsFA perovskite solar cell, d) PEAI-treated. e,f) Voltage as a function of time in e) CsFA perovskite solar cell, and f) PEAI-treated.

C.3 The Role of Br at Low Temperatures

C.3.1 UV-VIS

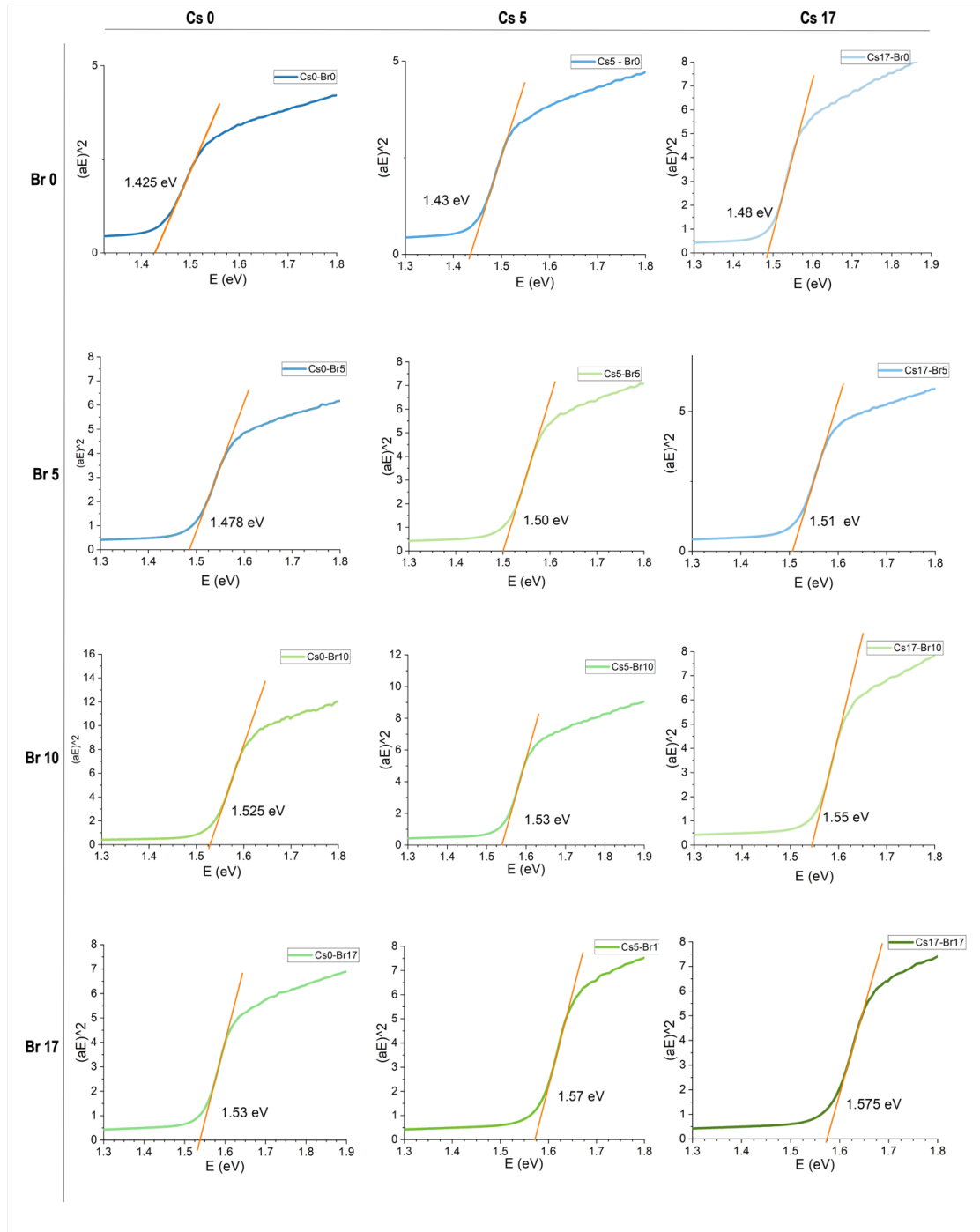


Figure CS20. Tauc-plots from UV-VIS absorption for the set of studied compositions.

C.3.2 *Le Bail Refinements*

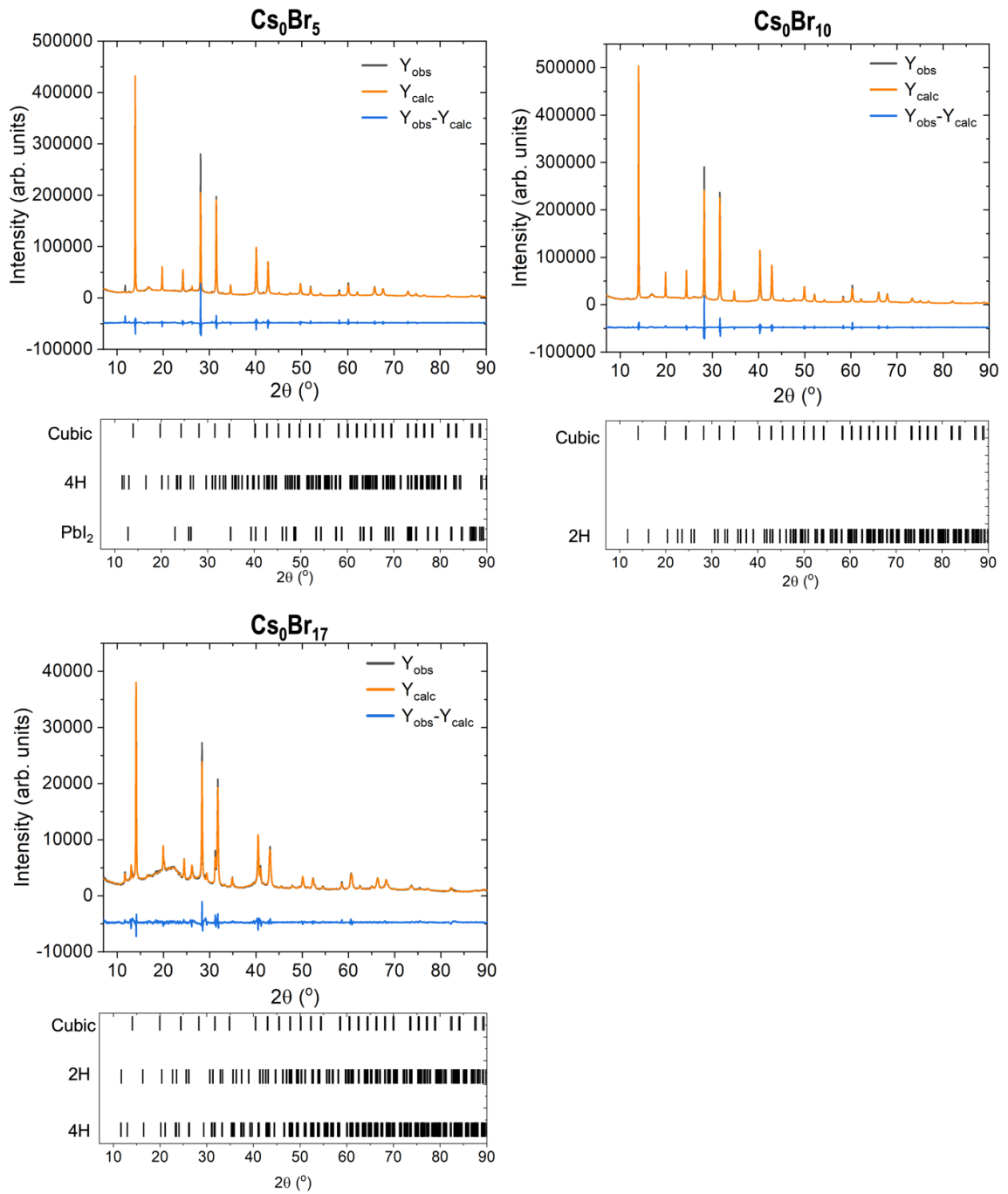


Figure CS21. Le Bail refinements from powder XRD at 300 K, compositions Cs 0 % and Br variations.

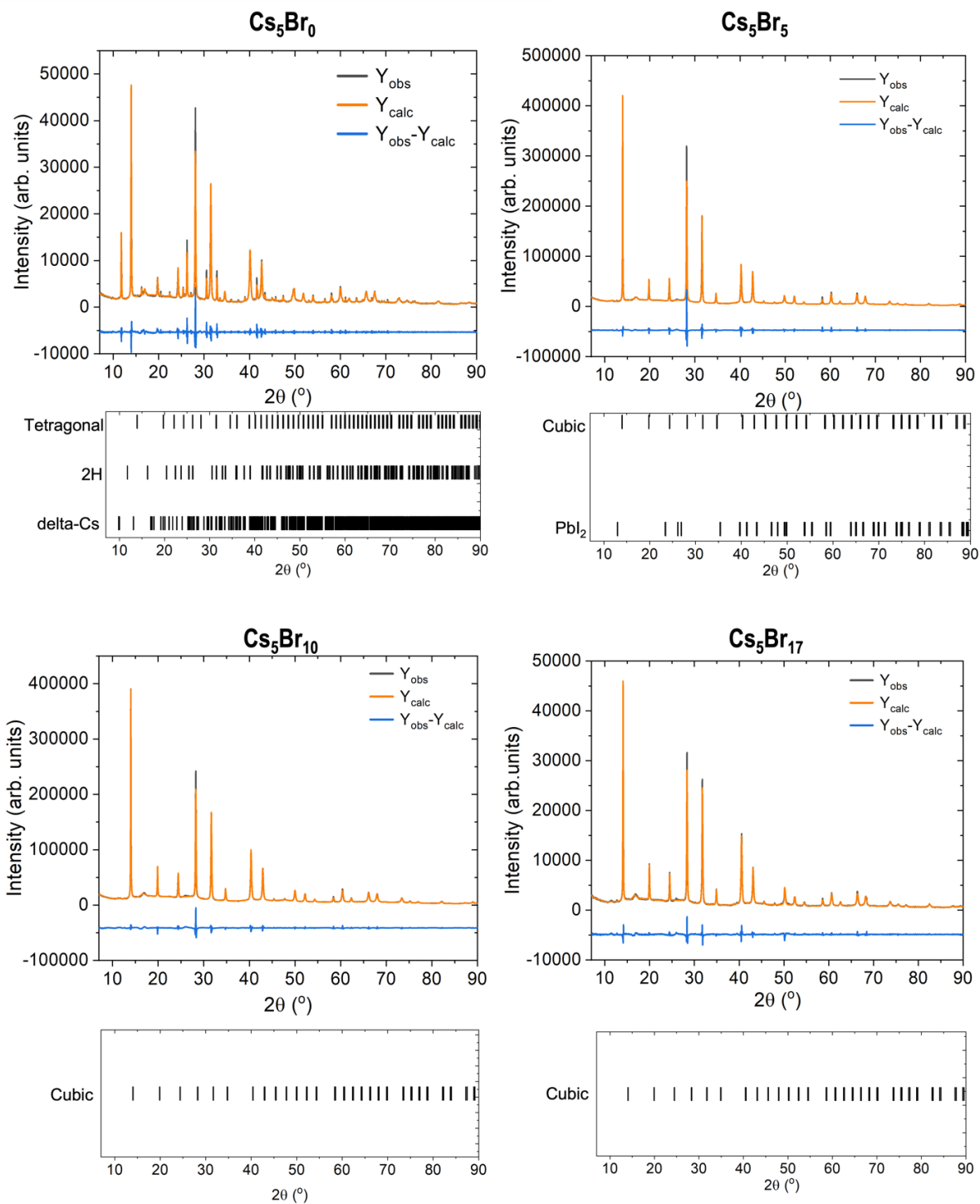


Figure CS22. Le Bail refinements from powder XRD at 300 K, compositions Cs 5 % and Br variations.

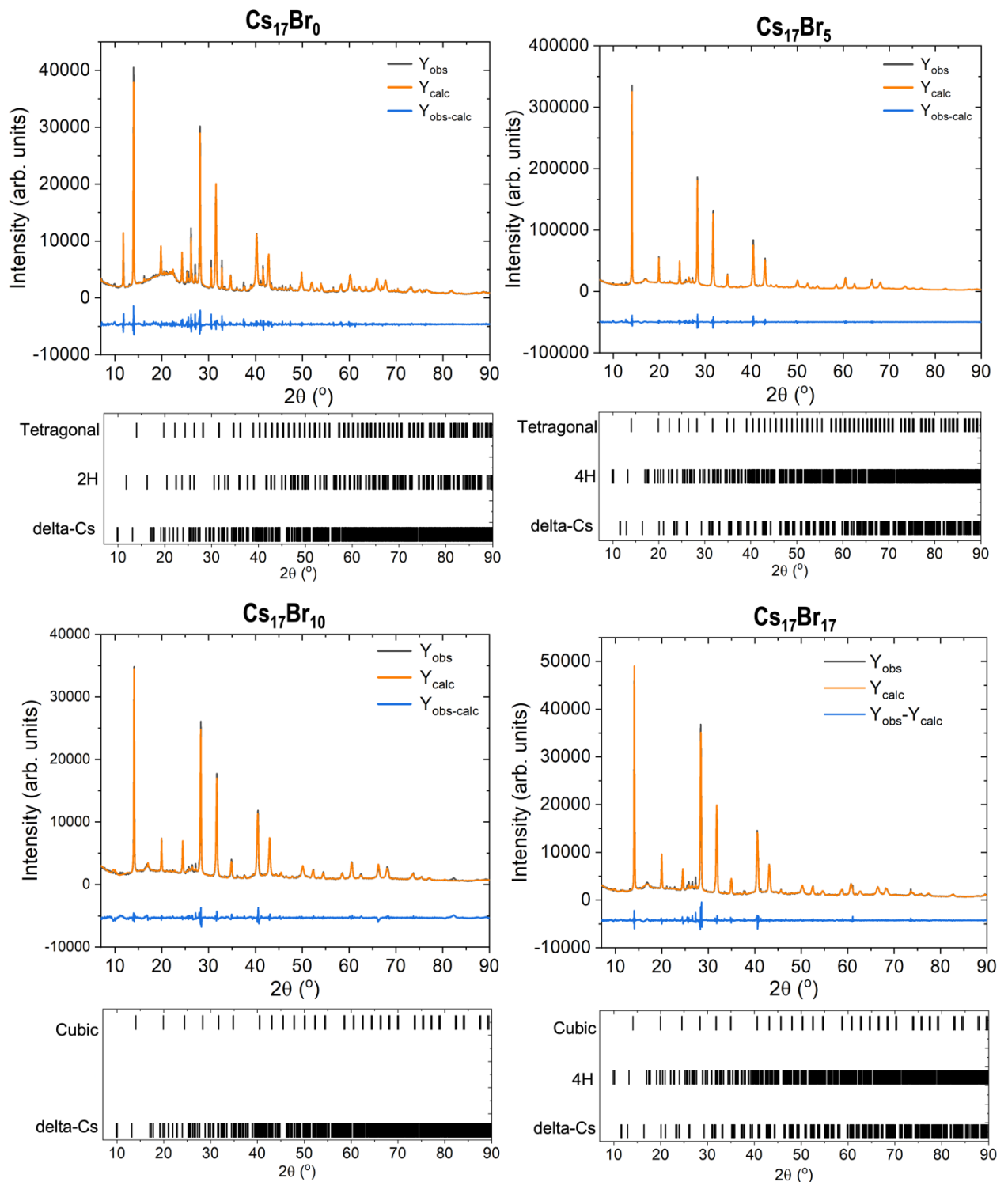


Figure CS23. Le Bail refinements from powder XRD at 300 K, compositions Cs 17 % and Br variations.

Table CS2. Lattice Parameters from Le Bail refinements for compositions at 300 K.

			Lattice Parameters						
	Br	Phase	Space group	a (Å)	b(Å)	c (Å)	alpha(°)	beta(°)	gamma(°)
Cs0	5	cubic	$Pm\bar{3}m$	6.35(0)	6.35(0)	6.35(0)	90	90	90
		4H	$P6_3/mmc$	8.81(6)	8.81(6)	14.73(0)	90	90	120
		PbI ₂	$P\bar{3}m1$	4.476(0)	4.476(0)	6.87(5)	90	90	120
	10	cubic	$Pm\bar{3}m$	6.33(1)	6.33(1)	6.33(1)	90	90	90
		2H	$P6_3/mmc$	8.72(8)	8.72(8)	7.85(0)	90	90	120
	17	cubic	$Pm\bar{3}m$	6.30(6)	6.30(6)	6.30(6)	90	90	90
		2H	$P6_3/mmc$	8.73(1)	8.73(1)		90	90	120
		4H	$P6_3/mmc$	8.80(7)	8.80(7)	15.16(6)	90	90	120
	Cs5	0	tetragonal	$P4/mbm$	8.99(1)	8.99(1)	6.35(9)	90	90
2H			$P6_3/mmc$	8.68(1)	8.68(1)	7.93(2)	90	90	120
delta Cs			$Pnma$	10.46(7)	4.79(4)	17.7(1)	90	90	90
5		cubic	$Pm\bar{3}m$	6.33(8)	6.33(8)	6.33(8)	90	90	90
		PbI ₂	$P\bar{3}m1$	4.38(5)	4.38(5)	6.81(8)	90	90	120
10		cubic	$Pm\bar{3}m$	6.31(9)	6.31(9)	6.31(9)	90	90	90
17		cubic	$Pm\bar{3}m$	6.29(8)	6.29(8)	6.29(8)	90	90	90
Cs17	0	tetragonal	$P4/mbm$	8.97(3)	8.97(3)	6.32(7)	90	90	90
		2H	$P6_3/mmc$	8.67(7)	8.67(7)	7.93(4)	90	90	120
		delta Cs	$Pnma$	10.45(8)	4.80(3)	17.68(2)	90	90	90
	5	tetragonal	$P4/mbm$	8.92(6)	8.92(6)	6.31(6)	90	90	90
		4H	$P6_3/mmc$	8.83(9)	8.83(9)	15.19(0)	90	90	120
		delta Cs	$Pnma$	10.42(6)	4.81(4)	17.41(0)	90	90	90
	10	cubic	$Pm\bar{3}m$	6.30(8)	6.30(8)	6.30(8)	90	90	90
		delta Cs	$Pnma$	10.41(0)	4.80(0)	17.6(0)	90	90	90
	17	cubic	$Pm\bar{3}m$	6.28(7)	6.28(7)	6.28(7)	90	90	90
		4H	$P6_3/mmc$	8.83(9)	8.83(9)	15.19(0)	90	90	120
		delta Cs	$Pnma$	10.43(5)	4.81(5)	17.40(8)	90	90	90

C.3.3 *In-situ* Low-Temperature Powder XRD

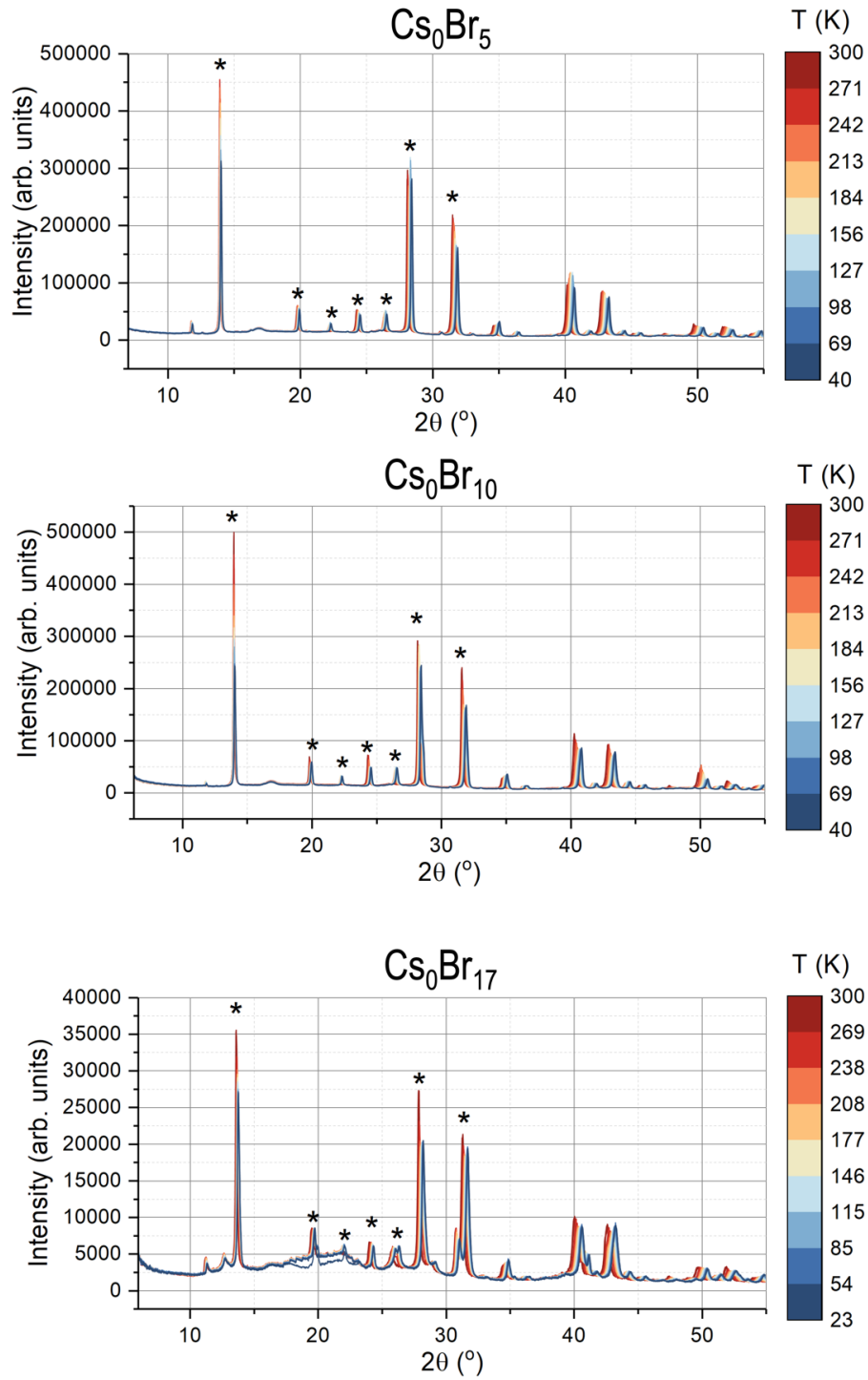


Figure CS24. Complete set of *in-situ* XRD from 300 K to 23 K, Cs 0 % and Br variations. The perovskite phases are marked with *, other peaks are from non-perovskite secondary phases.

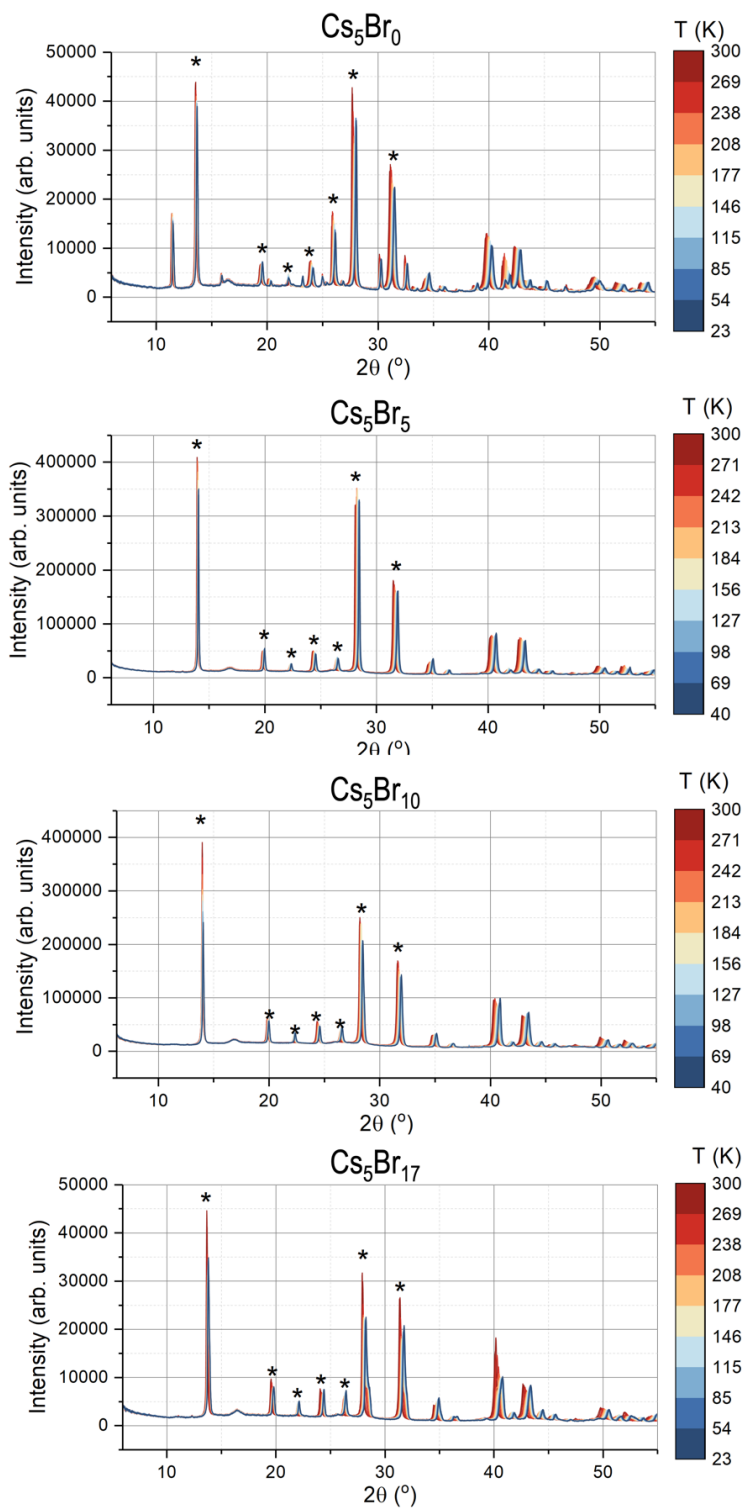


Figure CS25. Complete set of *in-situ* XRD from 300 K to 23 K, Cs 5 % and Br variations. The perovskite phases are marked with *, other peaks are from non-perovskite secondary phases.

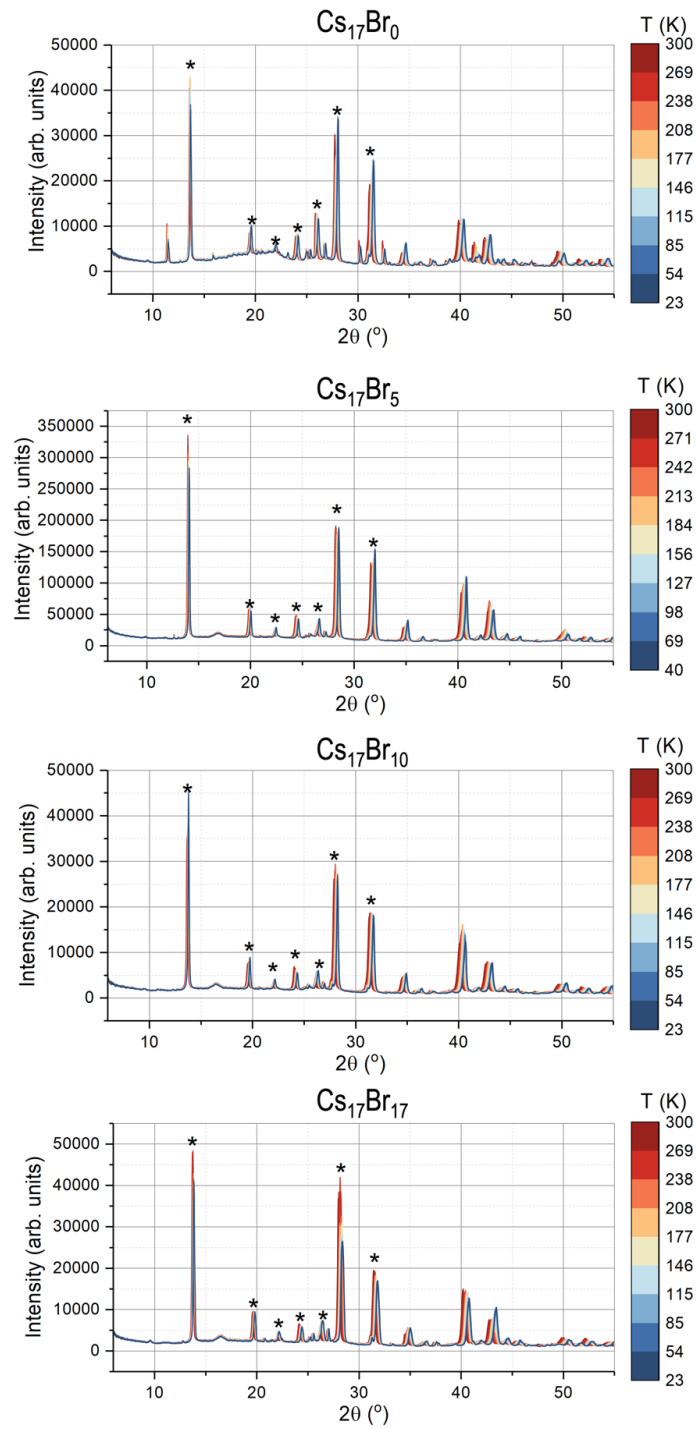


Figure CS26. Complete set of *in-situ* XRD from 300 K to 23 K, Cs 17 % and Br variations. The perovskite phases are marked with *, other peaks are from non-perovskite secondary phases.

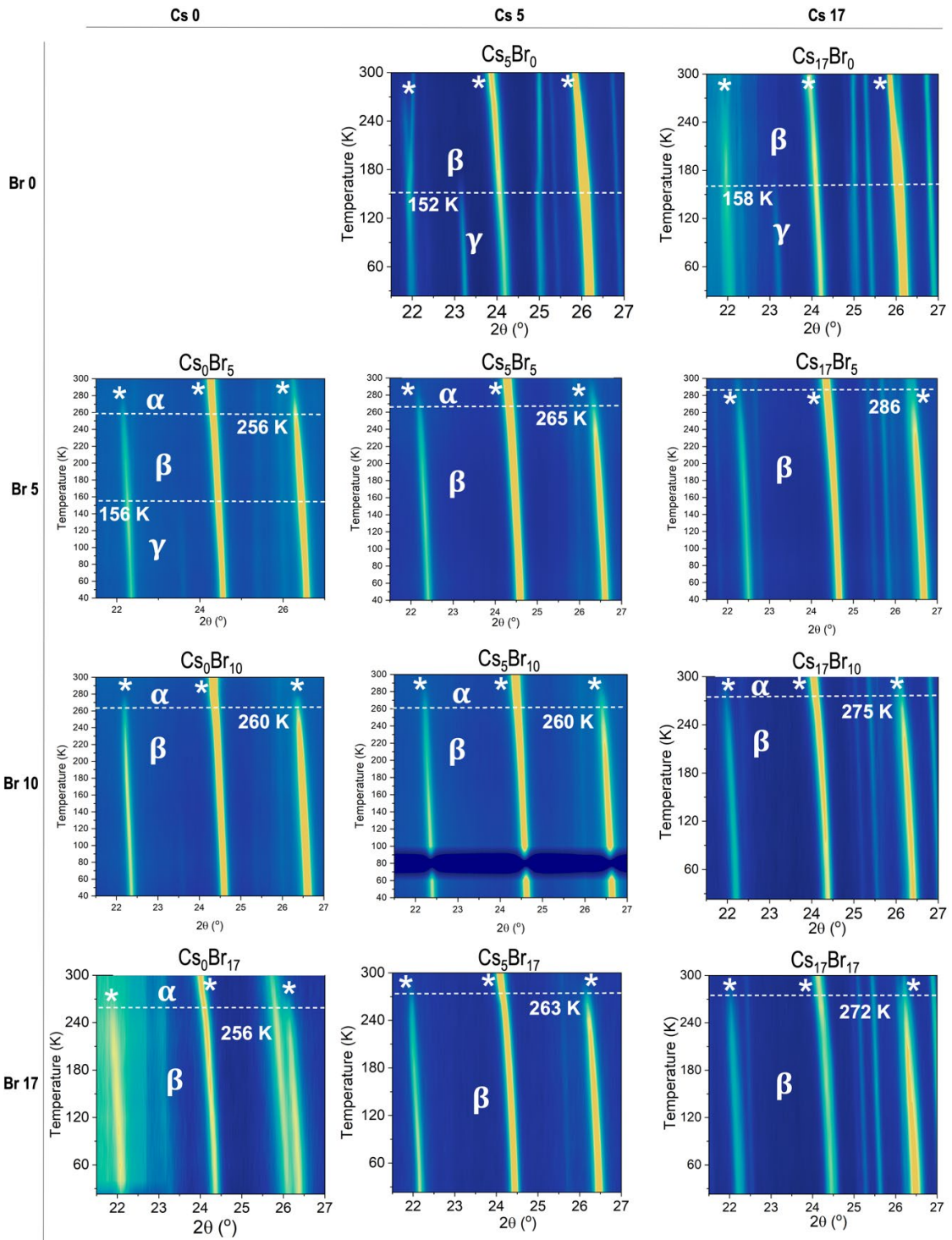


Figure CS27. Temperature versus diffraction plots, in the range of phase transitions for all (Cs,FA)Pb(I,Br)₃ compositions. The perovskite phases are marked with *, other peaks are from non-perovskite secondary phases. Note on *in-situ* XRD: The data for composition Cs5Br10 at 80 K was not saved.

Table CS3. Temperature phase transitions

		Temperature (K)	
	Br	cubic-tetragonal	tetragonal- orthorhombic
Cs 0	5	256	156
	10	260	-
	17	256	-
Cs 5	0	>300	152
	5	265	-
	10	260	-
	17	263	-
Cs 17	0	>300	158
	5	286	-
	10	275	-
	17	272	-

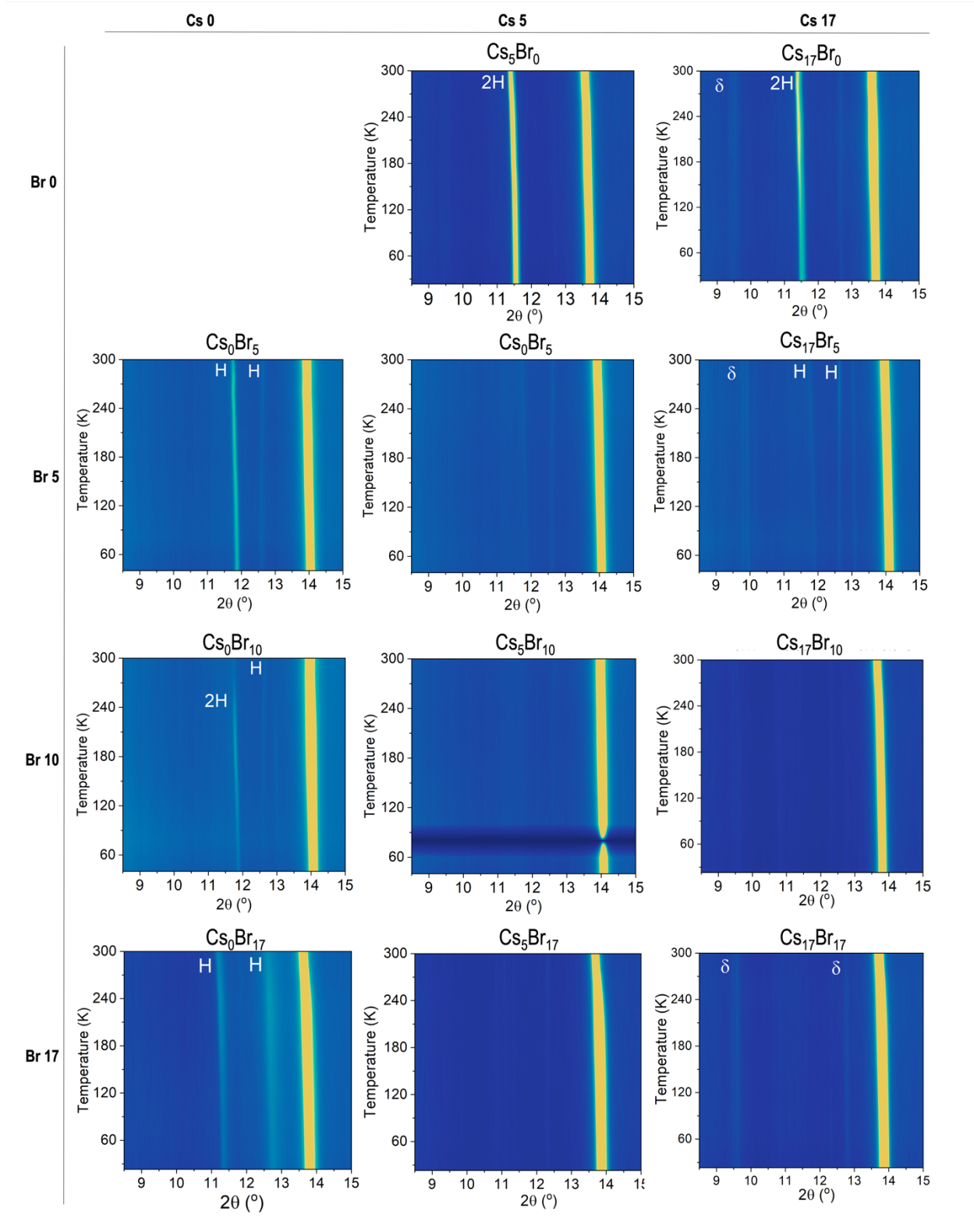


Figure CS28. Temperature versus diffraction plots, in the range of hexagonal phases for all $(\text{Cs,FA})\text{Pb}(\text{I,Br})_3$ compositions. The hexagonal phases are labeled with H.

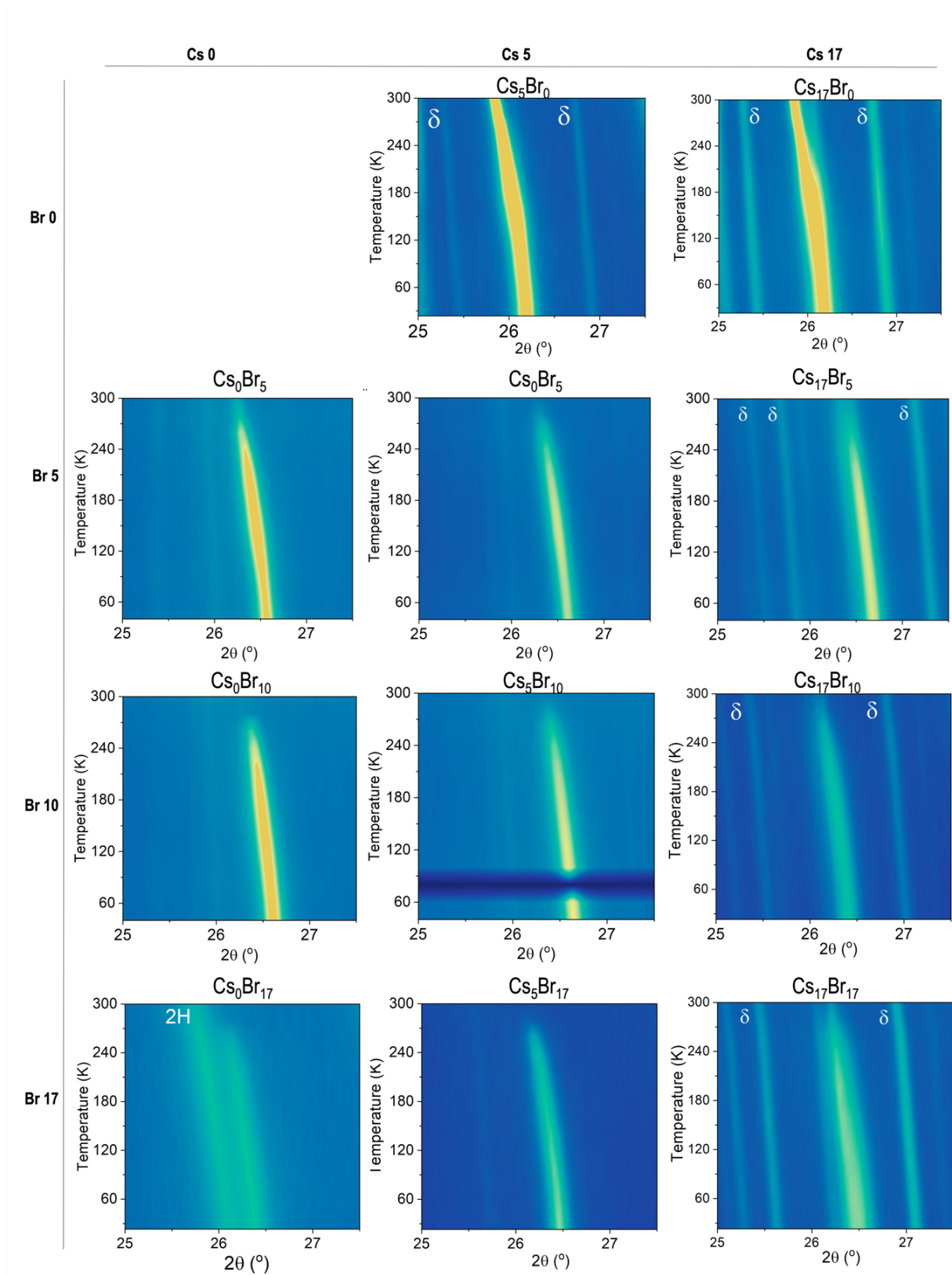


Figure CS29. Temperature versus diffraction plots, in the range of hexagonal phases for all $(\text{Cs,FA})\text{Pb}(\text{I,Br})_3$ compositions. The orthorhombic $\delta\text{-CsPbI}_3$ is labeled as δ .

APPENDIX D. PEER-REVIEWED PUBLICATIONS

Peer-Reviewed Research

- **Hidalgo J.***; Atourki, L.*; Li, R.; Castro-Mendez, A.F.; Kim, S.; Sherman, E.A.; Bieber, A.S.; Sher, M.J.; Nienhaus, L.; Perini, C.A.R.; Correa-Baena, J.P. (2023) “Bulky Cation Hinders Undesired Secondary Phases in FAPbI₃ Perovskite Solar Cells”. *Accepted in Materials Today*.
- **Hidalgo, J.**; An, Y.; Yehorova, D.; Li, R.; Breternitz, J.; Perini, C.A.R.; Hoell, A.; Boix, P.P.; Schorr, S.; Kretchmer, J.S.; Correa-Baena, J.P. (2023) “Solvent and A-site Cation Control Preferred Crystallographic Orientation in Bromine-Based Perovskite Thin Films” *Chemistry of Materials*, 35, 11, 4181-4191.
- Perini, C.A.R.; Castro-Mendez, A.F.; Kodalle, T.; Ravello, M.; **Hidalgo, J.**; Gomez-Dominguez, M.; Li, R.; Taddei, M.; Giridharagopal, R.; Pothoof, J.; Sutter-Fella, C.; Ginger, D.S.; Correa-Baena, J.P. (2023) “Vapor-deposited n=2 Ruddlesden-Popper Interface Layers Aid Charge Carrier Extraction in Perovskite Solar Cells”, *ACS Energy Letters*, 8, 3, 1408-1415.
- Perini, C.A.R.; Rojas-Gatjens, E.; Ravello, M.; Castro-Mendez, A.F.; **Hidalgo, J.**; An, Y.; Kim, S.; Lai, B.; Li, R.; Silva-Acuña, C.; Correa-Baena, J.P. (2022) “Interface Reconstruction from Ruddlesden-Popper Structures Impacts Stability in Lead Halide Perovskite Solar Cells” *Advanced Materials*, 34, 51, 2204726.
- Castro-Mendez, A.F.; Perini, C.A.R.; **Hidalgo, J.**; Ranke, D.; Vagott, J.N.; An, Y.; Lai, B.; Luo, Y.; Li, R.; Correa-Baena, J.P. (2022) “Formation of a Secondary Phase in Thermally Evaporated MAPbI₃ and Its Effects on Solar Cell Performance”, *ACS Appl. Mater. Interfaces*, 14, 30, 34269-34280.
- Vagott, J.N.; Bairley, K.; **Hidalgo, J.**; Perini, C.A.R.; Castro-Mendez, A.F.; Lombardo, S.; Lai, B.; Zhang, L.; Kisslinger, K.; Kacher, J.; Correa-Baena, J.P. (2022) “PbI₂ Nanocrystal Growth by Atomic Layer Deposition from Pb(tmhd)₂ and HI”, *Chemistry of Materials*, 34 (6), 2553-2561.
- Yuce, H.; Perini, C.A.R.; **Hidalgo, J.**; Castro-Mendez, A.F.; Evans, C.; Betancur, P.F.; Vagott, J.N.; An, Y.; Bairley, K.; Demir, M.M.; Correa-Baena, J.P. (2022) “Understanding

the impact of SrI₂ additive on the properties of Sn-based halide perovskites”, *Optical Materials*, 111806, ISSN 0925-3467.

- An, Y.; Perini, C.A.R.; **Hidalgo, J.**; Castro-Mendez, A.F.; Vagott, J.N.; Li, R.; Saidi, W.A.; Wang, S.; Li, X.; Correa-Baena, J.P. (2021) “Identifying high-performance and durable methylammonium-free lead halide perovskites via high-throughput synthesis and characterization”. *Energy & Environmental Science*, 14, 6638-6654
- Erodici, M. P.; Pierone, P. J.; Hartono, N. T. P.; **Hidalgo, J.**; Lai, B.; Buonassisi, T.; Correa-Baena, J.-P.; Sher, M.-J. (2021) “Enhanced Charge Carrier Lifetime and Mobility as a Result of Rb and Cs Incorporation in Hybrid Perovskite”. *Appl. Phys. Lett.*, 118 (6), 063901.
- **Hidalgo, J.**; Perini, C.A.R.; Castro-Mendez, A.F.; Jones, D.; Kobler, H.; Lai, B.; Li, R.; Sun, S.; Abate, A.; Correa-Baena, J.P. (2020) “Moisture-induced crystallographic re-orientations and effects on charge carrier extraction in metal halide perovskite solar cells”. *ACS Energy Letters*, 5, 3526-3534.
- Wang, Ti.; Jin, L.; **Hidalgo, J.**; Chu, W.; Snaider, J.M.; Deng, S.; Zhu, T.; Lai, B.; Prezhdo, O.; Correa-Baena, J.P.; Huang, Li. (2020) “Protecting hot carriers by tuning hybrid perovskite structures with alkali cations”. *Science Advances*, 6, 43, eabb1336
- Phung, N.; Felix, R.; Meggiolaro, D.; Al-Ashouri, A.; Sousa e Silva, G.; Hartmann, C.; **Hidalgo, J.**; Kobler, H.; Mosconi, E.; Lai, B.; Gunder, R.; Li, M.; Wang, K.; Wang, Z.; Nie, K.; Handick, E.; Wilks, R.G.; Marquez, J.A.; Rech, B.; Unold, T.; Correa-Baena, J.P.; Albrecht, S.; De Angelis, F.; Bar, M.; Abate, A. (2020) “The Doping Mechanism of Halide Perovskite Unveiled by Alkaline Earth Metals”. *Journal of the American Chemical Society*, 142, 2364-2374.

Reviews and Perspectives

- Jones, D.; An, Y.; **Hidalgo, J.**; Evans, C.; Vagott, J.N.; Correa-Baena, J.P. (2021) “Polymers and interfacial modifiers for durable perovskite solar cells: a review”. *Journal of Materials Chemistry C*, 9, 12509-12522.
- Hoye, R. L. Z.; **Hidalgo, J.**; Jagt, R. A.; Correa-Baena, J. P.; Fix, T.; MacManus-Driscoll, J. L. (2021) “The Role of Dimensionality on the Optoelectronic Properties of Oxide and Halide Perovskites, and Their Halide Derivatives”. *Advanced Energy Materials*, 12, 4, 2100499.

- An, Y.; **Hidalgo, J.**; Perini, C. A. R.; Castro-Méndez, A. F.; Vagott, J. N.; Bairley, K.; Wang, S.; Li, X.; Correa-Baena, J. P. (2021) “Structural Stability of Formamidinium- and Cesium-Based Halide Perovskites”. *ACS Energy Letters*, 6 (5), 1942–1969.
- **Hidalgo J.***; Castro-Méndez, A.F.*; Correa-Baena, J.P. (2019) “Imaging and Mapping Characterization Tools for Perovskite Solar Cells”. *Advanced Energy Materials*, 9, 1900444.
- Castro-Méndez, A.F; **Hidalgo, J.**; Correa-Baena, J.P. (2019) “The Role of Grain Boundaries in Perovskite Solar Cells”. *Advanced Energy Materials*, 9, 38, 1901489.

Under Review and Preparation

- **Hidalgo J.**; Kaiser, W.; An, Y.; Li, R.; Oh, Z.; Castro-Mendez, A.F.; LaFollette, D.K.; Kim, S.; Lai, B.; Breternitz, J.; Schorr, S.; Perini, C.A.R.; Mosconi, E.; De Angelis, F.; Correa-Baena, J.P. (2023) “Synergistic Role of Water and Oxygen Leads to Degradation in Formamidinium-Based Halide Perovskites”. *Manuscript under review in the Journal of the American Chemical Society*.
- **Hidalgo, J.**; Breternitz, J.; Toebbens, D.; Correa-Baena, J.P.; Schorr, S.(2023) “Br-Induced Suppression of Low-Temperature Phase Transitions in Mixed Cation Mixed Halide Perovskites”, *under preparation*.

*co-first author

REFERENCES

- (1) Arno Smets; Klaus Jager; Olindo Isabella; Rene Van Swaaij; Miro Zeman. *Solar Energy: The Physics and Engineering of Photovoltaic Conversion Technologies and Systems*; UIT Cambridge: England, 2016.
- (2) George M. Whitesides; George W. Crabtree. Don't Forget Long-Term Fundamental Research in Energy. *Science* **2007**, *315* (5813), 796–798. <https://doi.org/10.1126/science.1140362>.
- (3) IEA. *IEA: Energy Sankey*; 2020. <https://www.iea.org/sankey/> (accessed 2023-04-26).
- (4) T.F. Stocker; D. Qin; G.K. Plattner; M.M. B. Tignor; S.K. Allen; J. Boschung; A. Nauels; Y. Xia; V. Bex; P.M Midgley. *Climate Change 2013 - The Physical Science Basis: Working Group I Contribution to the Fifth Assessment Report of the Intergovernmental Panel on Climate Change*; Cambridge University Press: Cambridge, United Kingdom, 2014.
- (5) IRENA. *Renewable Energy Statistics 2022*; ISBN: 978-92-9260-446-2. <https://www.irena.org/publications/2022/Jul/Renewable-Energy-Statistics-2022>.
- (6) IEA. *IEA: Monthly Electricity Statistics*; 2023. <https://www.iea.org/data-and-statistics/data-tools/monthly-electricity-statistics> (accessed 2023-04-26).
- (7) Michael Taylor; Pablo Ralon; Sonia Al-Zoghoul. *Renewable Power Generation: Costs in 2021*; ISBN 978-92-9260-452-3I; IRENA, 2022. <https://www.irena.org/publications/2022/Jul/Renewable-Power-Generation-Costs-in-2021>.
- (8) IEA. *Renewables 2021: Analysis and Forecasts to 2026*; 2021. <https://www.iea.org/reports/renewables-2021>.
- (9) Jošt, M.; Kegelmann, L.; Korte, L.; Albrecht, S. Monolithic Perovskite Tandem Solar Cells: A Review of the Present Status and Advanced Characterization Methods Toward 30% Efficiency. *Advanced Energy Materials* **2020**, *10* (26), 1904102. <https://doi.org/10.1002/aenm.201904102>.
- (10) Werner, J.; Niesen, B.; Ballif, C. Perovskite/Silicon Tandem Solar Cells: Marriage of Convenience or True Love Story? – An Overview. *Advanced Materials Interfaces* **2018**, *5* (1), 1700731. <https://doi.org/10.1002/admi.201700731>.
- (11) Wolfgang Tress. Maximum Efficiency and Open-Circuit Voltage of Perovskite Solar Cells. In *Organic-Inorganic Halide Perovskite Photovoltaics: From Fundamentals to Device Architectures*; Springer: Switzerland, 2016.
- (12) NREL; U.S Department of Energy. *NREL: Best Research-Cell Efficiency Chart*; 2023. <https://www.nrel.gov/pv/cell-efficiency.html>.

- (13) Jaewang Park; Jongbeom Kim; Hyun-Sung Yun; Min Jae Paik; Eunseo Noh; Hyun Jung Mun; Min Gyu Kim; Tae Joo Shin; Sang Il Seok. Controlled Growth of Perovskite Layers with Volatile Alkylammonium Chlorides. *Nature* **2023**. <https://doi.org/10.1038/s41586-023-05825-y>.
- (14) Correa-Baena, J.P.; Saliba, M.; Buonassisi, T.; Gratzel, M.; Abate, A.; Tress, W.; Hagfeldt, A. Promises and Challenges of Perovskite Solar Cells. *Science* **2017**, *358*, 739–744. <https://doi.org/doi/10.1126/science.aam6323>.
- (15) Eperon, G. E.; Stranks, S. D.; Menelaou, C.; Johnston, M. B.; Herz, L. M.; Snaith, H. J. Formamidinium Lead Trihalide: A Broadly Tunable Perovskite for Efficient Planar Heterojunction Solar Cells. *Energy Environ. Sci.* **2014**, *7* (3), 982. <https://doi.org/10.1039/c3ee43822h>.
- (16) An, Y.; Hidalgo, J.; Perini, C. A. R.; Castro-Méndez, A.-F.; Vagott, J. N.; Bairley, K.; Wang, S.; Li, X.; Correa-Baena, J.-P. Structural Stability of Formamidinium- and Cesium-Based Halide Perovskites. *ACS Energy Lett.* **2021**, *6* (5), 1942–1969. <https://doi.org/10.1021/acsenerylett.1c00354>.
- (17) Aguiar, J. A.; Wozny, S.; Holesinger, T. G.; Aoki, T.; Patel, M. K.; Yang, M.; Berry, J. J.; Al-Jassim, M.; Zhou, W.; Zhu, K. In Situ Investigation of the Formation and Metastability of Formamidinium Lead Tri-Iodide Perovskite Solar Cells. *Energy Environ. Sci.* **2016**, *9* (7), 2372–2382. <https://doi.org/10.1039/C6EE01079B>.
- (18) Ma, C.; Eickemeyer, F. T.; Lee, S.-H.; Kang, D.-H.; Kwon, S. J.; Grätzel, M.; Park, N.-G. Unveiling Facet-Dependent Degradation and Facet Engineering for Stable Perovskite Solar Cells. *Science* **2023**, *379* (6628), 173–178. <https://doi.org/10.1126/science.adf3349>.
- (19) Weber, O. J.; Ghosh, D.; Gaines, S.; Henry, P. F.; Walker, A. B.; Islam, M. S.; Weller, M. T. Phase Behavior and Polymorphism of Formamidinium Lead Iodide. *Chem. Mater.* **2018**, *30* (11), 3768–3778. <https://doi.org/10.1021/acs.chemmater.8b00862>.
- (20) Gratia, P.; Zimmermann, I.; Schouwink, P.; Yum, J.-H.; Audinot, J.-N.; Sivula, K.; Wirtz, T.; Nazeeruddin, M. K. The Many Faces of Mixed Ion Perovskites: Unraveling and Understanding the Crystallization Process. *ACS Energy Lett.* **2017**, *2* (12), 2686–2693. <https://doi.org/10.1021/acsenerylett.7b00981>.
- (21) Brgoch, J.; Lehner, A. J.; Chabynyc, M.; Seshadri, R. Ab Initio Calculations of Band Gaps and Absolute Band Positions of Polymorphs of RbPbI₃ and CsPbI₃: Implications for Main-Group Halide Perovskite Photovoltaics. *J. Phys. Chem. C* **2014**, *118* (48), 27721–27727. <https://doi.org/10.1021/jp508880y>.
- (22) Aristidou, N.; Eames, C.; Sanchez-Molina, I.; Bu, X.; Kosco, J.; Islam, M. S.; Haque, S. A. Fast Oxygen Diffusion and Iodide Defects Mediate Oxygen-Induced Degradation of Perovskite Solar Cells. *Nat Commun* **2017**, *8* (1), 15218. <https://doi.org/10.1038/ncomms15218>.
- (23) Guo, R.; Han, D.; Chen, W.; Dai, L.; Ji, K.; Xiong, Q.; Li, S.; Reb, L. K.; Scheel, M. A.; Pratap, S.; Li, N.; Yin, S.; Xiao, T.; Liang, S.; Oechsle, A. L.; Weindl, C. L.; Schwartzkopf,

- M.; Ebert, H.; Gao, P.; Wang, K.; Yuan, M.; Greenham, N. C.; Stranks, S. D.; Roth, S. V.; Friend, R. H.; Müller-Buschbaum, P. Degradation Mechanisms of Perovskite Solar Cells under Vacuum and One Atmosphere of Nitrogen. *Nat Energy* **2021**, *6* (10), 977–986. <https://doi.org/10.1038/s41560-021-00912-8>.
- (24) Nakamura, Y.; Shibayama, N.; Fujiwara, K.; Koganezawa, T.; Miyasaka, T. Degradation Mechanism of Halide Perovskite Crystals under Concurrent Light and Humidity Exposure. *ACS Materials Lett.* **2022**, *4* (12), 2409–2414. <https://doi.org/10.1021/acsmaterialslett.2c00744>.
- (25) Saliba, M.; Matsui, T.; Seo, J.-Y.; Domanski, K.; Correa-Baena, J.-P.; Nazeeruddin, M. K.; Zakeeruddin, S. M.; Tress, W.; Abate, A.; Hagfeldt, A.; Grätzel, M. Cesium-Containing Triple Cation Perovskite Solar Cells: Improved Stability, Reproducibility and High Efficiency. *Energy Environ. Sci.* **2016**, *9* (6), 1989–1997. <https://doi.org/10.1039/C5EE03874J>.
- (26) Kubicek, M.; Bork, A. H.; Rupp, J. L. M. Perovskite Oxides – a Review on a Versatile Material Class for Solar-to-Fuel Conversion Processes. *J. Mater. Chem. A* **2017**, *5* (24), 11983–12000. <https://doi.org/10.1039/C7TA00987A>.
- (27) Peña, M. A.; Fierro, J. L. G. Chemical Structures and Performance of Perovskite Oxides. *Chem. Rev.* **2001**, *101* (7), 1981–2018. <https://doi.org/10.1021/cr980129f>.
- (28) The ABX₃ Perovskite Structure. In *Perovskites*; 2016; pp 1–41. <https://doi.org/10.1002/9781118935651.ch1>.
- (29) Richard J.D Tilley. *Perovskites: Structure-Property Relationships*, 1st ed.; Wiley: United Kingdom, 2016.
- (30) Jarvist M. Frost; Aron Walsh. Molecular Motion and Dynamic Crystal Structures of Hybrid Halide Perovskites. In *Organic-Inorganic Halide Perovskite Photovoltaics: From Fundamentals to Device Architectures*; Springer: Switzerland, 2016.
- (31) Goldschmidt, V. M. Die Gesetze der Krystallochemie. *Naturwissenschaften* **1926**, *14* (21), 477–485. <https://doi.org/10.1007/BF01507527>.
- (32) Li, Z.; Yang, M.; Park, J.-S.; Wei, S.-H.; Berry, J. J.; Zhu, K. Stabilizing Perovskite Structures by Tuning Tolerance Factor: Formation of Formamidinium and Cesium Lead Iodide Solid-State Alloys. *Chem. Mater.* **2016**, *28* (1), 284–292. <https://doi.org/10.1021/acs.chemmater.5b04107>.
- (33) Weller, M. T.; Weber, O. J.; Henry, P. F.; Di Pumpo, A. M.; Hansen, T. C. Complete Structure and Cation Orientation in the Perovskite Photovoltaic Methylammonium Lead Iodide between 100 and 352 K. *Chem. Commun.* **2015**, *51* (20), 4180–4183. <https://doi.org/10.1039/C4CC09944C>.
- (34) Breternitz, J.; Lehmann, F.; Barnett, S. A.; Nowell, H.; Schorr, S. Role of the Iodide–Methylammonium Interaction in the Ferroelectricity of CH₃NH₃PbI₃. *Angewandte*

- (35) López, C. A.; Martínez-Huerta, M. V.; Alvarez-Galván, M. C.; Kayser, P.; Gant, P.; Castellanos-Gomez, A.; Fernández-Díaz, M. T.; Fauth, F.; Alonso, J. A. Elucidating the Methylammonium (MA) Conformation in MAPbBr₃ Perovskite with Application in Solar Cells. *Inorg. Chem.* **2017**, *56* (22), 14214–14219. <https://doi.org/10.1021/acs.inorgchem.7b02344>.
- (36) Franz, A.; Többsens, D. M.; Lehmann, F.; Kärgell, M.; Schorr, S. The Influence of Deuteration on the Crystal Structure of Hybrid Halide Perovskites: A Temperature-Dependent Neutron Diffraction Study of FAPbBr₃. *Acta Crystallogr B Struct Sci Cryst Eng Mater* **2020**, *76* (2), 267–274. <https://doi.org/10.1107/S2052520620002620>.
- (37) Zhao, B.; Jin, S.-F.; Huang, S.; Liu, N.; Ma, J.-Y.; Xue, D.-J.; Han, Q.; Ding, J.; Ge, Q.-Q.; Feng, Y.; Hu, J.-S. Thermodynamically Stable Orthorhombic γ -CsPbI₃ Thin Films for High-Performance Photovoltaics. *J. Am. Chem. Soc.* **2018**, *140* (37), 11716–11725. <https://doi.org/10.1021/jacs.8b06050>.
- (38) Näsström, H.; Becker, P.; Márquez, J. A.; Shargaieva, O.; Mainz, R.; Unger, E.; Unold, T. Dependence of Phase Transitions on Halide Ratio in Inorganic CsPb(Br_xI_{1-x})₃ Perovskite Thin Films Obtained from High-Throughput Experimentation. *J. Mater. Chem. A* **2020**, *8* (43), 22626–22631. <https://doi.org/10.1039/D0TA08067E>.
- (39) Cottingham, P.; Brutchey, R. L. Depressed Phase Transitions and Thermally Persistent Local Distortions in CsPbBr₃ Quantum Dots. *Chem. Mater.* **2018**, *30* (19), 6711–6716. <https://doi.org/10.1021/acs.chemmater.8b02295>.
- (40) Charles, B.; Weller, M. T.; Rieger, S.; Hatcher, L. E.; Henry, P. F.; Feldmann, J.; Wolverson, D.; Wilson, C. C. Phase Behavior and Substitution Limit of Mixed Cesium-Formamidinium Lead Triiodide Perovskites. *Chem. Mater.* **2020**, *32* (6), 2282–2291. <https://doi.org/10.1021/acs.chemmater.9b04032>.
- (41) Liu, Y.; Zhang, Y.; Zhu, X.; Feng, J.; Spanopoulos, I.; Ke, W.; He, Y.; Ren, X.; Yang, Z.; Xiao, F.; Zhao, K.; Kanatzidis, M.; Liu, S. (Frank). Triple-Cation and Mixed-Halide Perovskite Single Crystal for High-Performance X-Ray Imaging. *Advanced Materials* **2021**, *33* (8), 2006010. <https://doi.org/10.1002/adma.202006010>.
- (42) Li, Z.; Park, J.-S.; Walsh, A. Evolutionary Exploration of Polytypism in Lead Halide Perovskites. *Chem. Sci.* **2021**, *12* (36), 12165–12173. <https://doi.org/10.1039/D1SC03098A>.
- (43) Trots, D. M.; Myagkota, S. V. High-Temperature Structural Evolution of Caesium and Rubidium Triiodoplumbates. *Journal of Physics and Chemistry of Solids* **2008**, *69* (10), 2520–2526. <https://doi.org/10.1016/j.jpcs.2008.05.007>.
- (44) Yi, C.; Luo, J.; Meloni, S.; Boziki, A.; Ashari-Astani, N.; Grätzel, C.; Zakeeruddin, S. M.; Röthlisberger, U.; Grätzel, M. Entropic Stabilization of Mixed A-Cation ABX₃ Metal

- Halide Perovskites for High Performance Perovskite Solar Cells. *Energy Environ. Sci.* **2016**, *9* (2), 656–662. <https://doi.org/10.1039/C5EE03255E>.
- (45) Ghosh, D.; Smith, A. R.; Walker, A. B.; Islam, M. S. Mixed A-Cation Perovskites for Solar Cells: Atomic-Scale Insights Into Structural Distortion, Hydrogen Bonding, and Electronic Properties. *Chem. Mater.* **2018**, *30* (15), 5194–5204. <https://doi.org/10.1021/acs.chemmater.8b01851>.
- (46) Ghosh, D.; Walsh Atkins, P.; Islam, M. S.; Walker, A. B.; Eames, C. Good Vibrations: Locking of Octahedral Tilting in Mixed-Cation Iodide Perovskites for Solar Cells. *ACS Energy Lett.* **2017**, *2* (10), 2424–2429. <https://doi.org/10.1021/acseenergylett.7b00729>.
- (47) Hui, W.; Chao, L.; Lu, H.; Xia, F.; Wei, Q.; Su, Z.; Niu, T.; Tao, L.; Du, B.; Li, D.; Wang, Y.; Dong, H.; Zuo, S.; Li, B.; Shi, W.; Ran, X.; Li, P.; Zhang, H.; Wu, Z.; Ran, C.; Song, L.; Xing, G.; Gao, X.; Zhang, J.; Xia, Y.; Chen, Y.; Huang, W. Stabilizing Black-Phase Formamidinium Perovskite Formation at Room Temperature and High Humidity. *Science* **2021**, *371* (6536), 1359–1364. <https://doi.org/10.1126/science.abf7652>.
- (48) Park, B.; Kwon, H. W.; Lee, Y.; Lee, D. Y.; Kim, M. G.; Kim, G.; Kim, K.; Kim, Y. K.; Im, J.; Shin, T. J.; Seok, S. I. Stabilization of Formamidinium Lead Triiodide α -Phase with Isopropylammonium Chloride for Perovskite Solar Cells. *Nat Energy* **2021**, *6* (4), 419–428. <https://doi.org/10.1038/s41560-021-00802-z>.
- (49) Etgar, L. The Merit of Perovskite's Dimensionality; Can This Replace the 3D Halide Perovskite? *Energy Environ. Sci.* **2018**, *11* (2), 234–242. <https://doi.org/10.1039/C7EE03397D>.
- (50) Smith, I. C.; Hoke, E. T.; Solis-Ibarra, D.; McGehee, M. D.; Karunadasa, H. I. A Layered Hybrid Perovskite Solar-Cell Absorber with Enhanced Moisture Stability. *Angewandte Chemie International Edition* **2014**, *53* (42), 11232–11235. <https://doi.org/10.1002/anie.201406466>.
- (51) Liao, J.-F.; Rao, H.-S.; Chen, B.-X.; Kuang, D.-B.; Su, C.-Y. Dimension Engineering on Cesium Lead Iodide for Efficient and Stable Perovskite Solar Cells. *J. Mater. Chem. A* **2017**, *5* (5), 2066–2072. <https://doi.org/10.1039/C6TA09582H>.
- (52) Gélvez-Rueda, M. C.; Fridriksson, M. B.; Dubey, R. K.; Jager, W. F.; Van Der Stam, W.; Grozema, F. C. Overcoming the Exciton Binding Energy in Two-Dimensional Perovskite Nanoplatelets by Attachment of Conjugated Organic Chromophores. *Nat Commun* **2020**, *11* (1), 1901. <https://doi.org/10.1038/s41467-020-15869-7>.
- (53) Gao, P.; Bin Mohd Yusoff, A. R.; Nazeeruddin, M. K. Dimensionality Engineering of Hybrid Halide Perovskite Light Absorbers. *Nat Commun* **2018**, *9* (1), 5028. <https://doi.org/10.1038/s41467-018-07382-9>.
- (54) Grancini, G.; Roldán-Carmona, C.; Zimmermann, I.; Mosconi, E.; Lee, X.; Martineau, D.; Nabey, S.; Oswald, F.; De Angelis, F.; Graetzel, M.; Nazeeruddin, M. K. One-Year Stable Perovskite Solar Cells by 2D/3D Interface Engineering. *Nat Commun* **2017**, *8* (1), 15684. <https://doi.org/10.1038/ncomms15684>.

- (55) Ma, C.; Leng, C.; Ji, Y.; Wei, X.; Sun, K.; Tang, L.; Yang, J.; Luo, W.; Li, C.; Deng, Y.; Feng, S.; Shen, J.; Lu, S.; Du, C.; Shi, H. 2D/3D Perovskite Hybrids as Moisture-Tolerant and Efficient Light Absorbers for Solar Cells. *Nanoscale* **2016**, *8* (43), 18309–18314. <https://doi.org/10.1039/C6NR04741F>.
- (56) De Wolf, S.; Holovsky, J.; Moon, S.-J.; Löper, P.; Niesen, B.; Ledinsky, M.; Haug, F.-J.; Yum, J.-H.; Ballif, C. Organometallic Halide Perovskites: Sharp Optical Absorption Edge and Its Relation to Photovoltaic Performance. *J. Phys. Chem. Lett.* **2014**, *5* (6), 1035–1039. <https://doi.org/10.1021/jz500279b>.
- (57) Yin, W.-J.; Shi, T.; Yan, Y. Unusual Defect Physics in CH₃NH₃PbI₃ Perovskite Solar Cell Absorber. *Appl. Phys. Lett.* **2014**, *104* (6), 063903. <https://doi.org/10.1063/1.4864778>.
- (58) Brandt, R. E.; Stevanović, V.; Ginley, D. S.; Buonassisi, T. Identifying Defect-Tolerant Semiconductors with High Minority-Carrier Lifetimes: Beyond Hybrid Lead Halide Perovskites. *MRS Communications* **2015**, *5* (2), 265–275. <https://doi.org/10.1557/mrc.2015.26>.
- (59) Tennyson, E. M.; Doherty, T. A. S.; Stranks, S. D. Heterogeneity at Multiple Length Scales in Halide Perovskite Semiconductors. *Nat Rev Mater* **2019**, *4* (9), 573–587. <https://doi.org/10.1038/s41578-019-0125-0>.
- (60) Dunlap-Shohl, W. A.; Zhou, Y.; Padture, N. P.; Mitzi, D. B. Synthetic Approaches for Halide Perovskite Thin Films. *Chem. Rev.* **2019**, *119* (5), 3193–3295. <https://doi.org/10.1021/acs.chemrev.8b00318>.
- (61) Thomas Kirchartz; Uwe Rau. Introduction to Thin-Film Photovoltaics. In *Advanced Characterization Techniques for Thin Film Solar Cells*; Wiley-VCH: Germany, 2011.
- (62) Unger, E. L.; Kegelman, L.; Suchan, K.; Sörell, D.; Korte, L.; Albrecht, S. Roadmap and Roadblocks for the Band Gap Tunability of Metal Halide Perovskites. *J. Mater. Chem. A* **2017**, *5* (23), 11401–11409. <https://doi.org/10.1039/C7TA00404D>.
- (63) Tao, S.; Schmidt, I.; Brocks, G.; Jiang, J.; Tranca, I.; Meerholz, K.; Olthof, S. Absolute Energy Level Positions in Tin- and Lead-Based Halide Perovskites. *Nat Commun* **2019**, *10* (1), 2560. <https://doi.org/10.1038/s41467-019-10468-7>.
- (64) An, Y.; Perini, C. A. R.; Hidalgo, J.; Castro-Méndez, A.-F.; Vagott, J. N.; Li, R.; Saidi, W. A.; Wang, S.; Li, X.; Correa-Baena, J.-P. Identifying High-Performance and Durable Methylammonium-Free Lead Halide Perovskites *via* High-Throughput Synthesis and Characterization. *Energy Environ. Sci.* **2021**, *14* (12), 6638–6654. <https://doi.org/10.1039/D1EE02691G>.
- (65) Muhammad, Z.; Liu, P.; Ahmad, R.; Jalali-Asadabadi, S.; Franchini, C.; Ahmad, I. Revealing the Quasiparticle Electronic and Excitonic Nature in Cubic, Tetragonal, and Hexagonal Phases of FAPbI₃. *AIP Advances* **2022**, *12* (2), 025330. <https://doi.org/10.1063/5.0076738>.

- (66) Zhao, X.; Tang, T.; Xie, Q.; Gao, L.; Lu, L.; Tang, Y. First-Principles Study on the Electronic and Optical Properties of the Orthorhombic CsPbBr₃ and CsPbI₃ with *Cmcm* Space Group. *New J. Chem.* **2021**, *45* (35), 15857–15862. <https://doi.org/10.1039/D1NJ02216D>.
- (67) Kamminga, M. E.; De Wijs, G. A.; Havenith, R. W. A.; Blake, G. R.; Palstra, T. T. M. The Role of Connectivity on Electronic Properties of Lead Iodide Perovskite-Derived Compounds. *Inorg. Chem.* **2017**, *56* (14), 8408–8414. <https://doi.org/10.1021/acs.inorgchem.7b01096>.
- (68) Dastidar, S.; Hawley, C. J.; Dillon, A. D.; Gutierrez-Perez, A. D.; Spanier, J. E.; Fafarman, A. T. Quantitative Phase-Change Thermodynamics and Metastability of Perovskite-Phase Cesium Lead Iodide. *J. Phys. Chem. Lett.* **2017**, *8* (6), 1278–1282. <https://doi.org/10.1021/acs.jpcclett.7b00134>.
- (69) Cho, J.; DuBose, J. T.; Kamat, P. V. Charge Carrier Recombination Dynamics of Two-Dimensional Lead Halide Perovskites. *J. Phys. Chem. Lett.* **2020**, *11* (7), 2570–2576. <https://doi.org/10.1021/acs.jpcclett.0c00392>.
- (70) Xiao, Z.; Meng, W.; Wang, J.; Mitzi, D. B.; Yan, Y. Searching for Promising New Perovskite-Based Photovoltaic Absorbers: The Importance of Electronic Dimensionality. *Mater. Horiz.* **2017**, *4* (2), 206–216. <https://doi.org/10.1039/C6MH00519E>.
- (71) Shao, S.; Loi, M. A. The Role of the Interfaces in Perovskite Solar Cells. *Advanced Materials Interfaces* **2020**, *7* (1), 1901469. <https://doi.org/10.1002/admi.201901469>.
- (72) Mahmood, K.; Sarwar, S.; Mehran, M. T. Current Status of Electron Transport Layers in Perovskite Solar Cells: Materials and Properties. *RSC Adv.* **2017**, *7* (28), 17044–17062. <https://doi.org/10.1039/C7RA00002B>.
- (73) Rombach, F. M.; Haque, S. A.; Macdonald, T. J. Lessons Learned from Spiro-OMeTAD and PTAA in Perovskite Solar Cells. *Energy Environ. Sci.* **2021**, *14* (10), 5161–5190. <https://doi.org/10.1039/D1EE02095A>.
- (74) Ke, L.; Luo, S.; Ren, X.; Yuan, Y. Factors Influencing the Nucleation and Crystal Growth of Solution-Processed Organic Lead Halide Perovskites: A Review. *J. Phys. D: Appl. Phys.* **2021**, *54* (16), 163001. <https://doi.org/10.1088/1361-6463/abd728>.
- (75) Kumar, J.; Srivastava, P.; Bag, M. Advanced Strategies to Tailor the Nucleation and Crystal Growth in Hybrid Halide Perovskite Thin Films. *Front. Chem.* **2022**, *10*, 842924. <https://doi.org/10.3389/fchem.2022.842924>.
- (76) Whitehead, C. B.; Özkar, S.; Finke, R. G. LaMer's 1950 Model of Particle Formation: A Review and Critical Analysis of Its Classical Nucleation and Fluctuation Theory Basis, of Competing Models and Mechanisms for Phase-Changes and Particle Formation, and Then of Its Application to Silver Halide, Semiconductor, Metal, and Metal-Oxide Nanoparticles. *Mater. Adv.* **2021**, *2* (1), 186–235. <https://doi.org/10.1039/D0MA00439A>.

- (77) Thanh, N. T. K.; Maclean, N.; Mahiddine, S. Mechanisms of Nucleation and Growth of Nanoparticles in Solution. *Chem. Rev.* **2014**, *114* (15), 7610–7630. <https://doi.org/10.1021/cr400544s>.
- (78) Li, B.; Binks, D.; Cao, G.; Tian, J. Engineering Halide Perovskite Crystals through Precursor Chemistry. *Small* **2019**, *15* (47), 1903613. <https://doi.org/10.1002/sml.201903613>.
- (79) Stampelcoskie, K. G.; Manser, J. S.; Kamat, P. V. Dual Nature of the Excited State in Organic–Inorganic Lead Halide Perovskites. *Energy Environ. Sci.* **2015**, *8* (1), 208–215. <https://doi.org/10.1039/C4EE02988G>.
- (80) Yan, K.; Long, M.; Zhang, T.; Wei, Z.; Chen, H.; Yang, S.; Xu, J. Hybrid Halide Perovskite Solar Cell Precursors: Colloidal Chemistry and Coordination Engineering behind Device Processing for High Efficiency. *J. Am. Chem. Soc.* **2015**, *137* (13), 4460–4468. <https://doi.org/10.1021/jacs.5b00321>.
- (81) Flatken, M. A.; Radicchi, E.; Wendt, R.; Buzanich, A. G.; Härk, E.; Pascual, J.; Mathies, F.; Shargaieva, O.; Prause, A.; Dallmann, A.; De Angelis, F.; Hoell, A.; Abate, A. Role of the Alkali Metal Cation in the Early Stages of Crystallization of Halide Perovskites. *Chem. Mater.* **2022**, *34* (3), 1121–1131. <https://doi.org/10.1021/acs.chemmater.1c03563>.
- (82) Flatken, M. A.; Hoell, A.; Wendt, R.; Härk, E.; Dallmann, A.; Prause, A.; Pascual, J.; Unger, E.; Abate, A. Small-Angle Scattering to Reveal the Colloidal Nature of Halide Perovskite Precursor Solutions. *J. Mater. Chem. A* **2021**, *9* (23), 13477–13482. <https://doi.org/10.1039/D1TA01468D>.
- (83) Petrov, A. A.; Fateev, S. A.; Khrustalev, V. N.; Li, Y.; Dorovatovskii, P. V.; Zubavichus, Y. V.; Goodilin, E. A.; Tarasov, A. B. Formamidinium Haloplumbate Intermediates: The Missing Link in a Chain of Hybrid Perovskites Crystallization. *Chem. Mater.* **2020**, *32* (18), 7739–7745. <https://doi.org/10.1021/acs.chemmater.0c02156>.
- (84) Lee, J. W.; Yu, H.; Lee, K.; Bae, S.; Kim, J.; Han, G. R.; Hwang, D.; Kim, S. K.; Jang, J. Highly Crystalline Perovskite-Based Photovoltaics via Two-Dimensional Liquid Cage Annealing Strategy. *J. Am. Chem. Soc.* **2019**, *141* (14), 5808–5814. <https://doi.org/10.1021/jacs.8b13423>.
- (85) Saliba, M.; Correa-Baena, J.-P.; Wolff, C. M.; Stolterfoht, M.; Phung, N.; Albrecht, S.; Neher, D.; Abate, A. How to Make over 20% Efficient Perovskite Solar Cells in Regular (*n-i-p*) and Inverted (*p-i-n*) Architectures. *Chem. Mater.* **2018**, *30* (13), 4193–4201. <https://doi.org/10.1021/acs.chemmater.8b00136>.
- (86) Rivnay, J.; Mannsfeld, S. C. B.; Miller, C. E.; Salleo, A.; Toney, M. F. Quantitative Determination of Organic Semiconductor Microstructure from the Molecular to Device Scale. *Chem. Rev.* **2012**, *112* (10), 5488–5519. <https://doi.org/10.1021/cr3001109>.
- (87) Jens Als-Nielsen; Des McMorrow. *Elements of Modern X-Ray Physics*, 2nd ed.; Wiley: United Kingdom, 2011.

- (88) Renaud, G.; Lazzari, R.; Leroy, F. Probing Surface and Interface Morphology with Grazing Incidence Small Angle X-Ray Scattering. *Surface Science Reports* **2009**, *64* (8), 255–380. <https://doi.org/10.1016/j.surfrep.2009.07.002>.
- (89) Hao, X.; Chen, M.; Wang, L.; Cao, Z.; Li, Y.; Han, S.; Zhang, M.; Yu, K.; Zeng, J. *In Situ* SAXS Probing the Evolution of the Precursors and Onset of Nucleation of ZnSe Colloidal Semiconductor Quantum Dots. *Chem. Commun.* **2020**, *56* (13), 2031–2034. <https://doi.org/10.1039/C9CC09274A>.
- (90) Qin, M.; Chan, P. F.; Lu, X. A Systematic Review of Metal Halide Perovskite Crystallization and Film Formation Mechanism Unveiled by In Situ GIWAXS. *Advanced Materials* **2021**, *33* (51), 1–28. <https://doi.org/10.1002/adma.202105290>.
- (91) Gilles, B. Grazing Incidence Diffraction: A Review. *LTPCM, ENSEEG BP 75*, 177–204.
- (92) Qin, M.; Xue, H.; Zhang, H.; Hu, H.; Liu, K.; Li, Y.; Qin, Z.; Ma, J.; Zhu, H.; Yan, K.; Fang, G.; Li, G.; Jeng, U. S.; Brocks, G.; Tao, S.; Lu, X. Precise Control of Perovskite Crystallization Kinetics via Sequential A-Site Doping. *Advanced Materials* **2020**, *32* (42), 1–11. <https://doi.org/10.1002/adma.202004630>.
- (93) *Atomic Scattering Factors*. https://henke.lbl.gov/optical_constants/asf.html (accessed 2023-05-04).
- (94) B.D Cullity; S.R Stock. *Elements of X-Ray Diffraction*, Third Edition.; Pearson: Edinburgh, 2014.
- (95) Hoell, A.; Zizak, I.; Mokrani, L. Einrichtung Zur Kleinwinkelstreuung Zur Analyse Der Nanostruktur an Proben Mittels Röntgenstrahlung. DE102006029449B3, 2007.
- (96) Krumrey, M.; Ulm, G. High-Accuracy Detector Calibration at the PTB Four-Crystal Monochromator Beamline. *Nuclear Instruments & Methods in Physics Research: Section A* **2001**, No. 467–468, 1175–1178. [https://doi.org/DOI: 10.1016/S0168-9002\(01\)00598-8](https://doi.org/DOI: 10.1016/S0168-9002(01)00598-8).
- (97) Keiderling, U. The New “BerSANS-PC” Software for Reduction and Treatment of Small Angle Neutron Scattering Data. *Applied Physics A: Materials Science & Processing* **2002**, *74* (0), s1455–s1457. <https://doi.org/10.1007/s003390201561>.
- (98) John F. Moulder; William F. Stickle; Peter E. Sobol; Kenneth D. Bomben. *Handbook of X-Ray Photoelectron Spectroscopy*; Physical Electronics, Inc.: Eden Prairie, Minnesota, USA, 1992.
- (99) Hidalgo, J.; Castro-Méndez, A.-F.; Correa-Baena, J.-P. Imaging and Mapping Characterization Tools for Perovskite Solar Cells. *Advanced Energy Materials* **2019**, *9* (30), 1900444. <https://doi.org/10.1002/aenm.201900444>.

- (100) Makula, P.; Pacia, M.; Macyk, W. How To Correctly Determine the Band Gap Energy of Modified Semiconductor Photocatalysts Based on UV–Vis Spectra. *J. Phys. Chem. Lett.* **2018**, *9* (23), 6814–6817. <https://doi.org/10.1021/acs.jpcclett.8b02892>.
- (101) Köbler, H.; Neubert, S.; Jankovec, M.; Glažar, B.; Haase, M.; Hilbert, C.; Topič, M.; Rech, B.; Abate, A. High-Throughput Aging System for Parallel Maximum Power Point Tracking of Perovskite Solar Cells. *Energy Technology* **2022**, *10* (6), 2200234. <https://doi.org/10.1002/ente.202200234>.
- (102) Rakocevic, L.; Ernst, F.; Yim, N. T.; Vashishtha, S.; Aernouts, T.; Heumueller, T.; Brabec, C. J.; Gehlhaar, R.; Poortmans, J. Reliable Performance Comparison of Perovskite Solar Cells Using Optimized Maximum Power Point Tracking. *Solar RRL* **2019**, *3* (2), 1800287. <https://doi.org/10.1002/solr.201800287>.
- (103) Khenkin, M. V.; Katz, E. A.; Abate, A.; Bardizza, G.; Berry, J. J.; Brabec, C.; Brunetti, F.; Bulović, V.; Burlingame, Q.; Di Carlo, A.; Cheacharoen, R.; Cheng, Y.-B.; Colsmann, A.; Cros, S.; Domanski, K.; Dusza, M.; Fell, C. J.; Forrest, S. R.; Galagan, Y.; Di Girolamo, D.; Grätzel, M.; Hagfeldt, A.; Von Hauff, E.; Hoppe, H.; Kettle, J.; Köbler, H.; Leite, M. S.; Liu, S.; Loo, Y.-L.; Luther, J. M.; Ma, C.-Q.; Madsen, M.; Manceau, M.; Matheron, M.; McGehee, M.; Meitzner, R.; Nazeeruddin, M. K.; Nogueira, A. F.; Odabaşı, Ç.; Osherov, A.; Park, N.-G.; Reese, M. O.; De Rossi, F.; Saliba, M.; Schubert, U. S.; Snaith, H. J.; Stranks, S. D.; Tress, W.; Troshin, P. A.; Turkovic, V.; Veenstra, S.; Visoly-Fisher, I.; Walsh, A.; Watson, T.; Xie, H.; Yıldırım, R.; Zakeeruddin, S. M.; Zhu, K.; Lira-Cantu, M. Consensus Statement for Stability Assessment and Reporting for Perovskite Photovoltaics Based on ISOS Procedures. *Nat Energy* **2020**, *5* (1), 35–49. <https://doi.org/10.1038/s41560-019-0529-5>.
- (104) Ajay Kumar Jena; Tsutomu Miyasaka. Hysteresis Characteristics and Device Stability. In *Organic-Inorganic Halide Perovskite Photovoltaics: From Fundamentals to Device Architectures*; Springer: Switzerland, 2016.
- (105) Juan Bisquert; Germa Garcia-Belmonte; Antonio Guerrero. Impedance Characteristics of Hybrid Organometal Halide Perovskite Solar Cells. In *Organic-Inorganic Halide Perovskite Photovoltaics*; Springer: Switzerland, 2016.
- (106) Chiang, C.-H.; Wu, C.-G. A Method for the Preparation of Highly Oriented MAPbI₃ Crystallites for High-Efficiency Perovskite Solar Cells to Achieve an 86% Fill Factor. *ACS Nano* **2018**, *12* (10), 10355–10364. <https://doi.org/10.1021/acsnano.8b05731>.
- (107) Petrus, M. L.; Hu, Y.; Moia, D.; Calado, P.; Leguy, A. M. A.; Barnes, P. R. F.; Docampo, P. The Influence of Water Vapor on the Stability and Processing of Hybrid Perovskite Solar Cells Made from Non-Stoichiometric Precursor Mixtures. *ChemSusChem* **2016**, *9* (18), 2699–2707. <https://doi.org/10.1002/cssc.201600999>.
- (108) Hidalgo, J.; Perini, C. A. R.; Castro-Mendez, A.-F.; Jones, D.; Köbler, H.; Lai, B.; Li, R.; Sun, S.; Abate, A.; Correa-Baena, J.-P. Moisture-Induced Crystallographic Reorientations and Effects on Charge Carrier Extraction in Metal Halide Perovskite Solar Cells. *ACS Energy Lett.* **2020**, *5* (11), 3526–3534. <https://doi.org/10.1021/acsenerylett.0c01964>.

- (109) Flannery, L.; Ogle, J.; Powell, D.; Tassone, C.; Whittaker-Brooks, L. Voltage Bias Stress Effects in Metal Halide Perovskites Are Strongly Dependent on Morphology and Ion Migration Pathways. *J. Mater. Chem. A* **2020**, *8* (47), 25109–25119. <https://doi.org/10.1039/D0TA10371C>.
- (110) Zheng, G.; Zhu, C.; Ma, J.; Zhang, X.; Tang, G.; Li, R.; Chen, Y.; Li, L.; Hu, J.; Hong, J.; Chen, Q.; Gao, X.; Zhou, H. Manipulation of Facet Orientation in Hybrid Perovskite Polycrystalline Films by Cation Cascade. *Nature Communications* **2018**, *9* (1), 1–11. <https://doi.org/10.1038/s41467-018-05076-w>.
- (111) Joseph Kline, R.; McGehee, M. D.; Toney, M. F. Highly Oriented Crystals at the Buried Interface in Polythiophene Thin-Film Transistors. *Nature Mater* **2006**, *5* (3), 222–228. <https://doi.org/10.1038/nmat1590>.
- (112) Vasileiadou, E. S.; Hadar, I.; Kepenekian, M.; Even, J.; Tu, Q.; Malliakas, C. D.; Friedrich, D.; Spanopoulos, I.; Hoffman, J. M.; Dravid, V. P.; Kanatzidis, M. G. Shedding Light on the Stability and Structure–Property Relationships of Two-Dimensional Hybrid Lead Bromide Perovskites. *Chem. Mater.* **2021**, *33* (13), 5085–5107. <https://doi.org/10.1021/acs.chemmater.1c01129>.
- (113) Kulbak, M.; Gupta, S.; Kedem, N.; Levine, I.; Bendikov, T.; Hodes, G.; Cahen, D. Cesium Enhances Long-Term Stability of Lead Bromide Perovskite-Based Solar Cells. *J. Phys. Chem. Lett.* **2016**, *7* (1), 167–172. <https://doi.org/10.1021/acs.jpcclett.5b02597>.
- (114) Ijaz, P.; Imran, M.; Soares, M. M.; Tolentino, H. C. N.; Martín-García, B.; Giannini, C.; Moreels, I.; Manna, L.; Krahne, R. Composition-, Size-, and Surface Functionalization-Dependent Optical Properties of Lead Bromide Perovskite Nanocrystals. *J. Phys. Chem. Lett.* **2020**, *11* (6), 2079–2085. <https://doi.org/10.1021/acs.jpcclett.0c00266>.
- (115) Leyden, M. R.; Meng, L.; Jiang, Y.; Ono, L. K.; Qiu, L.; Juarez-Perez, E. J.; Qin, C.; Adachi, C.; Qi, Y. Methylammonium Lead Bromide Perovskite Light-Emitting Diodes by Chemical Vapor Deposition. *J. Phys. Chem. Lett.* **2017**, *8* (14), 3193–3198. <https://doi.org/10.1021/acs.jpcclett.7b01093>.
- (116) Gavranovic, S.; Pospisil, J.; Zmeskal, O.; Novak, V.; Vanysek, P.; Castkova, K.; Cihlar, J.; Weiter, M. Electrode Spacing as a Determinant of the Output Performance of Planar-Type Photodetectors Based on Methylammonium Lead Bromide Perovskite Single Crystals. *ACS Appl. Mater. Interfaces* **2022**, *14* (17), 20159–20167. <https://doi.org/10.1021/acsami.1c24362>.
- (117) Hu, C.; Shivarudraiah, S. B.; Sung, H. H. Y.; Williams, I. D.; Halpert, J. E.; Yang, S. Discovery of a New Intermediate Enables One-Step Deposition of High-Quality Perovskite Films via Solvent Engineering. *Solar RRL* **2021**, *5* (4), 2000712. <https://doi.org/10.1002/solr.202000712>.
- (118) Rezaee, E.; Zhang, W.; Silva, S. R. P. Solvent Engineering as a Vehicle for High Quality Thin Films of Perovskites and Their Device Fabrication. *Small* **2021**, *17* (25), 2008145. <https://doi.org/10.1002/sml.202008145>.

- (119) Shargaieva, O.; Näsström, H.; Smith, J. A.; Töbrens, D.; Munir, R.; Unger, E. Hybrid Perovskite Crystallization from Binary Solvent Mixtures: Interplay of Evaporation Rate and Binding Strength of Solvents. *Mater. Adv.* **2020**, *1* (9), 3314–3321. <https://doi.org/10.1039/D0MA00815J>.
- (120) Petrov, A. A.; Sokolova, I. P.; Belich, N. A.; Peters, G. S.; Dorovatovskii, P. V.; Zubavichus, Y. V.; Khrustalev, V. N.; Petrov, A. V.; Grätzel, M.; Goodilin, E. A.; Tarasov, A. B. Crystal Structure of DMF-Intermediate Phases Uncovers the Link Between $\text{CH}_3\text{NH}_3\text{PbI}_3$ Morphology and Precursor Stoichiometry. *J. Phys. Chem. C* **2017**, *121* (38), 20739–20743. <https://doi.org/10.1021/acs.jpcc.7b08468>.
- (121) Soe, C. M. M.; Nie, W.; Stoumpos, C. C.; Tsai, H.; Blancon, J.-C.; Liu, F.; Even, J.; Marks, T. J.; Mohite, A. D.; Kanatzidis, M. G. Understanding Film Formation Morphology and Orientation in High Member 2D Ruddlesden–Popper Perovskites for High-Efficiency Solar Cells. *Advanced Energy Materials* **2018**, *8* (1), 1700979. <https://doi.org/10.1002/aenm.201700979>.
- (122) Hamill, J. C.; Schwartz, J.; Loo, Y.-L. Influence of Solvent Coordination on Hybrid Organic–Inorganic Perovskite Formation. *ACS Energy Lett.* **2018**, *3* (1), 92–97. <https://doi.org/10.1021/acsenerylett.7b01057>.
- (123) Petrov, A. A.; Ordinartsev, A. A.; Fateev, S. A.; Goodilin, E. A.; Tarasov, A. B. Solubility of Hybrid Halide Perovskites in DMF and DMSO. *Molecules* **2021**, *26* (24), 7541. <https://doi.org/10.3390/molecules26247541>.
- (124) Dutta, N. S.; Noel, N. K.; Arnold, C. B. Crystalline Nature of Colloids in Methylammonium Lead Halide Perovskite Precursor Inks Revealed by Cryo-Electron Microscopy. *J. Phys. Chem. Lett.* **2020**, *11* (15), 5980–5986. <https://doi.org/10.1021/acs.jpcllett.0c01975>.
- (125) Ray, A.; Maggioni, D.; Baranov, D.; Dang, Z.; Prato, M.; Akkerman, Q. A.; Goldoni, L.; Caneva, E.; Manna, L.; Abdelhady, A. L. Green-Emitting Powders of Zero-Dimensional Cs_4PbBr_6 : Delineating the Intricacies of the Synthesis and the Origin of Photoluminescence. *Chem. Mater.* **2019**, *31* (18), 7761–7769. <https://doi.org/10.1021/acs.chemmater.9b02944>.
- (126) Bo Chen; Zhengshan J. Yu; Salman Manzoor; Shen Wang; William Weigand; Zhenhua Yu; Guang Yang; Zhenyi Ni; Zuezeng Dai; Zachary C. Holman; Jinsong Huang. Blade-Coated Perovskites on Textured Silicon for 26%-Efficient Monolithic Perovskite/Silicon Tandem Solar Cells | Elsevier Enhanced Reader. *Joule* **2020**, *4*, 850–864. <https://doi.org/10.1016/j.joule.2020.01.008>.
- (127) Zhang, J.; Zhang, L.; Li, X.; Zhu, X.; Yu, J.; Fan, K. Binary Solvent Engineering for High-Performance Two-Dimensional Perovskite Solar Cells. *ACS Sustainable Chem. Eng.* **2019**, *7* (3), 3487–3495. <https://doi.org/10.1021/acssuschemeng.8b05734>.

- (128) Keller, T.; Nickel, N. H.; Rappich, J. Competition of Iodide/Bromide Ions in the Formation of Methylammonium Lead Halide in Different Solvents. *J. Phys. Chem. C* **2022**, *126* (41), 17656–17662. <https://doi.org/10.1021/acs.jpcc.2c03740>.
- (129) Steele, J. A.; Solano, E.; Jin, H.; Prakasam, V.; Braeckvelt, T.; Yuan, H.; Lin, Z.; de Kloe, R.; Wang, Q.; Rogge, S. M. J.; Van Speybroeck, V.; Chernyshov, D.; Hofkens, J.; Roeffaers, M. B. J. Texture Formation in Polycrystalline Thin Films of All-Inorganic Lead Halide Perovskite. *Advanced Materials* **2021**, *33* (13), 1–9. <https://doi.org/10.1002/adma.202007224>.
- (130) Feigin, L.A.; Svergun, D.I. *Structure Analysis by Small-Angle X-Ray and Neutron Scattering*; Plenum Press, New York, 1987.
- (131) Qin, F.; Wang, Z.; Wang, Z. L. Anomalous Growth and Coalescence Dynamics of Hybrid Perovskite Nanoparticles Observed by Liquid-Cell Transmission Electron Microscopy. *ACS Nano* **2016**, *10* (11), 9787–9793. <https://doi.org/10.1021/acs.nano.6b04234>.
- (132) Ogle, J.; Powell, D.; Amerling, E.; Smilgies, D.-M.; Whittaker-Brooks, L. Quantifying Multiple Crystallite Orientations and Crystal Heterogeneities in Complex Thin Film Materials. *CrystEngComm* **2019**, *21* (38), 5707–5720. <https://doi.org/10.1039/C9CE01010F>.
- (133) Wang, K.-H.; Li, L.-C.; Shellaiah, M.; Wen Sun, K. Structural and Photophysical Properties of Methylammonium Lead Tribromide (MAPbBr₃) Single Crystals. *Sci Rep* **2017**, *7* (1), 13643. <https://doi.org/10.1038/s41598-017-13571-1>.
- (134) Schueller, E. C.; Laurita, G.; Fabini, D. H.; Stoumpos, C. C.; Kanatzidis, M. G.; Seshadri, R. Crystal Structure Evolution and Notable Thermal Expansion in Hybrid Perovskites Formamidinium Tin Iodide and Formamidinium Lead Bromide. *Inorg. Chem.* **2018**, *57* (2), 695–701. <https://doi.org/10.1021/acs.inorgchem.7b02576>.
- (135) Oner, S. M.; Sezen, E.; Yordanli, M. S.; Karakoc, E.; Deger, C.; Yavuz, I. Surface Defect Formation and Passivation in Formamidinium Lead Triiodide (FAPbI₃) Perovskite Solar Cell Absorbers. *J. Phys. Chem. Lett.* **2022**, *13* (1), 324–330. <https://doi.org/10.1021/acs.jpcllett.1c03645>.
- (136) Kirstein, E.; Yakovlev, D. R.; Glazov, M. M.; Zhukov, E. A.; Kudlacik, D.; Kalitukha, I. V.; Sapega, V. F.; Dimitriev, G. S.; Semina, M. A.; Nestoklon, M. O.; Ivchenko, E. L.; Kopteva, N. E.; Dirin, D. N.; Nazarenko, O.; Kovalenko, M. V.; Baumann, A.; Höcker, J.; Dyakonov, V.; Bayer, M. The Landé Factors of Electrons and Holes in Lead Halide Perovskites: Universal Dependence on the Band Gap. *Nat Commun* **2022**, *13* (1), 3062. <https://doi.org/10.1038/s41467-022-30701-0>.
- (137) Butler, K. T.; Frost, J. M.; Walsh, A. Band Alignment of the Hybrid Halide Perovskites CH₃NH₃PbCl₃, CH₃NH₃PbBr₃ and CH₃NH₃PbI₃. *Mater. Horiz.* **2015**, *2* (2), 228–231. <https://doi.org/10.1039/C4MH00174E>.

- (138) Chen, Y.; Zhou, W.; Chen, X.; Zhang, X.; Gao, H.; Ouedraogo, N. A. N.; Zheng, Z.; Han, C. B.; Zhang, Y.; Yan, H. In Situ Management of Ions Migration to Control Hysteresis Effect for Planar Heterojunction Perovskite Solar Cells. *Advanced Functional Materials* **2022**, *32* (1), 2108417. <https://doi.org/10.1002/adfm.202108417>.
- (139) Chen, B.; Yang, M.; Priya, S.; Zhu, K. Origin of J – V Hysteresis in Perovskite Solar Cells. *J. Phys. Chem. Lett.* **2016**, *7* (5), 905–917. <https://doi.org/10.1021/acs.jpcllett.6b00215>.
- (140) McGovern, L.; Koschany, I.; Grimaldi, G.; Muscarella, L. A.; Ehrler, B. Grain Size Influences Activation Energy and Migration Pathways in MAPbBr₃ Perovskite Solar Cells. *J. Phys. Chem. Lett.* **2021**, *12* (9), 2423–2428. <https://doi.org/10.1021/acs.jpcllett.1c00205>.
- (141) Liu, P.; Wang, W.; Liu, S.; Yang, H.; Shao, Z. Fundamental Understanding of Photocurrent Hysteresis in Perovskite Solar Cells. *Advanced Energy Materials* **2019**, *9* (13), 1803017. <https://doi.org/10.1002/aenm.201803017>.
- (142) Liu, J.; Hu, M.; Dai, Z.; Que, W.; Pature, N. P.; Zhou, Y. Correlations between Electrochemical Ion Migration and Anomalous Device Behaviors in Perovskite Solar Cells. *ACS Energy Lett.* **2021**, *6* (3), 1003–1014. <https://doi.org/10.1021/acsenerylett.0c02662>.
- (143) Zhu, X.; Du, M.; Feng, J.; Wang, H.; Xu, Z.; Wang, L.; Zuo, S.; Wang, C.; Wang, Z.; Zhang, C.; Ren, X.; Priya, S.; Yang, D.; Liu, S. (Frank). High-Efficiency Perovskite Solar Cells with Imidazolium-Based Ionic Liquid for Surface Passivation and Charge Transport. *Angewandte Chemie International Edition* **2021**, *60* (8), 4238–4244. <https://doi.org/10.1002/anie.202010987>.
- (144) Oranskaia, A.; Yin, J.; Bakr, O. M.; Brédas, J.-L.; Mohammed, O. F. Halogen Migration in Hybrid Perovskites: The Organic Cation Matters. *J. Phys. Chem. Lett.* **2018**, *9* (18), 5474–5480. <https://doi.org/10.1021/acs.jpcllett.8b02522>.
- (145) Pitarch-Tena, D.; Ngo, T. T.; Vallés-Pelarda, M.; Pauporté, T.; Mora-Seró, I. Impedance Spectroscopy Measurements in Perovskite Solar Cells: Device Stability and Noise Reduction. *ACS Energy Lett.* **2018**, *3* (4), 1044–1048. <https://doi.org/10.1021/acsenerylett.8b00465>.
- (146) Yoo, S.M.; Yoon, S.J.; Anta, J.A.; Lee, H.J.; Boix, P.P; Mora-Seró, I. An Equivalent Circuit for Perovskite Solar Cell Bridging Sensitized to Thin Film Architectures. *Joule* **3**, 2535–2549. <https://doi.org/DOI: 10.1016/j.joule.2019.07.014>.
- (147) Zarazua, I.; Bisquert, J.; Garcia-Belmonte, G. Light-Induced Space-Charge Accumulation Zone as Photovoltaic Mechanism in Perovskite Solar Cells. *J. Phys. Chem. Lett.* **2016**, *7* (3), 525–528. <https://doi.org/10.1021/acs.jpcllett.5b02810>.
- (148) Riquelme, A. J.; Valadez-Villalobos, K.; Boix, P. P.; Oskam, G.; Mora-Seró, I.; Anta, J. A. Understanding Equivalent Circuits in Perovskite Solar Cells. Insights from Drift-

- Diffusion Simulation. *Phys. Chem. Chem. Phys.* **2022**, *24* (26), 15657–15671. <https://doi.org/10.1039/D2CP01338J>.
- (149) Fassl, P.; Ternes, S.; Lami, V.; Zakharko, Y.; Heimfarth, D.; Hopkinson, P. E.; Paulus, F.; Taylor, A. D.; Zaumseil, J.; Vaynzof, Y. Effect of Crystal Grain Orientation on the Rate of Ionic Transport in Perovskite Polycrystalline Thin Films. *ACS Appl. Mater. Interfaces* **2019**, *11* (2), 2490–2499. <https://doi.org/10.1021/acsami.8b16460>.
- (150) Eames, C.; Frost, J. M.; Barnes, P. R. F.; O'Regan, B. C.; Walsh, A.; Islam, M. S. Ionic Transport in Hybrid Lead Iodide Perovskite Solar Cells. *Nature Communications* **2015**, *6* (May), 2–9. <https://doi.org/10.1038/ncomms8497>.
- (151) Zarick, H. F.; Soetan, N.; Erwin, W. R.; Bardhan, R. Mixed Halide Hybrid Perovskites: A Paradigm Shift in Photovoltaics. *J. Mater. Chem. A* **2018**, *6* (14), 5507–5537. <https://doi.org/10.1039/C7TA09122B>.
- (152) Rehman, W.; McMeekin, D. P.; Patel, J. B.; Milot, R. L.; Johnston, M. B.; Snaith, H. J.; Herz, L. M. Photovoltaic Mixed-Cation Lead Mixed-Halide Perovskites: Links between Crystallinity, Photo-Stability and Electronic Properties. *Energy Environ. Sci.* **2017**, *10* (1), 361–369. <https://doi.org/10.1039/C6EE03014A>.
- (153) Roldán-Carmona, C.; Gratia, P.; Zimmermann, I.; Grancini, G.; Gao, P.; Graetzel, M.; Nazeeruddin, M. K. High Efficiency Methylammonium Lead Triiodide Perovskite Solar Cells: The Relevance of Non-Stoichiometric Precursors. *Energy Environ. Sci.* **2015**, *8* (12), 3550–3556. <https://doi.org/10.1039/C5EE02555A>.
- (154) Jacobsson, T. J.; Correa-Baena, J.-P.; Halvani Anaraki, E.; Philippe, B.; Stranks, S. D.; Bouduban, M. E. F.; Tress, W.; Schenk, K.; Teuscher, J.; Moser, J.-E.; Rensmo, H.; Hagfeldt, A. Unreacted PbI_2 as a Double-Edged Sword for Enhancing the Performance of Perovskite Solar Cells. *J. Am. Chem. Soc.* **2016**, *138* (32), 10331–10343. <https://doi.org/10.1021/jacs.6b06320>.
- (155) Park, B.; Kedem, N.; Kulbak, M.; Lee, D. Y.; Yang, W. S.; Jeon, N. J.; Seo, J.; Kim, G.; Kim, K. J.; Shin, T. J.; Hodes, G.; Cahen, D.; Seok, S. I. Understanding How Excess Lead Iodide Precursor Improves Halide Perovskite Solar Cell Performance. *Nat Commun* **2018**, *9* (1), 3301. <https://doi.org/10.1038/s41467-018-05583-w>.
- (156) Correa-Baena, J.-P.; Luo, Y.; Brenner, T. M.; Snaider, J.; Sun, S.; Li, X.; Jensen, M. A.; Hartono, N. T. P.; Nienhaus, L.; Wiegold, S.; Poindexter, J. R.; Wang, S.; Meng, Y. S.; Wang, T.; Lai, B.; Holt, M. V.; Cai, Z.; Bawendi, M. G.; Huang, L.; Buonassisi, T.; Fenning, D. P. Homogenized Halides and Alkali Cation Segregation in Alloyed Organic-Inorganic Perovskites. *Science* **2019**, *363* (6427), 627–631. <https://doi.org/10.1126/science.aah5065>.
- (157) Zhang, L.; Ju, M.-G.; Liang, W. The Effect of Moisture on the Structures and Properties of Lead Halide Perovskites: A First-Principles Theoretical Investigation. *Phys. Chem. Chem. Phys.* **2016**, *18* (33), 23174–23183. <https://doi.org/10.1039/C6CP01994C>.

- (158) Mosconi, E.; Azpiroz, J. M.; De Angelis, F. *Ab Initio* Molecular Dynamics Simulations of Methylammonium Lead Iodide Perovskite Degradation by Water. *Chem. Mater.* **2015**, *27* (13), 4885–4892. <https://doi.org/10.1021/acs.chemmater.5b01991>.
- (159) Zhou, W.; Zhao, Y.; Shi, C.; Huang, H.; Wei, J.; Fu, R.; Liu, K.; Yu, D.; Zhao, Q. Reversible Healing Effect of Water Molecules on Fully Crystallized Metal–Halide Perovskite Film. *J. Phys. Chem. C* **2016**, *120* (9), 4759–4765. <https://doi.org/10.1021/acs.jpcc.5b11465>.
- (160) Aranda, C.; Cristobal, C.; Shoostari, L.; Li, C.; Huettner, S.; Guerrero, A. Formation Criteria of High Efficiency Perovskite Solar Cells under Ambient Conditions. *Sustainable Energy Fuels* **2017**, *1* (3), 540–547. <https://doi.org/10.1039/C6SE00077K>.
- (161) Leguy, A. M. A.; Hu, Y.; Campoy-Quiles, M.; Alonso, M. I.; Weber, O. J.; Azarhoosh, P.; Van Schilfgaarde, M.; Weller, M. T.; Bein, T.; Nelson, J.; Docampo, P.; Barnes, P. R. F. Reversible Hydration of $\text{CH}_3\text{NH}_3\text{PbI}_3$ in Films, Single Crystals, and Solar Cells. *Chem. Mater.* **2015**, *27* (9), 3397–3407. <https://doi.org/10.1021/acs.chemmater.5b00660>.
- (162) Gangishetty, M. K.; Scott, R. W. J.; Kelly, T. L. Effect of Relative Humidity on Crystal Growth, Device Performance and Hysteresis in Planar Heterojunction Perovskite Solar Cells. *Nanoscale* **2016**, *8* (12), 6300–6307. <https://doi.org/10.1039/C5NR04179A>.
- (163) Li, D.; Bretschneider, S. A.; Bergmann, V. W.; Hermes, I. M.; Mars, J.; Klasen, A.; Lu, H.; Tremel, W.; Mezger, M.; Butt, H.-J.; Weber, S. A. L.; Berger, R. Humidity-Induced Grain Boundaries in MAPbI_3 Perovskite Films. *J. Phys. Chem. C* **2016**, *120* (12), 6363–6368. <https://doi.org/10.1021/acs.jpcc.6b00335>.
- (164) Philippe, B.; Saliba, M.; Correa-Baena, J.-P.; Cappel, U. B.; Turren-Cruz, S.-H.; Grätzel, M.; Hagfeldt, A.; Rensmo, H. Chemical Distribution of Multiple Cation (Rb^+ , Cs^+ , MA^+ , and FA^+) Perovskite Materials by Photoelectron Spectroscopy. *Chem. Mater.* **2017**, *29* (8), 3589–3596. <https://doi.org/10.1021/acs.chemmater.7b00126>.
- (165) Zhang, W.; Xiong, J.; Li, J.; Daoud, W. A. Mechanism of Water Effect on Enhancing the Photovoltaic Performance of Triple-Cation Hybrid Perovskite Solar Cells. *ACS Appl. Mater. Interfaces* **2019**, *11* (13), 12699–12708. <https://doi.org/10.1021/acsami.8b20264>.
- (166) Gong, X.; Li, M.; Shi, X.-B.; Ma, H.; Wang, Z.-K.; Liao, L.-S. Controllable Perovskite Crystallization by Water Additive for High-Performance Solar Cells. *Advanced Functional Materials* **2015**, *25* (42), 6671–6678. <https://doi.org/10.1002/adfm.201503559>.
- (167) Zheng, G.; Zhu, C.; Chen, Y.; Zhang, J.; Chen, Q.; Gao, X.; Zhou, H. Microstructure Variations Induced by Excess PbX_2 or AX within Perovskite Thin Films. *Chem. Commun.* **2017**, *53* (96), 12966–12969. <https://doi.org/10.1039/C7CC07534K>.
- (168) Schlipf, J.; Müller-Buschbaum, P. Structure of Organometal Halide Perovskite Films as Determined with Grazing-Incidence X-Ray Scattering Methods. *Advanced Energy Materials* **2017**, *7* (16), 1700131. <https://doi.org/10.1002/aenm.201700131>.
- (169) Nick Day. Crystallography Open Database, 2023. <http://www.crystallography.net/cod/>.

- (170) Howard, J. M.; Tennyson, E. M.; Barik, S.; Szostak, R.; Waks, E.; Toney, M. F.; Nogueira, A. F.; Neves, B. R. A.; Leite, M. S. Humidity-Induced Photoluminescence Hysteresis in Variable Cs/Br Ratio Hybrid Perovskites. *J. Phys. Chem. Lett.* **2018**, *9* (12), 3463–3469. <https://doi.org/10.1021/acs.jpcclett.8b01357>.
- (171) Leblebici, S. Y.; Leppert, L.; Li, Y.; Reyes-Lillo, S. E.; Wickenburg, S.; Wong, E.; Lee, J.; Melli, M.; Ziegler, D.; Angell, D. K.; Ogletree, D. F.; Ashby, P. D.; Toma, F. M.; Neaton, J. B.; Sharp, I. D.; Weber-Bargioni, A. Facet-Dependent Photovoltaic Efficiency Variations in Single Grains of Hybrid Halide Perovskite. *Nat Energy* **2016**, *1* (8), 16093. <https://doi.org/10.1038/nenergy.2016.93>.
- (172) Bae, S.; Park, J.-S.; Han, I. K.; Shin, T. J.; Jo, W. H. CH₃NH₃PbI₃ Crystal Orientation and Photovoltaic Performance of Planar Heterojunction Perovskite Solar Cells. *Solar Energy Materials and Solar Cells* **2017**, *160*, 77–84. <https://doi.org/10.1016/j.solmat.2016.10.019>.
- (173) Stuckelberger, M.; West, B.; Nietzold, T.; Lai, B.; Maser, J. M.; Rose, V.; Bertoni, M. I. Engineering Solar Cells Based on Correlative X-Ray Microscopy. *J. Mater. Res.* **2017**, *32* (10), 1825–1854. <https://doi.org/10.1557/jmr.2017.108>.
- (174) Eperon, G. E.; Habisreutinger, S. N.; Leijtens, T.; Bruijnaers, B. J.; Van Franeker, J. J.; deQuilettes, D. W.; Pathak, S.; Sutton, R. J.; Grancini, G.; Ginger, D. S.; Janssen, R. A. J.; Petrozza, A.; Snaith, H. J. The Importance of Moisture in Hybrid Lead Halide Perovskite Thin Film Fabrication. *ACS Nano* **2015**, *9* (9), 9380–9393. <https://doi.org/10.1021/acs.nano.5b03626>.
- (175) Roose, B.; Ummadisingu, A.; Correa-Baena, J. P.; Saliba, M.; Hagfeldt, A.; Graetzel, M.; Steiner, U.; Abate, A. Spontaneous Crystal Coalescence Enables Highly Efficient Perovskite Solar Cells. *Nano Energy* **2017**, *39*, 24–29. <https://doi.org/10.1016/j.nanoen.2017.06.037>.
- (176) Givargizov, E. I. Artificial Epitaxy (Graphoepitaxy). In *Handbook of crystal growth: thin films and epitaxy, Growth Mechanisms and Dynamics*; Hurlé, D. T. J., Ed.; Elsevier Science, 1994; p 984.
- (177) Ho, K.; Wei, M.; Sargent, E. H.; Walker, G. C. Grain Transformation and Degradation Mechanism of Formamidinium and Cesium Lead Iodide Perovskite under Humidity and Light. *ACS Energy Lett.* **2021**, *6* (3), 934–940. <https://doi.org/10.1021/acsenergylett.0c02247>.
- (178) Zheng, C.; Rubel, O. Unraveling the Water Degradation Mechanism of CH₃NH₃PbI₃. *J. Phys. Chem. C* **2019**, *123* (32), 19385–19394. <https://doi.org/10.1021/acs.jpcc.9b05516>.
- (179) Kye, Y.-H.; Yu, C.-J.; Jong, U.-G.; Chen, Y.; Walsh, A. Critical Role of Water in Defect Aggregation and Chemical Degradation of Perovskite Solar Cells. *J. Phys. Chem. Lett.* **2018**, *9* (9), 2196–2201. <https://doi.org/10.1021/acs.jpcclett.8b00406>.
- (180) Shirayama, M.; Kato, M.; Miyadera, T.; Sugita, T.; Fujiseki, T.; Hara, S.; Kadowaki, H.; Murata, D.; Chikamatsu, M.; Fujiwara, H. Degradation Mechanism of CH₃NH₃PbI₃

- Perovskite Materials upon Exposure to Humid Air. *Journal of Applied Physics* **2016**, *119* (11), 115501. <https://doi.org/10.1063/1.4943638>.
- (181) Lin, J.; Lai, M.; Dou, L.; Kley, C. S.; Chen, H.; Peng, F.; Sun, J.; Lu, D.; Hawks, S. A.; Xie, C.; Cui, F.; Alivisatos, A. P.; Limmer, D. T.; Yang, P. Thermochromic Halide Perovskite Solar Cells. *Nature Mater* **2018**, *17* (3), 261–267. <https://doi.org/10.1038/s41563-017-0006-0>.
- (182) Kaiser, W.; Ricciarelli, D.; Mosconi, E.; Alothman, A. A.; Ambrosio, F.; De Angelis, F. Stability of Tin- versus Lead-Halide Perovskites: Ab Initio Molecular Dynamics Simulations of Perovskite/Water Interfaces. *J. Phys. Chem. Lett.* **2022**, *13* (10), 2321–2329. <https://doi.org/10.1021/acs.jpcllett.2c00273>.
- (183) He, J.; Fang, W.-H.; Long, R.; Prezhdo, O. V. Superoxide/Peroxide Chemistry Extends Charge Carriers' Lifetime but Undermines Chemical Stability of CH₃NH₃PbI₃ Exposed to Oxygen: Time-Domain *Ab Initio* Analysis. *J. Am. Chem. Soc.* **2019**, *141* (14), 5798–5807. <https://doi.org/10.1021/jacs.8b13392>.
- (184) Aristidou, N.; Sanchez-Molina, I.; Chotchuangchutchaval, T.; Brown, M.; Martinez, L.; Rath, T.; Haque, S. A. The Role of Oxygen in the Degradation of Methylammonium Lead Trihalide Perovskite Photoactive Layers. *Angew. Chem. Int. Ed.* **2015**, *54* (28), 8208–8212. <https://doi.org/10.1002/anie.201503153>.
- (185) Ouyang, Y.; Shi, L.; Li, Q.; Wang, J. Role of Water and Defects in Photo-Oxidative Degradation of Methylammonium Lead Iodide Perovskite. *Small Methods* **2019**, *3* (7), 1900154. <https://doi.org/10.1002/smt.201900154>.
- (186) Rajendra Kumar, G.; Dennyson Savariraj, A.; Karthick, S. N.; Selvam, S.; Balamuralitharan, B.; Kim, H.-J.; Viswanathan, K. K.; Vijaykumar, M.; Prabakar, K. Phase Transition Kinetics and Surface Binding States of Methylammonium Lead Iodide Perovskite. *Phys. Chem. Chem. Phys.* **2016**, *18* (10), 7284–7292. <https://doi.org/10.1039/C5CP06232B>.
- (187) Godding, J. S. W.; Ramadan, A. J.; Lin, Y.-H.; Schutt, K.; Snaith, H. J.; Wenger, B. Oxidative Passivation of Metal Halide Perovskites. *Joule* **2019**, *3* (11), 2716–2731. <https://doi.org/10.1016/j.joule.2019.08.006>.
- (188) Siegler, T. D.; Dunlap-Shohl, W. A.; Meng, Y.; Yang, Y.; Kau, W. F.; Sunkari, P. P.; Tsai, C. E.; Armstrong, Z. J.; Chen, Y.-C.; Beck, D. A. C.; Meilä, M.; Hillhouse, H. W. Water-Accelerated Photooxidation of CH₃NH₃PbI₃ Perovskite. *J. Am. Chem. Soc.* **2022**, *144* (12), 5552–5561. <https://doi.org/10.1021/jacs.2c00391>.
- (189) Moot, T.; Dikova, D. R.; Hazarika, A.; Schloemer, T. H.; Habisreutinger, S. N.; Leick, N.; Dunfield, S. P.; Rosales, B. A.; Harvey, S. P.; Pfeilsticker, J. R.; Teeter, G.; Wheeler, L. M.; Larson, B. W.; Luther, J. M. Beyond Strain: Controlling the Surface Chemistry of CsPbI₃ Nanocrystal Films for Improved Stability against Ambient Reactive Oxygen Species. *Chem. Mater.* **2020**, *32* (18), 7850–7860. <https://doi.org/10.1021/acs.chemmater.0c02543>.

- (190) Lahiri, N.; Song, D.; Zhang, X.; Huang, X.; Stoerzinger, K. A.; Carvalho, O. Q.; Adiga, P. P.; Blum, M.; Rosso, K. M. Interplay between Facets and Defects during the Dissociative and Molecular Adsorption of Water on Metal Oxide Surfaces. *J. Am. Chem. Soc.* **2023**, *145* (5), 2930–2940. <https://doi.org/10.1021/jacs.2c11291>.
- (191) Cheng, S.; Zhong, H. What Happens When Halide Perovskites Meet with Water? *J. Phys. Chem. Lett.* **2022**, *13* (10), 2281–2290. <https://doi.org/10.1021/acs.jpcclett.2c00166>.
- (192) Caddeo, C.; Saba, M. I.; Meloni, S.; Filippetti, A.; Mattoni, A. Collective Molecular Mechanisms in the $\text{CH}_3\text{NH}_3\text{PbI}_3$ Dissolution by Liquid Water. *ACS Nano* **2017**, *11* (9), 9183–9190. <https://doi.org/10.1021/acsnano.7b04116>.
- (193) Raval, P.; Kennard, R. M.; Vasileiadou, E. S.; Dahlman, C. J.; Spanopoulos, I.; Chabiny, M. L.; Kanatzidis, M.; Manjunatha Reddy, G. N. Understanding Instability in Formamidinium Lead Halide Perovskites: Kinetics of Transformative Reactions at Grain and Subgrain Boundaries. *ACS Energy Lett.* **2022**, *7* (4), 1534–1543. <https://doi.org/10.1021/acsenerylett.2c00140>.
- (194) Frost, J. M.; Butler, K. T.; Brivio, F.; Hendon, C. H.; Van Schilfgaarde, M.; Walsh, A. Atomistic Origins of High-Performance in Hybrid Halide Perovskite Solar Cells. *Nano Lett.* **2014**, *14* (5), 2584–2590. <https://doi.org/10.1021/nl500390f>.
- (195) Caddeo, C.; Marongiu, D.; Meloni, S.; Filippetti, A.; Quochi, F.; Saba, M.; Mattoni, A. Hydrophilicity and Water Contact Angle on Methylammonium Lead Iodide. *Adv. Mater. Interfaces* **2018**, 1801173. <https://doi.org/10.1002/admi.201801173>.
- (196) Meggiolaro, D.; Mosconi, E.; De Angelis, F. Mechanism of Reversible Trap Passivation by Molecular Oxygen in Lead-Halide Perovskites. *ACS Energy Lett.* **2017**, *2* (12), 2794–2798. <https://doi.org/10.1021/acsenerylett.7b00955>.
- (197) Walsh, A.; Scanlon, D. O.; Chen, S.; Gong, X. G.; Wei, S.-H. Self-Regulation Mechanism for Charged Point Defects in Hybrid Halide Perovskites. *Angewandte Chemie International Edition* **2015**, *54* (6), 1791–1794. <https://doi.org/10.1002/anie.201409740>.
- (198) Conings, B.; Drijkoningen, J.; Gauquelin, N.; Babayigit, A.; D'Haen, J.; D'Olieslaeger, L.; Ethirajan, A.; Verbeeck, J.; Manca, J.; Mosconi, E.; Angelis, F. D.; Boyen, H.-G. Intrinsic Thermal Instability of Methylammonium Lead Trihalide Perovskite. *Advanced Energy Materials* **2015**, *5* (15), 1500477. <https://doi.org/10.1002/aenm.201500477>.
- (199) Wang, Q.; Abate, A. Strategies toward Stable Perovskite Solar Cells. *Advanced Materials Interfaces* **2018**, *5* (22), 1800264. <https://doi.org/10.1002/admi.201800264>.
- (200) Hu, Y.; Schlipf, J.; Wussler, M.; Petrus, M. L.; Jaegermann, W.; Bein, T.; Müller-Buschbaum, P.; Docampo, P. Hybrid Perovskite/Perovskite Heterojunction Solar Cells. *ACS Nano* **2016**, *10*, 5999–6007. <https://doi.org/10.1021/acsnano.6b01535>.
- (201) Wang, Z.; Lin, Q.; Chmiel, F. P.; Sakai, N.; Herz, L. M.; Snaith, H. J. Efficient Ambient-Air-Stable Solar Cells with 2D–3D Heterostructured Butylammonium-Caesium-

- Formamidinium Lead Halide Perovskites. *Nature Energy* **2017**, *2* (9), 17135. <https://doi.org/10.1038/nenergy.2017.135>.
- (202) Li, N.; Zhu, Z.; Chueh, C. C.; Liu, H.; Peng, B.; Petrone, A.; Li, X.; Wang, L.; Jen, A. K. Y. Mixed Cation FA_xPEA_{1-x}PbI₃ with Enhanced Phase and Ambient Stability toward High-Performance Perovskite Solar Cells. *Advanced Energy Materials* **2017**, *7* (1). <https://doi.org/10.1002/aenm.201601307>.
- (203) Lee, J. W.; Dai, Z.; Han, T. H.; Choi, C.; Chang, S. Y.; Lee, S. J.; De Marco, N.; Zhao, H.; Sun, P.; Huang, Y.; Yang, Y. 2D Perovskite Stabilized Phase-Pure Formamidinium Perovskite Solar Cells. *Nature Communications* **2018**, *9* (1), 1–10. <https://doi.org/10.1038/s41467-018-05454-4>.
- (204) Chen, P.; Bai, Y.; Wang, S.; Lyu, M.; Yun, J. H.; Wang, L. In Situ Growth of 2D Perovskite Capping Layer for Stable and Efficient Perovskite Solar Cells. *Advanced Functional Materials* **2018**, *28* (17). <https://doi.org/10.1002/adfm.201706923>.
- (205) Hartono, N. T. P.; Thapa, J.; Tiihonen, A.; Oviedo, F.; Batali, C.; Yoo, J. J.; Liu, Z.; Li, R.; Marrón, D. F.; Bawendi, M. G.; Buonassisi, T.; Sun, S. How Machine Learning Can Help Select Capping Layers to Suppress Perovskite Degradation. *Nature Communications* **2020**, *11* (1), 1–9. <https://doi.org/10.1038/s41467-020-17945-4>.
- (206) Song, S.; Yang, S. J.; Choi, J.; Han, S. G.; Park, K.; Lee, H.; Min, J.; Ryu, S.; Cho, K. Surface Stabilization of a Formamidinium Perovskite Solar Cell Using Quaternary Ammonium Salt. *ACS Applied Materials and Interfaces* **2021**, *13* (31), 37052–37062. <https://doi.org/10.1021/acsami.1c07690>.
- (207) Byravnand, M. M.; Saliba, M. Defect Passivation of Perovskite Films for Highly Efficient and Stable Solar Cells. *Solar RRL* **2021**, *5* (8). <https://doi.org/10.1002/solr.202100295>.
- (208) Song, S.; Yang, S. J.; Choi, W.; Lee, H.; Sung, W.; Park, C.; Cho, K. Molecular Engineering of Organic Spacer Cations for Efficient and Stable Formamidinium Perovskite Solar Cell. *Advanced Energy Materials* **2020**, *10* (42), 1–10. <https://doi.org/10.1002/aenm.202001759>.
- (209) Jiang, Q.; Zhao, Y.; Zhang, X.; Yang, X.; Chen, Y.; Chu, Z.; Ye, Q.; Li, X.; Yin, Z.; You, J. Surface Passivation of Perovskite Film for Efficient Solar Cells. *Nature Photonics* **2019**, *13* (7), 460–466. <https://doi.org/10.1038/s41566-019-0398-2>.
- (210) Hoye, R. L. Z.; Hidalgo, J.; Jagt, R. A.; Correa-Baena, J. P.; Fix, T.; MacManus-Driscoll, J. L. The Role of Dimensionality on the Optoelectronic Properties of Oxide and Halide Perovskites, and Their Halide Derivatives. *Advanced Energy Materials* **2022**, *12* (4). <https://doi.org/10.1002/aenm.202100499>.
- (211) Hartono, N. T. P.; Tremblay, M. H.; Wiegold, S.; Dou, B.; Thapa, J.; Tiihonen, A.; Bulovic, V.; Nienhaus, L.; Marder, S. R.; Buonassisi, T.; Sun, S. Tailoring Capping-Layer Composition for Improved Stability of Mixed-Halide Perovskites. *Journal of Materials Chemistry A* **2022**, *10* (6), 2957–2965. <https://doi.org/10.1039/d1ta07870d>.

- (212) Thrithamarassery Gangadharan, D.; Ma, D. Searching for Stability at Lower Dimensions: Current Trends and Future Prospects of Layered Perovskite Solar Cells. *Energy and Environmental Science* **2019**, *12* (10), 2860–2889. <https://doi.org/10.1039/c9ee01591d>.
- (213) Kore, B. P.; Zhang, W.; Hoogendoorn, B. W.; Safdari, M.; Gardner, J. M. Moisture Tolerant Solar Cells by Encapsulating 3D Perovskite with Long-Chain Alkylammonium Cation-Based 2D Perovskite. *Communications Materials* **2021**, *2* (1), 1–10. <https://doi.org/10.1038/s43246-021-00200-8>.
- (214) Wang, H.; Bian, H.; Jin, Z.; Liang, L.; Bai, D.; Wang, Q.; Liu, S. F. Synergy of Hydrophobic Surface Capping and Lattice Contraction for Stable and High-Efficiency Inorganic CsPbI₂Br Perovskite Solar Cells. *Solar RRL* **2018**, *2* (12), 1–7. <https://doi.org/10.1002/solr.201800216>.
- (215) An, Y.; Hidalgo, J.; Perini, C. A. R.; Castro-Méndez, A. F.; Vagott, J. N.; Bairley, K.; Wang, S.; Li, X.; Correa-Baena, J. P. Structural Stability of Formamidinium- And Cesium-Based Halide Perovskites. *ACS Energy Letters* **2021**, *6* (5), 1942–1969. <https://doi.org/10.1021/acseenergylett.1c00354>.
- (216) Masi, S.; Gualdrón-Reyes, A. F.; Mora-Seró, I. Stabilization of Black Perovskite Phase in FAPbI₃ and CsPbI₃. *ACS Energy Letters* **2020**, *5* (6), 1974–1985. <https://doi.org/10.1021/acseenergylett.0c00801>.
- (217) Salim, K. M. M.; Masi, S.; Gualdrón-Reyes, A. F.; Sánchez, R. S.; Barea, E. M.; Krečmarová, M.; Sánchez-Royo, J. F.; Mora-Seró, I. Boosting Long-Term Stability of Pure Formamidinium Perovskite Solar Cells by Ambient Air Additive Assisted Fabrication. *ACS Energy Letters* **2021**, *6* (10), 3511–3521. <https://doi.org/10.1021/acseenergylett.1c01311>.
- (218) Hui, W.; Chao, L.; Lu, H.; Xia, F.; Wei, Q.; Su, Z.; Niu, T.; Tao, L.; Du, B.; Li, D.; Wang, Y.; Dong, H.; Zuo, S.; Li, B.; Shi, W.; Ran, X.; Li, P.; Zhang, H.; Wu, Z.; Ran, C.; Song, L.; Xing, G.; Gao, X.; Zhang, J.; Xia, Y.; Chen, Y.; Huang, W. Stabilizing Black-Phase Formamidinium Perovskite Formation at Room Temperature and High Humidity. *Science* **2021**, *371* (6536), 1359–1364. <https://doi.org/10.1126/science.abf7652>.
- (219) Kim, M.; Kim, G. H.; Lee, T. K.; Choi, I. W.; Choi, H. W.; Jo, Y.; Yoon, Y. J.; Kim, J. Y. J. W. J. Y. J. W.; Lee, J.; Huh, D.; Lee, H.; Kwak, S. K.; Kim, J. Y. J. W. J. Y. J. W.; Kim, D. S. Methylammonium Chloride Induces Intermediate Phase Stabilization for Efficient Perovskite Solar Cells. *Joule* **2019**, *3* (9), 2179–2192. <https://doi.org/10.1016/j.joule.2019.06.014>.
- (220) Zhou, Y.; Herz, L. M.; Jen, A. K.; Saliba, M. Advances and Challenges in Understanding the Microscopic Structure–Property–Performance Relationship in Perovskite Solar Cells. *Nature Energy* **2022**. <https://doi.org/10.1038/s41560-022-01096-5>.
- (221) Gratia, P.; Zimmermann, I.; Schouwink, P.; Yum, J. H.; Audinot, J. N.; Sivula, K.; Wirtz, T.; Nazeeruddin, M. K. The Many Faces of Mixed Ion Perovskites: Unraveling and Understanding the Crystallization Process. *ACS Energy Letters* **2017**, *2* (12), 2686–2693. <https://doi.org/10.1021/acseenergylett.7b00981>.

- (222) Gratia, P.; Zimmermann, I.; Schouwink, P.; Yum, J. H.; Audinot, J. N.; Sivula, K.; Wirtz, T.; Nazeeruddin, M. K. The Many Faces of Mixed Ion Perovskites: Unraveling and Understanding the Crystallization Process. *ACS Energy Letters* **2017**, *2* (12), 2686–2693. <https://doi.org/10.1021/acsenergylett.7b00981>.
- (223) Stoumpos, C. C.; Cao, D. H.; Clark, D. J.; Young, J.; Rondinelli, J. M.; Jang, J. I.; Hupp, J. T.; Kanatzidis, M. G. Ruddlesden-Popper Hybrid Lead Iodide Perovskite 2D Homologous Semiconductors. *Chemistry of Materials* **2016**, *28* (8), 2852–2867. <https://doi.org/10.1021/acs.chemmater.6b00847>.
- (224) Cao, D. H.; Stoumpos, C. C.; Farha, O. K.; Hupp, J. T.; Kanatzidis, M. G. 2D Homologous Perovskites as Light-Absorbing Materials for Solar Cell Applications. *Journal of the American Chemical Society* **2015**, *137* (24), 7843–7850. <https://doi.org/10.1021/jacs.5b03796>.
- (225) Duim, H.; Adjokatse, S.; Kahmann, S.; ten Brink, G. H.; Loi, M. A. The Impact of Stoichiometry on the Photophysical Properties of Ruddlesden–Popper Perovskites. *Advanced Functional Materials* **2020**, *30* (5). <https://doi.org/10.1002/adfm.201907505>.
- (226) Marchenko, E. I.; Fateev, S. A.; Petrov, A. A.; Korolev, V. V.; Mitrofanov, A.; Petrov, A. V.; Goodilin, E. A.; Tarasov, A. B. Database of Two-Dimensional Hybrid Perovskite Materials: Open-Access Collection of Crystal Structures, Band Gaps, and Atomic Partial Charges Predicted by Machine Learning. *Chem. Mater.* **2020**, *32* (17), 7383–7388. <https://doi.org/10.1021/acs.chemmater.0c02290>.
- (227) Perini, C. A. R.; Rojas-Gatjens, E.; Ravello, M.; Castro-Mendez, A.-F.; Hidalgo, J.; An, Y.; Kim, S.; Lai, B.; Li, R.; Silva-Acuña, C.; Correa-Baena, J.-P. Interface Reconstruction from Ruddlesden–Popper Structures Impacts Stability in Lead Halide Perovskite Solar Cells. *Advanced Materials* **2022**, *34* (51), 2204726. <https://doi.org/10.1002/adma.202204726>.
- (228) Jacobsson, T. J.; Correa-Baena, J. P.; Halvani Anaraki, E.; Philippe, B.; Stranks, S. D.; Bouduban, M. E. F.; Tress, W.; Schenk, K.; Teuscher, J.; Moser, J. E.; Rensmo, H.; Hagfeldt, A. Unreacted PbI₂ as a Double-Edged Sword for Enhancing the Performance of Perovskite Solar Cells. *Journal of the American Chemical Society* **2016**, *138* (32), 10331–10343. <https://doi.org/10.1021/jacs.6b06320>.
- (229) Park, B. Wook; Kwon, H. W.; Lee, Y.; Lee, D. Y.; Kim, M. G.; Kim, G.; Kim, K. Jeong; Kim, Y. K.; Im, J.; Shin, T. J.; Seok, S. Il. Stabilization of Formamidinium Lead Triiodide α -Phase with Isopropylammonium Chloride for Perovskite Solar Cells. *Nature Energy* **2021**, *6* (8), 848. <https://doi.org/10.1038/s41560-021-00844-3>.
- (230) Cordero, F.; Craciun, F.; Trequattrini, F.; Generosi, A.; Paci, B.; Paoletti, A. M.; Pennesi, G. Stability of Cubic FAPbI₃ from X-Ray Diffraction, Anelastic, and Dielectric Measurements. *Journal of Physical Chemistry Letters* **2019**, *10* (10), 2463–2469. <https://doi.org/10.1021/acs.jpcllett.9b00896>.
- (231) deQuilettes, D. W.; Vorpahl, S. M.; Stranks, S. D.; Nagaoka, H.; Eperon, G. E.; Ziffer, M. E.; Snaith, H. J.; Ginger, D. S.; Quilettes, D. W. de; Vorpahl, S. M.; Stranks, S. D.;

- Nagaoka, H.; Eperon, G. E.; Ziffer, M. E.; Snaith, H. J.; Ginger, D. S.; deQuilettes, D. W.; Vorpahl, S. M.; Stranks, S. D.; Nagaoka, H.; Eperon, G. E.; Ziffer, M. E.; Snaith, H. J.; Ginger, D. S. Impact of Microstructure on Local Carrier Lifetime in Perovskite Solar Cells. *Science* **2015**, *348* (6235), 683–686. <https://doi.org/10.1126/science.aaa5333>.
- (232) Son, D. Y.; Lee, J. W.; Choi, Y. J.; Jang, I. H.; Lee, S.; Yoo, P. J.; Shin, H.; Ahn, N.; Choi, M.; Kim, D.; Park, N. G. Self-Formed Grain Boundary Healing Layer for Highly Efficient CH₃ NH₃ PbI₃ Perovskite Solar Cells. *Nature Energy* **2016**, *1* (7), 1–8. <https://doi.org/10.1038/nenergy.2016.81>.
- (233) Erodici, M. P.; Pierone, P. J.; Hartono, N. T. P.; Hidalgo, J.; Lai, B.; Buonassisi, T.; Correa-Baena, J. P.; Sher, M. J. Enhanced Charge Carrier Lifetime and Mobility as a Result of Rb and Cs Incorporation in Hybrid Perovskite. *Applied Physics Letters* **2021**, *118* (6). <https://doi.org/10.1063/5.0030206>.
- (234) Rehman, W.; Milot, R. L.; Eperon, G. E.; Wehrenfennig, C.; Boland, J. L.; Snaith, H. J.; Johnston, M. B.; Herz, L. M. Charge-Carrier Dynamics and Mobilities in Formamidinium Lead Mixed-Halide Perovskites. *Advanced Materials* **2015**, *27* (48), 7938–7944. <https://doi.org/10.1002/adma.201502969>.
- (235) Knight, A. J.; Wright, A. D.; Patel, J. B.; McMeekin, D. P.; Snaith, H. J.; Johnston, M. B.; Herz, L. M. Electronic Traps and Phase Segregation in Lead Mixed-Halide Perovskite. *ACS Energy Letters* **2019**, *4* (1), 75–84. <https://doi.org/10.1021/acscenergylett.8b02002>.
- (236) Wang, Q.; Dong, Q.; Li, T.; Gruverman, A.; Huang, J. Thin Insulating Tunneling Contacts for Efficient and Water-Resistant Perovskite Solar Cells. *Advanced Materials* **2016**, *28* (31), 6734–6739. <https://doi.org/10.1002/adma.201600969>.
- (237) Manser, J. S.; Saidaminov, M. I.; Christians, J. A.; Bakr, O. M.; Kamat, P. V. Making and Breaking of Lead Halide Perovskites. *Accounts of Chemical Research* **2016**, *49* (2), 330–338. <https://doi.org/10.1021/acs.accounts.5b00455>.
- (238) *Best Research-Cell Efficiency Chart | Photovoltaic Research | NREL*. <https://www.nrel.gov/pv/cell-efficiency.html> (accessed 2021-03-19).
- (239) Christians, J. A.; Schulz, P.; Tinkham, J. S.; Schloemer, T. H.; Harvey, S. P.; Tremolet de Villers, B. J.; Sellinger, A.; Berry, J. J.; Luther, J. M. Tailored Interfaces of Unencapsulated Perovskite Solar Cells for >1,000 Hour Operational Stability. *Nat Energy* **2018**, *3* (1), 68–74. <https://doi.org/10.1038/s41560-017-0067-y>.
- (240) Yang, S.; Chen, S.; Mosconi, E.; Fang, Y.; Xiao, X.; Wang, C.; Zhou, Y.; Yu, Z.; Zhao, J.; Gao, Y.; De Angelis, F.; Huang, J. Stabilizing Halide Perovskite Surfaces for Solar Cell Operation with Wide-Bandgap Lead Oxysalts. *Science* **2019**, *365* (6452), 473–478. <https://doi.org/10.1126/science.aax3294>.
- (241) Steele, J. A.; Jin, H.; Dovgaliuk, I.; Berger, R. F.; Braeckevelt, T.; Yuan, H.; Martin, C.; Solano, E.; Lejaeghere, K.; Rogge, S. M. J.; Notebaert, C.; Vandezande, W.; Janssen, K. P. F.; Goderis, B.; Debroye, E.; Wang, Y.-K.; Dong, Y.; Ma, D.; Saidaminov, M.; Tan, H.; Lu, Z.; Dyadkin, V.; Chernyshov, D.; Van Speybroeck, V.; Sargent, E. H.; Hofkens,

- J.; Roeffaers, M. B. J. Thermal Unequilibrium of Strained Black CsPbI₃ Thin Films. *Science* **2019**, *365* (6454), 679–684. <https://doi.org/10.1126/science.aax3878>.
- (242) Songvilay, M.; Giles-Donovan, N.; Bari, M.; Ye, Z.-G.; Minns, J. L.; Green, M. A.; Xu, G.; Gehring, P. M.; Schmalzl, K.; Ratcliff, W. D.; Brown, C. M.; Chernyshov, D.; Van Beek, W.; Cochran, S.; Stock, C. Common Acoustic Phonon Lifetimes in Inorganic and Hybrid Lead Halide Perovskites. *Phys. Rev. Materials* **2019**, *3* (9), 093602. <https://doi.org/10.1103/PhysRevMaterials.3.093602>.
- (243) Lehmann, F.; Franz, A.; Többens, D. M.; Levenco, S.; Unold, T.; Taubert, A.; Schorr, S. The Phase Diagram of a Mixed Halide (Br, I) Hybrid Perovskite Obtained by Synchrotron X-Ray Diffraction. *RSC Adv.* **2019**, *9* (20), 11151–11159. <https://doi.org/10.1039/C8RA09398A>.
- (244) Mozur, E. M.; Hope, M. A.; Trowbridge, J. C.; Halat, D. M.; Daemen, L. L.; Maughan, A. E.; Prisk, T. R.; Grey, C. P.; Neilson, J. R. Cesium Substitution Disrupts Concerted Cation Dynamics in Formamidinium Hybrid Perovskites. *Chem. Mater.* **2020**, *32* (14), 6266–6277. <https://doi.org/10.1021/acs.chemmater.0c01862>.
- (245) Simenas, M.; Balciunas, S.; Wilson, J. N.; Svirskas, S.; Kinka, M.; Garbaras, A.; Kalendra, V.; Gagor, A.; Szewczyk, D.; Sieradzki, A.; Maczka, M.; Samulionis, V.; Walsh, A.; Grigalaitis, R.; Banys, J. Suppression of Phase Transitions and Glass Phase Signatures in Mixed Cation Halide Perovskites. *Nat Commun* **2020**, *11* (1), 5103. <https://doi.org/10.1038/s41467-020-18938-z>.
- (246) Ray, A.; Martín-García, B.; Moliterni, A.; Casati, N.; Boopathi, K. M.; Spirito, D.; Goldoni, L.; Prato, M.; Giacobbe, C.; Giannini, C.; Di Stasio, F.; Krahne, R.; Manna, L.; Abdelhady, A. L. Mixed Dimethylammonium/Methylammonium Lead Halide Perovskite Crystals for Improved Structural Stability and Enhanced Photodetection. *Advanced Materials* **2022**, *34* (7), 2106160. <https://doi.org/10.1002/adma.202106160>.
- (247) Lee, J.-W.; Kim, D.-H.; Kim, H.-S.; Seo, S.-W.; Cho, S. M.; Park, N.-G. Formamidinium and Cesium Hybridization for Photo- and Moisture-Stable Perovskite Solar Cell. *Advanced Energy Materials* **2015**, *5* (20), 1501310. <https://doi.org/10.1002/aenm.201501310>.
- (248) Amat, A.; Mosconi, E.; Ronca, E.; Quarti, C.; Umari, P.; Nazeeruddin, Md. K.; Grätzel, M.; De Angelis, F. Cation-Induced Band-Gap Tuning in Organohalide Perovskites: Interplay of Spin–Orbit Coupling and Octahedra Tilting. *Nano Lett.* **2014**, *14* (6), 3608–3616. <https://doi.org/10.1021/nl5012992>.
- (249) Francisco-López, A.; Charles, B.; Alonso, M. I.; Garriga, M.; Campoy-Quiles, M.; Weller, M. T.; Goñi, A. R. Phase Diagram of Methylammonium/Formamidinium Lead Iodide Perovskite Solid Solutions from Temperature-Dependent Photoluminescence and Raman Spectroscopies. *J. Phys. Chem. C* **2020**, *124* (6), 3448–3458. <https://doi.org/10.1021/acs.jpcc.9b10185>.

- (250) Šimėnas, M.; Balčiūnas, S.; Svirskas, Š.; Kinka, M.; Ptak, M.; Kalendra, V.; Gagor, A.; Szewczyk, D.; Sieradzki, A.; Grigalaitis, R.; Walsh, A.; Maćzka, M.; Banys, J. Phase Diagram and Cation Dynamics of Mixed $MA_{1-x}FA_xPbBr_3$ Hybrid Perovskites. *Chem. Mater.* **2021**, *33* (15), 5926–5934. <https://doi.org/10.1021/acs.chemmater.1c00885>.
- (251) Mozur, E. M.; Maughan, A. E.; Cheng, Y.; Huq, A.; Jalarvo, N.; Daemen, L. L.; Neilson, J. R. Orientational Glass Formation in Substituted Hybrid Perovskites. *Chem. Mater.* **2017**, *29* (23), 10168–10177. <https://doi.org/10.1021/acs.chemmater.7b04017>.
- (252) Yang, B.; Ming, W.; Du, M.-H.; Keum, J. K.; Puretzky, A. A.; Rouleau, C. M.; Huang, J.; Geohegan, D. B.; Wang, X.; Xiao, K. Real-Time Observation of Order-Disorder Transformation of Organic Cations Induced Phase Transition and Anomalous Photoluminescence in Hybrid Perovskites. *Advanced Materials* **2018**, *30* (22), 1705801. <https://doi.org/10.1002/adma.201705801>.
- (253) Gao, F.; Zhao, Q. Facet Engineering: A Promising Pathway toward Highly Efficient and Stable Perovskite Photovoltaics. *J. Phys. Chem. Lett.* **2023**, *14* (19), 4409–4418. <https://doi.org/10.1021/acs.jpcclett.3c00709>.
- (254) Giannozzi, P.; Baroni, S.; Bonini, N.; Calandra, M.; Car, R.; Cavazzoni, C.; Ceresoli, D.; Chiarotti, G. L.; Cococcioni, M.; Dabo, I.; Dal Corso, A.; de Gironcoli, S.; Fabris, S.; Fratesi, G.; Gebauer, R.; Gerstmann, U.; Gougoussis, C.; Kokalj, A.; Lazzeri, M.; Martin-Samos, L.; Marzari, N.; Mauri, F.; Mazzarello, R.; Paolini, S.; Pasquarello, A.; Paulatto, L.; Sbraccia, C.; Scandolo, S.; Sclauzero, G.; Seitsonen, A. P.; Smogunov, A.; Umari, P.; Wentzcovitch, R. M. QUANTUM ESPRESSO: A Modular and Open-Source Software Project for Quantum Simulations of Materials. *J. Phys.: Condens. Matter* **2009**, *21* (39), 395502. <https://doi.org/10.1088/0953-8984/21/39/395502>.
- (255) Giannozzi, P.; Andreussi, O.; Brumme, T.; Bunau, O.; Buongiorno Nardelli, M.; Calandra, M.; Car, R.; Cavazzoni, C.; Ceresoli, D.; Cococcioni, M.; Colonna, N.; Carnimeo, I.; Dal Corso, A.; de Gironcoli, S.; Delugas, P.; DiStasio, R. A.; Ferretti, A.; Floris, A.; Fratesi, G.; Fugallo, G.; Gebauer, R.; Gerstmann, U.; Giustino, F.; Gorni, T.; Jia, J.; Kawamura, M.; Ko, H.-Y.; Kokalj, A.; Küçükbenli, E.; Lazzeri, M.; Marsili, M.; Marzari, N.; Mauri, F.; Nguyen, N. L.; Nguyen, H.-V.; Otero-de-la-Roza, A.; Paulatto, L.; Poncé, S.; Rocca, D.; Sabatini, R.; Santra, B.; Schlipf, M.; Seitsonen, A. P.; Smogunov, A.; Timrov, I.; Thonhauser, T.; Umari, P.; Vast, N.; Wu, X.; Baroni, S. Advanced Capabilities for Materials Modelling with Quantum ESPRESSO. *J. Phys.: Condens. Matter* **2017**, *29* (46), 465901. <https://doi.org/10.1088/1361-648X/aa8f79>.
- (256) Guo, Y.; Li, C.; Li, X.; Niu, Y.; Hou, S.; Wang, F. Effects of Rb Incorporation and Water Degradation on the Stability of the Cubic Formamidinium Lead Iodide Perovskite Surface: A First-Principles Study. *J. Phys. Chem. C* **2017**, *121* (23), 12711–12717. <https://doi.org/10.1021/acs.jpcc.7b01390>.
- (257) Moon, J.; Kwon, S.; Alahbakhshi, M.; Lee, Y.; Cho, K.; Zakhidov, A.; Kim, M. J.; Gu, Q. Surface Energy-Driven Preferential Grain Growth of Metal Halide Perovskites: Effects of Nanoimprint Lithography Beyond Direct Patterning. *ACS Appl. Mater. Interfaces* **2021**, *13* (4), 5368–5378. <https://doi.org/10.1021/acsami.0c17655>.

- (258) Cullity, B. D.; Stock, S. R. *Elements of X-Ray Diffraction*, Third edit.; Pearson Education Limited: London, 2014.
- (259) Sheridan, A. K.; Anwar, J. Kinetics of the Solid-State Phase Transformation of Form β to γ of Sulfanilamide Using Time-Resolved Energy-Dispersive X-Ray Diffraction. *Chem. Mater.* **1996**, *8* (5), 1042–1051. <https://doi.org/10.1021/cm950349z>.
- (260) Gil-González, E.; Perejón, A.; Sánchez-Jiménez, P. E.; Medina-Carrasco, S.; Kupčík, J.; Šubrt, J.; Criado, J. M.; Pérez-Maqueda, L. A. Crystallization Kinetics of Nanocrystalline Materials by Combined X-Ray Diffraction and Differential Scanning Calorimetry Experiments. *Crystal Growth & Design* **2018**, *18* (5), 3107–3116. <https://doi.org/10.1021/acs.cgd.8b00241>.
- (261) Qin, M.; Xue, H.; Zhang, H.; Hu, H.; Liu, K.; Li, Y.; Qin, Z.; Ma, J.; Zhu, H.; Yan, K.; Fang, G.; Li, G.; Jeng, U.; Brocks, G.; Tao, S.; Lu, X. Precise Control of Perovskite Crystallization Kinetics via Sequential A-Site Doping. *Adv. Mater.* **2020**, *32* (42), 2004630. <https://doi.org/10.1002/adma.202004630>.
- (262) Ciria-Ramos, I.; Navascués, N.; Diaw, F.; Furgeaud, C.; Arenal, R.; Ansón-Casaos, A.; Haro, M.; Juárez-Perez, E. J. Formamidinium Halide Salts as Precursors of Carbon Nitrides. *Carbon* **2022**, *196*, 1035–1046. <https://doi.org/10.1016/j.carbon.2022.05.051>.
- (263) Solanki, A.; Tavakoli, M. M.; Xu, Q.; Dintakurti, S. S. H.; Lim, S. S.; Bagui, A.; Hanna, J. V.; Kong, J.; Sum, T. C. Heavy Water Additive in Formamidinium: A Novel Approach to Enhance Perovskite Solar Cell Efficiency. *Advanced Materials* **2020**, *32* (23), 1907864. <https://doi.org/10.1002/adma.201907864>.
- (264) Hills-Kimball, K.; Nagaoka, Y.; Cao, C.; Chaykovsky, E.; Chen, O. Synthesis of Formamidinium Lead Halide Perovskite Nanocrystals through Solid–Liquid–Solid Cation Exchange. *J. Mater. Chem. C* **2017**, *5* (23), 5680–5684. <https://doi.org/10.1039/C7TC00598A>.
- (265) Yu, X.; Qin, Y.; Peng, Q. Probe Decomposition of Methylammonium Lead Iodide Perovskite in N_2 and O_2 by in Situ Infrared Spectroscopy. *J. Phys. Chem. A* **2017**, *121* (6), 1169–1174. <https://doi.org/10.1021/acs.jpca.6b12170>.
- (266) Perdew, J. P.; Burke, K.; Ernzerhof, M. Generalized Gradient Approximation Made Simple. *Phys. Rev. Lett.* **1996**, *77* (18), 3865–3868. <https://doi.org/10.1103/PhysRevLett.77.3865>.
- (267) Grimme, S.; Antony, J.; Ehrlich, S.; Krieg, H. A Consistent and Accurate *Ab Initio* Parametrization of Density Functional Dispersion Correction (DFT-D) for the 94 Elements H–Pu. *The Journal of Chemical Physics* **2010**, *132* (15), 154104. <https://doi.org/10.1063/1.3382344>.
- (268) Aron Walsh; elds22; Federico Brivio; Jarvist Moore Frost. WMD-Group/Hybrid-Perovskites: Collection 1, 2019. <https://doi.org/10.5281/zenodo.2641358>.

- (269) Yin, J.; Naphade, R.; Gutiérrez Arzaluz, L.; Brédas, J.-L.; Bakr, O. M.; Mohammed, O. F. Modulation of Broadband Emissions in Two-Dimensional $\langle 100 \rangle$ -Oriented Ruddlesden–Popper Hybrid Perovskites. *ACS Energy Lett.* **2020**, *5* (7), 2149–2155. <https://doi.org/10.1021/acsenergylett.0c01047>.
- (270) T. Kellersohn; E. Alici; D. Esser; H.D Lutz. Pb(IO₃)₂ - Das Erste Halogenat Eines Zweiwertigen Hauptgruppenmetalls Mit Schichtenstruktur- Kristallstruktur, IR- Und Ramanspektren. *Zeitschrift für Kristallographie* **1993**, No. 203, 225–233.
- (271) M. J. Frisch; et al. Gaussian 09: Revision D.01, 2016.
- (272) Cossi, M.; Rega, N.; Scalmani, G.; Barone, V. Energies, Structures, and Electronic Properties of Molecules in Solution with the C-PCM Solvation Model. *J. Comput. Chem.* **2003**, *24* (6), 669–681. <https://doi.org/10.1002/jcc.10189>.
- (273) Becke, A. D. Density-functional Thermochemistry. III. The Role of Exact Exchange. *The Journal of Chemical Physics* **1993**, *98* (7), 5648–5652. <https://doi.org/10.1063/1.464913>.
- (274) Wei, J.; Wang, Q.; Huo, J.; Gao, F.; Gan, Z.; Zhao, Q.; Li, H. Mechanisms and Suppression of Photoinduced Degradation in Perovskite Solar Cells. *Adv. Energy Mater.* **2021**, *11* (3), 2002326. <https://doi.org/10.1002/aenm.202002326>.
- (275) Hayyan, M.; Hashim, M. A.; AlNashef, I. M. Superoxide Ion: Generation and Chemical Implications. *Chem. Rev.* **2016**, *116* (5), 3029–3085. <https://doi.org/10.1021/acs.chemrev.5b00407>.
- (276) Ma, D.; Fu, Y.; Dang, L.; Zhai, J.; Guzei, I. A.; Jin, S. Single-Crystal Microplates of Two-Dimensional Organic–Inorganic Lead Halide Layered Perovskites for Optoelectronics. *Nano Res.* **2017**, *10* (6), 2117–2129. <https://doi.org/10.1007/s12274-016-1401-6>.
- (277) Straus, D. B.; Iotov, N.; Gau, M. R.; Zhao, Q.; Carroll, P. J.; Kagan, C. R. Longer Cations Increase Energetic Disorder in Excitonic 2D Hybrid Perovskites. *J. Phys. Chem. Lett.* **2019**, *10* (6), 1198–1205. <https://doi.org/10.1021/acs.jpcclett.9b00247>.